Doctoral Dissertation

博士論文

Dynamics and Symmetry Breaking of Collective Neutrino Oscillation in Core-Collapse Supernovae

(超新星爆発におけるニュートリノ集団振動のダイナミクスと非対称性)

A Dissertation Submitted for the Degree of Doctor of Philosophy

December 2021

令和 3 年 12 月 博士 (理学) 申請

Department of Astronomy, Graduate School of Science,

The University of Tokyo

東京大学大学院理学系研究科

天文学専攻

Masamichi Zaizen

財前 真理

Doctoral Dissertation

博士論文

Dynamics and Symmetry Breaking of Collective Neutrino Oscillation in Core-Collapse Supernovae

(超新星爆発におけるニュートリノ集団振動のダイナミクスと非対称性)

A Dissertation Submitted for the Degree of Doctor of Philosophy

December 2021

令和 3 年 12 月 博士 (理学) 申請

Department of Astronomy, Graduate School of Science,

The University of Tokyo

東京大学大学院理学系研究科

天文学専攻

Masamichi Zaizen

財前 真理

Supervisor:

- Professor Hideyuki Umeda

Committee in Charge:

- Professor Toshikazu Shigeyama, Chair
- Professor Tomonori Totani
- Professor Takeru Suzuki
- Professor Yudai Suwa
- Professor Shoichi Yamada

Abstract

Massive stars experience a core collapse and end their lives at the final stage of the stellar evolution. An enormous amount of neutrinos are released from the center and deposits the energy into the stalled shock wave to help the explosion. Neutrinos have essential roles in the explosion mechanism through neutrino heating. Neutrino observation from nearby core-collapse supernovae will help us to enrich our understanding of supernova physics. However, if neutrino oscillation interchanges different flavors, the flavor-dependent reactions can be modified. This dissertation presents the possibility and the impact of neutrino oscillation, mainly induced by the neutrino-neutrino interactions, inside the core-collapse supernovae.

In environments with high dense neutrino medium, such as core-collapse supernovae, the neutrino self-interaction can not be ignored and induce the nonlinear flavor mixing phenomenon called collective neutrino oscillation. This flavor conversion occurs at $\mathcal{O}(10 - 100)$ km near the proto-neutron star, and the phase space distribution among each flavor dramatically changes. Therefore, collective neutrino oscillation can potentially affect the neutrino signals, the explosive nucleosynthesis, and the explodability in core-collapse supernovae. However, the neutrino self-interactions are still poorly understood because the system is a complicated seven-dimensional problem. Many studies have adopted a simplified description, called the bulb model, to relax the complexity. Nevertheless, the flavor conversions demonstrate interesting spectral mixing features in the neutrino energy distribution. The non-trivial behaviors are in the spotlight, and the studies beyond the bulb model progress rapidly. Collective flavor instability is triggered if there exists a spectral crossing that the difference in the phase space distribution between neutrinos and antineutrinos changes the sign at some momentum. Currently, collective neutrino oscillation can be divided into two flavor instabilities: slow and fast modes. Slow flavor conversion is induced by a spectral crossing in the energy distribution, while fast one is by a crossing in the angular distributions.

In this dissertation, we report our studies on the development of slow and fast flavor conversion, respectively. The flavor evolution strongly depends on the assumption in the simulation system, and we focus on the dynamics and the symmetry breaking. First, we introduce the basic bulb model to simplify the neutrino self-interactions and demonstrate the flavor mixing phenomena. Then, we present the impacts beyond the bulb model.

The bulb model requires isotropic neutrino emission but demonstrates the most straightforward slow flavor conversions, called spectral splits that the energy distribution is swapped only above a critical energy. On the other hand, considering the global ge-

ometry effects, the collective effects can be suppressed by dense background matter. We find that collective neutrino oscillation is completely suppressed at all time epochs from the neutronization burst to the formation of a black hole under the high matter density profile in a failed supernova model. This model is an extreme case of core-collapse supernovae, but the suppression behaviors are probably general during the accretion phase. The neutrino self-interactions need to overcome the matter-induced phase dispersion to exhibit the collective flavor conversions. The bulb model calls for many assumptions, which inhibit the excitation of some flavor instabilities. Therefore, symmetry breaking induces a new collective instability and gives rise to more precise flavor conversions. Neutrino states are obtained as $\rho_\nu(r; E_\nu, \theta_\nu)$ in the traditional bulb model, but for the extended descriptions axial-symmetry breaking $(r; E_\nu, \theta_\nu, \varphi_\nu)$ and spatio-temporal symmetry breaking $(t; r, \Theta; E_\nu, \theta_\nu)$ are considered. Newly considered flavor instability can potentially overcome the matter suppression and induce the flavor conversions in the region where the complete matter suppression appears in the bulb model. Axial-symmetry breaking in direction provides a multi-azimuthal-angle instability and changes the geometry term of neutrino emission. We perform the first-ever three-flavor calculation of collective neutrino oscillation considering three-dimensional momentum space for an electron-capture supernova model with an $8.8M_\odot$ progenitor. By employing a realistic supernova model, not parametric neutrino properties, we find that the multi-azimuthal-angle instability partly breaks matter suppression and induces additional collective flavor conversions with three-flavor effects. Also, the translation symmetry breaking raises spatio-temporal instability in time and space. The inhomogeneity in time is the most likely to overcome the matter suppression. Still, we need to investigate the adiabatic growth of collective neutrino oscillation in detail for a realistic supernova model. In addition to the effects of symmetry breaking, the consideration of coherent neutrino-nucleus scattering also provides an impact beyond the bulb model. A small fraction of escaping neutrinos is scattered by the background nuclei and nucleons, changing the propagation direction. The direction-changing scattering generates a neutrino halo and makes intersection angles broader. If inward-scattered neutrinos can not be neglected, it is more challenging to compute the flavor conversion globally. On the other hand, if the contribution is minor compared to that from the outwardly propagating neutrino flux, we can treat it safely by extending the bulb description. We perform the first-ever numerical study of collective neutrino oscillation considering the neutrino halo for a $9.6M_\odot$ iron-core progenitor model. In our iron-core collapse supernova model, inwardly directed components can not be neglected in the region where the matter suppression is dominant. On the other hand, the outward contribution is dominant outside the shock front, and we can investigate the effects of the neutrino halo numerically. We find that halo neutrinos do not overcome the matter suppression but provide sharper spectral splits and delay the onset of collective neutrino oscillation.

Above the discussion is within the slow flavor conversion, and the isotropic angular distribution suppresses the fast instability. Fast flavor conversion is induced by a zero crossing in the neutrino lepton flavor number (NLFN) angular distribution. The angular

crossings are generated by various supernova dynamics and can locally excite the fast instability. In the preshock region of core-collapse supernovae, coherent neutrino-nucleus scattering forms the angular crossing in the backward direction due to the difference in the averaged energies between neutrinos and antineutrinos. If we consider the identical heavy-leptonic flavors $\nu_X = \bar{\nu}_X$, the electron lepton number (ELN) crossings induce the fast instability. On the other hand, in a realistic supernova model, microphysics breaks the condition, and non-zero μLN and τLN angular distributions appear. Muon production enhances the $\bar{\nu}_\mu$ emission and provides the strongly negative μLN angular distribution. We simulate the nonlinear flavor evolution with fast modes for the six-species angular distributions considering the microphysics. We find that fast instability is excited only in the $e - \tau$ sector and then propagates across the other sectors in the case including the vacuum mixing term. Also, we find for the first time the development of a cascade on spatial Fourier space due to the nonlinear mode coupling. Furthermore, we perform the flavor evolution for three types of angular distributions in a one-dimensional box with the (t, z, v_z) system. We find that a flavor wave excited during the linear phase propagates toward the positive-z direction and interacts with the backward-moving components. The nonlinear interference shifts the flavor waves from larger-scale to smaller-scale structures and establishes flavor equilibrium in space-averaging quantities. The flavor equilibrium is above or below the crossing direction and resembles the spectral splits in the slow flavor conversion. The description can be explained using the asymmetry ratio between neutrinos and antineutrinos. We can categorize the asymptotic behaviors by simulating fast flavor conversion for three types of angular distributions. In the case that the total number density of ν_e exceeds that of $\bar{\nu}_e$, fast flavor conversion seems to transfer the angular distribution from the positive ELN parts to the negative and makes the crossing shallower, following the global electron-family number conservation. In the case of the $\bar{\nu}_e$ excess, the contrary trends occur. If the description is universal, it will provide a crucial hint about incorporating fast flavor conversion to the core-collapse simulations.

Contents

List of Figures

List of Tables

Chapter 1

Introduction

1.1 Supernova neutrinos

In 1987, a supernova event emerged in the Large Magellanic Cloud at a distance of 50 kpc from the Milky Way. Neutrinos associated with the supernova event SN1987A were detected at Kamiokande-II [1, 2] in Japan and Irvine-Michigan-Brookhaven (IMB) detector [3] in the United States, which are both water Cherenkov detectors mainly sensitive to electron antineutrinos via the inverse-beta decay $\bar{\nu}_e + p \rightarrow e^+ n$. Electron scattering $\nu + e^- \rightarrow \nu + e^-$ is also a subdominant process in the detectors. Figure 1.1 shows the burst events of SN1987A in arrival time detected in the Kamiokande-II and the IMB detector [2]. The observed supernova neutrinos were only about 20 events within 13 seconds but sufficient for us to confirm our understanding of the stellar physics [4]. Many studies have estimated supernova properties such as neutrino luminosity, energy, and the emission duration from SN1987A [5–8]. The duration of electron antineutrinos in Kamiokande-II is

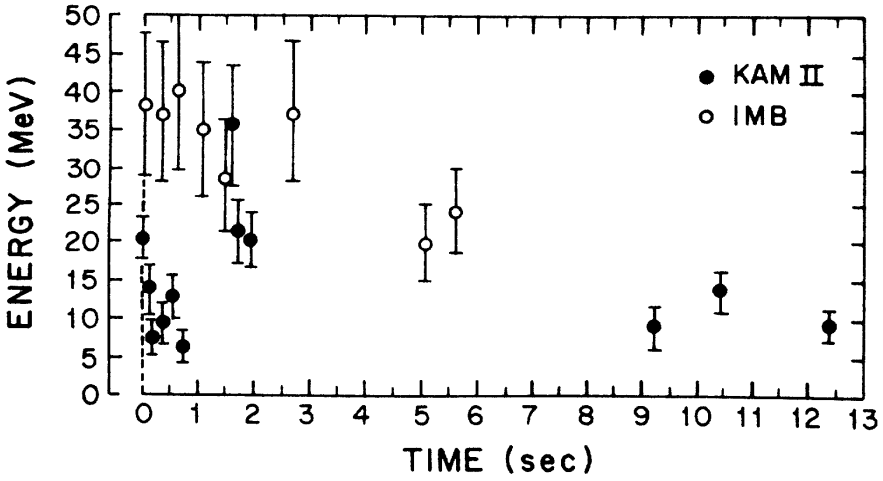

Figure 1.1. Neutrino burst signals from SN1987A detected in Kamiokande-II and IMB. 12 events in the Kamiokande-II and 8 events in the IMB detector are in arrival time and recoil electron/positron energy. (Reprinted figure from Ref. [2]; copyright (1988) by the American Physical Society.)

12.4 s and consistent with the time scale escaping from the proto-neutron star. It means that produced neutrinos are trapped inside the proto-neutron star through the beta equilibrium. Furthermore, the averaged neutrino energy was estimated as ~ 10 MeV and the total neutrino luminosity as $\sim 3 \times 10^{53}$ erg. It is roughly the same as the binding energy of a neutron star, and it suggests that the core collapse of the iron core triggers the supernova explosion. The observational neutrino properties are consistent with the prediction from the supernova theory. As mentioned above, neutrinos play essential roles in the explosive mechanism, and the observation in the future would further enrich our understanding of core-collapse supernovae. We use natural units and set $\hbar = c = 1$ in this dissertation unless indicated otherwise.

1.2 Stellar evolution

Stars preserve themselves by the inner pressure competing against the gravitational contraction. If the mass is heavier than $0.08 M_\odot$, the central temperature reaches $T_c \sim 10^7$ K, and the energy production contributes the thermal pressure through the nuclear burning of hydrogen to helium. The reaction sequence of hydrogen (H) burning is called the *pp* chain, and electron antineutrinos are emitted as the by-products. Neutrinos from the Sun have been observed in some detectors and enable us to monitor current solar activity, which light cannot. Stars keep staying on the main sequence in the Hertzsprung-Russell diagram during stable H-burning. When hydrogen in the core is exhausted, the central helium (He) core shrinks due to the self-gravity, and the star evolves away from the main sequence. If the central temperature increases to 10^8 K, He-fusion called the triple-alpha process occurs in the core. On the other hand, a star that is not massive enough to ignite He-core continues to shrink until prevented by electron degeneracy pressure and eventually ends as a white dwarf. Hydrostatic equilibrium for non-degenerate gases roughly requires the following relation between the central temperature and central density,

$$T_c^3 \rho_c^{-1} \propto M_c^2 \sim \text{constant}. \tag{1.1}$$

In other words, more massive stars with heavier cores are hotter and are allowed to proceed to the next burning stage. The dependency on the initial mass in evolution paths is well described in Fig. 1.2. Blue curves are stellar evolution tracks for each mass range, and colored regions represent instability processes through which the stars lead to death. The nuclear burning stops inside relatively lighter stars with $\lesssim 8 M_\odot$, and they evolve to white dwarfs. More massive stars pass the several burning stages and finally run into hydrodynamically unstable regions inducing gravitational core collapse. The death of stars is strongly sensitive to the initial mass.

1.2.1 Electron capture

After He-fusion, C-burning subsequently occurs in more massive stars with $\gtrsim 8 M_\odot$, and oxygen-neon-magnesium (O-Ne-Mg) cores are produced in the center. The stellar interior reaches electron degeneracy as seen in yellow dashed-lines of Fig. 1.2 and the self-gravity

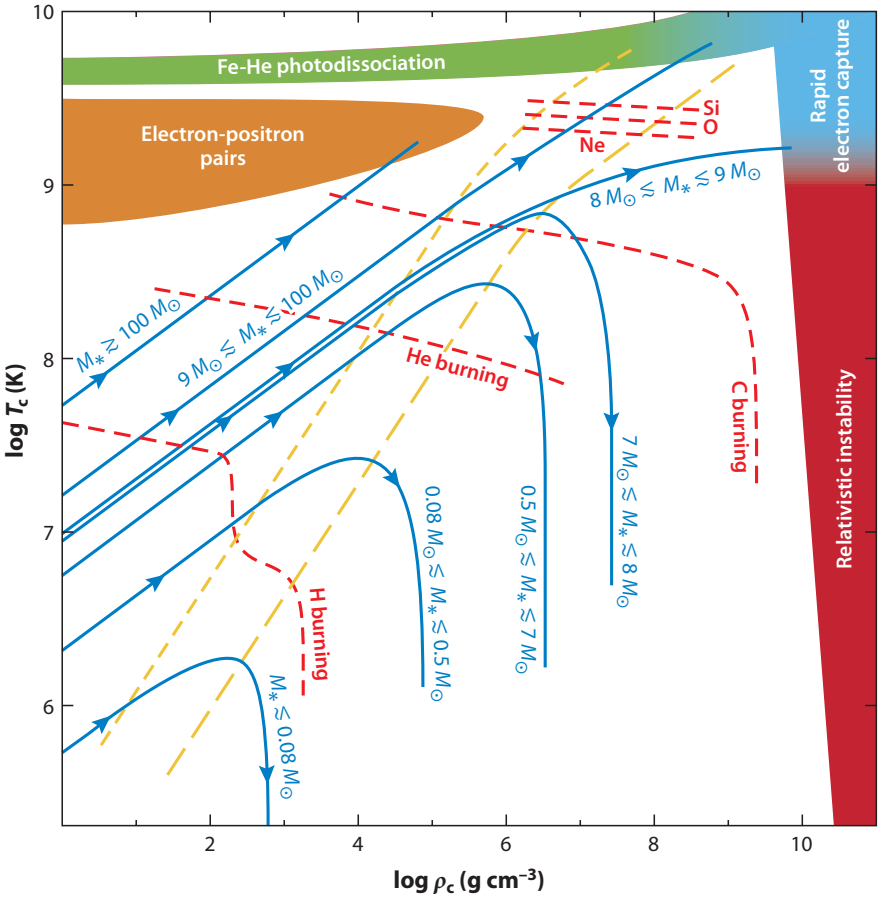

Figure 1.2. Schematic stellar evolution paths in the plane of central density ρ_c and central temperature T_c. Colored regions indicate instability processes inducing core collapse and yellow dashed-lines represent thresholds to reach electron degeneracy. (Republished with permission from Annual Reviews, Inc., from Ref. [9]; permission conveyed through Copyright Clearance Center, Inc.)

is partly supported by electron degeneracy pressure before Ne-burning. However, stars in a narrow mass window $8M_\odot \lesssim M \lesssim 9M_\odot$ experience electron-capture process $e^- + p \to n + \nu_e$ with protons in nuclei and free electrons (blue region in Fig. 1.2). In the core, two reactions mainly occur as follows: ${}^{20}\mathrm{Ne} + e^- \to {}^{20}\mathrm{F} + \nu_e$ and ${}^{24}\mathrm{Mg} + e^- \to {}^{24}\mathrm{Na} + \nu_e$ [10]. The condition satisfies that electron energy is above the Q-values for the electron capture reactions. The electron energy is roughly given by the Fermi energy of the relativistic degenerate electron,

$$\mu_e = \sqrt{p_\mathrm{F}^2 + m_e} \sim \left(3\pi^2 n_e\right)^{1/3} = 11 \text{ MeV} \left(\frac{\rho Y_e}{10^{10} \text{ g cm}^{-3}}\right)^{1/3}, \tag{1.2}$$

where p_F is the Fermi momentum and depends only on the electron density. The Fermi energy at the central density $\rho_c \sim 10^{10}$ g cm^{-3} is clearly over the Q-values for the electron capture reactions in the core [11]. Since the electron capture process reduces the electron degeneracy pressure and compresses the core, it enhances the electron capture reactions

further. Consequently, once electron capture reactions become possible, the core becomes hydrodynamically unstable and results in core collapse. Stars in this mass range lead to electron-capture supernovae and leave neutron stars behind [10, 12–18].

1.2.2 Photo-dissociation

Massive star with $\gtrsim 9M_\odot$ ignites the O-Ne-Mg core and finally forms an iron (Fe) core after passing several burning stages. Iron is a nucleus with the maximum binding energy per nucleon and stars can not proceed to the next nuclear burning stage. The Fe-core is mainly supported by the electron degeneracy pressure, not nuclear burning. Inert iron elements accumulate in the center, and the self-gravity heats the Fe-core to the central temperature $T_c \sim 5 \times 10^9$ K. Under the environments, the dissociation of Fe-group nuclei to α particles and free nucleons by thermal photons,

$$^{56}\mathrm{Fe} + \gamma \rightarrow 13\,^4\mathrm{He} + 4n \tag{1.3}$$

$$^4\mathrm{He} + \gamma \rightarrow 2p + 2n, \tag{1.4}$$

is favored and abrupt core contraction occurs. Since the Fermi energy μ_e of the degenerate electrons also rises as the central density increases, electron capture process for Fe-group nuclei, e.g., $^{56}\mathrm{Fe} + e^- \rightarrow {}^{56}\mathrm{Mn} + \nu_e$, proceeds and accelerates the core collapse. Photo-dissociation makes the core hydrodynamically unstable and triggers core-collapse supernovae, similar to electron capture supernovae. More detailed descriptions of the mechanism leading to the successful explosion will be reviewed in Sec. 1.3.

1.2.3 Electron-positron pair instability

The core of stars above $100M_\odot$ becomes hydrodynamically unstable through electron-positron pair creation at the central temperature $\gtrsim 10^9$ K and central density $\lesssim 10^6$ g cm^{-3} (orange region in Fig. 1.2) [19, 20]. The pair creation follows as

$$2\gamma \rightarrow e^- + e^+ \tag{1.5}$$

and the thermal energy of photons is converted into the rest-mass energy of e^-e^+. Therefore, the thermal pressure loses due to the energy absorption, and the stellar core becomes hydrodynamically unstable. The gravitational contraction compresses the core, and hence the thermal absorption rate increases further. The runaway process induces the core collapse. The core collapse increases the central temperature and ignites carbon, neon, and oxygen. Whether the thermal pressure from the explosive nuclear fusions exceeds the binding energy of stars themselves determines the final fates.

Stars with $100M_\odot \lesssim M \lesssim 140M_\odot$ are predicted to induce the pulsational pair-instability supernovae [21–24]. Electron-positron pair creation causes strong pulsation and mass loss but is insufficient to explode the progenitor. The stars form iron cores and lead to supernova explosions like normal core-collapse supernovae. Hence, the pulsational pair-instability supernovae leave a black hole as a compact remnant. Also, for stars above

$260M_\odot$, even the explosive O-burning can not hinder the sudden core contraction, and the stars lead to direct collapse into black holes.

In stars between 140 and $260M_\odot$, the explosion called pair-instability supernovae takes place in the end [21, 25–29]. Since the energy released from the runaway nuclear burning is enough to disrupt the whole star, no compact remnant is left behind. This mass range is attributed to gaps in the mass distribution of stellar black holes and is often called the pair-instability black hole mass gap [30].

1.3 Core-collapse supernovae

As mentioned in Sec. 1.2.1 and 1.2.2, electron capture and photo-dissociation at high temperature and high density makes the stellar core hydrodynamically unstable and triggers core collapse. The core collapse accelerates electron capture reactions in both cases and increases the number of neutrons inside the core. The stellar core forms a proto-neutron star through the process and should lead to a black hole if the core contraction continues without end. However, the neutronization and the matter accretion are hindered by neutrino trapping and core bounce. The detailed explosion scenario will be reviewed in the following sections.

1.3.1 Neutrino trapping

Electron neutrinos are emitted through electron capture reactions and can easily escape from the core just before the core collapse. The central density also rises as the neutronization of the stellar core proceeds, and hence the core is opaque to electron neutrinos when matter density is above $\rho \gtrsim 10^{11}$ g cm^{-3}. The opacity is mainly contributed to coherent neutrino-nucleus scatterings $\nu_e + A \to \nu_e + A$, with a nucleus $A(Z, N)$ with total nucleons A, proton number Z, and neutron number N. The differential cross section of neutrinos through coherent scatterings off nucleus $A(Z, N)$ is to leading order [31–34],

$$\frac{\mathrm{d}\sigma}{\mathrm{d}\Omega}(E_\nu, (A, Z)) = \frac{G_\mathrm{F}^2 E_\nu^2}{4\pi^2}\left[-2Z\sin^2\theta_\mathrm{W} + \frac{Z-N}{2}\right]^2 (1+\cos\theta) \tag{1.6}$$

$$= \frac{G_\mathrm{F}^2 E_\nu^2}{16\pi^2} A^2 \left[1 - \frac{2Z}{A}\left(1 - 2\sin^2\theta_\mathrm{W}\right)\right]^2 (1+\cos\theta), \tag{1.7}$$

where θ_W is the Weinberg angle. The cross section roughly depends on the square of neutrino energy E_ν and total nucleons A from Eq. (1.7). Since the electron degeneracy pressure supports Fe-core at the core collapse, the energy of electron neutrinos produced by the electron capture reactions are approximately estimated by the Fermi energy of degenerate electrons. When electron Fermi energy μ_e is much larger than the absolute Q values, the energy of electron neutrinos is given by [11].

$$E_{\nu_e} \approx \frac{5}{6}\mu_e = \frac{5}{6}\left(3\pi^2 \frac{\rho Y_e}{m_u}\right)^{1/3} = 7.2 \text{ MeV} \left(\frac{\rho}{10^{10} \text{ g cm}^{-3}}\right)^{1/3} \left(\frac{Y_e}{26/56}\right)^{1/3}. \tag{1.8}$$

Then, the mean free path of electron neutrinos inside the iron ($^{26}_{56}$Fe) core is

$$l_{\rm mfp} = \frac{1}{n_A \sigma} = \frac{4\pi}{G_{\rm F}^2 E_{\nu_e}^2} \frac{m_u}{\rho A} \left[1 - \frac{2Z}{A}\left(1 - 2\sin^2\theta_{\rm W}\right)\right]^{-2} \tag{1.9}$$

$$= 5.2 \times 10^2 \text{ km} \left(\frac{\rho}{10^{10} \text{ g cm}^{-3}}\right)^{-5/3}. \tag{1.10}$$

The radius of Fe-core is a few 1000 km and the mean free path is shorter than the core. Therefore, even electron neutrinos are scattered and diffuse inside the Fe-core. The dynamical timescale for the core collapse is

$$\tau_{\rm dyn} \equiv \frac{1}{\sqrt{G\rho}} = 12 \text{ ms} \left(\frac{\rho}{10^{11} \text{ g cm}^{-3}}\right)^{-1/2}. \tag{1.11}$$

On the other hand, the diffusion timescale of neutrinos from the core $R_{\rm core}$ is

$$\tau_{\rm diff} \equiv \frac{3R_{\rm core}^2}{l_{\rm mfp}} = 30 \text{ ms} \left(\frac{\rho}{10^{11} \text{ g cm}^{-3}}\right), \tag{1.12}$$

where we take the core radius as

$$R_{\rm core} = \left(\frac{3M_{\rm core}}{4\pi\rho}\right)^{1/3} = 1.8 \times 10^2 \text{ km} \left(\frac{\rho}{10^{11} \text{ g cm}^{-3}}\right)^{-1/3} \tag{1.13}$$

and the core mass is the Chandrasekhar mass without finite temperature correlation [35, 36]

$$M_{\rm core} \simeq 1.46 M_\odot \left(\frac{Y_e}{0.5}\right)^2 = 1.26 M_\odot \left(\frac{Y_e}{26/56}\right)^2. \tag{1.14}$$

Therefore, diffusive electron neutrinos are completely trapped in the collapsed core when the central density exceeds 10^{11} g cm^{-3}. The optical depth of neutrinos is defined by

$$\tau_\nu(r) = \int_r^\infty \frac{{\rm d}r}{l_{\rm mfp}} \tag{1.15}$$

and the radius R_ν satisfying $\tau_\nu = 2/3$ is particularly called a neutrino sphere [37]. The trapped neutrinos only leak out of the neutrino sphere little by little. Electron neutrinos freely escape with the lepton number from the core before the neutrino trapping. However, once electron neutrinos are trapped, the beta equilibrium $\mu_e + \mu_p = \mu_n + \mu_{\nu_e}$ is established in the core and the neutronization is also suppressed.

1.3.2 Core bounce and neutrino heating

After the neutrino trapping, the central density continuously rises due to the core collapse. When the core reaches a nuclear density $\rho_c \sim 10^{14}$ g cm^{-3}, it is suddenly supported by repulsive nuclear forces, and the collapse is stopped. The core bounce creates a shock wave between the boundary, pushing the free-falling outer core outward. The shock wave propagates through the outer core with the dissociation of nuclei A into free nucleons

p/n. The process reduces the cross section $\propto A^2$ of coherent scatterings and releases electron neutrinos trapped inside the neutrino sphere. Also, the dissociation breaks the beta equilibrium in the core and resumes electron capture reactions. Consequently, a large amount of electron neutrinos is released when the shock wave reaches the neutrino sphere, and it exhibits the rapid increase of electron neutrino luminosity called the neutronization burst.

The explosion succeeds if the shock wave can reach the photosphere of the progenitor. However, the shock wave gradually loses the kinetic energy while propagating through the accreting matter outwardly. In addition to wasting the kinetic energy to dissociate the Fe-group nuclei in the accreting matter with lower entropy, the shock wave also loses the thermal energy by electron neutrinos from the electron capture reactions behind the shock front. The shock wave completely stalls at a radius of ~ 200 km. If the stalled shock wave can not revive after that, the outer core keeps to accrete onto the proto-neutron star in the center, and the progenitor fails to explode. The thermal energy stored in the inner core is newly deposited into the stalled shock wave by the mechanism called neutrino heating [38]. Shock propagation raises the temperature and decreases the density, reducing electron degeneracy in the post-shock region. This effect induces several reactions associated with neutrino emissions. In such a matter profile, the thermal energy is converted into electron-positron pairs, $2\gamma \to e^- + e^+$. The appearance of positrons causes the positron-capture reaction and emits electron antineutrinos,

$$e^+ + n \to p + \bar{\nu}_e. \tag{1.16}$$

Also, all species of neutrinos are produced by the electron-positron annihilation, nucleon-nucleon breamsstralung, and neutrino-antineutrino annihilation:

$$e^- + e^+ \to \nu_\alpha + \bar{\nu}_\alpha \tag{1.17}$$

$$N + N \to N + N + \nu_\alpha + \bar{\nu}_\alpha \tag{1.18}$$

$$\nu_\alpha + \bar{\nu}_\alpha \to \nu_\beta + \bar{\nu}_\beta. \tag{1.19}$$

Note that the third process can convert electron/positron capture neutrinos into the non-electron type flavors. Heavy-leptonic flavor neutrinos ν_X are created only through these three reactions and μ/τ-capture processes do not occur. However, Bollig *et al.* has suggested that muon creation enhances neutrino emission and induces faster core contraction so that it can play non-negligible roles on the neutrino heating [39]. More detailed investigations on the microphysics are required to enrich our understanding of supernova physics.

A small fraction of electron-type neutrinos emitted from the center is absorbed in nucleons behind the stalled shock wave:

$$\nu_e + n \to e^- + p \tag{1.20}$$

$$\bar{\nu}_e + p \to e^+ + n. \tag{1.21}$$

The thermal energy in the center is transferred into the cold matter behind the stalled shock wave through the neutrino absorption. The energy deposition through the neutrino

heating process is sufficient for the stalled shock wave to revive, and the scenario is called a delayed explosion. In the region between the neutrino sphere and the stalled shock wave, both neutrino absorption and emission reactions occur. The area where the net energy balance is positive is called a gain or heating region, while for the negative is a cooling region. The radius at which heating and cooling rates with neutrinos are balanced is called a gain radius and is located at $R_g \sim 100$ km [40]. While the shock radius is outside the gain radius, the neutrino heating from the proto-neutron star in the center is effective. However, the stalled shock radius shrinks due to the accreting matter as time passes, and if the neutrino-driven shock revival is not in time, the progenitor fails to explode. Recently, the multi-dimensional effects that supports the delayed explosion scenario have been investigated [41], e.g., the neutrino-driven convection [42, 43] and the standing accretion shock instability (SASI) [44]. In addition, the possibility that neutrino flavor conversion can directly enhance the neutrino heating rates has been actively discussed (e.g., Ref. [45]). The feedback of the flavor mixing to the explosive physics remains to be explored.

1.4 Overview for neutrino oscillation

Neutrinos $(\nu_e, \nu_\mu, \nu_\tau)$ are mostly created in pairs with charged leptons via the charged-current weak interaction. They are called weak eigenstates or flavor eigenstates, and are not always identical to mass eigenstates (ν_1, ν_2, ν_3) in general. The discrepancy between weak eigenstates and mass eigenstates in the weak interaction has been found in the weak decay of quarks. Transitions across generation such as $s \to u$ are indeed seen in kaon decay $K^+ \to \pi^+\pi^0$ and the phenomena were explained as the linear combination between the mass eigenstates by introducing the Cabbibo angle [46]. Subsequently, the theory was generalized into the three-generation case and has supported the experimental results on the CP violation in K^0 systems [47]. The unitary transformation is called the Cabbibo-Kobayashi-Masukawa (CKM) matrix and connects the mass eigenstates of down-type quarks $(d, s, b)^T$ with the weak eigenstates. This mechanism is responsible for the flavor-changing weak interaction and the CP violation in $N \geq 3$ generation. Neutrino oscillation was proposed in analogy with the mixing of quarks [48, 49].

1.4.1 Neutrino oscillation in vacuum

If neutrinos are not massless particles, neutrinos can experience the flavor mixing similar to quarks. Flavor eigenstates $|\nu_\alpha\rangle$ are described by the coherent superposition of mass eigenstates $|\nu_i\rangle$:

$$\begin{pmatrix} \nu_e \\ \nu_\mu \\ \nu_\tau \end{pmatrix} = U \begin{pmatrix} \nu_1 \\ \nu_2 \\ \nu_3 \end{pmatrix}. \tag{1.22}$$

The unitary transformation U is the Pontecorvo-Maki-Nakagawa-Sakata (PMNS) matrix [51],

$$\begin{aligned} U &= R_{23}(\theta_{23})R_{13}(\theta_{13})R_{12}(\theta_{12}) \\ &= \begin{pmatrix} 1 & 0 & 0 \\ 0 & c_{23} & s_{23} \\ 0 & -s_{23} & c_{23} \end{pmatrix} \begin{pmatrix} c_{13} & 0 & s_{13}\mathrm{e}^{-\mathrm{i}\delta_{\mathrm{CP}}} \\ 0 & 1 & 0 \\ -s_{13}\mathrm{e}^{\mathrm{i}\delta_{\mathrm{CP}}} & 0 & c_{13} \end{pmatrix} \begin{pmatrix} c_{12} & s_{12} & 0 \\ -s_{12} & c_{12} & 0 \\ 0 & 0 & 1 \end{pmatrix} \qquad (1.23) \\ &= \begin{pmatrix} c_{12}c_{13} & s_{12}c_{13} & s_{13}\mathrm{e}^{-\mathrm{i}\delta_{\mathrm{CP}}} \\ -s_{12}c_{23} - c_{12}s_{13}s_{23}\mathrm{e}^{\mathrm{i}\delta_{\mathrm{CP}}} & c_{12}c_{23} - s_{12}s_{13}s_{23}\mathrm{e}^{\mathrm{i}\delta_{\mathrm{CP}}} & c_{13}s_{23} \\ s_{12}s_{23} - c_{12}s_{13}c_{23}\mathrm{e}^{\mathrm{i}\delta_{\mathrm{CP}}} & -c_{12}s_{23} - s_{12}s_{13}c_{23}\mathrm{e}^{\mathrm{i}\delta_{\mathrm{CP}}} & c_{13}c_{23} \end{pmatrix}, \qquad (1.24) \end{aligned}$$

where $c_{ij} = \cos\theta_{ij}$ and $s_{ij} = \sin\theta_{ij}$ denote mixing angles, and δ_{CP} is the CP-violating phase. The PMNS matrix transforms neutrino mass eigenstates $|\nu_i\rangle$ into flavor eigenstates $|\nu_\alpha\rangle$. The discrepancy between propagating states and weak-interaction states leads to flavor mixing. Table 1.1 represents up-to-date neutrino mixing parameters determined by the underground experimental data [50]. $\Delta m^2_{ij} = m^2_i - m^2_j$ is a squared-mass difference. Currently, neutrino mass ordering has not been fixed yet and two possible scenarios are considered on the sign of Δm^2_{32} as shown in Fig. 1.3. The positive sign is the normal mass ordering, $m_1 < m_2 < m_3$, and the negative is the inverted mass ordering, $m_3 < m_1 < m_2$.

In the description of massive neutrinos, lepton flavor is no longer conserved in neutrino propagation. The violation phenomenon is called neutrino oscillation, but it still preserves the total lepton number conservation. Here, we introduce the oscillation phenomena in the two-generation case. In the two-generation case, the discrepancy between mass eigenstates and flavor eigenstates is simply expressed as

$$\begin{pmatrix} \nu_e \\ \nu_\mu \end{pmatrix} = \begin{pmatrix} \cos\theta & \sin\theta \\ -\sin\theta & \cos\theta \end{pmatrix} \begin{pmatrix} \nu_1 \\ \nu_2 \end{pmatrix}. \qquad (1.25)$$

Hamiltonian of the mass eigenstates in vacuum is diagonalized and the energy eigenvalues are in the ultra-relativistic limit

$$E_i = \sqrt{p^2 + m_i^2} \approx p + \frac{m_i^2}{2p} \qquad (1.26)$$

Neutrino mixing parameters	
$\sin^2(\theta_{12})$	0.307 ± 0.013
Δm^2_{21}	$(7.53 \pm 0.18) \times 10^{-5}$ eV^2
$\sin^2(\theta_{23})$	0.539 ± 0.022 (Inverted)
	0.546 ± 0.021 (Normal)
Δm^2_{32}	$(-2.524 \pm 0.034) \times 10^{-3}$ eV^2 (Inverted)
	$(+2.453 \pm 0.033) \times 10^{-3}$ eV^2 (Normal)
$\sin^2(\theta_{13})$	0.0220 ± 0.0007
δ_{CP}	$1.36^{+0.20}_{-0.16}\pi$ rad

Table 1.1. Neutrino mixing parameters in Particle Data Group 2020 [50].

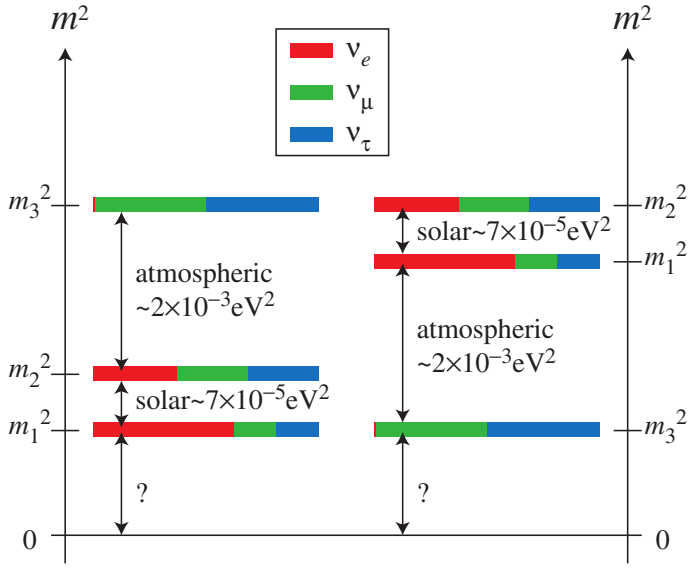

Figure 1.3. Two scenarios for neutrino mass ordering. It is still unknown whether m_3^2 is heavier or lighter than the other two mass eigenstates. Left mass ordering is called normal and right is inverted. (Republished with permission from IOP Publishing, Ltd, from Ref. [52]; permission conveyed through Copyright Clearance Center, Inc.)

The equation of motion for the flavor eigenstates is

$$\mathrm{i}\frac{\mathrm{d}}{\mathrm{d}t}\begin{pmatrix}\nu_e\\ \nu_\mu\end{pmatrix} = U\begin{pmatrix}E_1 & 0\\ 0 & E_2\end{pmatrix}U^\dagger\begin{pmatrix}\nu_e\\ \nu_\mu\end{pmatrix} \tag{1.27}$$

$$= \left[\begin{pmatrix}E & 0\\ 0 & E\end{pmatrix} + \begin{pmatrix}-\Delta E\cos 2\theta & \Delta E\sin 2\theta\\ \Delta E\sin 2\theta & \Delta E\cos 2\theta\end{pmatrix}\right]\begin{pmatrix}\nu_e\\ \nu_\mu\end{pmatrix}, \tag{1.28}$$

where $E = (E_1 + E_2)/2$ and $\Delta E = (E_2 - E_1)/2$. The first term is a common phase and does not affect the flavor evolution. Here, in assuming neutrinos with same momentum $p_i = p$, the energy difference is given by

$$\Delta E = \frac{m_2^2 - m_1^2}{4p} \approx \frac{\Delta m^2}{4E} \equiv \frac{\omega}{2}, \tag{1.29}$$

where ω is a vacuum frequency. Then, the equation of motion is simply expressed as

$$\mathrm{i}\frac{\mathrm{d}}{\mathrm{d}t}\begin{pmatrix}\nu_e\\ \nu_\mu\end{pmatrix} = \frac{\omega}{2}\begin{pmatrix}-\cos 2\theta & \sin 2\theta\\ \sin 2\theta & \cos 2\theta\end{pmatrix}\begin{pmatrix}\nu_e\\ \nu_\mu\end{pmatrix}. \tag{1.30}$$

The solutions are

$$\begin{pmatrix}\nu_e(t)\\ \nu_\mu(t)\end{pmatrix} = \begin{pmatrix}\cos\left(\frac{\omega t}{2}\right) + \mathrm{i}\cos 2\theta\sin\left(\frac{\omega t}{2}\right) & -\mathrm{i}\sin 2\theta\sin\left(\frac{\omega t}{2}\right)\\ -\mathrm{i}\sin 2\theta\sin\left(\frac{\omega t}{2}\right) & \cos\left(\frac{\omega t}{2}\right) - \mathrm{i}\cos 2\theta\sin\left(\frac{\omega t}{2}\right)\end{pmatrix}\begin{pmatrix}\nu_e(0)\\ \nu_\mu(0)\end{pmatrix}. \tag{1.31}$$

Therefore, the transition probability of electron neutrinos is

$$P_{\nu_e\to\nu_\mu} = |\langle\nu_e\,|\,\nu_\mu(t)\rangle|^2 = \sin^2 2\theta\sin^2\left(\frac{\omega t}{2}\right). \tag{1.32}$$

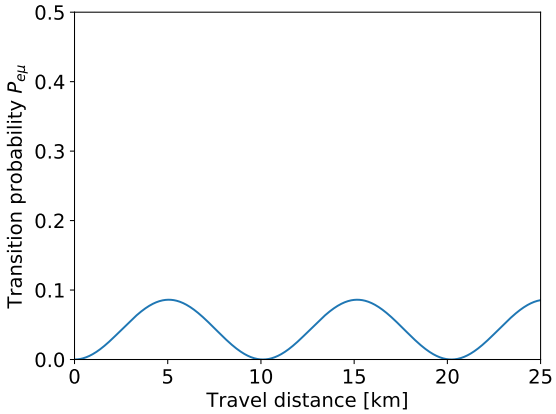

Figure 1.4. Transition probability $P_{\nu_e \to \nu_\mu}$ as a function of travel distance L. We adopt θ_{13} and Δm^2_{32} as oscillation parameters in the normal mass ordering in Table. 1.1.

Using neutrino travel distance $L = tc = t$, we can evaluate the typical oscillation length:

$$\frac{\omega}{2} L_{\text{typ}} = \pi \Rightarrow L_{\text{typ}} = \frac{2\pi}{\omega} = 2.48 \times 10^1 \text{ km} \left(\frac{E}{10 \text{ MeV}} \right) \left(\frac{10^{-3} \text{ eV}^2}{\Delta m^2} \right). \tag{1.33}$$

The amplitude depends only on the mixing angle θ and the wavelength on the neutrino energy and the squared-mass difference Δm^2. Figure 1.4 shows the transition probability $P_{\nu_e \to \nu_\mu}$ for neutrinos with 10 MeV as a function of travel distance L. By counting neutrinos with different travel distances, we can experimentally determine the squared-mass difference.

Figure 1.5 shows the zenith angle distribution of atmospheric neutrinos detected in Super-Kamiokande [53]. Atmospheric neutrinos are products associated with the air shower induced by the collision between cosmic rays and nuclei in the upper atmosphere. Mainly, the production processes are pion decay $\pi^+ \to \mu^+ + \nu_\mu$ and muon decay $\mu^+ \to e^+ + \bar{\nu}_\mu + \nu_e$. Neutrinos generated by the atmosphere above the detector travel about 15 km, while neutrinos going down to the detector through the Earth travel about 13000 km. Therefore, the zenith angle distribution of incident neutrinos corresponds to the travel distance from the atmosphere into the detector. The atmospheric neutrinos undergo neutrino oscillation until reaching a neutrino detector from the atmosphere. The oscillation phase depending on the travel distance appears in the zenith angle distribution of the observed counts in Fig. 1.5.

1.4.2 Neutrino oscillation in medium

In the previous section, we focus only on the case that neutrinos propagate in vacuum and ignore the effects from background matter. In fact, neutrinos travel through the medium such as the Sun and the envelope of supernovae and interact with the background electrons, protons, and neutrons. Neutrinos are scattered via Z^0 boson and $W^\pm$ bosons, and they are called neutral- and charged-current interactions, respectively. The left and middle panels in Fig. 1.6 shows the Feynman diagrams of neutrino-electron scatterings. We

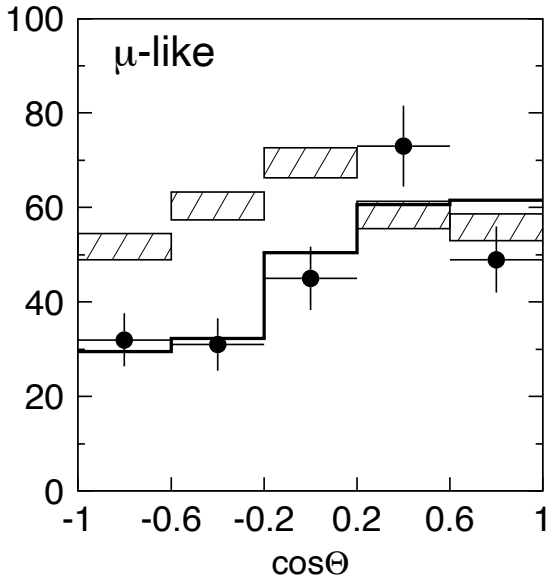

Figure 1.5. Zenith angle distribution of μ-like events for multi-GeV data sets. The observed number of muon neutrinos incoming through the Earth, $\Theta < 0$, is less than the expected number in ignoring the vacuum oscillation (shaded region). (Reprinted figure from Ref. [53]; copyright (1998) by the American Physical Society.)

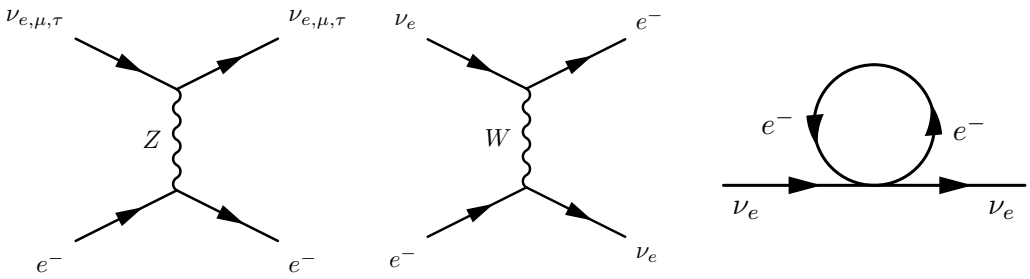

Figure 1.6. Neutral-current (left) and charged-current (middle) interactions with electrons. Right panel shows the diagram in the mean-field approximation for the background electrons.

need to consider the coherent forward scattering in the equation of motion for propagation in medium. Neutral-current process is flavor blind and just provides an overall phase shift. On the other hand, charged-current process with electrons is for only electron neutrinos and the asymmetry for the flavor interactions induces the modification of vacuum oscillation. To treat the scattering process, we adopt the mean-field approximation for the background electrons [54]. Right panel in Fig. 1.6 is the corresponding mean-field diagram averaging over electrons in background. Then, the coherent forward scattering just becomes a potential from the background and the Hamiltonian for propagation through

matter is

$$H = U\frac{1}{2E}\begin{pmatrix} m_1^2 & 0 & 0 \\ 0 & m_2^2 & 0 \\ 0 & 0 & m_3^2 \end{pmatrix}_{\text{mass}} U^\dagger + \begin{pmatrix} \sqrt{2}G_{\text{F}}n_e & 0 & 0 \\ 0 & 0 & 0 \\ 0 & 0 & 0 \end{pmatrix}_{\text{flavor}}. \tag{1.34}$$

The second term comes from the matter potentials and changes the effective neutrino masses. We can obtain the effective masses by diagonalizing the Hamiltonian in the flavor basis. In the two-generation case, the time evolution for the flavor eigenstates is recast as

$$\mathrm{i}\frac{\mathrm{d}}{\mathrm{d}t}\begin{pmatrix} \nu_e \\ \nu_\mu \end{pmatrix} = \begin{pmatrix} -\frac{\omega}{2}\cos 2\theta + \sqrt{2}G_{\text{F}}n_e & \frac{\omega}{2}\sin 2\theta \\ \frac{\omega}{2}\sin 2\theta & \frac{\omega}{2}\cos 2\theta \end{pmatrix}\begin{pmatrix} \nu_e \\ \nu_\mu \end{pmatrix} \tag{1.35}$$

$$= \tilde{U}\begin{pmatrix} \lambda_1 & 0 \\ 0 & \lambda_2 \end{pmatrix}\tilde{U}^\dagger\begin{pmatrix} \nu_e \\ \nu_\mu \end{pmatrix} \tag{1.36}$$

$$= \frac{\Delta\tilde{m}^2}{4E}\begin{pmatrix} -\cos 2\tilde{\theta} & \sin 2\tilde{\theta} \\ \sin 2\tilde{\theta} & \cos 2\tilde{\theta} \end{pmatrix}\begin{pmatrix} \nu_e \\ \nu_\mu \end{pmatrix}, \tag{1.37}$$

where $\tilde{U}$ is the PMNS matrix in matter composed of the effective mixing angle $\tilde{\theta}$, $\Delta\tilde{m}^2$ is the effective squared-mass difference, and the energy eigenvalues λ_i are

$$\lambda = \frac{\sqrt{2}}{2}G_{\text{F}}n_e \pm \sqrt{\left(\frac{\sqrt{2}}{2}G_{\text{F}}n_e - \frac{\omega}{2}\cos 2\theta\right)^2 + \left(\frac{\omega}{2}\right)^2\sin^2 2\theta}. \tag{1.38}$$

Equation (1.37) is a form after transforming to a traceless matrix for the Hamiltonian in vacuum and removing the common phase. Therefore, the relation between neutrino masses and the energy eigenvalues is

$$\tilde{m}_i^2 = \frac{m_1^2 + m_2^2}{2} + 2E\lambda_i. \tag{1.39}$$

The effective squared-mass difference can be given by

$$\begin{aligned}\Delta\tilde{m}^2 &= \sqrt{\left(2\sqrt{2}G_{\text{F}}n_eE - \Delta m^2\cos 2\theta\right)^2 + \left(\Delta m^2\sin 2\theta\right)^2} \\ &= \Delta m^2\sqrt{\left(\sqrt{2}G_{\text{F}}n_e/\omega - \cos 2\theta\right)^2 + \sin^2 2\theta}.\end{aligned} \tag{1.40}$$

And the effective mixing angle is

$$\sin 2\tilde{\theta} = \frac{\sin 2\theta}{\sqrt{\left(\sqrt{2}G_{\text{F}}n_e/\omega - \cos 2\theta\right)^2 + \sin^2 2\theta}}. \tag{1.41}$$

Figrue 1.7 shows the effective neutrino mass $\tilde{m}_i^2 - m_1^2$ (left) and the effective mixing angle $\tilde{\theta}$ (right) as a function of matter density ρY_e. The low-density limit means each oscillation parameter in vacuum. The energy levels for the propagation eigenstates cross and the effective squared-mass difference $\tilde{m}^2$ becomes minimum at a critical density ρ_{crit} as shown

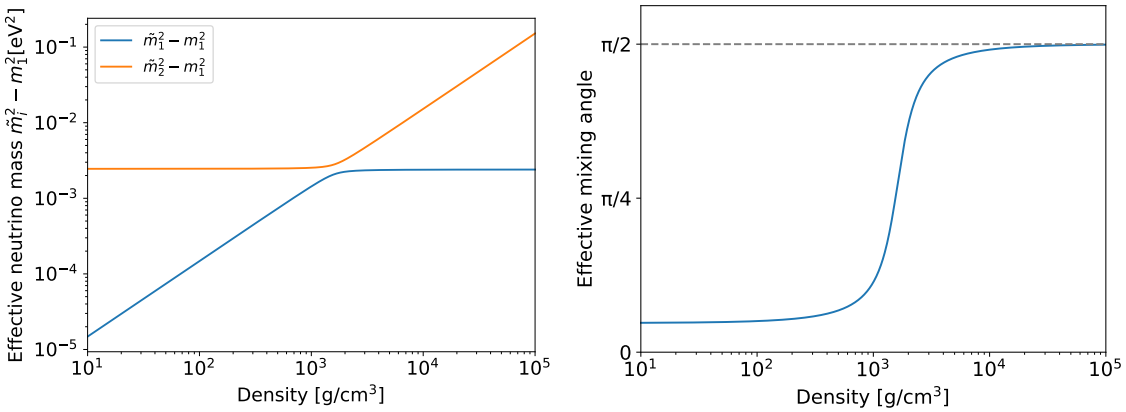

Figure 1.7. Effective neutrino mass $\tilde{m}_i^2 - m_1^2$ (left) and effective mixing angle $\tilde{\theta}$ (right) for neutrino energy 10 MeV as a function of matter density ρY_e

.

in the left panel of Fig. 1.7. The level crossing is called the Mikheyev – Smirnov – Wolfenstein (MSW) resonance [55, 56]. The critical electron number density is

$$n_{e,\mathrm{crit}} = \frac{\omega \cos 2\theta}{\sqrt{2} G_{\mathrm{F}}}, \tag{1.42}$$

and then the effective mixing angle becomes maximum $\sin 2\tilde{\theta} = 1$. In the high-density limit, $n_e \gg n_{e,\mathrm{crit}}$, the effective mixing angle approaches $\pi/2$ and the flavor basis is orthogonal to the mass basis in matter:

$$\begin{pmatrix} \nu_e \\ \nu_\mu \end{pmatrix} = \begin{pmatrix} 0 & 1 \\ -1 & 0 \end{pmatrix} \begin{pmatrix} \tilde{\nu}_1 \\ \tilde{\nu}_2 \end{pmatrix}. \tag{1.43}$$

Electron neutrinos become heavier via the charged-current interaction with electrons, and then ν_e is identical to $\tilde{\nu}_2$. On the other hand, $\nu_2 = \nu_e \sin\theta + \nu_\mu \cos\theta$ in vacuum and is almost ν_μ for $\theta = \theta_{13} \sim 0.15$. Therefore, ν_2 produced at a dense region changes from ν_e to ν_μ along the upper branch (solid orange line) in the left panel of Fig. 1.7. Then, the survival probability of electron neutrinos produced at a dense region $n_e \gg n_{e,\mathrm{crit}}$ is

$$P_{\nu_e \to \nu_e} = |\langle \nu_e \,|\, \nu_2 \rangle|^2 = \sin^2\theta \sim 0.022 \quad \text{for } \theta = \theta_{13}. \tag{1.44}$$

This means that the flavor eigenstates are significantly mixed through the MSW resonance.

In the above discussion, we have assumed the adiabatic transition around the level crossings. If the density gradient is too steep around the level crossings, the mass eigenstates can jump the energy gap $\Delta\tilde{m}^2_{\mathrm{res}}$. Then, $\tilde{\nu}_2$ undergoes the transition to $\tilde{\nu}_1$ beyond the level crossings and continues to be almost ν_e along the lower branch (blue solid line) in the left panel of Fig. 1.7. The condition where such a adiabatic transition occurs can be evaluated from the transition time scale and the energy gap as

$$\delta E \times \delta t \gg \hbar. \tag{1.45}$$

The transition time scale is

$$\delta t_{\rm res} = \frac{\delta r}{c} = \left(\frac{{\rm d}r}{{\rm d}n_e}\delta n_e\right)\Big|_{\rm res} = \left(\frac{{\rm d}r}{{\rm d}\ln n_e}\frac{\delta n_e}{n_e}\right)\Big|_{\rm res} \sim \left(\frac{{\rm d}r}{{\rm d}\ln n_e}\right)\Big|_{\rm res}\frac{\sin 2\theta}{\cos 2\theta} \tag{1.46}$$

from Eq. (1.41). Therefore, the adiabatic condition is written

$$\gamma \equiv \omega\frac{\sin^2 2\theta}{\cos 2\theta}\frac{{\rm d}r}{{\rm d}\ln n_e} \gg 1. \tag{1.47}$$

Using the adiabaticity parameter γ, we can rewrite the survival probability in Eq. (1.44) for a general case [57, 58] as

$$P_{\nu_e\to\nu_e} = \frac{1}{2} + \left(\frac{1}{2} - P_f\right)\cos 2\theta\cos 2\tilde{\theta}, \tag{1.48}$$

with a probability

$$P_f = \exp\left(-\frac{\pi}{2}\gamma\right). \tag{1.49}$$

In the high-density limit $n_e \gg n_{e,{\rm crit}}$, the survival probability reduces to

$$P_{\nu_e\to\nu_e} = \sin^2\theta + P_f\cos 2\theta \tag{1.50}$$

and agree with Eq. (1.44) when satisfying the adiabatic condition.

In the three-flavor framework, the mechanism of the MSW resonance is similar to the two-flavor approximation. The rotation in the sub-basis (ν_μ, ν_τ) through the mixing angle θ_{23} does not affect the MSW effects unless we consider heavy charged leptons. Hence, we adopt the rotated system of $(e - x - y)$ flavor basis instead of $(e - \mu - \tau)$ as

$$(\nu_e, \nu_x, \nu_y)^T = R_{23}^\dagger(\theta_{23})\,(\nu_e, \nu_\mu, \nu_\tau)^T \tag{1.51}$$

$$= R_{13}(\theta_{13})R_{12}(\theta_{12})\,(\nu_1, \nu_2, \nu_3)^T. \tag{1.52}$$

This convention enables us to separately pick the flavor mixing associated with the atmospheric Δm^2_{32} and the solar squared-mass difference Δm^2_{21} like as the two-flavor case. The Hamiltonian for the flavor basis (e, x, y) in matter is diagonalized by the effective PMNS matrix as

$$H = U\frac{1}{2E}\begin{pmatrix}0 & 0 & 0\\ 0 & \Delta m^2_{21} & 0\\ 0 & 0 & \Delta m^2_{31}\end{pmatrix}U^\dagger + \begin{pmatrix}\sqrt{2}G_{\rm F}n_e & 0 & 0\\ 0 & 0 & 0\\ 0 & 0 & 0\end{pmatrix} \tag{1.53}$$

$$= \tilde{U}\frac{1}{2E}\begin{pmatrix}k_1 & 0 & 0\\ 0 & k_2 & 0\\ 0 & 0 & k_3\end{pmatrix}\tilde{U}^\dagger, \tag{1.54}$$

where k_i is a mass eigenvalue in matter. The concrete expressions for k_i are [59–63]

$$k_1 = \frac{1}{3}s - \frac{1}{3}\sqrt{s^2 - 3t}\left[u + \sqrt{3\,(1 - u^2)}\right] \tag{1.55}$$

$$k_2 = \frac{1}{3}s - \frac{1}{3}\sqrt{s^2 - 3t}\left[u - \sqrt{3\,(1 - u^2)}\right] \tag{1.56}$$

$$k_3 = \frac{1}{3}s + \frac{2}{3}\sqrt{s^2 - 3t}, \tag{1.57}$$

where coefficients s, t, and u are given by

$$s = \Delta m^2_{21} + \Delta^2_{31} + a \tag{1.58}$$

$$t = \Delta m^2_{21}\Delta^2_{31} + a\left[\Delta m^2_{21}\left(1 - s^2_{12}c^2_{13}\right) + \Delta m^2_{31}\left(1 - s_{13}\right)\right] \tag{1.59}$$

$$u = \cos\left[\frac{1}{3}\arccos\left(\frac{2s^3 - 9st + 27a\Delta m^2_{21}\Delta m^2_{31}c^2_{12}c^2_{13}}{2\left(s^2 - 3t\right)^{3/2}}\right)\right], \tag{1.60}$$

where $a = 2\sqrt{2}G_{\mathrm{F}}n_eE$. Figure 1.8 shows the energy levels in both the normal (left) and inverted (right) mass ordering as a function of matter density ρY_e. The part of negative matter density corresponds to the channels for antineutrinos. The two level crossings are called the H- and L-resonances at higher and lower densities respectively. The H-resonance is associated with the atmospheric squared-mass difference $\Delta m^2_{32(31)}$, while the L-resonance is associated with the solar squared-mass difference Δm^2_{21}. In particular, the large MSW mixing occurs in the antineutrino channel because the H-resonance depends on the mass ordering. The critical density for each resonance is similarly given by

$$\rho^{\mathrm{H}}_{\mathrm{crit}} = \frac{1}{\sqrt{2}G_{\mathrm{F}}}\frac{\left|\Delta m^2_{32}\right|}{2E_\nu}\frac{m_p}{Ye}\cos 2\theta_{13} \sim 3\times 10^3\ \mathrm{g/cm^3}\left(\frac{10\ \mathrm{MeV}}{E_\nu}\right)\left(\frac{0.5}{Ye}\right) \tag{1.61}$$

$$\rho^{\mathrm{L}}_{\mathrm{crit}} = \frac{1}{\sqrt{2}G_{\mathrm{F}}}\frac{\Delta m^2_{21}}{2E_\nu}\frac{m_p}{Ye}\cos 2\theta_{12} \sim 4\times 10^1\ \mathrm{g/cm^3}\left(\frac{10\ \mathrm{MeV}}{E_\nu}\right)\left(\frac{0.5}{Ye}\right). \tag{1.62}$$

In the normal mass ordering case, ν_e is identical to $\tilde{\nu}_3$ at a high-density limit $\rho \gg \rho^{\mathrm{H}}_{\mathrm{crit}}$, while $\nu_3 = s_{13}\nu_e + c_{13}\nu_y$ in vacuum. Therefore, the survival probability is

$$P_{\nu_e\to\nu_e} = \left|\langle\nu_e\,|\,\nu_3\rangle\right|^2 = \sin^2\theta_{13} \sim 0.022. \tag{1.63}$$

In the inverted mass ordering case, ν_e is identical to $\tilde{\nu}_2$ at a high-density limit $\rho \gg \rho^{\mathrm{H}}_{\mathrm{crit}}$, while $\nu_2 = s_{12}c_{13}\nu_e + c_{12}\nu_x - s_{12}s_{13}\nu_y$ in vacuum. Therefore, the survival probability is

$$P_{\nu_e\to\nu_e} = \left|\langle\nu_e\,|\,\nu_2\rangle\right|^2 = \sin^2\theta_{12}\cos^2\theta_{13} \sim 0.3. \tag{1.64}$$

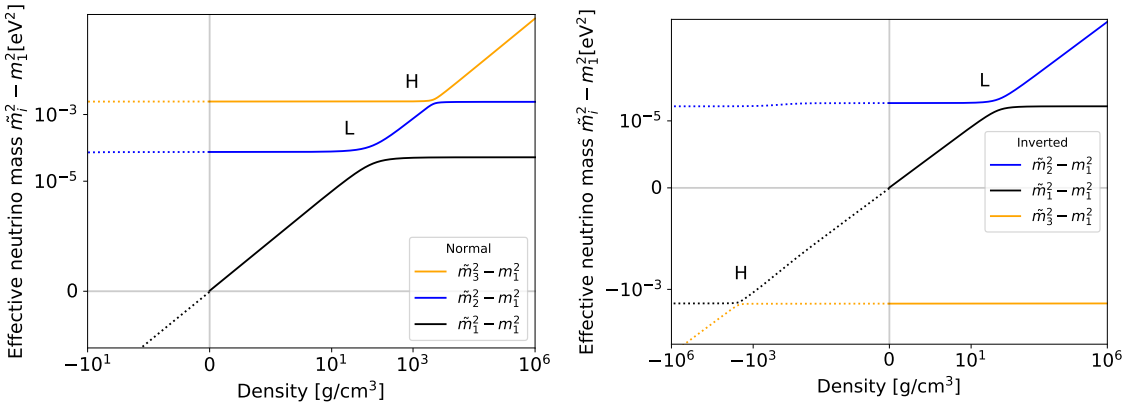

Figure 1.8. Effective neutrino mass $\tilde{m}^2_i - m^2_1$ in the normal (left) and inverted (right) mass ordering for neutrino energy 10 MeV as a function of matter density ρY_e. The part of negative matter density corresponds to the sector for antineutrinos (dotted).

As clearly seen in Fig. 1.8, the H-resonance emerges in the antineutrino sector and the survival probability of electron neutrinos does not display the large mixing. At a high-density limit, $\bar{\nu}_e$ is identical to $\tilde{\bar{\nu}}_3$ and undergoes the large mixing as well as the neutrino sector in the normal mass ordering.

Let us consider the flavor mixing in the supernova case. Neutrinos are produced in the center of the star, where the matter density is extremely high compared to at the level crossings $\rho_{\rm crit}^{H/L}$. Thereby, neutrino flavor eigenstates almost coincide with mass eigenstates and are given in the normal mass ordering case by:

$$\tilde{\nu}_3 = \nu_e,\ \tilde{\nu}_2 = \nu_y,\ \tilde{\nu}_1 = \nu_x. \tag{1.65}$$

Also, the fluxes are similarly written as

$$\tilde{f}_3^0 = f_{\nu_e}^0,\ \tilde{f}_2^0 = f_{\nu_y}^0,\ \tilde{f}_1^0 = f_{\nu_x}^0. \tag{1.66}$$

If the neutrinos adiabatically propagate through the level crossing, the fluxes in mass eigenstates at the surface of the star are simply expressed according to Fig. 1.8 as

$$f_3 = f_{\nu_e}^0,\ f_2 = f_{\nu_y}^0,\ f_1 = f_{\nu_x}^0. \tag{1.67}$$

These states are eigenstates of the Hamiltonian in vacuum, and the mass eigenstates individually travel a long distance to the Earth. Then, neutrinos lose the coherence during the propagation in vacuum so that we will observe the incoherent admixture of the neutrino fluxes of the mass eigenstates [64, 65]. Actually, a general solution for the probability in vacuum is

$$P(\nu_\alpha \to \nu_\beta) = \left| \sum_j U_{\alpha j} \mathrm{e}^{-\mathrm{i}E_j t} U_{\beta j}^* \right|^2 \tag{1.68}$$

$$= \sum_j |U_{\beta j}|^2 |U_{\alpha j}|^2 + \mathrm{Re} \sum_{j \neq k} U_{\beta j} U_{\beta k}^* U_{\alpha j}^* U_{\alpha k} \exp\left[-\mathrm{i}\omega t\right]. \tag{1.69}$$

If neutrinos travel a long distance, the last phase term is averaged out and the first mixing term only survives. In the supernova case, the flavor α is initially diagonalized so that the first term is modified as $|U_{\alpha j}|^2 \to \left|\tilde{U}_{\alpha j}\right|^2$ and leads to matter-dominated oscillation. Consequently, the net flux of electron neutrinos at a detector is restored using mixing angles at the location to

$$f_{\nu_e} = \sum_i |U_{ei}|^2 f_i = |U_{e1}|^2 f_1 + |U_{e2}|^2 f_2 + |U_{e3}|^2 f_3 \tag{1.70}$$

$$= c_{12}^2 c_{13}^2 f_1 + s_{12}^2 c_{13}^2 f_2 + s_{13}^2 f_3 \tag{1.71}$$

$$= c_{12}^2 c_{13}^2 f_{\nu_x}^0 + s_{12}^2 c_{13}^2 f_{\nu_y}^0 + s_{13}^2 f_{\nu_e}^0. \tag{1.72}$$

We can understand the mixing effects similarly for the antineutrino sectors and in the case of the inverted mass ordering. As long as neutrinos propagate adiabatically, the flux in each mass eigenstate remains unchanged from that at the production region and

only mixing angles change. Even if neutrinos travel an astronomical long-distance, the flux at the Earth is identical to that at the surface at the star. In other words, vacuum mixing has no influence on supernova neutrinos out of the star. This is essentially different from the case of pion decay at relatively lower density such as atmospheric and cosmic neutrinos. The neutrinos are not entirely diagonalized at the production region, and vacuum-dominated oscillation occurs during the propagation in vacuum via the first mixing term of Eq. (1.69).

In the case of non-adiabatic propagation, the description is not simple because the jump (flip) probability needs to be considered in Eq. 1.67. The gradients of the shock front and the envelope may potentially induce a non-adiabatic flavor transition [66–70]. The shock wave also propagates through the MSW H- and L-resonances in the supernova envelope as the shock expansion. Since the shock radius determines whether the adiabaticity may break or not, the modulation in energy spectrum observed at the Earth will present the information on the shock propagation. In the normal mass ordering, electron neutrinos becomes the tracer instead because the level crossing is in the neutrino channel. The modulation allows us to trace the shock propagation through the supernova envelope.

The Sun is also one of the most familiar sources and neutrinos are emitted as products in the nuclear fusions to balance with the gravity. Solar neutrinos are produced by several reactions and the energy profile depends on each process. Figure. 1.9 shows the nuclear fusion sequences, called the *pp* chain and the CNO cycle. The reaction rate depends on the

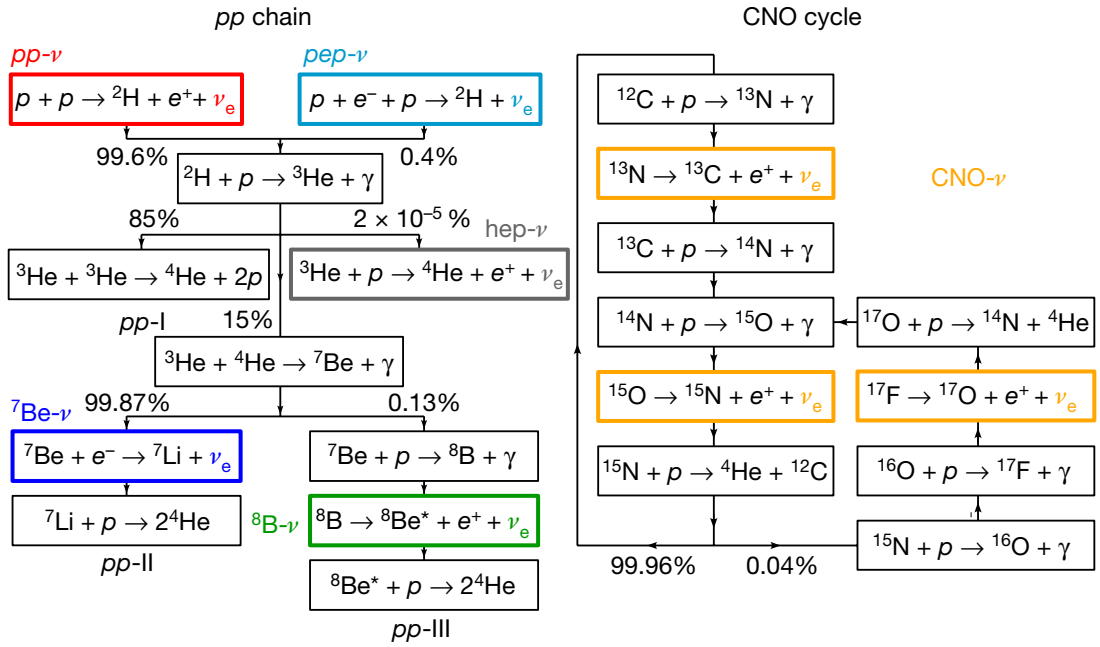

Figure 1.9. Nuclear fusion sequences in the *pp* chain and CNO cycle. Electron neutrinos in the *pp* chain are mainly produced by the *pp*, *pep*, hep reactions, the electron capture on ^{7}Be, and ^{8}B decay. (Reprinted by permission from Springer Nature Customer Service Centre GmbH: Ref. [71])

central temperature and abundance and the *pp* chain is a dominant contribution for low-mass stars like the Sun. The *pp* chain is a nuclear reaction to burn hydrogen into helium and ^{4}He is produced via four different branches: *pp*-I, *pp*-II, *pp*-III, and *pp*-IV (hep). Solar neutrinos are emitted from the *pp* and *pep* reactions, which are rate-limiting reactions, in addition to the *pp*-(II-IV) branches. The most energetic neutrinos of five reactions are emitted via the hep process (up to 18.77 MeV [72]), but the reaction rate is very rare and it is difficult to observe them. The *pp*-III branch is also rare compared to the *pp*-I and *pp*-II branches but generates nearly 1000 times more neutrinos than the hep reaction. The left panel of Fig. 1.10 shows the estimated neutrino energy spectra in the standard solar models [73]. The ^{8}B-neutrinos with the second highest energy $\leq$ 15 MeV are an important detection source over the high energy range, especially in the Sudbury Neutrino Observatory (SNO) and Super-Kamiokande with relatively high threshold energy. On the other hand, the *pp*-neutrinos which are products in the first step of the *pp* chain has the lowest energy (up to 0.42 MeV) but the predominant flux. Such solar neutrinos undergo an energy-dependent flavor mixing through the MSW resonance. The central density of the Sun is about 150 g cm^{-3} and neutrinos with more than a few MeV pass through the L-resonance. Thereby, the flux ratio in mass eigenstates is different in each neutrino process due to the energy dependence of the level crossing. The survival probability of electron neutrinos through matter can be approximately expressed as follows [71, 72, 74]:

$$P_{\nu_e \to \nu_e} = \frac{1}{2}\cos^4\theta_{13}\left(1 + \cos 2\tilde{\theta}_{12}\cos 2\theta_{12}\right), \tag{1.73}$$

where the effective mixing angle $\tilde{\theta}_{12}$ is determined at the location where the neutrino is produced as

$$\cos 2\tilde{\theta}_{12} = \frac{\cos 2\theta_{12} - \beta}{\sqrt{(\cos 2\theta_{12} - \beta)^2 + \sin^2 2\theta_{12}}} \tag{1.74}$$

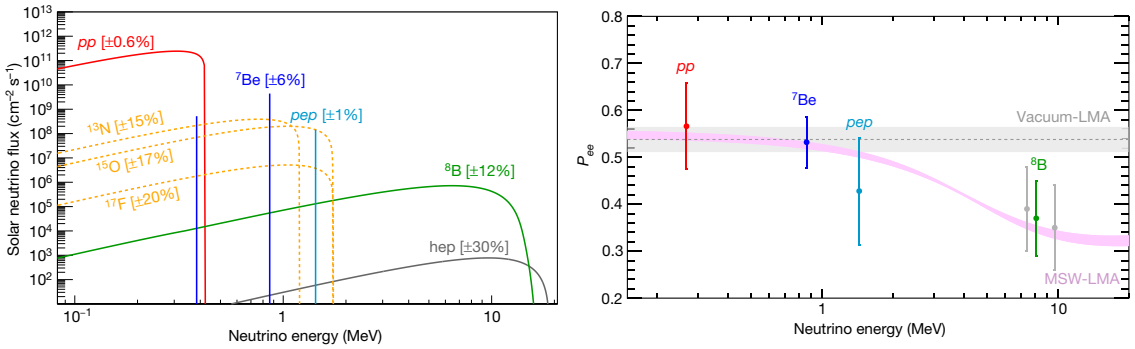

Figure 1.10. Left: energy spectra in solar neutrinos. Right: survival probability of electron neutrinos in the Borexino as a function of neutrino energy. Gray band is the case of ignoring the matter effects and is clearly different from the observation. (Reprinted by permission from Springer Nature Customer Service Centre GmbH: Ref. [71])

and

$$\beta = \frac{2\sqrt{2}G_{\rm F}\cos^2\theta_{13}n_eE_\nu}{\Delta m^2_{12}} = 0.22\cos^2\theta_{13}\left(\frac{E_\nu}{1\ {\rm MeV}}\right)\left(\frac{\mu_e\rho}{100\ {\rm g\ cm^{-3}}}\right)\left(\frac{7\times10^{-5}\ {\rm eV}^2}{\Delta m^2_{12}}\right). \quad (1.75)$$

For instance, the survival probability for neutrinos with 10 MeV, sufficiently larger than the critical energy, is

$$P_{\nu_e\to\nu_e} \simeq \frac{1}{2}\cos^4\theta_{13}\left(1-\cos 2\theta_{12}\right) \sim 0.31 \quad (1.76)$$

Also, low-energy neutrinos which do not propagate through the level crossing in the Sun experiences only a flavor mixing only in vacuum. The survival probability is

$$P_{\nu_e\to\nu_e} = \frac{1}{2}\cos^4\theta_{13}\left(1+\cos^2 2\theta_{12}\right) \sim 0.55. \quad (1.77)$$

Right panel of Fig. 1.10 shows the survival probability of electron neutrinos detected in the Borexino experiment as a function of neutrino energy [71]. Pink band with uncertainty is in the presence of matter effects and gray one is the case of ignoring it. The observation clearly represents the discrepancy with the absent of matter effects at higher energy, and both the vacuum- and matter-dominated flavor mixing emerge in the Sun.

1.4.3 Neutrino oscillation in neutrino gases

In the previous subsection, we have discussed the potentials from the background charged-leptons. However, neutrinos themselves can also interact with other neutrinos via the neutral-current process. The forward coherent scatterings of neutrinos with each other can not be ignored in the environments with dense neutrino gases such as core-collapse supernovae, early universe, and neutron-star mergers [75–77]. Figure 1.11 shows the diagram of the neutrino-neutrino interactions [54] like as the neutrino-electron scatterings in Fig. 1.6. This is a momentum exchange diagram and the momenta are transferred

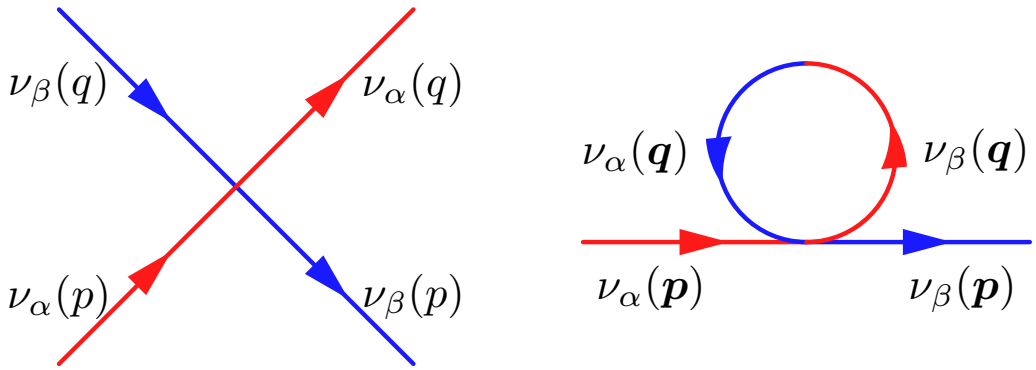

Figure 1.11. The diagrams in the neutrino-neutrino interaction in the left panel. Right panel shows the diagram in the mean-field approximation for the background neutrinos.

between neutrinos with flavors α and β by exchanging a Z boson. Focusing on the momentum p, we find as if a flavor eigenstate is changed from α to β. This four-point interaction has the complexity from the nonlinearity and many-body system. In particular, in core-collapse supernovae, the neutrino flux is $F_\nu = L_\nu/\langle E_\nu \rangle \sim 10^{58}$ s^{-1} and it is realistically impossible to solve the system directly. The interaction diagram of single-particle states can be similarly rewritten to the form in the mean-field approximation by the summation of background neutrino states as the right panel of Fig. 1.11 [54, 78]. Then, the Hamiltonian of the neutrino-neutrino interactions is given by

$$H_{\nu\nu}(t, \boldsymbol{p}) = \sqrt{2} G_{\rm F} \int \frac{{\rm d}^3 \boldsymbol{q}}{(2\pi)^3} (1 - \hat{\boldsymbol{p}} \cdot \hat{\boldsymbol{q}}) \left(\rho(t, \boldsymbol{q}) - \bar{\rho}(t, \boldsymbol{q}) \right), \tag{1.78}$$

where ρ is a neutrino density matrix and is described within three-flavor framework as

$$\rho_\nu = |\nu_\alpha\rangle \langle \nu_\beta| = \begin{pmatrix} \langle \nu_e \,|\, \nu_e \rangle & \langle \nu_e \,|\, \nu_\mu \rangle & \langle \nu_e \,|\, \nu_\tau \rangle \\ \langle \nu_\mu \,|\, \nu_e \rangle & \langle \nu_\mu \,|\, \nu_\mu \rangle & \langle \nu_\mu \,|\, \nu_\tau \rangle \\ \langle \nu_\tau \,|\, \nu_e \rangle & \langle \nu_\tau \,|\, \nu_\mu \rangle & \langle \nu_\tau \,|\, \nu_\tau \rangle \end{pmatrix}. \tag{1.79}$$

The diagonal term $\rho_{\alpha\alpha}$ is a flavor content for a flavor α and the off-diagonal term $\rho_{\alpha\beta}$ is a flavor correlation between α and β. If neutrino gasses are isotropic, the angular term $\hat{\boldsymbol{p}} \cdot \hat{\boldsymbol{q}}$ is averaged out and Eq. (1.78) is reduced to the asymmetry of neutrino density

$$H_{\nu\nu}(t) = \sqrt{2} G_{\rm F} \left[(n_{\nu_e} + n_{\nu_\mu} + n_{\nu_\tau}) - (n_{\bar{\nu}_e} + n_{\bar{\nu}_\mu} + n_{\bar{\nu}_\tau}) \right]. \tag{1.80}$$

Therefore, the strength depends on the neutrino density and can potentially become dominant with high neutrino flux. The time evolution for neutrino density matrix is expressed by the von-Neumann equation:

$$\mathrm{i} \frac{{\rm d}\rho_\nu}{{\rm d}t} = [H_{\nu\nu},\ \rho_\nu], \tag{1.81}$$

where $[*, *]$ is a commutation relation. The off-diagonal term $\rho_{\alpha\beta}$ is zero in initial pure states and the growth indicates the occurrence of flavor mixing in the $\alpha - \beta$ sector. The detailed behaviors of collective neutrino oscillation are shown below chapter 2. There is no evidence for the presence of collective neutrino oscillation yet because it is difficult to produce the neutrino-neutrino interactions in the neutrino experiments. Hence, neutrino observation from core-collapse supernovae is important astrophysical sites to prove the existence.

1.5 Aims and structure of this dissertation

The goal of this dissertation is to investigate numerically the behaviors of collective neutrino oscillation in core-collapse supernovae. Flavor conversion inside the core-collapse supernovae can significantly modify flavor-dependent reactions such as the neutrino-heating mechanism and the neutrino detection. The typical oscillation scale induced by the neutrino self-interactions depends on the neutrino density n_ν and is roughly $\lesssim \mathcal{O}(1)$ cm near the core. It is much smaller than the stellar structure and it is almost impossible to

combine core-collapse simulation with the nonlinear calculation of collective flavor conversion simultaneously. Thus, we perform post-process calculation of collective neutrino oscillation, and obtain the impact on the observational prediction at the Earth and the explosive mechanism.

Collective neutrino oscillation is divided into two types of oscillation modes by the mechanisms and the frequencies: *slow* and *fast* modes [79–82]. Flavor conversion driven by the slow modes has been traditionally investigated using a physical description called the *bulb model*. It enables us to calculate the collective flavor conversion in core-collapse supernovae instead of requiring many assumptions. Then, it has also been revealed that the geometry effects induced by background matter suppress the collective effects [83–85]. The matter suppression depends on the progenitor mass and collective neutrino oscillation is completely suppressed in some massive progenitor cases (see Sec. 3.1 in detail). On the other hand, it has also been suggested that symmetry breaking against the bulb model can overcome the matter suppression and provide significant flavor conversions in some cases [86–92]. One of them is axial-symmetry breaking and the growth of non-axisymmetric components can break the matter suppression [86]. Previous works have performed the numerical calculation under the two-flavor approximation and demonstrated the flavor conversion [87, 88]. However, they employed toy models for supernova properties and monochromatic energy distribution to reduce the computational costs. For the first time, we tackle the three-flavor calculation considering neutrino distribution on three-dimensional momentum space for a supernova model (see Sec. 3.2.2 in detail). Others are spatio-temporal instabilities induced by the inhomogeneity [89–92]. Homogeneous and pulsating modes can weaken the matter suppression and be excited even in the dense matter. The behaviors have been investigated by the linear stability analysis and highly pulsating modes are certainly excited on the constant density. However, the growth rate also decreases as the density declines so that the so-called adiabatic evolution is important in the flavor conversion. We need to simulate the nonlinear calculation for a supernova model in the future. In addition, we challenge neutrino halo effects induced by coherent neutrino-nucleus scatterings. Neutrino halo is created by the direction-changing scattering outside the neutrino sphere and provides a broader angular distribution [93, 94]. Halo neutrinos with larger intersection angles have an impact on the neutrino-neutrino interactions. In particular, the contribution from inwardly scattered flux can modify the bulb description. The previous work employed an electron-capture supernova model only at a neutronization burst [94]. In this case, collective neutrino oscillation does not occur until a radius of ~ 1000 km where the progenitor has a steep density gradient and it is driven simultaneously with the MSW flavor mixing. The situation is not a general description of collective flavor conversion so that the understanding of the halo effects are not also complete. We perform the first-ever numerical simulation of collective flavor conversion including the halo effects in the $9.6M_{\odot}$ iron-core progenitor (see Sec. 3.3 in detail).

Fast flavor conversion is triggered by the neutrino angular distribution and the survey for the possibility inside core-collapse supernovae requires detailed simulation adopting more accurate neutrino transports. Therefore, it has been investigated together with the devel-

opments of core-collapse simulation in the last few years. Most of the previous works were based on the linear stability analysis [95–104] and the nonlinear simulation but assuming homogeneous space [105–108]. Also, most of them employed the two-flavor approximation and have suppressed three-flavor effects. We demonstrate the nonlinear mode-coupling simulation for spatial Fourier modes with six-species angular distributions, and present the existence of a cascade in the spatial structure and the impact from μ/τ-flavor flux (see Sec. 4.2 in detail). And in the last year, the nonlinear simulation considering the spatial inhomogeneity has been worked [109–112] and detailed spatial structure of fast flavor conversion has been revealed. However, the studies of the asymptotic behaviors have used parametric angular distributions not based on supernova models, and also have not sufficiently covered with the types of angular distributions. We perform the dynamical calculation of fast flavor conversion with a spatial distribution for an angular distribution with a supernova model and categorize the asymptotic behaviors on the type (see Sec. 4.3 in detail).

This dissertation is organized as follows. Chapter 2 describes the classification of collective oscillation modes (i.e. slow and fast modes) and the symmetry breaking in collective neutrino oscillation. Chapter 3 shows the impact of symmetry breaking and relaxation against the bulb model in slow flavor conversion. Chapter 4 studies the nonlinear coupling effects and the asymptotic behaviors of fast flavor conversion. Finally, we summarize the dissertation in chapter 5.

Chapter 2

Neutrino flavor conversion

Neutrinos can easily escape from the source with almost no interactions with the background, different from lights. Therefore, the observation allows us to find the activity and structure near the emission source like as when SN1987A. On the other hand, as mentioned in chapter 1, neutrinos emitted from astronomical sites undergo mixing phenomena between flavor eigenstates in their propagation and lose the original flavor information. In particular, the coherent forward scattering of neutrinos with each other can not be ignore in the environments with high neutrino flux and induce nonlinear flavor conversions. The understanding of collective neutrino oscillation is required to obtain the detailed and beneficial information on supernova physics.

2.1 Neutrino oscillation in core-collapse supernovae

Neutrino flavor conversion inside core-collapse supernovae has a large influence on the supernova physics, e.g., explosion mechanism, nucleosynthesis, and observation. Figure 2.1 shows the schematic picture of the impact of neutrino oscillations on supernovae. The effect depends on whether flavor conversions occur inside or outside the stalled shock wave. According to the delayed explosion scenario, electron-type neutrinos deposit the energy to the stalled shock wave and powers the successful explosion. The efficiency of neutrino heating depends on the cross section of absorption, which is proportional to the square of neutrino energy E_ν^2. Since nonelectron-type neutrinos ν_X has higher energy at early phase, the efficiency would increase dramatically if the energy is transferred into electron-type neutrinos ν_e via the flavor conversion in the postshock region [113, 114].

The flavor evolution in weak eigenstates can be described by the equation of motion (EoM) for neutrino density matrices $\rho_\nu(t, \boldsymbol{x}, \Gamma)$ with the momentum space Γ at space-position $(t, \boldsymbol{x})$,

$$\mathrm{i}\left(\partial_t + \boldsymbol{v}\cdot\nabla\right)\rho_\nu(t,\boldsymbol{x},\Gamma) = \left[H(t,\boldsymbol{x},\Gamma), \rho_\nu(t,\boldsymbol{x},\Gamma)\right] + \mathcal{C}\left[\rho_\nu, \overline{\rho}_\nu\right]. \tag{2.1}$$

Also, the Hamiltonian $H(t, \boldsymbol{x}, \Gamma)$ is given by

$$H(t,\boldsymbol{x},\Gamma) = U\frac{M^2}{2E}U^\dagger + v^\mu\Lambda_\mu + \sqrt{2}G_\mathrm{F}\int \mathrm{d}\Gamma' v^\mu v_\mu \rho'_\nu, \tag{2.2}$$

where expresses three types of neutrino oscillations: vacuum, matter, and collective ef-

fects. M^2 in the first term is squared-mass matrix, $\mathrm{diag}(m_1^2, m_2^2, m_3^2)$, and gives initial perturbation seeds in the flavor correlation through mixing angles in the PMNS matrix. The second term in Eq.(2.2) induces matter oscillation, where $v^\mu = (1, \boldsymbol{v})$ and $\Lambda^\mu = \sqrt{2} G_\mathrm{F}\ \mathrm{diag}\left[\{j_\alpha^\mu\}\right]$, with j_α^μ the lepton number current of charged lepton α. We set the metric $\mathrm{diag}(+1, -1, -1, -1)$ in this dissertation. Under the assumption of isotropic background matter, the current term drops and the potential Λ_0 only survives. Hence, this Hamiltonian is simply expressed if we ignore potentials from positrons and heavy charged leptons,

$$H_\mathrm{MSW} = \sqrt{2} G_\mathrm{F} n_{e^-} \mathrm{diag}(1, 0, 0), \tag{2.3}$$

where n_{e^-} is electron number density as a function of radius r. The phase-space integration in the third term, neutrino-neutrino interactions, is $\int \mathrm{d}\Gamma = \int_{-\infty}^{+\infty} \mathrm{d}E E^2 \int \mathrm{d}\boldsymbol{v}/(2\pi)^3$ and we follow the flavor isospin convension, which covers antineutrinos as particles with negative energy and negative occupation number, $\bar{\rho}_\nu(E, \boldsymbol{v}) = -\rho_\nu(-E, \boldsymbol{v})$. The last term $\mathcal{C}$ in Eq.(2.1) represents the incoherent evolution derived from the collision, absorption, and emission of neutrinos.

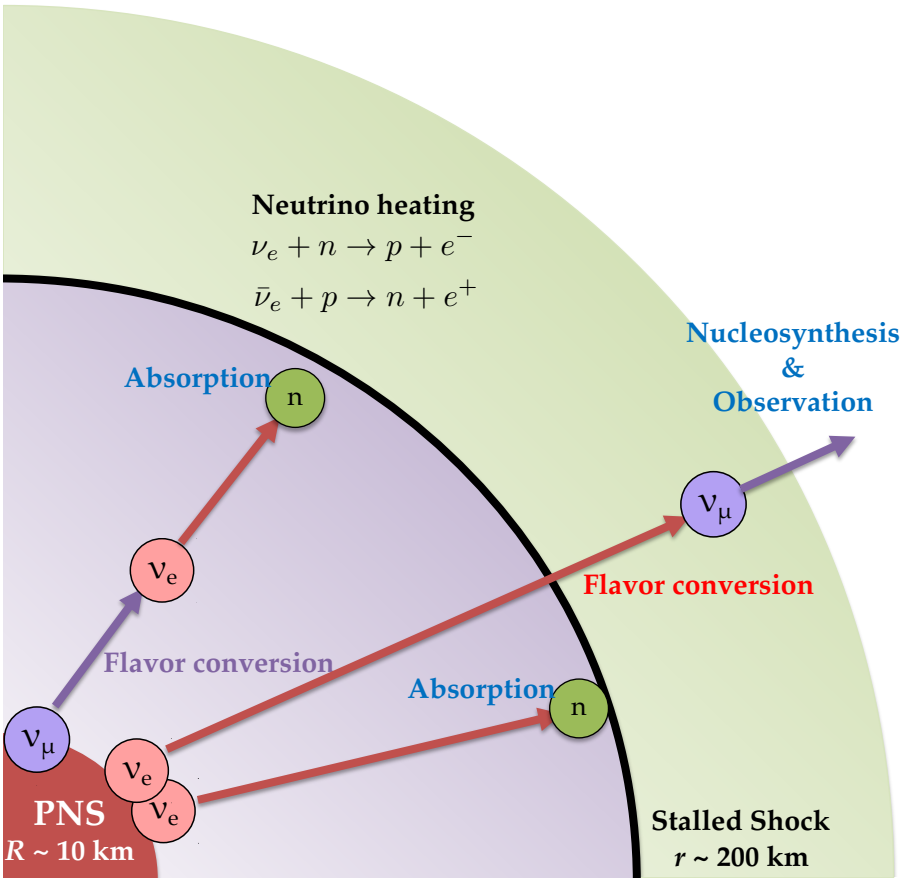

Figure 2.1. Schematic picture of the impact of flavor conversion on supernovae.

2.2 Bloch vector representation

The density matrix ρ for N-level systems can be expanded by the linear combination of an identity I and generators λ_i of $SU(N)$ [115];

$$\rho^{N\times N} = \frac{\mathrm{Tr}(\rho)}{N} I_N + \frac{1}{2}\sum_{i=1}^{N^2-1} P^i \lambda_i, \tag{2.4}$$

where the coefficients $\boldsymbol{P} \in \mathbb{R}^{N^2-1}$ are called the Bloch vectors. Under conditions $\mathrm{Tr}(\rho) = 1$ and $\mathrm{Tr}(\rho^2) \leq 1$, we found the restricted length of the Bloch vector $\boldsymbol{P}$

$$\mathrm{Tr}(\rho^2) = \frac{1}{N} + \frac{1}{2}\|\boldsymbol{P}\|^2 \leq 1 \tag{2.5}$$

$$\Rightarrow \quad \|\boldsymbol{P}\| \leq \sqrt{\frac{2(N-1)}{N}}. \tag{2.6}$$

This relation forms the Bloch vector space $B(\mathbb{R}^{N^2-1})$ called the Bloch ball with a radius $\sqrt{2(N-1)/N}$;

$$B\left(\mathbb{R}^{N^2-1}\right) = \left\{ \boldsymbol{P} = (P_1, P_2, ..., P_{N^2-1}) \in \mathbb{R}^{N^2-1} \,\middle|\, \|\boldsymbol{P}\| \leq \sqrt{\frac{2(N-1)}{N}} \right\}. \tag{2.7}$$

The equality holds and indicates its surface if the density matrix is a pure state, while mixed states are always inside the sphere. The evolution of the Bloch vector is described by Eq. (2.11) in the absence of the incoherent collision term and the norm $\|\boldsymbol{P}\|$ is clearly conserved by taking the dot product of $\boldsymbol{P}$. Therefore, $\|\boldsymbol{P}\|$ can be used as a conserved quantity in the system.

This expansion into the Bloch vector space can be performed for the Hermite matrix and the Hamiltonian in Eq. (2.2) can be also uniquely characterized in the Bloch vector space,

$$H = \frac{\mathrm{Tr}(H)}{N} I_N + \frac{1}{2}\boldsymbol{H}\cdot\boldsymbol{\lambda}. \tag{2.8}$$

On the other hand, the Bloch vector for the neutrino density matrix is especially called the polarization vector $\boldsymbol{P}$ [76]. A commutation operator of the generators follows the Lie algebra $su(N)$,

$$[\lambda_a, \lambda_b] = \sum_{c=1}^{N^2-1} 2\mathrm{i} f_{abc}\lambda_c, \tag{2.9}$$

where f_{abc} is a structure constant (completely antisymmetric tensor), and then the commutation relation in Eq. (2.1) is defined using the cross product "$\times$" as

$$\boldsymbol{H}\times\boldsymbol{P} \equiv \sum_{a,b=1}^{N^2-1} f_{abc} H_a P_b \, \hat{\boldsymbol{e}}_c. \tag{2.10}$$

For two-flavor approximation, the generators are the Pauli matrices $\boldsymbol{\sigma} \in \mathbb{R}^3$ and the Gell-Mann matrices $\boldsymbol{\Lambda} \in \mathbb{R}^8$ for the three-flavor framework. In the absence of the collision term $\mathcal{C}$, the EoM is simply transformed into the vector equation;

$$(\partial_t + \boldsymbol{v} \cdot \nabla)\, \boldsymbol{P}_{\omega,\boldsymbol{v}} = \left[\omega \boldsymbol{B} + \lambda \boldsymbol{L} + \mu_0 \int \mathrm{d}\Gamma' (1 - \boldsymbol{v} \cdot \boldsymbol{v}') \boldsymbol{P}_{\omega',\boldsymbol{v}'}\right] \times \boldsymbol{P}_{\omega,\boldsymbol{v}}, \tag{2.11}$$

where $\omega = \dfrac{\left|\Delta m^2_{32}\right|}{2E_\nu}$, $\lambda = \sqrt{2} G_{\mathrm{F}} n_{e^-}$, and $\mu_0 = \sqrt{2} G_{\mathrm{F}} \left(F_{\bar{\nu}_e} - F_{\bar{\nu}_x}\right)$ correspond to a typical frequency on each neutrino oscillation. For two-flavor approximation,

$$\boldsymbol{B} = (\sin 2\theta, 0, -\cos 2\theta) \tag{2.12}$$

$$\boldsymbol{L} = (0, 0, 1). \tag{2.13}$$

And for three-flavor framework,

$$\boldsymbol{B} = h\left(\boldsymbol{B}_H + \eta \boldsymbol{B}_L\right) \tag{2.14}$$

$$\boldsymbol{B}_H = s^2_{13} \hat{\boldsymbol{e}}_3 + \sin 2\theta_{13} \hat{\boldsymbol{e}}_4 + \frac{1}{\sqrt{3}} (1 - 3c^2_{13}) \hat{\boldsymbol{e}}_8 \tag{2.15}$$

$$\begin{aligned} \boldsymbol{B}_L = {} & c_{13} \sin 2\theta_{12} \hat{\boldsymbol{e}}_1 - s^2_{12} \sin 2\theta_{13} \hat{\boldsymbol{e}}_4 - s_{13} \sin 2\theta_{12} \hat{\boldsymbol{e}}_6 \\ & + (s^2_{12} c^2_{13} - c^2_{12}) \hat{\boldsymbol{e}}_3 + \frac{1}{\sqrt{3}} (1 - 3 s^2_{12} s^2_{13}) \hat{\boldsymbol{e}}_8 \end{aligned} \tag{2.16}$$

$$\boldsymbol{L} = \hat{\boldsymbol{e}}_3 + \frac{1}{\sqrt{3}} \hat{\boldsymbol{e}}_8 ., \tag{2.17}$$

where h is the sign of mass ordering and $\eta = \Delta m^2_{21} / \left|\Delta m^2_{32}\right|$ is the mass-squared difference ratio. P_3 and P_8 correspond to the diagonal terms of the density matrix ρ_ν and the initial conditions are given by

$$P^i_3(E, u, \varphi) = f_{\nu_e}(E, u, \varphi) - f_{\nu_x}(E, u, \varphi) \tag{2.18}$$

$$P^i_8(E, u, \varphi) = \frac{f_{\nu_e}(E, u, \varphi) + f_{\nu_x}(E, u, \varphi) - 2 f_{\nu_y}(E, u, \varphi)}{\sqrt{3}}. \tag{2.19}$$

In the above three-flavor framework, we adopt the rotated system of $(e - x - y)$ flavor basis instead of $(e - \mu - \tau)$ as

$$(\nu_e, \nu_x, \nu_y)^T = R^\dagger_{23}(\theta_{23}) (\nu_e, \nu_\mu, \nu_\tau)^T \tag{2.20}$$

$$= R_{13}(\theta_{13}) R_{12}(\theta_{12}) (\nu_1, \nu_2, \nu_3)^T. \tag{2.21}$$

This convention has been also used in the description of the MSW effects [65], and the H- and L-resonances correspond to flavor mixing in the $e - y$ and $e - x$ sectors, respectively. This rotated basis enables us to pick the flavor conversion associated with the atmospheric Δm^2_{31} and solar squared-mass difference Δm^2_{21} even in the case including the neutrino self-interactions.

2.3 Slow and fast modes

Collective neutrino oscillation is induced by the asymmetry between neutrinos and antineutrinos [81, 82]. If the difference $(\rho_\nu - \bar{\rho}_\nu)$ crosses between positive and negative values at some momentum on the phase space, collective instability can rise. The condition is especially called *spectral crossings*. Asymmetry in the energy distribution induces *slow instability* [79, 80] and that in the angular distribution triggers *fast instability* [95–99, 105]. The two types of flavor instabilities are different in the oscillation frequencies.

Slow instability is a collective flavor instability scaled by the vacuum term ω including the neutrino energy dependence and evolves with a frequency proportional to $(\langle\omega\rangle G_{\rm F} n_\nu)^{1/2}$, which $\langle\omega\rangle$ is the averaged vacuum frequency [116–118]. The slow modes have been often investigated for the stationary case and have demonstrated interesting nontrivial behaviors called spectral splits or swaps [119–121]. Spectral crossings in the energy distribution $f_\nu(E)$ are defined as a function of vacuum frequency ω [79, 80]:

$$g(\omega) = \frac{\left|\Delta m^2_{32}\right|}{2\omega^2} \begin{cases} f_{\nu_e}(E) - f_{\nu_X}(E) & \text{for } \omega > 0 \\ -f_{\bar{\nu}_e}(E) + f_{\bar{\nu}_X}(E) & \text{for } \omega < 0. \end{cases} \tag{2.22}$$

If the distribution with respect to the vacuum frequency ω has zero crossings $g(\omega_c) = 0$ at some ω_c, slow instability can emerge in the flavor correlation. Then, the flavor conversion occurs at several 100 km where neutrino density decreases below near $\langle\omega\rangle G_{\rm F}$ in core-collapse supernovae. Therefore, slow flavor conversion may not probably influence the explosion mechanism of core-collapse supernovae but significantly impact explosive nucleosynthesis and observation in neutrino detectors at the Earth.

Fast instability is driven only by the neutrino density and rises flavor conversions on scales $\sim G_{\rm F} n_\nu$ [95, 105, 122, 123]. Fast modes does not depend on the neutrino energy and can evolve without the vacuum term so that the oscillation frequency is much faster compared than slow instability supported by the vacuum frequency. The occurrence of fast flavor conversion is equivalent to the presence of zero crossings in neutrino flavor lepton number (NFLN) angular distribution [81]. Within the three-flavor framework, three types of pairwise flavor conversions are considered through the difference in the NFLN angular distributions $G^\alpha_{\boldsymbol{v}}$ for each flavor. In particular, if we adopt not the six-species treatments but the three-species $(\nu_e, \bar{\nu}_e, \nu_X)$ in the core-collapse simulation, the conditions for the NFLN differences reduce to for the electron lepton number (ELN) angular distribution $G^e_{\boldsymbol{v}}$:

$$G^e_{\boldsymbol{v}} = \sqrt{2} G_{\rm F} \int \frac{E^2 {\rm d}E}{2\pi^2} \left[f_{\nu_e}(E, \boldsymbol{v}) - f_{\bar{\nu}_e}(E, \boldsymbol{v}) \right]. \tag{2.23}$$

If the sign of the $G^e_{\boldsymbol{v}}$ changes from positive to negative or from negative to positive at some velocity direction v_c, fast pairwise flavor conversions can be triggered. The ELN crossings are very useful to survey the possibility of fast flavor conversions inside core-collapse supernovae. Figure 2.2 represents the space-time diagram of the appearance of ELN

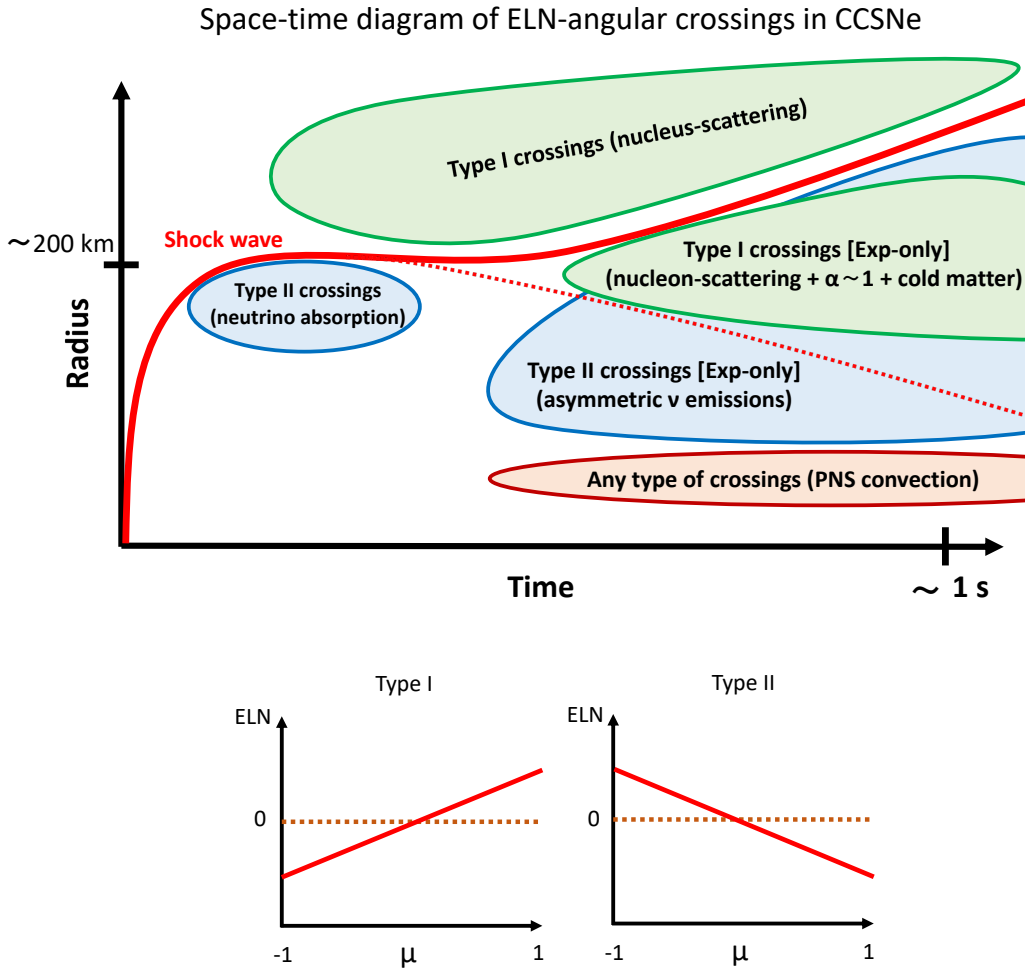

Figure 2.2. Top: Space-time diagram of the appearance of ELN crossings in the evolution of core-collapse supernovae. Bottom: Crossing type of the ELN angular distributions, I & II. (Reprinted figure from Ref. [104]; copyright (2021) by the American Physical Society.)

crossings in the evolution of core-collapse supernovae [104]. This diagram indicates that the ELN crossings are created through several supernova dynamics in both the post-shock and pre-shock region. The ELN angular distributions are divided into two crossing types, classified by the gradient at the crossing direction as shown in the bottom panel of Fig. 2.2. Type-I ELN angular distribution has the positive crossing in which the sign changes from negative to positive, while type-II is the negative crossing. Whether the ELN angular distribution has type-I or type-II crossing depends on how the asymmetry is generated through the SN dynamics. The five possibilities of the ELN crossing are represented in the space-time diagram. Notably, fast flavor conversion is potentially induced behind a stalled shock wave due to the neutrino absorption. The flavor mixing could enhance the neutrino heating process in the delayed explosion scenario of core-collapse supernovae.

2.4 Symmetry and Assumption

Collective neutrino oscillation is induced by nonlinear neutrino-neutrino interactions. The system follows the time evolution of the phase space of neutrino flavor states and we still face the seven-dimensional problems even if escaping the many-body problems under the mean-field approximation. To simplify the complicated system, one have assumed many symmetries and assumptions, and modeled a treatable description. The characterized set of assumptions is called the "Bulb model" [119], which requires a stationary isotropic and axial-symmetric emission from the single surface of neutrinosphere R_ν for all species. The requirements of isotropic emission completely suppress the occurrence of fast flavor conversion because the NFLN angular distribution is always positive or negative and does not have any angular crossings. The bulb model demonstrates only collective slow flavor conversion. The neutrino flux in the bulb model depends only on the radial direction r and in the momentum space, the neutrino energy E_ν and the emission angle θ_R, and does not allow any scatterings including the direction changing. Figure 2.3 presents the schematic picture of the bulb model. A neutrino intersection angle θ is restricted within the cone and the integration range depends on the radius r. The intersection angle at a given radius is characterized by neutrino trajectory with its emission angle θ_R and provides the one-to-one correspondence:

$$r \sin\theta = R_\nu \sin\theta_R \tag{2.24}$$

$$\cos\theta = \sqrt{1 - \sin^2\theta_R \frac{R_\nu^2}{r^2}}. \tag{2.25}$$

The transformation changes the polar-angle integration into

$$\int_0^{\theta_{\max}} \mathrm{d}\cos\theta = \frac{R_\nu^2}{2r^2} \int_0^1 \mathrm{d}\sin^2\theta_R \frac{1}{\sqrt{1 - \sin^2\theta_R \left(\frac{R_\nu}{r}\right)^2}} = \frac{R_\nu^2}{2r^2} \int_0^1 \mathrm{d}u \; v_{r,u}^{-1}, \tag{2.26}$$

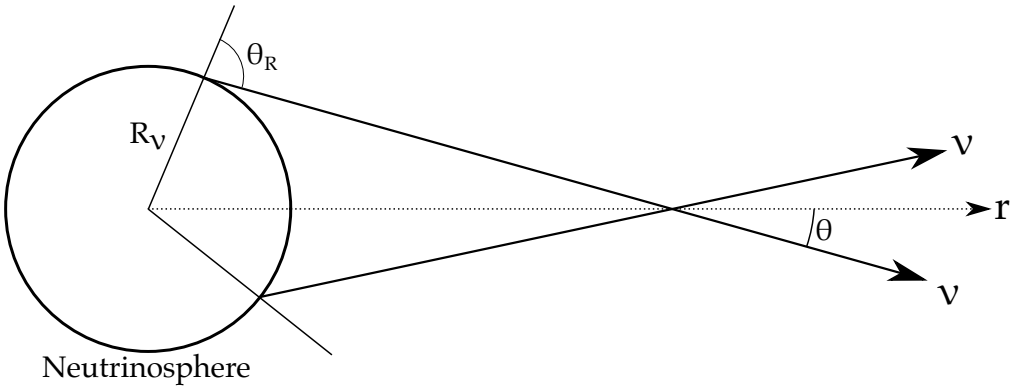

Figure 2.3. The schematic picture of the bulb model. All species are emitted from the single neutrinosphere.

where $v_{r,u} = \cos\theta$ is a radial velocity with angular mode $u = \sin^2\theta_R$. Therefore, the EoM in the radial direction is converted into

$$\partial_r \boldsymbol{P}_{\omega,u} = \left[\frac{\omega \boldsymbol{B} + \lambda \boldsymbol{L}}{v_{r,u}} + \mu_0 \frac{R_\nu^2}{2r^2} \int_{-\infty}^{+\infty} \mathrm{d}\omega' \int_0^1 \mathrm{d}u \left(\frac{1 - v_{r,u} v_{r,u'}}{v_{r,u} v_{r,u'}}\right) g_{\omega',u'} \boldsymbol{P}_{\omega',u'}\right] \times \boldsymbol{P}_{\omega,u}. \tag{2.27}$$

This formalism is especially called the "multiangle" approximation and has been investigated by many studies. In subsequent Sec. 3.1, we will present the multiangle calculation and interesting features.

We perform a test calculation within the two-flavor framework to investigate the spectral splits through the multiangle approximation in Eq. (2.27). We take neutrino properties in Tab. 2.1, which have been widely adopted in the previous works [88, 124]. ξ is called a pinching parameter and describes the amount of spectral pinching. We use a gamma distribution [125, 126] as an initial neutrino spectrum with flavor α on the surface of the neutrino sphere $R_\nu = 10$ km:

$$f_{\nu_\alpha}(E_\nu) = \frac{L_{\nu_\alpha}}{\langle E_{\nu_\alpha}\rangle} \frac{(E_\nu)^{\xi_\alpha}}{\Gamma(\xi_{\nu_\alpha}+1)} \left(\frac{\xi_{\nu_\alpha}+1}{\langle E_{\nu_\alpha}\rangle}\right)^{\xi_{\nu_\alpha}+1} \exp\left[-(\xi_{\nu_\alpha}+1)\frac{E_\nu}{\langle E_{\nu_\alpha}\rangle}\right]. \tag{2.28}$$

The original energy spectra $f_\nu(E)$ and energy crossings in $g(\omega)$ of Eq. (2.22) are shown in Fig. 2.4. Smaller ω corresponds to higher neutrino energy E_ν and this energy distribution has three zero crossings near $\omega = 0$. Therefore, flavor conversion can occur in neutrino

Flavor ν_α	Luminosity L_{ν_α}	Averaged energy $\langle E_{\nu_\alpha}\rangle$	Pinching parameter ξ_α
ν_e	2.4×10^{51} erg s^{-1}	12 MeV	3
$\bar{\nu}_e$	2.0×10^{51} erg s^{-1}	15 MeV	3
$\nu_X/\bar{\nu}_X$	1.5×10^{51} erg s^{-1}	18 MeV	3

Table 2.1. Properties for neutrino spectrum in a test calculation.

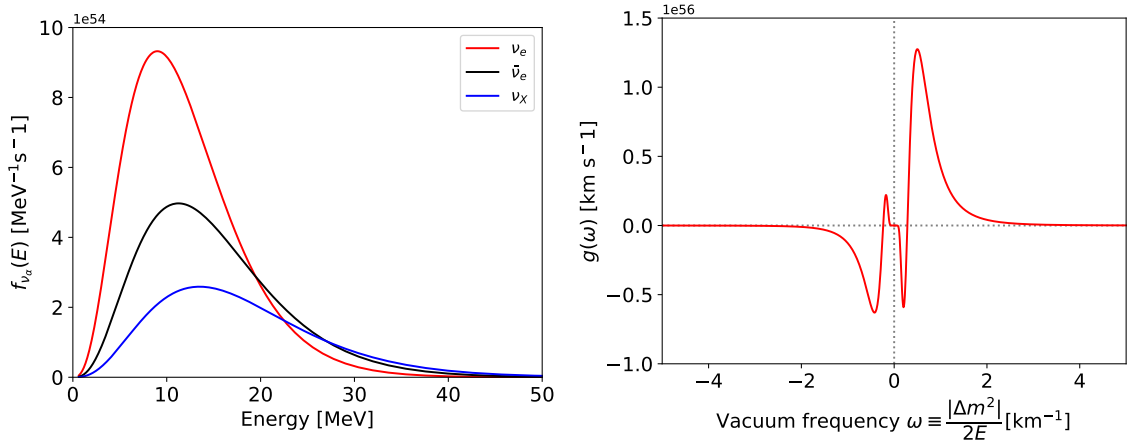

Figure 2.4. Left: initial energy spectra for $\nu_e, \bar{\nu}_e$, and ν_X. Right: spectral crossings in energy distribution as a function of the vacuum frequency ω. Negative ω means antineutrino channel.

and antineutrino channels across the infinite energy $\omega = 0$. We neglect the matter term $\lambda = 0$ and assume small mixing angle $\theta_m = 10^{-3}$ to mimic the matter suppression, which will be discussed in Sec. 3.1. Figure 2.5 shows the behaviors of spectral splits in a test calculation. Top panels are neutrino spectra and bottom one is the radial evolution of the survival probability of electron neutrinos for each energy. Neutrinos over all energy ranges collectively undergo the flavor conversion at $r \sim 80$ km but the survival probabilities are split into two types. Energy spectra for neutrinos are swapped between ν_e and ν_X only above a critical energy 10 MeV. On the other hand, antineutrino sector exhibits the flavor exchange above $\sim$ 1 MeV. The flavor swaps in both channels across $\omega = 0$ are consistent with the spectral crossings in Fig. 2.4. Collective neutrino oscillation transfers high energy tail in the nonelectron-type neutrinos into the electron-type neutrinos and hence can affect several neutrino reactions via the charged-current interactions [127–131]. If this slow instability can be excited inside the stalled shock wave during the accretion phase, collective neutrino oscillation can enhance the neutrino heating process. However, the onset radius is outside it in the most of cases. The reason will be discussed below the

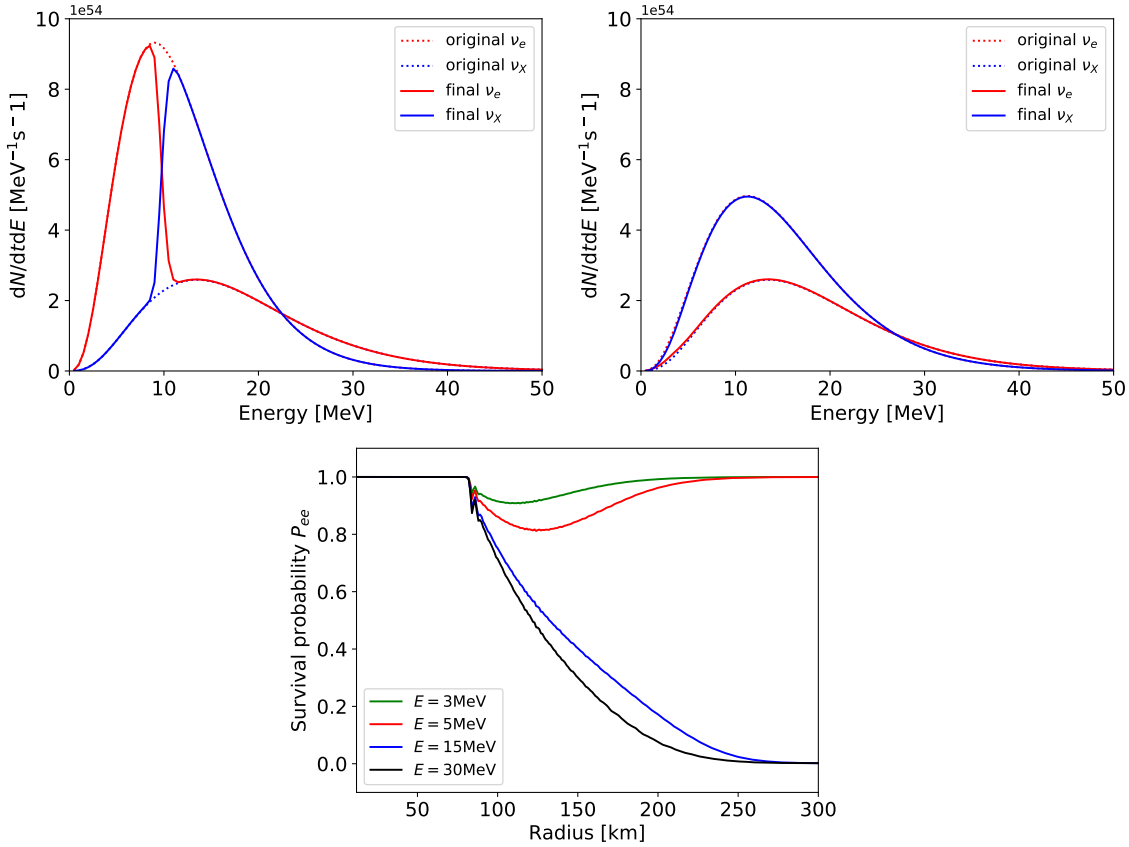

Figure 2.5. Energy spectra for neutrinos (top left) and antineutrinos (top right) after collective neutrino oscillation in the inverted mass ordering. Neutrino spectra are split above a critical energy 10 MeV. Dotted lines are original spectra and solid ones are final spectra after collective neutrino oscillation. Bottom panel shows the survival probability of electron neutrinos for each energy.

Sec. 3.1.

Slow flavor conversion in the bulb model demonstrates interesting spectral splits. The multiangle simulation imposes many assumptions and symmetries, while the requirements are not real in nature. We will discuss the effects of symmetry breaking on collective flavor conversion in the following chapter 3. In Sec. 3.1, we demonstrate the effects of matter suppression on collective slow conversion. In Sec. 3.2, we here introduce the description removing the assumptions for slow instability and mainly discuss the axial-symmetry breaking in direction. The breaking induces new flavor instabilities and can affect the flavor contents. In Sec. 3.3, we consider the coherent neutrino-nucleus elastic scattering against the bulb model. The direction changing scatterings make broader intersection angles and change the bulb description.

In chapter 4, we take up the anisotropic neutrino angular distribution which can trigger fast instability. In particular, the coherent scatterings in the preshock region of core-collapse supernovae generate the inward-going components and the backward crossing can lead to fast flavor conversion. In Sec. 4.2, we focus on the three-flavor effects due to the angular distributions for the heavy-leptonic flavors and the inclusion case of the vacuum term. In Sec. 4.3, we challenge the local flavor evolution of the fast instability.

Chapter 3

Slow Flavor Conversion

Slow flavor instability is triggered by the asymmetry of the energy distribution. Since the channel of antineutrinos in Eq. 2.22 set the negative sign for the distribution, the existence of energy crossing are always expected even if we consider only electron-type flavors or employ monochromatic energy spectra. Therefore, collective slow flavor conversions are possible inside core-collapse supernovae unless the vacuum term driving slow instability is neglected. Detailed information on the neutrino phase space is irrespective of the slow instability and we do not require core-collapse supernova models by the Boltzmann solver with the highest computational costs, which can resolve the neutrino angular distribution. Thanks to the mildness of the crossing conditions, many studies have been done in both the linear and nonlinear regime, and have revealed the influence of flavor conversions on neutrino observation and explosive nucleosynthesis. In this chapter, we introduce three interesting behaviors of slow flavor conversions, following my previous papers [132–134]: matter-induced suppression, symmetry breaking, and neutrino halo.

3.1 Matter Suppression

The neutrino-neutrino interaction couples all traveling neutrinos and the self-coupling system forces the synchronization of oscillation phase and induces the collective effects. The collective effect maintains coherence among neutrinos with different angular modes. On the other hand, the presence of background matter prevents the self-coupling effect. Matter term in Eq.(2.27) includes the dependence on a radius r and an angular mode u. In the large-distance limit $r \gg R_\nu$,

$$\frac{\lambda}{v_{r,u}} \simeq \lambda \left(1 + u\frac{R_\nu^2}{2r^2}\right) = \lambda + u\lambda\frac{R_\nu^2}{2r^2}. \tag{3.1}$$

The first term is independent of the radius and angular modes, and ignored as a common phase of plane wave solutions. However, the second term includes the information on neutrino trajectory. Neutrinos arriving at a certain radius r along different trajectories $(r, u \neq 0)$ have travelled longer distances relative to the radial direction $(r, u = 0)$. The trajectory dependence changes effective charged-current potential for each angular mode. Therefore, the mode coupling among different neutrino trajectories results in the oscillation phase dispersion [83]. To lead to collective flavor conversion, the phase syn-

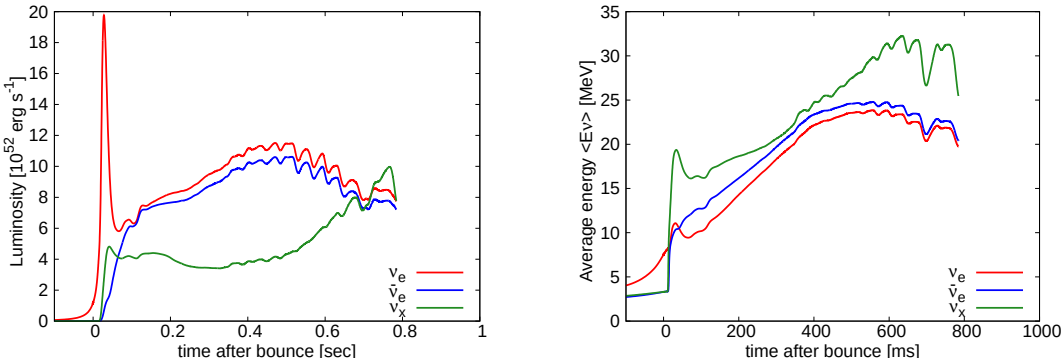

Figure 3.1. The time evolution of neutrino luminosity L_{ν_α} (left) and averaged energy $\langle E_{\nu_\alpha} \rangle$ (right) in a failed SN model with $40 M_\odot$.

chronization induced by the collective effect needs to overcome the matter-induced phase dispersion. Actually, high matter density near the proto-neutron star in CCSNe can suppress the collective effect completely in spite of high neutrino density [84, 85, 132]. In this chapter, we will discuss the multiangle matter suppression, especially in failed SNe as reviewing our previous paper [132].

3.1.1 Complete matter suppression in failed SNe

Massive stars experience core collapse at the final stage of stellar evolution. In the delayed explosion scenario, neutrino heating process powers a stalled shock wave and helps to succeed the explosion. However, some fraction of the high-mass progenitors fail to explode, which is called a failed SN (e.g., Refs. [135–137]). The intense matter accretion of the outer layer prevents the stalled shock wave from reviving, unlike the successful SNe. The matter which is not blown away by this shock wave continuously accretes into the PNS, and the central temperature and density raise compared to in the successful SNe. The unlimited accretion phase produces more energetic neutrinos in failed SNe until the neutrino sphere is wrapped by the event horizon after the formation of a black hole. In this chapter, we employ the spherically symmetric 1D failed supernova simulation [135, 136] with a progenitor having $40 M_\odot$ [138] and adopt the equation of state by Lattimer and Swesty with an incompressibility of 220 MeV (LS220-EOS) [139]. Figure 3.1 shows the time evolution of neutrino luminosity L_{ν_α} (left) and averaged energy $\langle E_{\nu_\alpha} \rangle$ (right) in a failed SN model with $40 M_\odot$ [132]. In this model, the black hole formation happens at the postbounce time $t_{\rm pb} = 783$ ms and the neutrino emission stops. The averaged neutrino energy finally increases to ~ 30 MeV and is higher than ~ 15 MeV in the successful SNe. Figure 3.2 represents density profiles at $t_{\rm pb} = 30, 100, 500$, and 600 ms. The shock wave is located around 100 km at the early epoch $t_{\rm pb} = 30$ and 100 ms, while it forms the accretion shock at the late epoch $t_{\rm pb} = 500$ and 600 ms.

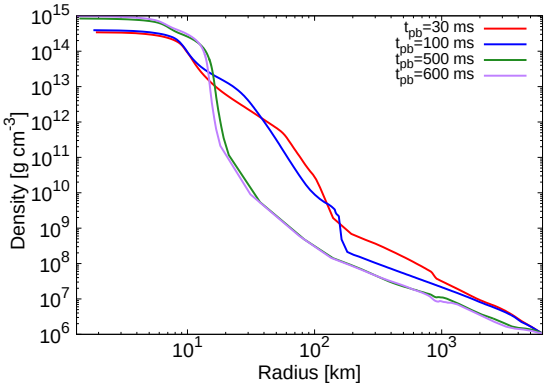

Figure 3.2. Density profiles at $t_{\rm pb} = 30, 100, 500$, and 600 ms.

3.1.2 Numerical setup & results

Collective flavor conversion provides spectral splits depending on the energy distribution. Here, we use a gamma distribution [125, 126] as an initial neutrino spectrum with flavor α on the surface of the neutrino sphere:

$$f_{\nu_\alpha}(E_\nu) = \frac{L_{\nu_\alpha}}{\langle E_{\nu_\alpha}\rangle}\frac{(E_\nu)^{\xi_\alpha}}{\Gamma(\xi_{\nu_\alpha}+1)}\left(\frac{\xi_{\nu_\alpha}+1}{\langle E_{\nu_\alpha}\rangle}\right)^{\xi_{\nu_\alpha}+1}\exp\left[-(\xi_{\nu_\alpha}+1)\frac{E_\nu}{\langle E_{\nu_\alpha}\rangle}\right], \tag{3.2}$$

where ξ_{ν_α} is a pinching parameter given by

$$\xi_{\nu_\alpha} = \frac{\langle E^2_{\nu_\alpha}\rangle - 2\langle E_{\nu_\alpha}\rangle^2}{\langle E_{\nu_\alpha}\rangle^2 - \langle E^2_{\nu_\alpha}\rangle}. \tag{3.3}$$

In this energy distribution, we use the energy resolution of $N_E = 200 \in [0, 100]$ MeV. And we adopt the polar angular resolution of $N_u = 2000 \in [0, 1]$ to avoid the occurrence of artificial oscillation.

We first show the numerical results in the inverted mass ordering case at $t_{\rm pb} = 600$ ms as an example. Figure 3.3 represents the radial evolution of survival probability P_{ee} of electron neutrinos at 20 MeV. In the case of red line, we adopt the density profile in Fig. 3.2 as it is, while we manually reduce the electron density by a factor of 100 in green line. We call the former the standard case and the latter the low-density case. And blue line is in the case of the single-angle approximation, which ignores any dependence on the neutrino trajectories from the neutrino sphere [119]. In the single-angle approximation, the multiangle term in the Hamiltonian is reduced to the geometric factor along the radial direction $u = 0$:

$$D_r \equiv \int_0^1 {\rm d}u'\ (1 - v_{r,u}v_{r,u'})\Big|_{u=0} = \frac{1}{2}\left[1 - \sqrt{1 - \frac{R_\nu^2}{r^2}}\right]^2. \tag{3.4}$$

The single-angle geometry of the neutrino self-interaction does not induce the multiangle decoherence and collective neutrino oscillation does not have any influence from the matter

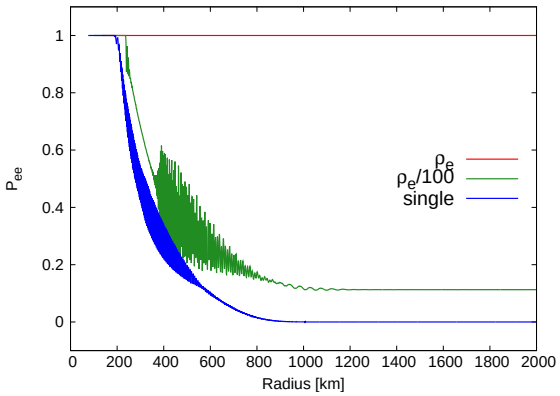

Figure 3.3. The radial evolution of survival probability P_{ee} of electron neutrinos at 20 MeV at $t_{\rm pb} = 600$ ms. Red and green lines are in the standard case and the low-density case, respectively. Blue line correspond to the single-angle case.

suppression. In the standard case, we find that collective neutrino oscillation is completely suppressed. On the other hand, collective flavor conversion occurs at $r \sim 200$ km in the low-density case. The onset radius and survival probability is similar to the single-angle case, and demonstrates the quasi-single angle behaviors.

The multiangle matter suppression dominates collective neutrino oscillation at all time snapshots in this failed supernova model. The absence of flavor conversions can be confirmed by the linear stability analysis in the subsequent subsection.

3.1.3 Linear stability analysis

We introduce the linear stability analysis to understand the multiangle matter suppression. Collective neutrino oscillation is a nonlienar effect, but the onset of the flavor conversion is still in the linear order. Therefore, the linear stability analysis has been used to investigate whether collective flavor conversion can occur [80]. Here, we simply consider two-flavor approximation because three-flavor effects does not directly change the multiangle matter suppression. We can decompose the density matrix to see the evolution of the off-diagonal parts:

$$\rho_\nu = \frac{{\rm Tr}(\rho_\nu)}{2}\mathbb{I}_2 + \frac{f_{\nu_e} - f_{\nu_x}}{2}\begin{pmatrix} s & S \\ S^* & -s \end{pmatrix} = \frac{{\rm Tr}(\rho_\nu)}{2}\mathbb{I}_2 + g\mathbb{S}. \tag{3.5}$$

To the linear order, we assume $|S| \ll 1$ and $s = 1$, and we can get the linearized equation for S from Eq.(2.27) in the bulb model as

$$\mathrm{i}v_{r,u}\partial_r S = \left[-\omega + \lambda + \mu\int {\rm d}\Gamma'(1 - \boldsymbol{v}\cdot\boldsymbol{v}')g'\right]S - \mu\int {\rm d}\Gamma'(1-\boldsymbol{v}\cdot\boldsymbol{v}')g'S'. \tag{3.6}$$

Here we select a fast-rotating frame where the vacuum term oscillates quickly and the off-diagonal term averages to zero [80, 83]. Assuming the isotropic emission $g(\omega, u, \varphi) =$

$g(\omega)/2\pi$ and the large-distance limit $r \gg R_\nu$, we can rewrite it as

$$\mathrm{i}\partial_r S_{\omega,u} = \left(\frac{-\omega+\lambda+\epsilon\mu}{v_{r,u}}\right) S_{\omega,u} - \mu\int_{-\infty}^{+\infty}\mathrm{d}\omega'\int_0^1 \mathrm{d}u'\left(\frac{1-v_{r,u}v_{r,u'}}{v_{r,u}v_{r,u'}}\right) g_{\omega'}S_{\omega',u'} \tag{3.7}$$

$$\simeq \left(-\omega+u\bar{\lambda}^*\right) S_{\omega,u} - \mu^*\int_{-\infty}^{+\infty}\mathrm{d}\omega'\int_0^1 \mathrm{d}u'(u+u')g_{\omega'}S_{\omega',u'}, \tag{3.8}$$

where the effective matter potential $\bar{\lambda}^*$ is given by the multiangle potential μ^* and λ^* as follows:

$$\bar{\lambda}^* = \lambda^* + \epsilon\mu^* = (\lambda+\epsilon\mu)\frac{R_\nu^2}{2r^2}. \tag{3.9}$$

Also, we ignore a small distance-dependent shift of ω derived from $v_{r,u}^{-1}$. Note that the energy spectrum g is normalized as $\int_{-\infty}^{0}\mathrm{d}\omega' g_\omega = -1$ and hence the asymmetry parameter $\epsilon = \int_{-\infty}^{+\infty}\mathrm{d}\omega' g_\omega$. The eigenvalue equation for the plane wave ansatz $S_{\omega,u} = Q_{\omega,u}\mathrm{e}^{-\mathrm{i}\Omega r}$ is

$$\left[-\omega+u\bar{\lambda}^*-\Omega\right] Q_{\omega,u} = \mu^*\int_{-\infty}^{+\infty}\mathrm{d}\omega'\int_0^1\mathrm{d}u'(u+u')g_{\omega'}Q_{\omega',u'}. \tag{3.10}$$

The right-hand side is simply the linear form $A+Bu$ and the eigenfunction $Q_{\omega,u}$ should be led as

$$Q_{\omega,u} = \frac{A+Bu}{-\omega+u\bar{\lambda}^*-\Omega}. \tag{3.11}$$

By substituting it into the eigenvalue equation, we get

$$\begin{pmatrix} I_1-1 & I_2 \\ I_0 & I_1-1\end{pmatrix}\begin{pmatrix} A \\ B\end{pmatrix} = 0, \tag{3.12}$$

where

$$I_n = \mu^*\int \mathrm{d}\omega\mathrm{d}u\frac{u^n g_\omega}{-\omega+u\bar{\lambda}^*-\Omega}. \tag{3.13}$$

Then, the physical and nontrivial solutions are

$$D(\Omega) \equiv (I_1-1)^2 - I_0 I_2 = 0. \tag{3.14}$$

If Ω satisfying this condition has a positive imaginary part $\kappa = \mathrm{Im}(\Omega)$, the off-diagonal term S of the density matrix will take a flavor instability and grows exponentially at the radius. The instability is called the bimodal (BM) instability in the inverted mass ordering case and the multi-zenith-angle (MZA) instability in the normal mass ordering case. We find whether collective flavor conversion can occur by investigating the existence of these instabilities.

Here, we consider a monochromatic spectrum with some fixed energy ($\omega = \pm\omega_0$),

$$g_\omega = (1+\epsilon)\delta(\omega-\omega_0) - \delta(\omega+\omega_0). \tag{3.15}$$

The collective effect suggests that all neutrinos start to oscillate at the same onset radius because the self-interaction potential itself does not depend on the neutrino energy but the

difference in the flux. We can hence simplify the treatments of the momentum integration in the collective term. In this simple model, we analytically perform the integration in Eq.(3.13) as

$$I_n = \frac{\mu^*}{\bar{\lambda}^*}\left[(1+\epsilon)\left\{\alpha_+^n \ln\left(1-\frac{1}{\alpha_+}\right)+\sum_{j=0}^{n-1}\frac{1}{n-j}\alpha_+^j\right\} - \left\{\alpha_-^n \ln\left(1-\frac{1}{\alpha_-}\right)+\sum_{j=0}^{n-1}\frac{1}{n-j}\alpha_-^j\right\}\right], \tag{3.16}$$

where

$$\alpha_\pm = \frac{\Omega \pm \omega_0}{\bar{\lambda}^*}. \tag{3.17}$$

We can obtain the growth rate by surveying Ω on the complex plane by the root-finding algorithms such as the Newton's method.

Figure 3.4 shows the contour of the growth rates κ in the BM case at $t_{\rm bp} = 600$ ms. If density profile intersects the shaded region, the flavor instability develops locally. However, in this case, the density profile passes over the unstable region and it means that high matter density completely suppresses the collective flavor conversion. The results from the linear stability analysis is consistent with no flavor conversion in Fig.3.3. In the low-density case, neutrinos propagate through the density profile and undergo the BM flavor instability. The intersection point $r \sim 200$ km of the density profile with the unstable region roughly matches the onset radius of the collective flavor conversion in the numerical simulation. This confirms the linear stability analysis is useful for us to investigate the competition between the collective effect and the matter suppression.

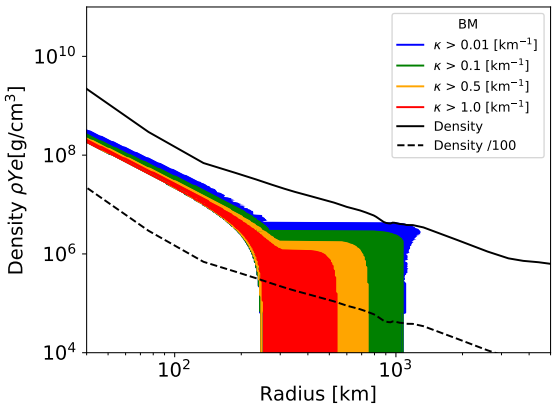

Figure 3.4. Contour map of the growth rates κ in the BM case at $t_{\rm bp} = 600$ ms. Density profile is over the shaded unstable region and neutrinos do not undergo the BM instability.

3.1.4 Angular resolution and spurious mode

Here, we discuss angular resolution problems associated with the matter suppression. Figure 3.5 shows the radial evolution of the survival probabilities for four kinds of angular bins: $N_u = 500, 1000, 1500$, and 2000. Artificial flavor evolution emerges in the insufficient angular binning $N_u \lesssim 1500$. It results from the growth of "spurious modes" derived from the discrete angular integration and the suppression for the spurious instabilities requires many amount of angular bins [140, 141]. The presence of these unphysical modes can be easily understood by the discrete scheme in the linear stability analysis. We assume the hair-comb spectrum following Ref. [140] as

$$g_{\omega,u} = [(1+\epsilon)\delta(\omega-\omega_0) - \delta(\omega+\omega_0)]\, H(u) \tag{3.18}$$

$$H(u) = \frac{1}{N_u}\sum_{j=1}^{N_u} \delta\left(\frac{j-1/2}{N_u} - u\right). \tag{3.19}$$

Then, the integration in I_n is

$$I_n = \frac{\mu^*}{N_u}\sum_{j=1}^{N_u}\left[\frac{(1+\epsilon)\left(\frac{j-1/2}{N_u}\right)^n}{-\omega_0 - \Omega + \frac{j-1/2}{N_u}\bar{\lambda}^*} - \frac{\left(\frac{j-1/2}{N_u}\right)^n}{+\omega_0 - \Omega + \frac{j-1/2}{N_u}\bar{\lambda}^*}\right]. \tag{3.20}$$

For $N_u = 1$, the single-angle case, Eq. (3.14) becomes a quadratic equation for Ω and we can solve it exactly as

$$\Omega = -\frac{\epsilon\mu^* - \bar{\lambda}^*}{2} \pm \sqrt{\omega_0^2 + (2+\epsilon)\mu^*\omega_0 + \left(\frac{\epsilon\mu^*}{2}\right)^2}. \tag{3.21}$$

The condition that Ω has a positive imaginary part is

$$\frac{2\omega_0}{\epsilon^2}\left[-(2+\epsilon) - 2\sqrt{1+\epsilon}\right] < \mu^* < \frac{2\omega_0}{\epsilon^2}\left[-(2+\epsilon) + 2\sqrt{1+\epsilon}\right] \tag{3.22}$$

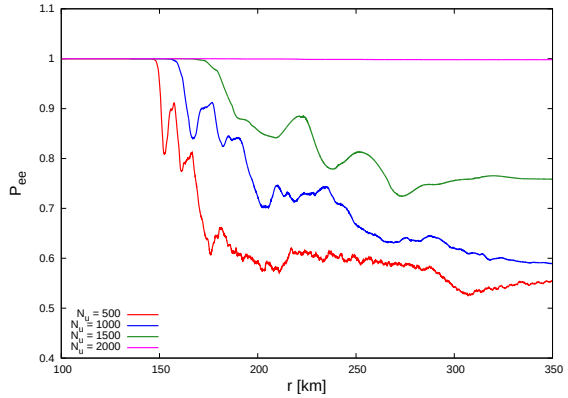

Figure 3.5. Same as Fig. 3.3 but for the comparison of angular resolutions of $N_u = 500, 1000, 1500$, and 2000 in the standard case.

and the mass ordering is inverted, $\omega_0 < 0$, for positive μ. The growth rate in Eq. (3.21) is independent of matter density λ because the multi-angle phase dispersion does not work in the single-angle case.

If we consider $N_u \geq 2$ case, Eq. (3.14) gives polynomials of Ω with $2N_u$ roots. One of them corresponds to the physical solution uniquely derived from Eq. (3.16). The others are artificial modes yielded by the discretization of the angular integration. Therefore, spurious modes always emerge as long as we adopt finite angular bins in numerical calculations. And the spurious modes possess comparable growth rate ImΩ with the physical solution and we need to avoid accidentally picking up the non-physical modes. If we employ sufficient angular resolutions, the spurious modes are far from the μ range shown in Eq. (3.22). However, in the insufficient cases, the spurious modes stay near or just on the μ range, where the collective instability has non-zero growth rates, and consequently cover over the physical mode. This is a discussion within the linear regime, but the presence of spurious modes largely affects the flavor evolution during the early phase even in the nonlinear simulations and induces the artificial behaviors as shown in Fig. 3.5. In the linear regime, we can avoid spurious modes to arise only by analytically performing the angular integration for the distribution fitted with polynomials [141].

3.1.5 Neutrino signal prediction

Finally, we discuss the detectability of neutrinos from the failed supernova model. Emitted neutrinos from the center undergo collective neutrino oscillation and then the MSW resonance. Above the simulation, collective neutrino oscillation is completely suppressed at all time snapshots in our employed failed supernova model. Therefore, only the MSW H- and L-resonances affect the detected neutrino spectra. Now, we consider two representative neutrino detectors, Super-Kamiokande and DUNE. We evaluate the event rates, assuming that the distance to the target failed supernova is $d = 10$ kpc as a typical distance in our Galaxy.

Super-Kamiokande is a water Cherenkov detector in Japan. In the fourth experiment (SK-IV), the fiducial volume is 22.5 kton and the threshold energy is 3.5 MeV corresponding to recoil electron kinetic energy [142, 143]. Water Cherenkov detectors have a high sensitivity to inverse beta decay (IBD; $p(\bar{\nu}_e, e^+)n$) reaction and electron antineutrinos can be detected via this reaction. The threshold energy for $\bar{\nu}_e$ is $E_{\rm th} = 4.79$ MeV because of the mass difference between proton and neutron. We take the cross section σ of IBD reaction from [144].

The Deep Underground Neutrino Experiment (DUNE) is a proposed neutrino experiment in the United States [145]. A Liquid Argon Time-Projection Chamber can provide a detection of electron neutrino via a charged-current reaction $^{40}{\rm Ar}(\nu_e, e^-)^{40}{\rm K}^*$. DUNE will be composed of four detectors with the fiducial volume 10 kton and the total fiducial volume of liquid argon is designed to be 40 kton. The threshold energy of this charged-current reaction has not been determined yet, but here, we assume that the electron energy cut-off is 5 MeV. Due to the energy difference between ^{40}Ar and $^{40}{\rm K}^*$, the threshold energy for electron neutrinos is 8.28 MeV. We take the cross section of $^{40}{\rm Ar}(\nu_e, e^-)^{40}{\rm K}^*$

from [146].

The event rate detected by Super-Kamiokande and DUNE is simply estimated as

$$\frac{\mathrm{d}N_\nu}{\mathrm{d}t} = \frac{N_{\mathrm{target}}}{4\pi d^2} \int_{E_{\mathrm{th}}}^{\infty} \mathrm{d}E \; f_{\nu_\alpha}(E)\sigma(E), \tag{3.23}$$

where N_{target} is the number of target particles in the tank, d is the distance to a failed supernova and f_{ν_α} is the angle-averaged neutrino spectrum arriving at the detector. In Super-Kamiokande, the target particle is a proton of pure water H_2O in the tank, while it is an argon in DUNE case. Here, we do not consider actual detection efficiency, detector responses, or energy resolution for simplicity. The MSW effects strongly depend on the neutrino mass ordering because the channel where the H-resonance occurs is different between the normal and inverted cases as shown in Fig. 1.8. For the normal mass ordering, the observed electron-type neutrino spectra at the Earth are identical to those at the surface of the star according to the discussion in Sec. 1.4.2 and are given by

$$f^{\mathrm{obs}}_{\nu_e} = s^2_{13} f_{\nu_e} + c^2_{13}\left(c^2_{12} f_{\nu_x} + s^2_{12} f_{\nu_y}\right) \tag{3.24}$$

$$f^{\mathrm{obs}}_{\bar{\nu}_e} = c^2_{13}\left(c^2_{12} f_{\bar{\nu}_e} + s^2_{12} f_{\bar{\nu}_x}\right) + s^2_{13} f_{\bar{\nu}_y}. \tag{3.25}$$

For the inverted mass ordering,

$$f^{\mathrm{obs}}_{\nu_e} = c^2_{13}\left(s^2_{12} f_{\nu_e} + c^2_{12} f_{\nu_x}\right) + s^2_{13} f_{\nu_y}. \tag{3.26}$$

$$f^{\mathrm{obs}}_{\bar{\nu}_e} = s^2_{13} f_{\bar{\nu}_e} + c^2_{13}\left(s^2_{12} f_{\bar{\nu}_x} + c^2_{12} f_{\bar{\nu}_y}\right). \tag{3.27}$$

We assume the adiabatic transitions in the MSW resonances above the simple descriptions. In this case, f_{ν_α} is an original neutrino spectrum for a flavor α in the absence of collective neutrino oscillation.

Figure 3.6 shows the time evolution of the event rate and the accumulated detection number at Super-Kamiokande. There are big differences between the inverted and normal mass orderings in the neutrino detection rate. In particular, the accumulated neutrino

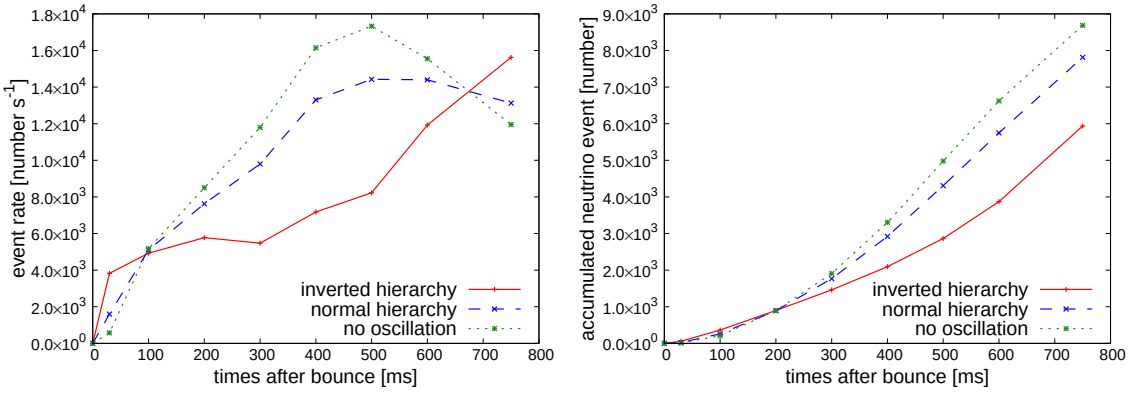

Figure 3.6. The event rate (left) and accumulated event number (right) at Super-Kamiokande from a failed supernova at $d = 10$ kpc. The inverted mass ordering, the normal mass ordering, and no oscillation case are shown by red solid, blue dashed, and green dotted lines.

event number in the normal mass ordering is 1.5 times (about 2,000 events) larger than in the inverted mass ordering at stopped time $t \sim 750$ ms at Super-Kamiokande. Since the adiabatic H-resonance provides the complete conversion, $\bar{\nu}_e \leftrightarrow \bar{\nu}_y$, only in the channel of antineutrinos in the inverted mass ordering, the spectrum of $\bar{\nu}_e$ observed at Super-Kamiokande is almost identical to the original spectra of heavy-leptonic flavor neutrinos. This means that the event rate in the inverted mass ordering can be regarded as the evolution of the number flux of non-electron type neutrinos. On the other hand, the H-resonance in the normal mass ordering does not almost mix the antineutrino channel according to the level crossing scheme. Therefore the mixed spectra with $\bar{\nu}_e$ and $\bar{\nu}_x$ by the L resonance will be detected. These features produce the result that the accumulated event number in the inverted mass ordering is smaller than that in the normal mass ordering.

The event rate in the normal mass order peaks at $t_{\rm pb} = 500$ ms, while the event rate in the inverse mass ordering increases continuously until black hole formation. The event rate decreases at the late phase because the spectrum observed in the normal mass ordering partly contains $\bar{\nu}_e$ spectrum. In Fig. 3.1, the increase in neutrino luminosity and averaged energy of $\bar{\nu}_e$ stops at 500 ms, while those of $\bar{\nu}_x$ continue to increase. The difference is derived from the behaviors of the neutrino sphere for each flavor. The neutrino sphere radii of ν_e and $\bar{\nu}_e$ depend on both the charged-current and the neutral-current reactions with nucleons. On the other hand, ν_x interacts only via neutral-current reactions and diffuses to escape at smaller radius. Since the temperature inside the neutrino sphere increases due to the contraction of the proto-neutron star, the. production rate of heavy-leptonic pairs increases $(e^- + e^+ \nu_x + \bar{\nu}_x)$ due to the thermalized electron-positron pairs. This leads to a dramatic increase in the luminosity of ν_x.

Figure 3.7 shows the predicted event number of electron neutrinos at DUNE. The event rate at $t_{\rm pb} = 30$ ms presents the absence of small peak in the normal mass ordering. In the inverted mass ordering, the H-resonance has little impact on ν_e and the L-resonance mixes

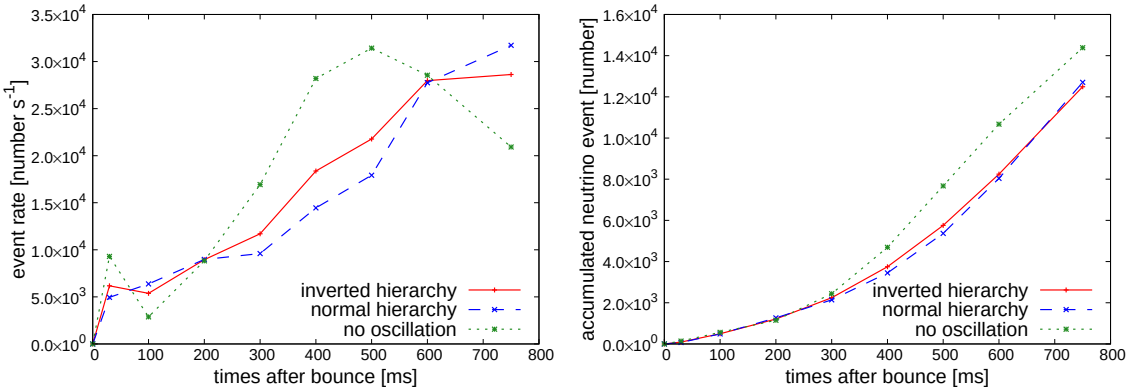

Figure 3.7. The event rate (top) and accumulated event number (bottom) at DUNE from a failed supernova at $d = 10$ kpc. The inverted mass ordering, the normal mass ordering, and no oscillation case are shown by red solid, blue dashed, and green dotted lines.

ν_e and ν_y, while the H-resonance causes the complete conversion $\nu_e \leftrightarrow \nu_y$ in the normal mass ordering and the prominent peak signal of the neutronization burst is completely lost. Therefore if the peak at the early phase is observed in the event rate, it means that the mass ordering is inverted.

No significant difference can be seen for the accumulated neutrino event numbers in both mass orderings. This is because the cross sections via charged-current reaction are more sensitive to high energy neutrinos than those via IBD reaction in water Cherenkov detectors. Higher energy tail than the peak of neutrino spectrum become dominant in the event rate, and the tail of neutrino spectra has smaller difference in flavors than around the peak. So the mixed spectra by the MSW resonances are almost identical between both mass orderings.

We note that this tendency of neutrino emission depends on the progenitor structure and the mass accretion rate at the neutrino sphere of the proto-neutron stars. In the case of failed supernovae with large mass accretion rates, corresponding to our model, the time evolution of the neutrino spectra will be similar to the one obtained in this study [136, 137, 147]. We would observe the time evolution of the event rate similar to the one expected above. On the other hand, failed supernovae with small mass accretion rate show the decrease of luminosities for all flavor neutrinos at late time [147]. Since the luminosity of ν_x expresses the similar behavior to that of ν_e, the differences between the neutrino mass orderings would not be seen in the event rate.

3.1.6 Short summary

We have performed collective neutrino oscillation within the three-flavor framework using an one-dimensional failed supernova model of a $40M_\odot$ progenitor with LS220-EOS. We predicted the time evolution of the event number for current and future detectors, assuming that a failed supernova emerges at 10 kpc as a Galactic event.

It turns out that collective neutrino oscillation in the failed supernova model is completely suppressed by the matter-induced effects at all time epochs from the neutronization burst to the formation of a black hole. The outer core and envelope will not stop accreting because the stalled shock wave does not revive in failed supernovae. Therefore, accreting matter is not blown away at radii $\mathcal{O}(100)$ km where collective neutrino oscillation can occur generally and the dense matter effects continuously suppress the growth of collective flavor instability. As a consequence, our observed neutrino spectra undergo only the MSW resonance in the envelope. The simple description enables us to easily understand neutrino spectra detected at neutrino detectors. Our evaluations in the detection of the neutronization burst and the time variation of the event rates indicate the potential to solve the neutrino mass ordering problem.

Our calculation is based on the traditional bulb model $\rho_\nu(r; E_\nu, \theta_\nu)$, which neglects the effects such as symmetry breaking and coherent scatterings outside the neutrino sphere. Also, we consider only the slow flavor instability and employ the isotropic angular distribution suppressing the excitation of fast flavor instability. Such further investigations will be discussed in the subsequent sections and chapters.

3.2 Symmetry Breaking

The traditional bulb model requires stationary flavor states, spherical symmetry in the space, and axial-symmetry in the neutrino trajectories to reduce the dimensionality in the phase space. The simplified model has even revealed the interesting features of the neutrino self-interactions such as spectral splits and multiangle matter suppression. We have introduced them in the above, but assumed only the inverted mass ordering case. The bulb model in the normal mass ordering case exposes the multi-zenith-angle (MZA) instability, which is often self-suppressed by neutrinos themselves and would be stable. Raffelt *et al.* [86] pointed out that the relaxation of the axial symmetry creates a new flavor instability. This is called the multi-azimuthal-angle (MAA) instability and is found only in the normal mass ordering. It means that the effect of axial symmetry breaking is stable in the inverted mass ordering. As a consequence, the bimodal (BM) and MAA instabilities work as unstable modes for simple neutrino spectrum in both mass orderings. Recently, global analyses of multiple neutrino experimental results suggest that the normal mass ordering is preferred over the inverted case [148–154]. Thus, the possibility of collective flavor conversion in the normal mass ordering is needed to investigate in detail. Previous works have revealed significant flavor conversion in the normal mass ordering case but imposed several approximations to reduce the computational costs [86–88]. Some studies have employed parametric properties as supernova models and not sufficiently discussed multi-angle matter suppression. And others have used core-collapse simulation models but adopted two-flavor monochromatic energy distributions instead of multi-energy case within three-flavor framework. We have first performed the numerical calculation of three-flavor collective neutrino oscillation on three-dimensional momentum space for a supernova simulation model. And we have extended the traditional two-flavor linear stability analysis scheme into more accurate three-flavor one considering vacuum mixing angles. Our work can provide more detailed and accurate flavor conversion. In addition, spatial and temporal inhomogeneity can trigger a new collective flavor instability [89–92]. The non-stationarity can particularly weaken the multi-angle matter suppression through the highly pulsating modes and provide unstable flavor evolution in the deep region in core-collapse supernovae even for slow modes. However, the inclusion of the spatio-temporal inhomogeneity makes the simulation more difficult and we only take it into account within the linear stability analysis. In this Section, we mainly discuss the effects of three-flavor neutrino conversion with the MAA instability, following Ref. [134].

3.2.1 Spatio-temporal Instability

We first consider the symmetry breaking against axial-symmetry and spatio-temporal homogeneities simultaneously. We restore the derivative term and multiangle term including azimuthal-angle distribution which are ignored in the traditional bulb model. The lin-

earized EoM is given by

$$\mathrm{i}\left(\partial_t + \boldsymbol{v}\cdot\nabla\right) S_{\omega,u,\varphi} = \left(-\omega + \lambda + \epsilon\mu\right) S_{\omega,u,\varphi} - \mu \int \mathrm{d}\Gamma'(1-\boldsymbol{v}\cdot\boldsymbol{v}')g'_{\omega,u,\varphi}S'_{\omega,u,\varphi}. \quad (3.28)$$

Here, we assume the flavor correlation S in the form $S \propto Q_{p,\boldsymbol{k}}\mathrm{e}^{-\mathrm{i}(pt+\boldsymbol{k}\cdot\boldsymbol{x}_T+\Omega r)}$ which grows in the radial direction.

$$\left[\frac{-\omega+\bar{\lambda}-p-\boldsymbol{v}_T\cdot\boldsymbol{k}}{v_{r,u}} - \Omega_{p,\boldsymbol{k}}\right] Q_{p,\boldsymbol{k}} = \frac{\mu}{v_{r,u}} \int \mathrm{d}\Gamma'(1-\boldsymbol{v}\cdot\boldsymbol{v}')g'_{\omega,u,\varphi}Q'_{p,\boldsymbol{k}}, \quad (3.29)$$

where subscript T expresses transverse components against the radial direction. Comparing it to Eq. 3.10 in the traditional bulb model, effective matter term $\bar{\lambda}$ is shifted into $(\bar{\lambda}-p-\boldsymbol{v}_T\cdot\boldsymbol{k})$ by spatio-temporal inhomogeneities p and $\boldsymbol{k}$ in the l.h.s., and azimuthal-angles φ are included in the multiangle term in the r.h.s.. If the inhomogeneous frequencies are comparable to effective matter potential, they can cancel the multiangle matter suppression. The pulsating modes p have the same radial velocity dependence as the matter term $\bar{\lambda}$ and act like as the negative matter term. If neutrino flavor eigenstates have continuous temporal distributions, then there is always a flavor instability satisfying $p \simeq \bar{\lambda}$. On the other hand, the spacial inhomogeneity $\boldsymbol{v}_T\cdot\boldsymbol{k}$ has dependences on the transverse velocity $\boldsymbol{v}_T$ and only a part of velocities can completely cancel the matter term even if $|\boldsymbol{k}| \simeq \bar{\lambda}$. In the stationary case, the transverse components can not overcome the matter suppression as in the temporal modes.

We demonstrate a test calculation to confirm whether the cancellation of matter suppression is induced by the temporal instability. To focus the impact of pulsating modes, we assume axial symmetry in neutrino trajectories like as the traditional bulb model again. We take neutrino properties in Table 2.1 but choose monochromatic energy spectra in Eq. (3.15) to simplify. Figure 3.8 represents the flavor unstable regions for a stationary bulb model $p = 0$ and a pulsating mode $p \neq 0$ corresponding to $\rho Y_e = 10^8$ g cm^{-3}. Flavor instability with a nonzero pulsating mode $p \neq 0$ is clearly raised to higher matter density compared to the stationary mode $p = 0$. Neutrinos can obtain nonzero growth rates even at higher density where matter suppression is dominant. The frequency of the pulsating mode in Fig. 3.8 is $p \sim 3.9\times10^4$ km$^{-1} \sim 1.2\times10^{10}$ Hz and is required to be too fast compared to the fluctuation created in a supernova dynamics. According to Refs. [91, 155], pair correlations of neutrino field could lead to sufficiently fast-oscillating fluctuations. If the mechanism can seed initial perturbation like a white noise, the temporal instability may be able to cancel out the matter effects. However, collective neutrino oscillation do not always grow sufficiently even if neutrinos obtain such a perturbation. The width of the unstable region becomes much narrower than the stationary case in Fig. 3.8. We need to consider the adiabaticity of both neutrino potentials and matter effects in the flavor evolution. Neutrinos may run through the density profile before the flavor instability evolves sufficiently to induce the flavor conversions. If the decline of the growth rate is much faster than the radial evolution of the flavor instability, the temporal instability would be damped. The investigation of the adiabaticity is required for realistic core-collapse supernova models in the future.

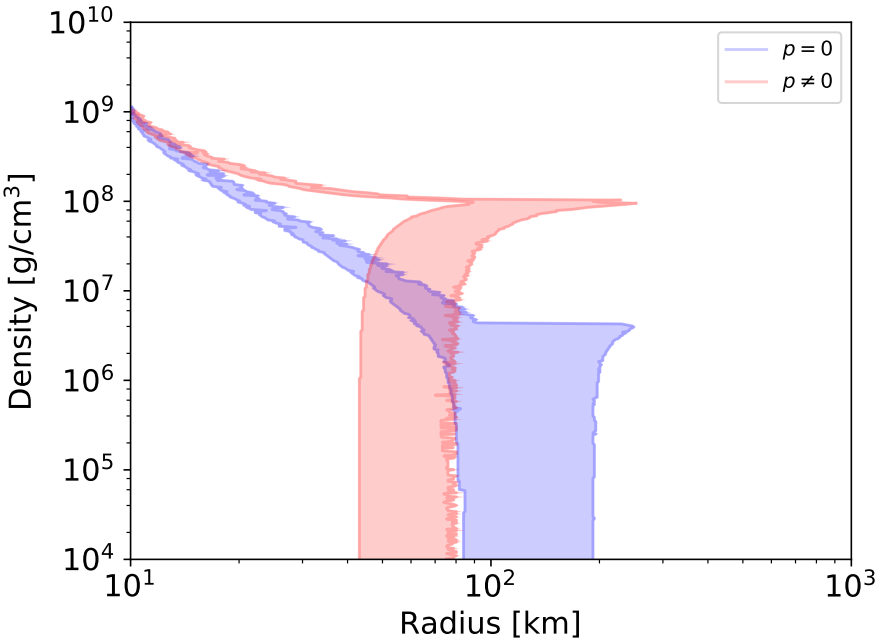

Figure 3.8. Schematic picture of flavor instability with temporal inhomogeneities p corresponding to $\rho = 10^8$ g cm^{-3}. Pulsating modes with $p \neq 0$ are excited even at high matter density.

3.2.2 Multi-Azimuthal-Angle Instability

In the previous section, we have discussed the impact of spatio-temporal inhomogeneities on the matter suppression. Symmetry breaking on the traditional bulb model are also brought by the azimuthal-angle distribution. We ignore the inhomogeneous evolution again below the discussion to evaluate the impact of the axial-symmetry breaking. Before imposing the axial symmetry, the intersection angle originally expresses with the transverse velocity $\boldsymbol{\beta}$ as

$$1 - \boldsymbol{v}\cdot\boldsymbol{v}' = 1 - \cos\theta\cos\theta' - \sin\theta\sin\theta'\cos(\varphi - \varphi') \tag{3.30}$$

$$= 1 - v_{r,u}v_{r,u'} - \sqrt{uu'}\frac{R_\nu^2}{r^2}\cos(\varphi - \varphi') \tag{3.31}$$

$$= 1 - v_{r,u}v_{r,u'} - \boldsymbol{\beta}\cdot\boldsymbol{\beta}'. \tag{3.32}$$

The MAA term $\boldsymbol{\beta}\cdot\boldsymbol{\beta}'$ breaks axial symmetry in neutrino trajectories. Figure 3.9 shows the schematic picture of the bulb model including the azimuthal angle. Then, the Hamiltonian along the radial direction for neutrinos is

$$H_{E,u,\varphi} = \frac{1}{v_{r,u}}\left(U\frac{M^2}{2E}U^\dagger + \sqrt{2}G_{\rm F}n_eL\right) + \mu\frac{R_\nu^2}{2r^2}\int\frac{{\rm d}E'{\rm d}u'{\rm d}\varphi'}{2\pi}\left(\frac{1 - v_{r,u}v_{r,u'} - \boldsymbol{\beta}\cdot\boldsymbol{\beta}'}{v_{r,u}v_{r,u'}}\right)(\rho' - \bar{\rho}'). \tag{3.33}$$

When (anti-)neutrino flux emitted from the neutrinosphere is axial symmetric, the MAA term equals to zero due to the periodic integral of the cosine and the Hamiltonian $H_{E,u,\varphi}$ is identical to $H_{E,u}$ in the traditional bulb model. Interestingly, the matter term in Eq. (3.33) is unchanged compared to the traditional bulb model even if we consider the azimuthal-angle distribution in the neutrino trajectory. The travel distance is same on each azimuthal-angular mode as seen in Fig. 3.9. Therefore, spurious modes do not emerge in the azimuthal-angular integration and the resolution is independent of the matter-induced potential.

In Sec. 3.1.3, we have introduced the linear stability analysis in the two-flavor approximation. It is sufficient to evaluate the suppression behaviors of collective effects but inadequate to discuss the onset radius within three-flavor framework. In particular, three-flavor effects depend on the mixing angle even in the axial symmetric case [156, 157]. We extend the linear stability analysis into the three-flavor scheme including mixing angles. Same as the two-flavor approximation, we decompose the density matrix to

$$\begin{aligned}\rho_\nu = \frac{\mathrm{Tr}(\rho_\nu)}{3}\mathbb{I}_3 &+ \frac{f_{\nu_e} - f_{\nu_x}}{3}\begin{pmatrix} s_1 & S_1 & 0 \\ S_1^* & -s_1 & 0 \\ 0 & 0 & 0 \end{pmatrix} \\ &+ \frac{f_{\nu_e} - f_{\nu_y}}{3}\begin{pmatrix} s_2 & 0 & S_2 \\ 0 & 0 & 0 \\ S_2^* & 0 & -s_2 \end{pmatrix} \\ &+ \frac{f_{\nu_x} - f_{\nu_y}}{3}\begin{pmatrix} 0 & 0 & 0 \\ 0 & s_3 & S_3 \\ 0 & S_3^* & -s_3 \end{pmatrix} \qquad (3.34) \\ &\equiv \frac{\mathrm{Tr}(\rho_\nu)}{3}\mathbb{I}_3 + \sum_{j=1}^{3} g_j \mathbb{S}_j. \qquad (3.35)\end{aligned}$$

Three S_j indicates the possibility of flavor conversions in the $e-x$, $e-y$, and $x-y$ sectors. If $f_{\nu_x} = f_{\nu_y}$ is given in the employed neutrino distribution, the third term $j = 3$

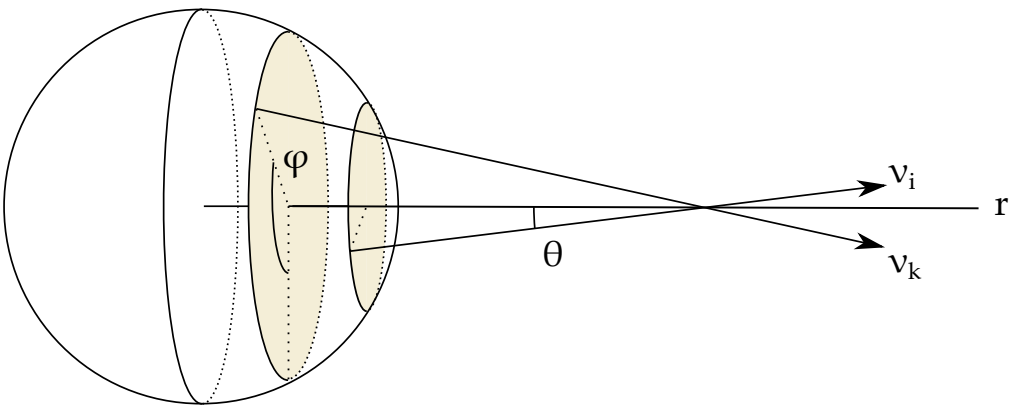

Figure 3.9. Schematic picture of the extended bulb model $\rho(E, \theta, \varphi)$.

is canceled. The $e-x$ and $e-y$ sectors are decoupled in the linear order and $x-y$ flavor conversion can not occur [158]. However, nonlinear effect can induce a flavor correlation in the $x-y$ sector due to the second order of $S_{1,2}$.

In a fast-rotating frame [80], the vacuum term is simply given by

$$\begin{aligned} H_{\rm vac} \to \langle H_{\rm vac} \rangle &= \frac{1}{2E} \begin{pmatrix} 0 & 0 & 0 \\ 0 & \Delta m^2_{21} & 0 \\ 0 & 0 & \Delta m^2_{31} \end{pmatrix} \\ &= {\rm diag}(0, \omega_L, \omega_H). \end{aligned} \tag{3.36}$$

$\omega_{H/L}$ can induce the flavor conversions in the $e-y$ and $e-x$ sectors and the subscripts H/L correspond to the notation of the MSW resonance. To linear order, the linearized EoM for j is

$$\mathrm{i}\partial_r S_j = \left(\frac{-\omega_j + \lambda_j + \mu_j}{v_{r,u}} \right) S_j - \mu \frac{R_\nu^2}{2r^2} \int \frac{{\rm d}\omega' {\rm d}u' {\rm d}\varphi'}{2\pi} \left(\frac{1 - v_{r,u} v_{r,u'} - \boldsymbol{\beta} \cdot \boldsymbol{\beta}'}{v_{r,u} v_{r,u'}} \right) g'_j S'_j, \tag{3.37}$$

where

$$\mu_j = \mu \int {\rm d}\Gamma' \, (1 - \boldsymbol{v} \cdot \boldsymbol{v}') \, g'_j \tag{3.38}$$

$$\lambda_1 = \lambda_2 = \lambda, \quad \lambda_3 = 0 \tag{3.39}$$

$$\omega_1 = \omega_L, \ \omega_2 = \omega_H, \ \omega_3 = \omega_H - \omega_L. \tag{3.40}$$

Here we ignore the number density $n_{e^+,\mu^\pm,\tau^\pm}$ of positrons and heavy leptons. Recent SN simulation [39] has presented the possibility of muon creation in the proto-neutron star and the impact on the dynamics. However, we here neglect it for simplicity (see the discuss in Ref. [158] for the including case). In the three-species treatments ($\nu_\alpha = e, \bar{e}, X$) and the isotropic neutrino emission, the self-interaction potential is given by

$$\mu_1 = \mu_2 = \epsilon\mu = \sqrt{2} G_{\rm F} \frac{\Phi_{\nu_e} - \Phi_{\bar{\nu}_e}}{4\pi r^2}, \ \mu_3 = 0. \tag{3.41}$$

In the large-distance approximation, the linearized EoM is

$$\mathrm{i}\partial_r S_j = \left(u\bar{\lambda}_j - \omega_j \right) S_j - \mu^* \int {\rm d}\Gamma' \left[u + u' - 2\sqrt{uu'} \cos(\varphi - \varphi') \right] g'_j S'_j. \tag{3.42}$$

This equation differs from Eq. (3.10) only in the MAA term. Similarly, we assume the plane wave $S_j \propto Q_j \mathrm{e}^{-\mathrm{i}\omega_j r}$ and we get

$$\left(u\bar{\lambda}_j - \omega_j - \Omega_j \right) Q_j = \mu^* \int {\rm d}\Gamma' \left(u + u' - 2\sqrt{uu'} c_\varphi c_{\varphi'} - 2\sqrt{uu'} s_\varphi s_{\varphi'} \right) g'_j Q'_j, \tag{3.43}$$

where $c_\varphi = \cos\varphi$ and $s_\varphi = \sin\varphi$. The r.h.s. has the form $A_0 + A_1 u + A_2 \sqrt{u} c_\varphi + A_3 \sqrt{u} s_\varphi$ as a function of polar and azimuthal angle u and φ. Therefore, the l.h.s. must be also that form and by substituting the eigenfunction

$$Q_j = \frac{A_0 + A_1 u + A_2 \sqrt{u} c_\varphi + A_3 \sqrt{u} s_\varphi}{u\bar{\lambda}_j - \omega_j - \Omega_j} \tag{3.44}$$

we obtain

$$\begin{pmatrix} I_{j,1}-1 & I_{j,2} & 0 & 0 \\ I_{j,0} & I_{j,1}-1 & 0 & 0 \\ 0 & 0 & -(I_{j,1}+1) & 0 \\ 0 & 0 & 0 & -(I_{j,1}+1) \end{pmatrix} \begin{pmatrix} A_0 \\ A_1 \\ A_2 \\ A_3 \end{pmatrix} = 0, \tag{3.45}$$

where

$$I_{j,n} = \mu^* \int \mathrm{d}\omega_j \mathrm{d}u \frac{u^n g_j}{u\bar{\lambda}_j - \omega_j - \Omega_j}. \tag{3.46}$$

Nonzero determinants are nontrivial solutions and we finally get

$$D(\Omega_j) \equiv (I_{j,1}-1)^2 - I_{j,0}I_{j,2} = 0 \quad \text{(for BM and MZA)} \tag{3.47}$$

$$\equiv I_{j,1} + 1 = 0 \quad \text{(for MAA)}. \tag{3.48}$$

The former condition stems from the coefficients A_0 and A_1, and does not depend on azimuthal angle φ. This corresponds to the multiangle term in the traditional bulb model and induces the BM and MZA instabilities. It is same as Eq. (3.14) in the axial symmetric case. On the other hand, the latter arises from the coefficients A_2 and A_3 associated with dependence on the azimuthal angle φ, and causes a new instability in non-axial symmetric case. This is called the MAA instability and unstable only in the normal mass ordering case. In the inverted mass ordering case, the BM is dominant even in the inclusion of azimuthal angular distribution. If the employed model gives $f_{\nu_x} = f_{\nu_y}$, that is, $g_3 = 0$, Eq. (3.46) for $j = 3$ vanishes and the growth rate is undefined. Flavor evolution in the $x - y$ sector is present only in the nonlinear regime.

This formalism is based on the fast-rotating frame and can not describe the three-flavor effects exactly. To include the dependence on mixing angles, we substitute the diagonalized Hamiltonian for $\langle H_{\mathrm{vac}} \rangle + H_{\mathrm{MSW}}$, following the approach in Ref. [156]:

$$H'_{\mathrm{diag}} \approx \begin{pmatrix} \lambda + \omega_H \left(s_{13}^2 + \eta c_{13}^2 s_{12}^2\right) & 0 & 0 \\ 0 & \omega_H \eta c_{12}^2 & 0 \\ 0 & 0 & \omega_H \left(c_{13}^2 + \eta s_{12}^2 s_{13}^2\right), \end{pmatrix} \tag{3.49}$$

where $\eta = \omega_L/\omega_H$ is the mass-squared difference ratio. The conversion relation between H'_{diag} and $\langle H_{\mathrm{vac}} \rangle + H_{\mathrm{MSW}}$ is simply given by

$$\lambda \to \lambda + \omega_H \left(s_{13}^2 + \eta c_{13}^2 s_{12}^2\right) \tag{3.50}$$

$$\omega_L \to \omega_H \eta c_{12}^2 \tag{3.51}$$

$$\omega_H \to \omega_H \left(c_{13}^2 + \eta s_{12}^2 s_{13}^2\right). \tag{3.52}$$

Therefore, the nontrivial equations for the growth rate with the dependence on mixing angles are

$$I_{1,n} = \mu^* \int \mathrm{d}\omega_H \mathrm{d}u \frac{u^n g_1}{u\bar{\lambda} - \omega_H L_{\mathrm{mix}} - \Omega_1} \tag{3.53}$$

$$I_{2,n} = \mu^* \int \mathrm{d}\omega_H \mathrm{d}u \frac{u^n g_2}{u\bar{\lambda} - \omega_H H_{\mathrm{mix}} - \Omega_2}, \tag{3.54}$$

where

$$L_{\rm mix} = \eta \left(c_{12}^2 - s_{12}^2 c_{13}^2\right) - s_{13}^2 \tag{3.55}$$

$$H_{\rm mix} = \cos 2\theta_{13} \left(1 - \eta s_{12}^2\right). \tag{3.56}$$

In this transformation, we ignore a small angular-dependent shift $u\omega$ as with the usual scheme of linear stability analysis. We can obtain the behaviors of three-flavor effects derived from the BM, MZA, and MAA instabilities by using the expanded linear stability analysis into the three-flavor frameworks including mixing angles.

3.2.3 Numerical setup

We employ a two-dimensional electron-capture supernova (ECSN) model with an $8.8M_\odot$ progenitor [159] (the setup of the envelope is same to that of Ref. [14]). As was done in Ref. [133], the hydrodynamic simulation has been performed by 3DnSNe code. (see the references [160–163] for recent applications). The method for the hydrodynamic evolution is summarized in Ref. [133]. The two-dimensional simulation is computed on a spherical polar coordinate with spatial resolution of $(N_r, N_\Theta) = (512, 128)$. While the radial grid is logarithmically spaced and covers from 0 to 5000 km, the polar grids covers from 0 to π uniformly.

The equation of state used in the simulation is the Lattimer and Swesty with incompressibility of $K = 220$ MeV [139]. Although the code employs the relatively simple neutrino transport scheme of IDSA (Isotropic Diffusion Source Approximation) [164], it nevertheless can provide consistent results on neutrino luminosities and average energies with more sophisticated schemes (see Ref. [161] for a detailed comparison).

Figure 3.10 shows the time evolution of neutrino luminosity L_{ν_α} (top), averaged energy $\langle E_{\nu_\alpha} \rangle$ (bottom left), and rms energy $\langle E_{\nu_\alpha}^2 \rangle$ (bottom right) in the ECSN model with $8.8M_\odot$. The emission properties in $\nu_e, \bar{\nu}_e$, and ν_X are red solid, blue dotted, and black dashed lines, respectively. The pinching parameters for a flavor α are obtained from Eq. 3.3 using the averaged and rms energy.

The left panel of Figure 3.11 shows the time evolution of the averaged shock radius (black curve) and the matter density (color contours). The (neutrino-driven) shock expansion can be seen at around postbounce time $t_{\rm pb} = 100$ ms, and the accreting matter is blown away. Thereby, the matter density increases until around 200 ms at radii where collective neutrino oscillation can be induced. The growth of the shock front has a large influence on the activity of collective flavor conversion, and we can divide the behaviors into four phases. As we explain below, these are the suppression phase, window phase, re-suppression phase, and revival phase.

The right panel of Fig. 3.11 shows the electron number density along the northern pole at the representative snapshots of each phase, 100, 150, and 300 ms. In the early stage of ECSNe, collective neutrino oscillation is suppressed by the excess of electron neutrinos due to neutronization bursts and heavy accretion matter; this corresponds to the suppression phase, $t_{\rm pb} < 100$ ms. The propagation of the shock wave then leads to

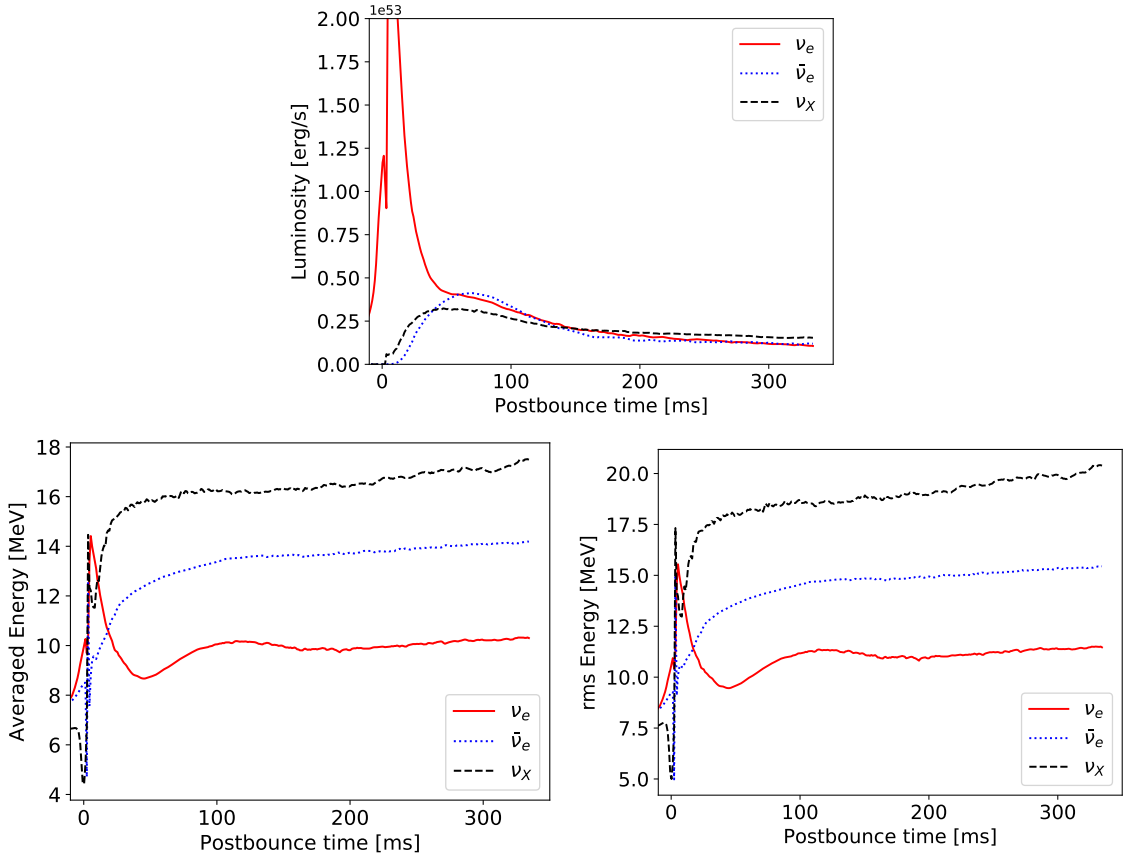

Figure 3.10. Time evolution of neutrino luminosity L_{ν_α} (top), averaged energy $\langle E_{\nu_\alpha} \rangle$ (bottom left), and rms energy $\langle E^2_{\nu_\alpha} \rangle$ (bottom right) in the ECSN model with $8.8 M_\odot$. Flavors $\nu_e, \bar{\nu}_e$, and ν_X are red solid, blue dotted, and black dashed lines, respectively.

a window in which the collective effect overcomes the phase dispersion due to matter decoherence; this is the window phase, 100 ms $\leq t_{\rm pb} <$ 150 ms. After the shock revival, the blown matter increases the density profile so that the matter effects again inhibit the collective flavor transformation; this is the re-suppression phase and spans the times 150 ms $\leq t_{\rm pb} <$ 250 ms. Finally, the self-induced effects revive during the cooling epoch as the matter density decreases; this is the revival phase beginning at $t_{\rm pb} = 250$ ms.

3.2.4 Nonlinear regime

Figure 3.12 shows the radial evolution of the transition probability of electron neutrinos averaged over energy and angular distributions at 100 (left) and 300 ms (right). Collective neutrino oscillation is completely suppressed at 150 ms in both cases and we do not show it in this figure. Here, we divide it into two types of transition probability in $e - x$ sector and $e - y$ sector. These two sectors are associated with solar mass-squared difference Δm^2_{21} and atmospheric mass-squared difference Δm^2_{31}, respectively. Note that the two-flavor frameworks adopted by previous works [87, 88] do not show the three-flavor effects

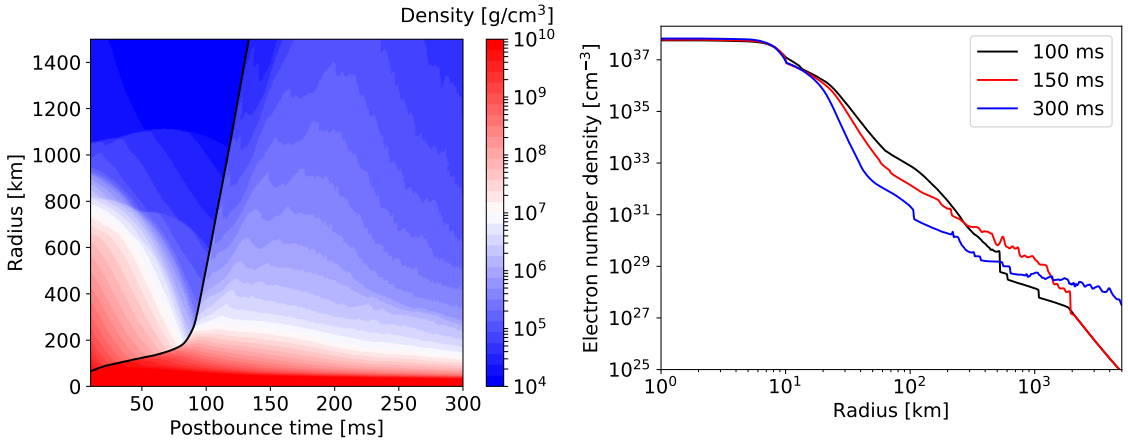

Figure 3.11. Density profile. Left: Color contours represent the time evolution of the averaged density profile. Black line is the time evolution of the averaged shock radius. Right: electron number density profile n_e along the northern pole at postbounce time $t_{\rm pb} = 100$ (black), 150 (red), and 300 ms (blue).

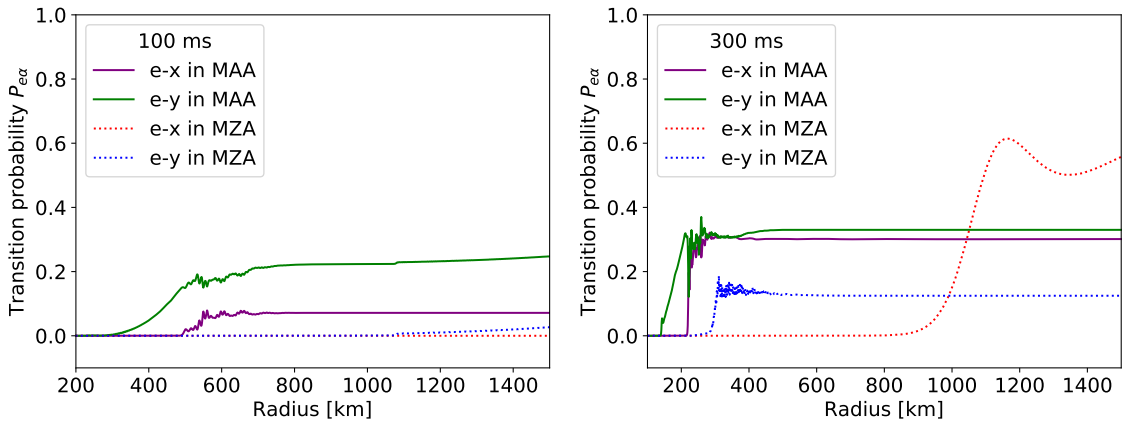

Figure 3.12. Radial evolution of the transition probability of electron neutrinos into non-electron types at 100 ms (top panel) and 300 ms (bottom panel). Solid lines correspond to the MAA case and dotted lines correspond to the MZA case. The MZA instability is completely suppressed, while the MAA effects lead to flavor conversions at 100 ms. Flavor conversions are seen in both MZA and MAA cases, especially beyond 1000 km where oscillation appears in the MZA case in the $e - x$ sector at 300 ms.

and can only provide flavor conversion in the $e - y$ sector.

At 100 ms (top panel of Figure 3.12), collective neutrino oscillations occur only in the MAA case (solid line), and are completely suppressed in the MZA case (dotted line). This different behaviors are due to the large flavor asymmetry ϵ at this time snapshot, which leads to stable flavor modes in the MZA case in the normal mass ordering. In the MAA case (solid line), the $e - y$ sector starts flavor mixing from 250 km and the $e - x$ sector around 500 km. This difference in onset radius is due to the balance between the vacuum term and the collective term. Collective neutrino oscillation that arises in the

present calculations is sometimes called slow modes, and unlike fast flavor conversion [122], they are induced on the scale of the vacuum oscillation frequency $\omega_{H/L}$. The oscillation frequency μ slows down with decreasing neutrino density, and the growth rate increases at the radius where $\mu \sim \omega$ is satisfied. As a result, the onset of flavor mixing associated with Δm^2_{21} in the $e-x$ sector is slower than in the $e-y$ sector by a mass-squared difference ratio η. This is a simple understanding; in fact, the onset radius also depends on the mixing angle. The $e-x$ flavor transformation occurs, but its transition probability is less than 10%. The $e-y$ flavor transformation is still dominant, so even for the MAA case, it resembles the two-flavor framework at 100 ms. For both MAA and MZA, the transition probability in the $e-y$ sector appears to gradually increase beyond 1000 km, but this is induced by the H-resonance of the MSW effects and not by self-interaction.

At 300 ms (lower part of Figure 3.12), the situation changes dramatically, and collective flavor conversions occur in both the MAA and MZA cases. The $e-y$ transformation (blue dotted line) in the MZA case starts at 200 km and the growth is saturated around 300 km. In particular, the $e-x$ sector of the MZA case (dotted red line) shows a large flavor mixing around 1000 km. This peculiar flavor transformation is unrelated to the H-resonance as observed at 100 ms. This snapshot is with a flux ordering, commonly referred to as multiple crossings, which have been investigated in Refs. [79, 124, 165, 166]. Multiple crossings lead to three-flavor effects leading to $e-x$ mixing, and this behavior can occur in both the inverted and normal mass ordering cases. On the other hand, the onset radius in the MAA case is much smaller than in the MZA case, both in the $e-x$ and $e-y$ sectors. In the MAA case, the $e-y$ conversion starts at 130 km and the $e-x$ conversion occurs at 220 km. The $e-x$ conversion in the MAA case is faster than in the MZA case. Also, the transition probability in each flavor is nearly 1/3, and thus the neutrino ensemble appears to have reached flavor equilibrium. The multi-angle decoherence caused by this MAA instability was reported by Ref. [87]. When the neutrino flavor asymmetry is large, flavor equilibrium is not established at 100 ms. This fact is consistent with previous studies in the two-flavor framework [87].

Figure 3.13 shows the radial evolution of the dipole term in $\cos\varphi$ of the off-diagonal term of the density matrix ρ_ν at 100, 150, and 300 ms. This value indicates the growth of azimuthal-angle instability [87] and is defined as

$$P^{(x)} = \sqrt{(P^{(1)})^2 + (P^{(2)})^2} \tag{3.57}$$

$$P^{(y)} = \sqrt{(P^{(4)})^2 + (P^{(5)})^2}, \tag{3.58}$$

where

$$P^{(m)} = \int \frac{\mathrm{d}E\mathrm{d}u\mathrm{d}\varphi}{2\pi} P^{(m)}_{E,u,\varphi} \cos\varphi. \tag{3.59}$$

These $P^{(1,2,4,5)}$ corresponds to the real and imaginary components of the off-diagonal term of the neutrino density matrix rho_ν, which is initially set to zero. The flavor conversion due to the MAA instability occurs at a radius where this dipole term approaches the order of one. If other instabilities drives the flavor mixing, this dipole term need not be

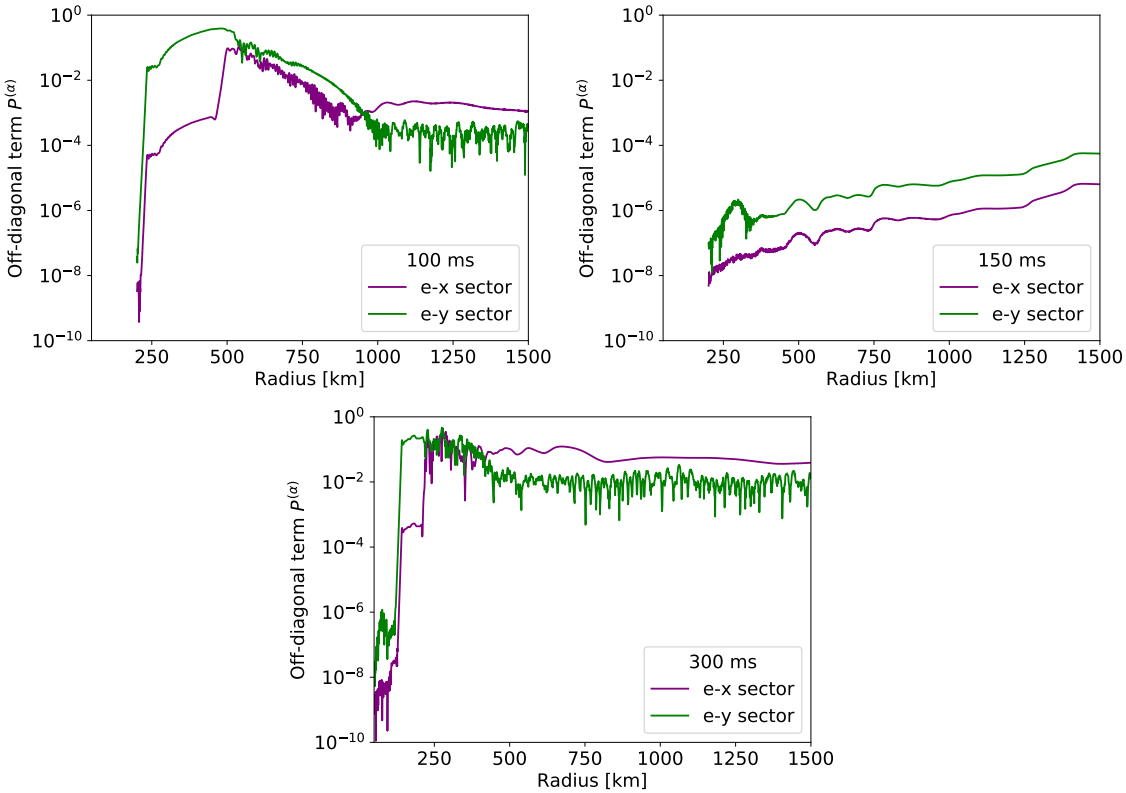

Figure 3.13. Radial evolution of the dipole term in $\cos\varphi$ of off-diagonal terms at 100 ms (top left), 150 ms (top right), and 300 ms (bottom). Purple lines correspond to the $e-x$ sector and green lines to the $e-y$ sector. At 100 ms and 300 ms, flavor instability steeply grows, while the growth is suppressed at 150 ms.

sufficiently large. Comparing these off-diagonal terms with the transition probabilities in the MAA case, we see that the steeply growing feature is directly related to the onset radius of the flavor conversion. It is clear that the MAA instability induces the collective flavor conversions at 100 and 300 ms. We also find that this flavor instability cannot grow sufficiently under dense background matter at 150 ms, despite the given perturbation.

Figure 3.14 shows neutrino and antineutrino spectra at 1500 km at 100 ms. The left panels show the MAA case, and the right panels are the MAZA case. The upper panels are the neutrino spectrum, the lower panels the antineutrinos. The flavor conversion is completely suppressed in the MZA case at this time snapshot, and neutrinos pass through only the H-resonance beyond 1000 km. In the normal mass ordering case, the H-resonance induces the almost complete $e-y$ conversion to the neutrino sector, but since neutrinos have not yet reached the high energy range, spectral exchange is only seen in the low energy range below 5 MeV. In the MAA case, spectral swaps in the $e-y$ sector occur above 10 MeV, and are negligible in the $e-x$ sector. In the antineutrino sector, the final electron antineutrino spectrum is almost converted to the original non-electron type spectrum. And three-flavor effects due to nonlinear evolution provide additional $x-y$ conversion above 15 MeV. The features of these swaps are similar to the spectral splits caused by the bimodal instability of the inverse mass ordering [157]. This is due to the

large flavor asymmetry $\epsilon > 1$, and we observe a quasi-single angle behavior [87, 167]. The bump features in the ν_y spectrum are transferred into electron neutrinos through the H-resonance at larger radius.

Figure 3.15 shows the energy spectra of neutrinos and antineutrinos at 300 ms, and flavor conversions are seen in both the MAA and MAZA cases. In the MAA case, the average transition probability for each flavor in the neutrino sector is almost 1/3, and the final spectra are identical below 15 MeV. In the antineutrino sector, all flavors reach flavor equipartition above 20 MeV. Thus, the neutrino ensemble can achieve partial flavor equilibrium due to the MAA effects. In addition, the MSW resonances do not significantly affect the final spectra under flavor equilibrium. On the other hand, both neutrinos and antineutrinos do not reach the flavor equilibrium in the MZA case. The spectral splits that occur in the $e-y$ sector in the neutrino spectra around 300 km is transferred to the ν_x spectrum through large radius oscillations in the $e-x$ sector. The swap structure escapes

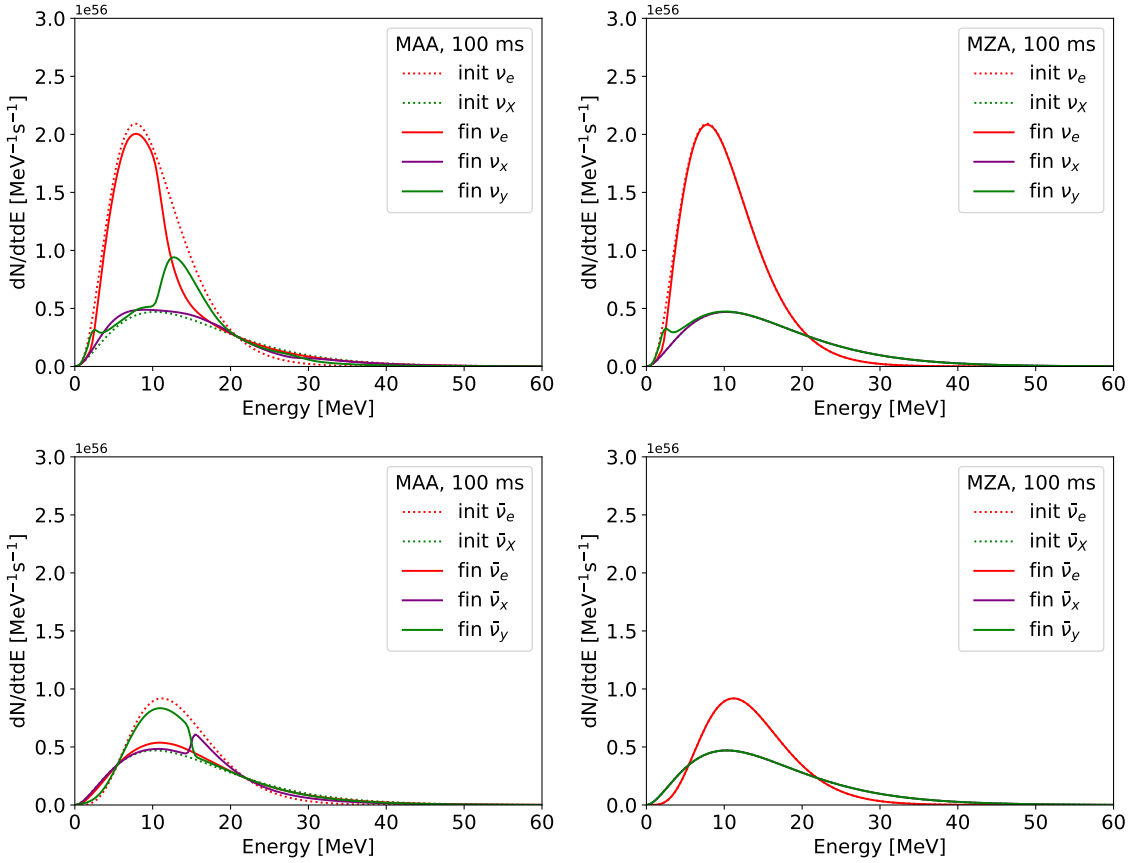

Figure 3.14. Neutrino and antineutrino spectra at 1500 km at 100 ms. Left panels are the MAA case and right panels are the MZA case. Top panels are neutrino spectra and bottom panels are the antineutrino sector. The dotted lines are for original spectra and the solid ones are for final spectra after collective neutrino oscillation. In the MAA case, spectral splits appear, while flavor conversions are completely suppressed in the MZA case. Low-energy transitions in neutrino spectra occur due to the H-resonance.

into the non-electron neutrinos, but will return through subsequent MSW resonances.

3.2.5 Linear regime

In this section, we discuss our linear stability analyses to interpret our numerical results. In particular, we focus on three-flavor effects on the MAA instability because previous works have discussed only within the two-flavor framework. We show the growth rate maps of the MZA and MAA instability at 100 and 300 ms obtained by solving Eq. (3.48).

Figure 3.16 shows contours of growth rates $\kappa_{H/L}$ in the MZA case at 100 ms. In the left panel, the density profile (solid red line) passes through gap between the unstable regions in both the $e-x$ and $e-y$ sectors, and it is consistent with our nonlinear results that flavor conversions do not happen. The density profile goes across the narrow unstable region of the $e-x$ sector, but does not deeply invade into the regions with large growth rate. This is not enough for flavor instability to grow because the growth rate immediately becomes

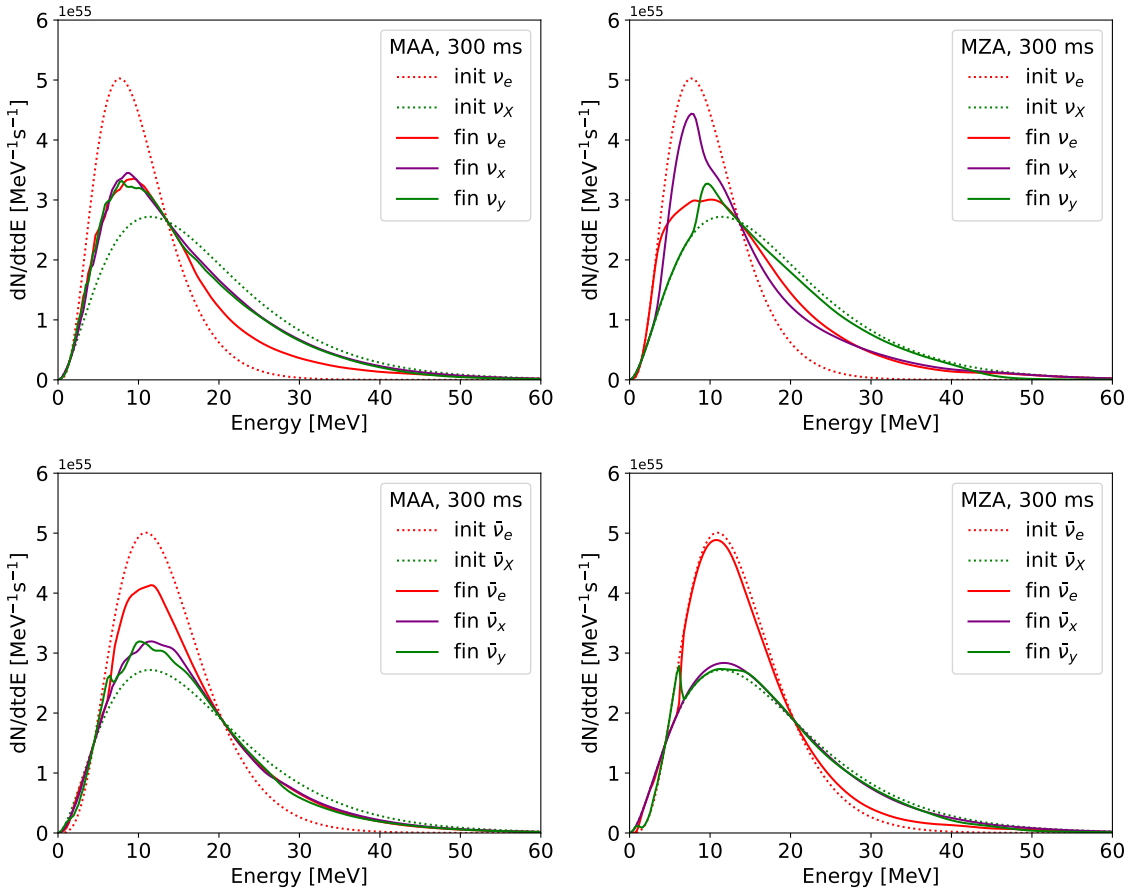

Figure 3.15. The same as Fig. 3.14, but for 300 ms. Neutrino spectra of three flavors are almost identical and there are no splits in the MAA case. The same features are observed for antineutrinos. In the MZA case, split features in the neutrino sector are shifted by $e-x$ conversion subsequent to $e-y$ conversion. In the antineutrino case, $e-x$ conversion is tiny and a small low-energy splits occurs in the $e-y$ sector only.

weaker again.

The behaviors of the three-flavor effect in the MZA case depends on the value of θ_{13}, as described in Ref. [156]. When a small or zero value is adopted, the stability analysis shows different growth rates, particularly in the $e-x$ sector. We discuss the effect in the three-flavor framework employing a small mixing angle $\theta_{13} = 10^{-3}$ to investigate the effect of mixing angle, as once adopted in Refs. [121, 124, 166]. Comparing the small mixing angle case in the right panel of Fig. 3.16 to in the experimental value case, we see that the unstable region int the $e-x$ sector shifts to a smaller radius and the growth rate also becomes much smaller. When we evaluate the growth rate using Eq. (3.46) instead of Eq. (3.54), ignoring the mixing angle, the unstable region in the $e-x$ sector will shift to a much smaller radius and the growth rate will be underestimated. Therefore, even if the density profile intersects the unstable region, the growth rate is small enough to suppress the collective effects. Even in the ordinary case where the experimental values are adopted, the growth rate of the $e-x$ sector is still small, but it is sufficiently large to satisfy $\kappa_L r > 1$, which is larger than the $e-y$ sector. Collective neutrino oscillation possibly occurs only in the $e-x$ sector, depending on the model investigated, as mentioned in Ref. [156]. It has also been found that the unstable region in the $e-y$ sector is almost independent of the value of θ_{13}. As long as we discuss the possibility and the onset of the flavor evolution within the two-flavor framework, the inclusion of θ_{13} has no impact. However, when treating all flavors as in this study, the mixing angles should be considered even in the linear stability analysis.

The instability contour maps for the MAA case at 100 ms are shown in Fig. 3.17. Because of the partial overlap of the unstable regions, the $e-x$ and $e-y$ sectors are divided into two panels (top and bottoms). In each sector, the onset radius of collective neutrino oscillation, obtained from our numerical calculations, is indicated by the vertical dotted line. The lines are clearly consistent with the intersection radius of the density profile

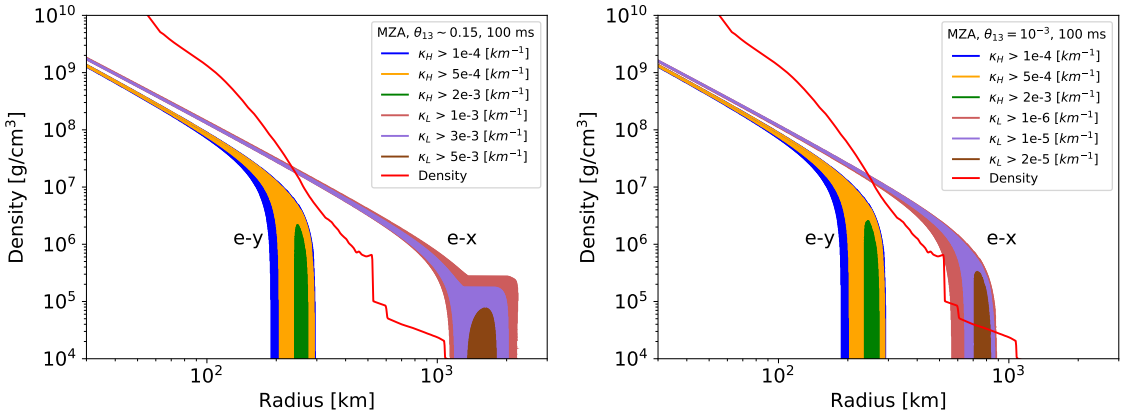

Figure 3.16. Contour map of the growth rate $\kappa_{H/L}$ in the MZA case at 100 ms. Left panel is for ordinary mixing angle case and right panel is for small mixing angle case, $\theta_{13} = 10^{-3}$. The unstable regions are labeled for the $e-y$ and $e-x$ sectors. Red line shows the density profile. Flavor instability can grow if the density profile intersects the patched regions.

(solid red line) with the unstable regions. This can be easily understood by comparing the linear regime with the radial evolution of the dipole modes of the off-diagonal term in Fig 3.13. The dipole modes of the off-diagonal term evolve steeply at the radius where neutrinos pass through the unstable region and acquire the large growth rates. Compared to the growth rate in the $e-y$ sector, that in the $e-x$ sector is much smaller, and does not satisfy the condition $\kappa_L r > 1$. Nonetheless, the flavor conversion in the $e-x$ sector appears in our nonlinear simulation. This is because we consider only the two sectors to be completely decoupled in the linear regime. Our numerical simulation includes the nonlinear effects and the rapid evolution of the $e-y$ sector can trigger the instability seeds in the $e-x$ sector, whose growth is more rapid than predicted [166]. The behaviors are similarly found in the radial evolution of the dipole modes of the off-diagonal terms. In fact, the growth of the MAA instability in the $e-x$ sector starts after the $e-y$ sector has evolved.

We show the contour map of the unstable regions with the small mixing angle in the bottom right panel of Fig. 3.17. The growth rate is larger and also shifts to a larger radius

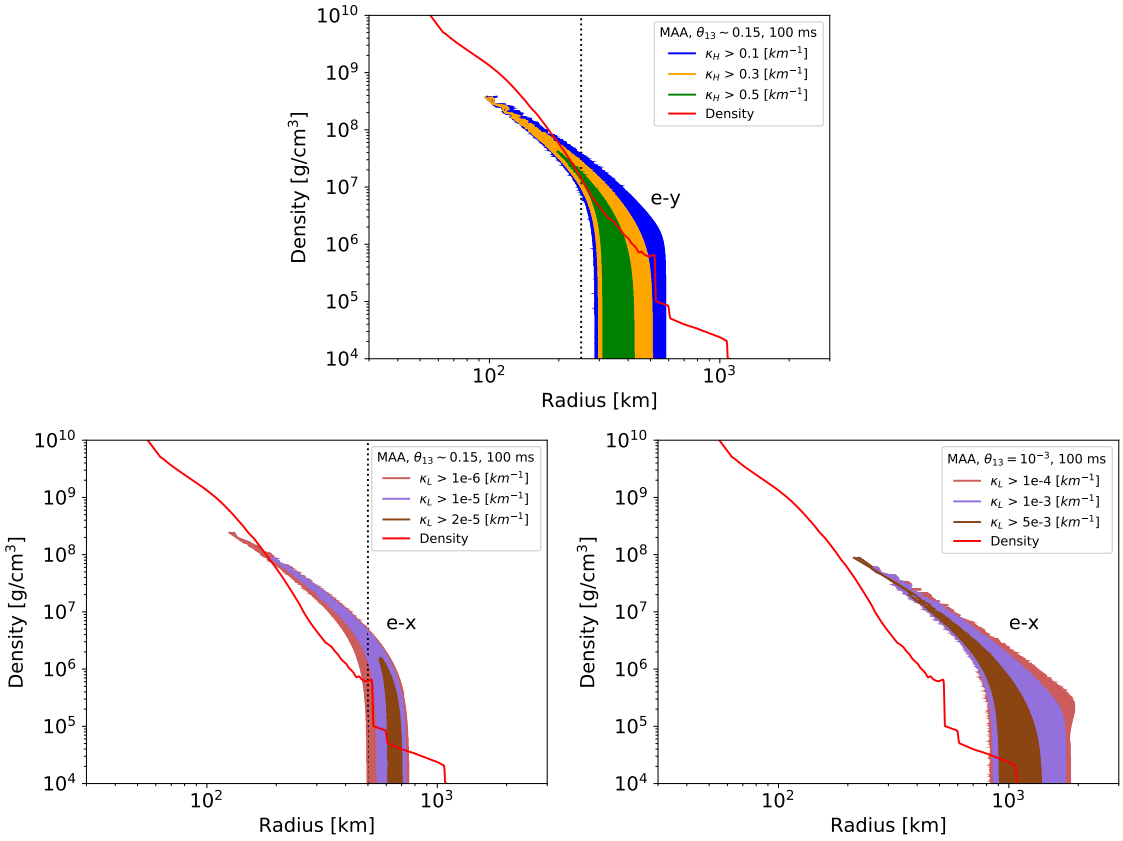

Figure 3.17. The same as Fig. 3.16, but for the MAA case. Here, $e-y$ (top) and $e-x$ (bottom panels) sectors are separately plotted. We do not show the contour plot in the small mixing angle case in $e-y$ sector because it is almost identical to the experimental value case. The vertical dotted line indicates the onset radius of collective neutrino oscillations in our numerical scheme in each sector.

compared than in the bottom left panel where the experimental mixing angle is adopted. This is contrary to the MZA case, where the instability associated with Δm^2_{21} is enhanced for the non-small mixing angle θ_{13}. This difference in the dependence is attributed to the oscillation mechanism for the MAA and MZA instability respectively. According to Ref. [157], the sign of the Bloch vector $\boldsymbol{B}$ of the vacuum Hamiltonian affects whether flavor mixing becomes unstable in the bulb model,

$$B_{e-y} \sim -h\omega_H \cos 2\theta_{13} \tag{3.60}$$

$$B_{e-x} \sim -\omega_L \left(\cos 2\theta_{12} - c^2_{12}s^2_{13}\right) + h\omega_H s^2_{13}. \tag{3.61}$$

The sign of Eq. (3.60) is determined by the sign h of Δm^2_{31}, and it is always positive in the inverted mass ordering. In the MZA case, the positive sign is preferred to destabilize the flavor sector. For the normal mass ordering, Eq. (3.60) is always negative and the $e-y$ sector is basically stable. On the other hand, the sign of Eq. (3.61) depends on not only the mass ordering but the value of the mixing angle θ_{13}. For a fixed mixing angle θ_{12} to the experimental value, the sign is always negative in the inverted mass ordering and three-flavor effects in the $e-x$ sector are stable. In the normal mass ordering case, the condition that Eq. (3.61) is positive is

$$\sin^2\theta_{13} > \frac{\cos 2\theta_{12}}{h\omega_H/\omega_L + \cos^2\theta_{12}}. \tag{3.62}$$

The experimental value $\theta_{13} \sim 0.14$ satisfies the condition, while the small mixing value $\theta_{13} \sim 10^{-3}$ adopted in the previous studies suggests the sign of Eq. (3.61) is negative. Therefore, the flavor correlation in the $e-x$ sector becomes unstable, and a faster growth rate can be obtained than when the mixing angle θ_{13} is small. In our numerical results, the $e-y$ conversion occurs in the MAA case though it is potentially stable in the MZA case. This suggests that the MAA effect reverses the meaning of the sign and the negative value is preferred in the unstable criterion. This is consistent with the dependence of the growth rate of the $e-x$ sector on the mixing angle θ_{13}, which is opposite to the MZA case. As in the MZA case, ignoring the mixing angle results in a larger shift of the unstable region. Thus, the absence of the mixing angles or using different values for the linear stability analysis will misrepresent the possibility of flavor transformation or lack thereof in the three-flavor framework.

Figure 3.18 shows the contour maps in the MZA and MAA cases at 300 ms. The onset of our numerical results (vertical dotted line) coincides with the intersection radius of the density profile (solid red line) with the unstable region. Unlike $t = 100$ ms in the MZA case, the density profile goes through both the unstable region and collective flavor conversion occurs in the nonlinear simulation. Multiple spectral crossings provide unstable modes and break the self-induced suppression at small radii. In the MAA case, the density profile enters the unstable region at 100 km and does not go out of the unstable region until $r \sim 1000$ km. Therefore, unlike the case of 100 ms, the growth rate does not suddenly weaken and the flavor instability is well developed. Comparing the MAA case to the MZA case, we find that the narrow region at small radii in the MZA case stays on

higher matter density, and the flavor instability in the MAA case is weaker than that in the MZA case. Previous studies have reported that the MAA instability is more likely to be suppressed in neutrino spectra with multiple crossings [88]. Actually, the lowness of the narrow region indicates suppression behaviors in the MAA case.

3.2.6 Signal prediction

Finally, we make signal predictions at current and future detectors, Super-Kamiokande and DUNE (see Sec. 3.1.5 for the detector designs). We numerically calculate the flavor evolution including vacuum, matter, and collective effects until 1500 km. At this radius, the neutrino density is small enough and self-induced effects cease. The emitted neutrinos propagate through the H- and L-resonance in the outer envelope of the progenitor and undergo additional mixing. Here, we assume these MSW effects induce adiabatic resonances mixing. For the normal mass ordering case, the MSW flavor mixing is described in Eqs. 3.24 and 3.25. In Sec. 3.1.5, we have used the original neutrino spectrum for f_{ν_α} because collective neutrino oscillation is completely suppressed in our failed super-

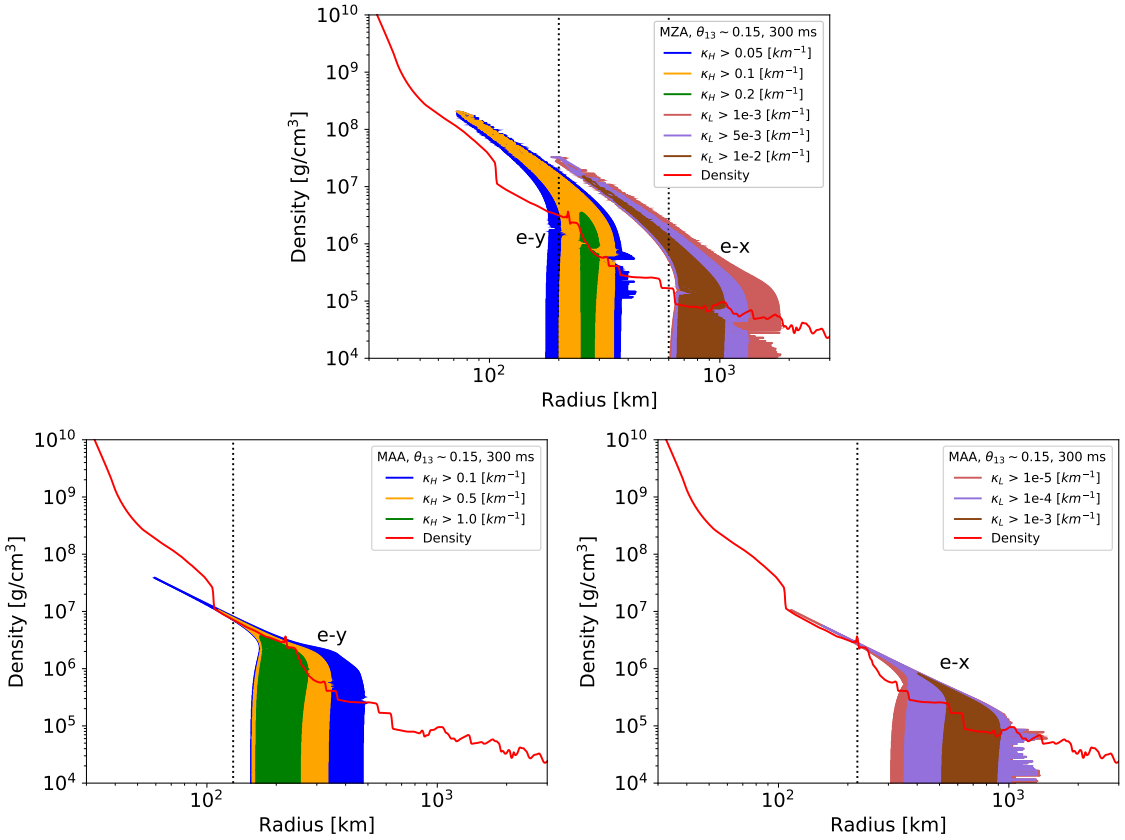

Figure 3.18. The same as Fig. 3.16, but for 300 ms and we also show both the MAA and MZA cases. The top panel is the MZA case in both the $e-x$ and $e-y$ sectors. The bottom left and right panels are the MAA case in the $e-x$ and $e-y$ sectors, respectively. Here, we show only the experimental mixing angle case.

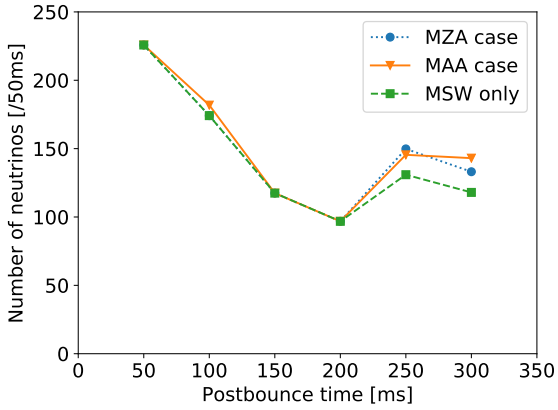

Figure 3.19. Detected IBD event rate per 50 ms bins at Super-Kamiokande from an ECSN at 10 kpc. The MAA case, the MZA case, and the MSW only case are shown as orange solid, blue dotted, and green dashed lines, respectively. The inclusion of collective neutrino oscillation tends to increase the IBD event rate.

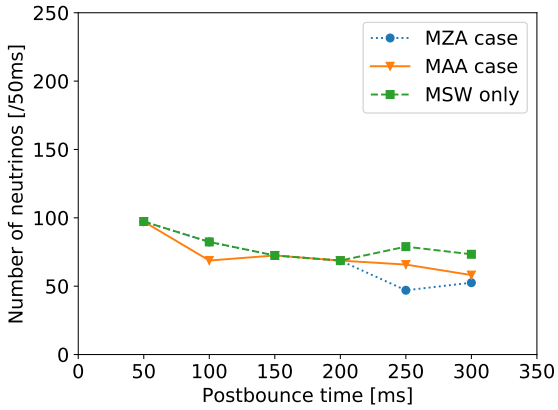

Figure 3.20. The same as Fig. 3.19, but for ν_e CC at DUNE. In contrast to $\bar{\nu}_e$, the inclusion of collective neutrino oscillation tends to decrease the ν_e event rate.

nova model. However, our numerical simulation for an electron-capture supernova model shows the flavor conversion and we should use the energy distribution at 1500 km after the collective flavor conversions. We evaluate the event rate, assuming a supernova event with an $8.8M_\odot$ progenitor at $d = 10$ kpc as a representative distance in our Galaxy.

Figure 3.19 shows the time evolution of the event rate per 50 ms at Super-Kamiokande. Here, we present three types of cases: the MZA, MAA, and MSW only cases, all for the normal mass ordering. The presence of complete matter suppression switches over time and four phases emerge. The phase transition is due to the radial expansion of the shock wave. When collective neutrino oscillation overcomes the matter suppression, the event rate tends to increase compared to the MSW only case. The IBD cross section strongly depends on the neutrino energy and the high-energy tail of the neutrino spectra

is a dominant part for the event rate. The high-energy tail is more pronounced for non-electron neutrinos, so the extent to which the ν_X spectral tail is mixed in with the electron neutrinos determines the difference in the event rates. In the normal mass ordering case, only $c_{13}^2 s_{12}^2 \sim 0.3$ of $\bar{\nu}_x$ and $s_{13}^2 \sim 0.02$ of $\bar{\nu}_y$ spectra are mixed in with the $\bar{\nu}_e$ spectrum. On the other hand, collective neutrino oscillations results in an additional $e - X$ conversion, increasing the event rate by $\sim 20\%$ in the 300 ms case.

Figure 3.20 shows the time evolution of the neutrino event rate at DUNE. The shock propagation similarly affect the predicted neutrino event rate, while the effects of collective neutrino oscillation is contrary to the Super-Kamiokande case. The revival of collective neutrino oscillation tends to decrease the event rate and it follows from the complete MSW mixing through the H-resonance. The H-resonance completely switches between electron neutrinos and heavy-leptonic flavors. Since collective neutrino oscillation occurs in both MZA and MAA cases, the final spectrum of the electron neutrino is not a pure non-electron spectrum. Therefore, the presence of collective flavor conversion reduces the contribution from the high-energy tail of the original non-electron neutrinos in the detected electron-neutrino spectrum. The difference between the MZA and MAA cases is also clearly shown compared to the Super-Kamiokande case. At 300 ms, the MZA case is even unstable due to multiple crossings and collective neutrino oscillation occurs. On the other hand, the MAA instability induces the multi-angle decoherence, leading to flavor equipartition in the neutrino ensemble. In the MAA case, the spectral shapes of ν_x and ν_y are identical, so the observed electron neutrino spectrum has a relatively large contribution from the spectral tail of ν_X after passing through the MSW resonance. Thus, the electron neutrino spectrum in the MZA case is more different from that in the MSW-only case than in the MAA case.

3.2.7 Section summary

We have introduced the impact of symmetry breaking on the traditional bulb model; spatio-temporal instability and axial-symmetry breaking can potentially overcome the multi-angle matter suppression. We have discussed the possibility of the temporal instability still using the linear stability analysis.In the linear regime, non-zero pulsating modes cancel out the effective matter density and provides the growth rate on the higher matter density. However, the unstable region becomes smaller and narrower than the stationary bulb model. The growth rate weakens again and the flavor instability may decay before it sufficiently grows.

And We have performed the first-ever numerical study of three-flavor collective neutrino oscillation including the axial-symmetry breaking in a realistic electron-capture supernova (ECSN) model with an $8.8 M_\odot$ progenitor. The azimuthal angular distribution of emitted neutrinos triggers axial-symmetry breaking and causes the multi-azimuthal-angle (MAA) effects. The MAA instability can be enhanced even in the normal mass ordering, under which axial symmetric (MZA) case is potentially stable. To interpret our results, we have also extended the linear stability analysis into three-flavors including mixing angles. Finally, we make signal predictions for a Galactic supernova event considering current and

future detectors by using our obtained neutrino spectra.

We found that the MAA effects can overcome the matter suppression at time snapshots when the MZA instability is completely suppressed. The spectral splits appear even in the MAA case and are similar to the axial-symmetric case in the inverted mass ordering case. The growth rate in the $e-x$ sector is much smaller than in the $e-y$ sector and provides partial flavor conversion. Also, interesting is the dependence of the mixing angle θ_{13} on the $e-x$ sector. In the MZA case, the application of the latest non-small experimental value rises the instability associated with Δm^2_{21} and can cause $e-x$ flavor conversions at much larger radii even in the normal mass ordering. However, the inclusion of the MAA effect is contrary to the MZA case and weakens the growth rate. In this sense, the MAA case in the normal mass ordering resembles the axial-symmetric case in the inverted mass ordering at early time snapshots. The consideration of axial-symmetry breaking makes us possible to discuss more generally in the neutrino signal prediction.

We found that the neutrino event rates at Super-Kamiokande and DUNE show systematic changes when collective neutrino oscillation survives against the multi-angle matter suppression. During the neutronization burst and the accretion phase, collective neutrino oscillation is suppressed by the excess of electron neutrinos and heavy accreting matter; we call this the suppression phase. Later, flavor conversions overcome matter suppression around 100 ms in our ECSN model, and we call this the window phase. Neutrinos undergo matter suppression effects again around 150 ms as the matter profile increases and the neutrino flux decreases; we call this the re-suppression phase. Finally, the self-induced effects revive around 300 ms during the cooling phase; we call this the revival phase. Note that these phases are only what we found on our ECSN model and they may not necessarily be generic.

When we treat the axial-symmetry breaking, we have imposed the assumption that the transverse evolution can be ignored in order to extend the bulb model. Actually, we need to also consider the spatio-temporal instability, as discussed in Sec. 3.2.1, that requires a major modification in the traditional bulb model. The investigation of the global solutions including the multi-dimensional spatial and temporal evolution is still open and there is still much work needed to challenge the computational complexity of the self-induced interactions.

3.3 Neutrino halo

In the previous section, we have discussed the impact of symmetry breaking on the bulb model. It modifies the neutrino geometry and derivative term in the flavor evolution, and has revealed the existence of flavor instabilities which are suppressed in the traditional bulb model. The simple numerical model still requires isotropic and free-streaming neutrino emission, and provides us a safe and treatable descriptions. Cherry *et al.* [93, 94] has pointed out that some fraction of emitted neutrinos can experience coherent neutrino-nucleus scattering outside the neutrino sphere and change the travel directions. The scattered neutrinos form a neutrino halo and provides broader angular distributions than

the bulb emission. The neutrino self-interaction potential depends on the intersection angles and the wider halo flux potentially affects the collective flavor conversion. However, at the same time, the non-negligible inwardly scattered flux can destroy the bulb framework and make the global flavor mixing simulation much more difficult due to the complexity and computational costs. If the contribution can be neglected compared to the outward-propagating components, we can evaluate the effect of halo neutrinos by extending the traditional bulb model into the bulb+halo model. In Ref. [94], the halo effects were investigated in an O-Ne-Mg core-collapse supernova model at neutronization burst. The progenitor possesses a steep density gradient in the envelope where collective neutrino oscillation occurs together with the MSW-driven flavor mixing. Inside the gradient, it is completely suppressed and the contribution from the halo neutrinos can be safely estimated. However, the situation is special and no one knows more general halo effects such as later time snapshots when flavor conversion occurs inside the gradient and iron-core progenitor cases. In this section, we will discuss the impact of the neutrino halo for an iron-core collapse supernova model, following our challenging work [133].

3.3.1 Model setup

We perform a two-dimensional (axi-symmetric) core-collapse simulation with a $9.6\,\mathrm{M}_\odot$ zero-metallicity model (Z9.6) provided by A. Heger (2017, private communication, this model is a extension of Heger et al. 2010 [168] toward the lower mass). This progenitor is a non-rotating star and has an iron-core in the center, different from O-Ne-Mg progenitor used in previous work [94]. The hydrodynamical simulation is performed by 3DnSNe code (recent application reference [161, 169]), and we show the electron density profile along the north polar direction at 86, 136, and 186 ms in Fig. 3.24. This two-dimensional simulation is computed on a spherical polar coordinate with spatial resolution of $(N_r, N_\Theta) = (512, 128)$. This radial grid covers from the center to an outer boundary of 5000 km. A piecewise linear method with gEoMetrical correction is used to reconstruct variables at the cell edge, where a modified van Leer limiter is employed to satisfy the condition of total variation diminishing (TVD) [170]. The numerical flux is calculated by HLLC solver [171]. We adopt the equation of state by Lattimer & Swesty with incompressibility of $K = 220$ MeV [139]. These features of the time evolution are related to the shock propagation. Numerical explosion simulations under spherical symmetry are apt to fail the shock revival and do not provide the correct neutrino signals. In order to investigate the time evolution of halo effects and collective neutrino oscillation, successfully exploding supernova models are required. We have found the Z9.6 model explodes successfully even in spherically symmetric simulation (consistent with [172]), but we here employ a two-dimensional simulation to understand more general neutrino halo structure. The halo structure strongly couples to the hydrodynamics of supernovae and two-dimensional halo effects are different from their spherical symmetric counterparts [100, 101, 103]. We finally calculate collective neutrino oscillations along the north polar direction from the accretion phase until the shock revival.

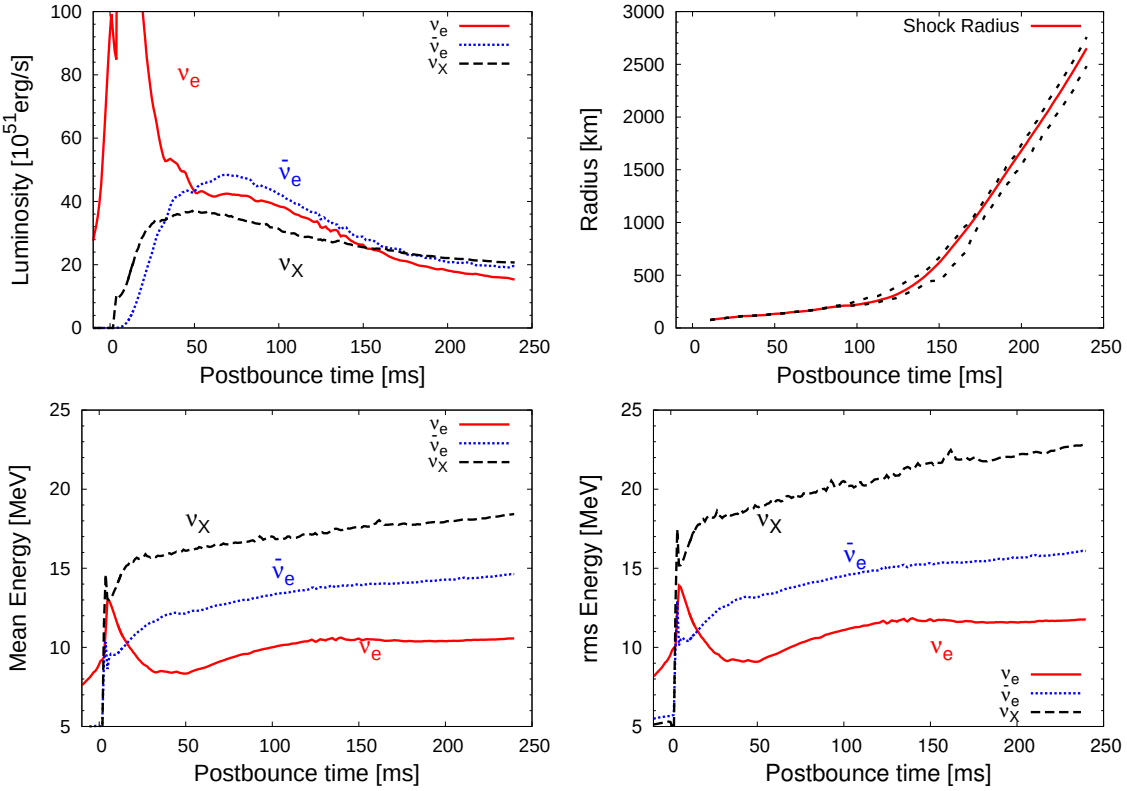

Figure 3.21. The top panels show the time evolution of neutrino luminosity (left) and shock wave radius (right). In the bottom panels, we show averaged energy (left) and rms energy (right). In neutrino luminosity and average energy, $\nu_e, \bar{\nu}_e$, and ν_X are red solid, blue dotted, and black dashed line, respectively. For the shock radius figure, dotted lines show the maximum and minimum radius.

3.3.2 Construction of halo model

Our process for making the predictions of collective neutrino oscillation including the halo effects from core-collapse supernovae simulations consists of the following four steps:

1. Post processing single time snapshots of the neutrino emission from the hydrodynamical simulation of the 3DnSNe code to account for the re-direction of halo neutrinos and creating a 4D map of the energy and angular distribution of halo neutrinos in all radial and angular zones.
2. We survey the radii where matter suppression completely suppresses collective neutrino oscillation at each time snapshot. We use a point inside the radius at which the matter suppression ceases as the starting point for the calculation of collective neutrino oscillation.
3. To safely proceed with a collective neutrino oscillation calculation, we verify that the contribution from the halo neutrinos to the neutrino flavor transformation EoM at all radii above the starting point identified in step 2 is suitably "small" where

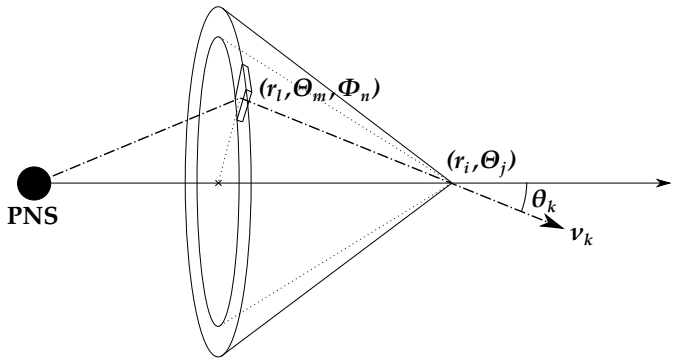

Figure 3.22. Schematic description for equation (3.67). Emitted neutrinos are scattered at a position (r_l, Θ_m, Φ_n) towards position (r_i, Θ_j) with the local radial intersection angle $\theta_{[i,j],[l,m,n]}$. Neutrinos with the local polar angle θ_k at (r_i, Θ_j) are given by summation over (l, m, n) along trajectory θ_k.

this is set to be less than 10% of the $\nu - \nu$ forward scattering interaction.

4. Use the map of the halo neutrinos generated in the first step to populate the outward directed neutrino emission trajectory bins (including the bulb emission) at the calculation starting point and performing a halosphere style [94] collective neutrino oscillation calculation. In this sense, we are creating a validation check for what regions of the envelope are safe to treat in terms of the initial condition formulation of the collective neutrino oscillation problem, and what regions require the treatment of the full boundary value problem. We have found that for the example of the Z9.6 progenitor, we can safely employ the initial condition solution method we describe for the epochs of the SNe explosion which exhibit collective neutrino oscillations.

First, We will describe how we calculate the halo neutrino distribution in detail. To map the halo neutrino population, we calculate the contribution of the single direction-changing scattering. The cross section of the enhanced neutrino-nucleus interaction for a nucleus with total nucleons, A, proton number, Z, and neutron number, N, is first calculated by Tubbs and Schramm [31] to leading order,

$$\sigma\left[E_\nu, (Z,N)\right] \approx \frac{G_F^2}{\pi} E_\nu^2 \left[\frac{1}{2}\left(C_A - C_V\right)\right) A + \frac{1}{2}\left(2 - C_A - C_V\right)\left(Z - N\right)\Bigg]^2 , \tag{3.63}$$

with weak interaction coupling constants $C_A = 1/2$ and $C_V = 1/2 + 2\sin^2\theta_W = 0.9446$, taking the Weinberg angle to be $\sin^2\theta_W = 0.2223$. This coherent scattering is nearly isotropic and newly forms a neutrino halo inside the core-collapse supernovae.

Figure 3.22 shows the geometry of the formation of the neutrino halo population. At each spatial point (r, Θ, Φ), some fraction of emitted neutrinos is scattered and accumulated into the halo population ρ^{halo}. The scattering population and remaining parts are obtained as

$$\frac{\mathrm{d}}{\mathrm{d}r}\rho^{\mathrm{halo}}\left(r, \Theta_j, \alpha, E_\nu\right) = \Gamma^{\mathrm{halo}}\left(r, \Theta_j, E_\nu\right)\rho^{\mathrm{ray}}\left(r, \Theta_j, \alpha, E_\nu\right) , \tag{3.64}$$

and,

$$\frac{\mathrm{d}}{\mathrm{d}r}\rho^{\mathrm{ray}}\left(r,\Theta_j,\alpha,E_\nu\right)=-\Gamma^{\mathrm{halo}}\left(r,\Theta_j,E_\nu\right)\rho^{\mathrm{ray}}\left(r,\Theta_j,\alpha,E_\nu\right)\,, \tag{3.65}$$

with the neutrino scattering rate,

$$\Gamma^{\mathrm{halo}}\left(r,\Theta_j,E_\nu\right)=\sum_\beta\sigma\left[E_\nu,\left(Z,N\right)_\beta\right]\rho_\beta\left(r,\Theta_j\right)\,, \tag{3.66}$$

taking Θ_j and the index j to denote the trajectory and angular bin, respectively, of the two-dimensional core-collapse supernova data, α indexes the neutrino flavor state, β indexes the species of nucleus/nucleon for which we calculate scattering rates, and the local density of a nuclear species along a given trajectory is $\rho_\beta\left(r,\Theta_j\right)$. For simplicity, the index β is classified into four species: protons, neutrons, ^{4}He, and a heavy species given by $\langle(Z,N)\rangle$. The neutrino halo distribution can not be obtained by integrating Eqs. (3.64) and (3.65) at each radial (i) and angular (j) grid outwardly along each trajectory j from the neutrino sphere. The integration quantity is the total scattered or free-streaming neutrino number density and does not exhibit the angular distribution incoming into a certain position (r,Θ). We need to re-distribute the isotropically scattered halo neutrinos. Shown in Fig. 3.22, a neutrino flux at a position (r_i,Θ_j) must be summed over halo neutrinos scattered at a position (r_l,Θ_m,Φ_n). The energy and angular number density distribution ρ^{halo} of the halo neutrinos in each radial and polar angle grid (i,j) is then,

$$\rho^{\mathrm{halo}}\left(\alpha,E_\nu,\theta_k,r_i,\Theta_j\right)=\sum_{l,m,n}\Omega_{[i,j],[l,m,n]}\Pi\left(\theta_k;\theta_{[i,j],[l,m,n]},\delta_{[i,j],[l,m,n]}/2\right)\Delta\theta_k\rho^{\mathrm{halo}}\left(\alpha,E_\nu,r_l,\Theta_m\right), \tag{3.67}$$

where θ_k is the local polar angle relative to the position (r_i,Θ_j),

$$\theta_{[i,j],[l,m,n]}=\cos^{-1}\left(\hat{r}_{i,j}\cdot\left(\vec{r}_{i,j}-\vec{r}_{l,m,n}\right)/|\vec{r}_{i,j}-\vec{r}_{l,m,n}|\right)\,, \tag{3.68}$$

representing the local radial intersection angle with the emission from a grid (l,m,n) at the position (i,j). The incident ray has finite angular size $\delta_{[i,j],[l,m,n]}$ as viewed from the target zone and we need to split the scattered neutrino across a range of θ_k bins, centered on $\theta_{[i,j],[l,m,n]}$. We approximate this distribution to be uniform in the local azimuthal coordinates, so the total number density of neutrinos arriving in the θ_k angular bin is reduced by a factor of $\Pi\left(\theta_k;\theta_{[i,j],[l,m,n]},\delta_{[i,j],[l,m,n]}/2\right)\Delta\theta_k$, where $\Pi(x;a,b)$ is the rectangular function on the interval $a\pm b$, normalized so that the sum $\sum_k\Pi\left(\theta_k;\theta_{[i,j],[l,m,n]},\delta_{[i,j],[l,m,n]}/2\right)\Delta\theta_k\equiv 1$. The relative flux dilution of halo sources is accounted for by the solid angle term, $\Omega_{[i,j],[l,m,n]}$, which is the solid angle subtended by the target position (i,j), relative to the source grid (l,m,n), assuming that all zones are roughly spherical with radius $\mathcal{R}_{l,m,n}=(3V_{l,m,n}/4\pi)^{1/3}$ and $\mathcal{R}_{i,j}=\mathcal{R}_{l=i,m=j,n=0}$. By evaluating Eq. (3.67) everywhere within the supernova data set, we obtain an initial neutrino halo map. The accumulated neutrino halo distributions include both the inwardly and outwardly going neutrino flux at the position (r_i,Θ_j). Therefore, we can not simulate the collective flavor conversion using the halo populations within the bulb framework and we need to split the two directed components.

Next, we evaluate the contribution of halo neutrinos to the self-interaction potential. The contributions from the outgoing and inward-going neutrinos at the position (r_i, Θ_j) are given by

$$H^{\rm out}_{\nu\nu}(r_i, \Theta_j) = \sum_{\alpha, E_\nu} \sqrt{2} G_{\rm F} \int_1^0 (1 - \cos\theta_{\rm ref} \cos\theta) \left[\rho_{\nu_\alpha}(E_\nu, \theta, r_i, \Theta_j) - \bar{\rho}_{\nu_\alpha}(E_\nu, \theta, r_i, \Theta_j)\right] {\rm d}\cos\theta \,, \tag{3.69}$$

and

$$H^{\rm in}_{\nu\nu}(r_i, \Theta_j) = \sum_{\alpha, E_\nu} \sqrt{2} G_{\rm F} \int_0^{-1} (1 - \cos\theta_{\rm ref} \cos\theta) \left[\rho_{\nu_\alpha}(E_\nu, \theta, r_i, \Theta_j) - \bar{\rho}_{\nu_\alpha}(E_\nu, \theta, r_i, \Theta_j)\right] {\rm d}\cos\theta \,, \tag{3.70}$$

where ρ_{ν_α} is the total number density summing over the halo neutrinos $\rho^{\rm halo}$ and the free-streaming components $\rho^{\rm ray}$ which do not undergo any direction-changing scattering. Here, we choose the $\nu - \nu$ interaction contributions for a radially directed neutrino with $\cos\theta_{\rm ref} = 1$ as a reference trajectory. Note that this formalism is based only on the diagonal terms of neutrino density matrix ρ_{ν_α} and requires that the off-diagonal terms are still zero. In other words, the neutrinos do not undergo any flavor conversion and the flavor instabilities are much less than unity.

In order to provide a quantitative criterion that we can safely calculate collective neutrino oscillation within the bulb framework, we require a ratio $H^{\rm in}/H^{\rm out}$ to be less than 10% at all radii where we perform the flavor evolution. Mapping the ratio of $H^{\rm in}/H^{\rm out}$ at all points within the supernova data is the first step in checking for safety. Figure 3.23 shows the results of the safety check for some time snapshots.

The second step is to check that the density matrices remain almost diagonalized inside the radii where we evaluate Eqs. (3.69) and (3.70), and collective flavor instability does not grow at all. The scattering rate depends on the matter density and the contribution from the inward-going halo neutrinos increases in the dense matter. On the other hand, in the high matter density, collective neutrino oscillation tends to be completely suppresses due to the phase dispersion. To find the maximum radius $r_{\rm init}$ where matter suppression is dominant and suppresses the growth of the off-diagonal terms, we calculate the collective flavor conversions without the halo populations.

The third step is to verify whether the contribution ratio $H^{\rm in}/H^{\rm out}$ is less than 0.1 in the region where collective neutrino oscillation overcomes the matter suppression. While the ratio may grow larger than 10% at some radii along a given trajectory, we can neglect the impact of the neutrino halo on the collective flavor conversion if the regions are within the complete matter suppression. We can safely calculate collective neutrino oscillation including outwardly-propagating halo neutrinos if the radii where the contribution condition $H^{\rm in}/H^{\rm out} < 0.1$ is satisfied is greater than $r_{\rm init}$.

The last and fourth step is to set the initial conditions for performing the flavor evolution in the bulb+halo model. We form a halo sphere with a radius R_H instead of the neutrino sphere R_ν and assume that neutrinos are free-streamingly emitted from the halo sphere similar to the original bulb model, following Ref. [94]. We define the halo sphere radius to

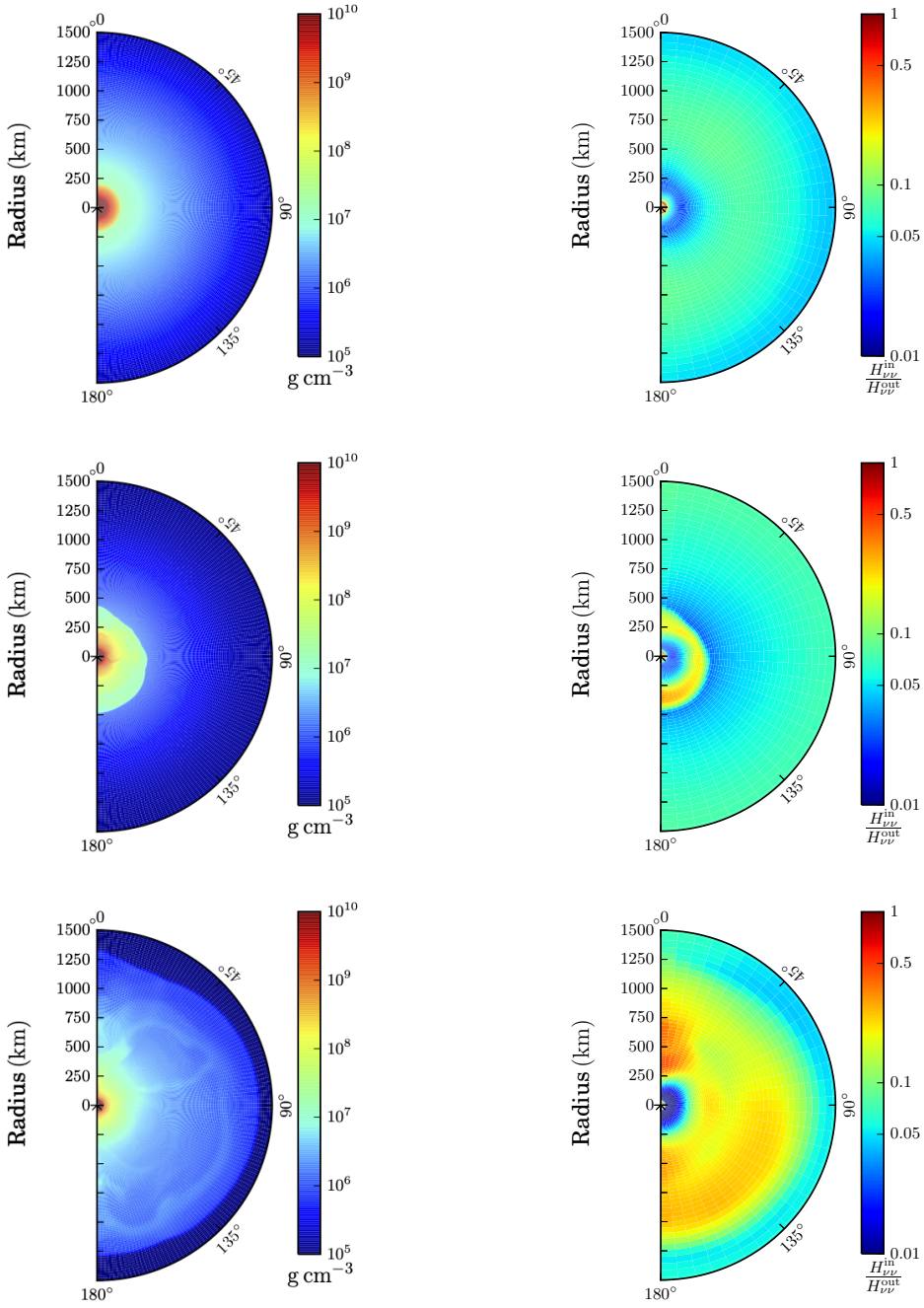

Figure 3.23. Density profile (left) and Halo contribution (right). These figures show three time snapshots, postbounce time 86 ms, 136 ms, and 186 ms, from top to bottom. Color scale for the right panels indicates the ratio of the self-interaction Hamiltonian of inward contribution to outward one. An region where this ratio exceeds 0.1 should not be treated by the bulb+halo model.

be $15-20\%$ less than the calculation onset radius $r_{\rm init}$ of collective neutrino oscillation. Then, neutrinos near the surface of the halo sphere have intersection angles relative to the radial direction on the range $0 < \theta < \pi/2$ despite outside the neutrino sphere. Eventually, the phase space distribution on the surface of the halo sphere is obtain by

$$\rho_{\nu_\alpha}(E_\nu, \theta)|_{r=R_H} = \rho^{\rm ray}_{\nu_\alpha}(E_\nu, \theta, r_i = R_H, \Theta_j) + \rho^{\rm halo}_{\nu_\alpha}(E_\nu, \theta, r_i = R_H, \Theta_j). \tag{3.71}$$

3.3.3 Magnitude of Halo

We show the density profile and the halo contribution at 86, 136, and 186 ms in Fig. 3.23. This halo contribution expresses the ratio $H^{\rm in}/H^{\rm out}$ of the neutrino self-interaction potential of inward-going neutrinos to outward ones. The inward-scattered neutrino flux can not be neglected in the regions where this ratio is larger than 0.1. In particular, the dangerous region expands over the whole map in the stellar envelope at 186 ms. However, we find an escape route along 45 degree direction, which is generated by the two-dimensional density structure and neutrino flux distribution. Comparing the halo contribution (left panels) to the density profile (right), we find that the dangerous region is correlated to the regions inside the shock front and steeply decreases outside the shock wave. This feature is similar to the steep density gradient in a O-Ne-Mg core-collapse supernova model in Ref. [94]. Therefore, the density gradient of the shock wave provides the same effect as the density gradient in the envelope of O-Ne-Mg stars. Thus, We can safely calculate collective neutrino oscillation ignoring inwardly scattered neutrinos outside the shock wave. In this case, the halo sphere surface almost corresponds to the shock front and the collective flavor conversion does not occur inside the pseudo-emission source. Using this bulb+halo model, we investigate the impacts of outward-going neutrino flux on collective neutrino oscillation.

3.3.4 Numerical results

In our model, the shock wave propagates outwardly within the occurrence region of collective neutrino oscillation. This propagation varies the density structure in this region as time passes, and changes the behaviors of the multi-angle matter suppression. We show the time evolution of the density profile along the north polar direction at 86, 136, and 186 ms in Fig. 3.24. Collective neutrino oscillation is completely suppressed by the matter effects at 186 ms. On the other hand, the contribution ratio at this time snapshot alerts us to the ruin of the bulb framework and the matter effects suppress the impact of the inward-scattered neutrino flux.

Figure 3.25 shows the radial evolution of the survival probability of electron neutrinos averaged over the energy and angular distribution at $t = 86$ ms (left) and 136 ms (right). At 86 ms, the shock front is located around 200 km and collective neutrino oscillation occurs outside the shock wave. The electron density gradually decreases with increasing radius, and flavor conversions occur at $r \sim 400\,{\rm km}$. In the with-halo case, the onset radius of the flavor conversion is clearly delayed. The inclusion of halo neutrinos is suggested

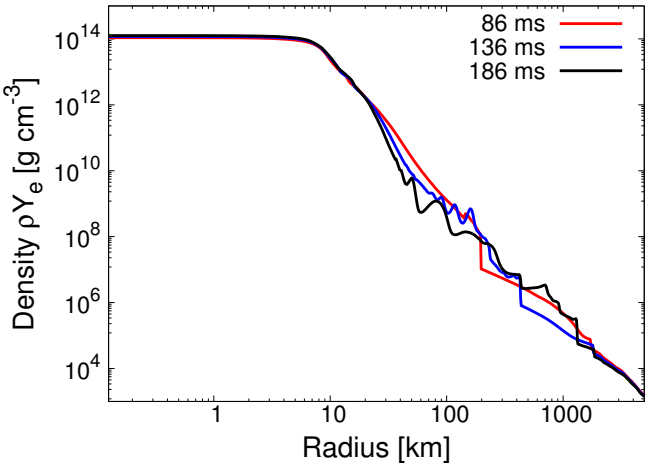

Figure 3.24. Electron density profile along the north pole at postbounce time $t_{\rm pb} = 86, 136$, and 186 ms. Shock wave propagates from 200 km to 1000 km.

to provide additional multi-angle matter suppression on collective neutrino oscillation. This matter suppression is caused by the phase dispersion due to broadening the angular modes. Intersection angles in the absence of the neutrino halo depend roughly on the inverse square of the radius in the large-distance limit $r \gg R_{nu}$. On the other hand, the halo neutrinos have broader angular distributions even at large radii and can provide additional phase dispersion. This is one of the neutrino halo effects. At 136 ms, there is no difference in the onset radii between the no-halo and with-halo cases, different from at 86 ms. The shock wave is located at $r \sim 430$ km at this time snapshot, and neutrinos get free from the matter suppression just after passing through the shock front and the collective flavor instability also grows rapidly. Therefore, the onset radius even in the with-halo case is almost identical to that in the no-halo case.

Next, we show the contour maps of the survival probability on the energy-impact parameter plane after the collective neutrino oscillation ceases at $r = 1200$ km at a representative snapshot $t = 136$ ms in Fig. .3.26. The left panels are in the no-halo case and

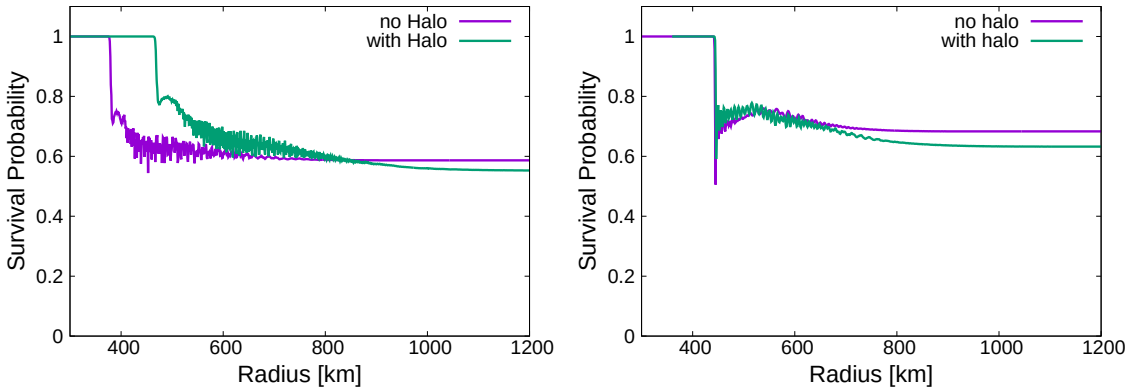

Figure 3.25. The radial evolution of the energy and angle averaged $\nu_{\rm e}$ survival probability at postbounce time 86 ms (left) and 136 ms (right).

the right ones in the with-halo case. The top panels show the survival probability of electron neutrinos and the bottom ones are for antineutrinos. The vertical axis correspond to the impact parameter $b = r \sin\theta_R$ of neutrinos escaping from the surface of the emission source. In the no-halo case, the surface radius is $r = R_\nu$ and it is $r = R_H$ for the with-halo case. In the with-halo case, neutrino emissions with the impact parameter beyond the radius of the original neutrino sphere $R_\nu = 30$ km correspond to the contribution only from the neutrino halo. The flavor conversion for neutrinos in the no-halo case clearly exhibits spectral splits, as shown in the previous work [119]. In the with-halo case, the halo contributions give additional flavor conversions in the relatively lower impact parameter region. These additional oscillations deform the neutrino spectra and affect the detection at Earth.

Finally, we show the neutrino spectra averaged over the angular distributions after collective neutrino oscillation ceases at $r = 1200$ km at $t = 136$ ms in Fig. 3.27. The left panels are in the no-halo case and the right ones are in the with-halo case. The halo contributions provide additional flavor conversions above ~ 10 MeV in both neutrino and

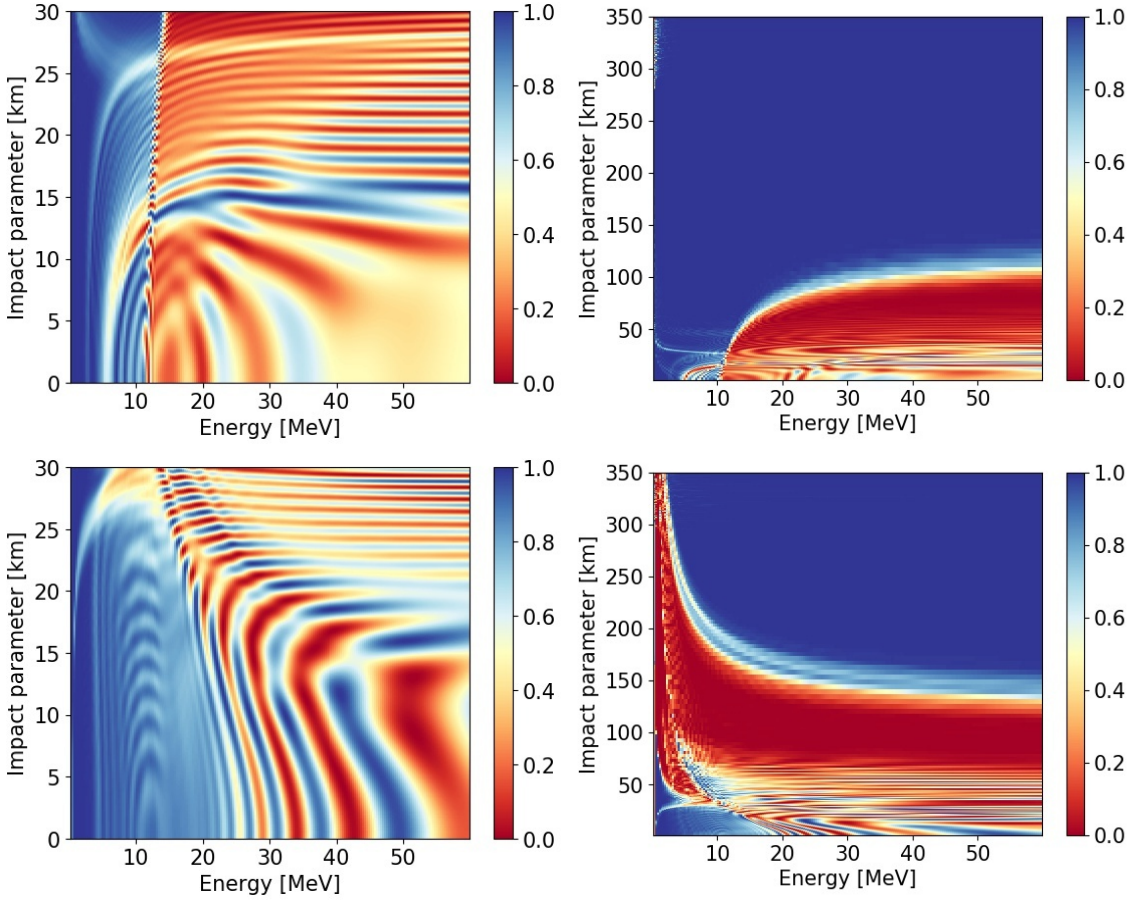

Figure 3.26. Contour maps of the survival probability for neutrinos (upper panels) and antineutrinos (bottom panels) on the energy-impact parameter plane at $r = 1200$ km at postbounce time 136 ms. Left panels are the no-halo case and right panels are the with-halo case.

antineutrino sectors. This feature appears in the contour maps of the survival probability in Fig. 3.26. The halo effects sharpen the spectral splits induced by collective neutrino oscillation. On the other hand, below $\sim$ 10 MeV for antineutrinos, additional flavor conversions present in the coutour maps on the energy-impact parameter plane do not exhibit any spectral features. This is because the scattering rates in the lower energy are much smaller and the contribution from the free-streaming components becomes more dominant.

3.3.5 Signal prediction

For the Z9.6 model, we find that the matter suppression hinders collective neutrino oscillation at early and late time epochs, with the exception of a window from $t_{\rm pb} = 70$ ms to $t_{\rm pb} = 170$ ms during the shock revival phase. As a comparison in neutrino signals from the Z9.6 model, we consider three situations as follows: no collective neutrino oscillation,

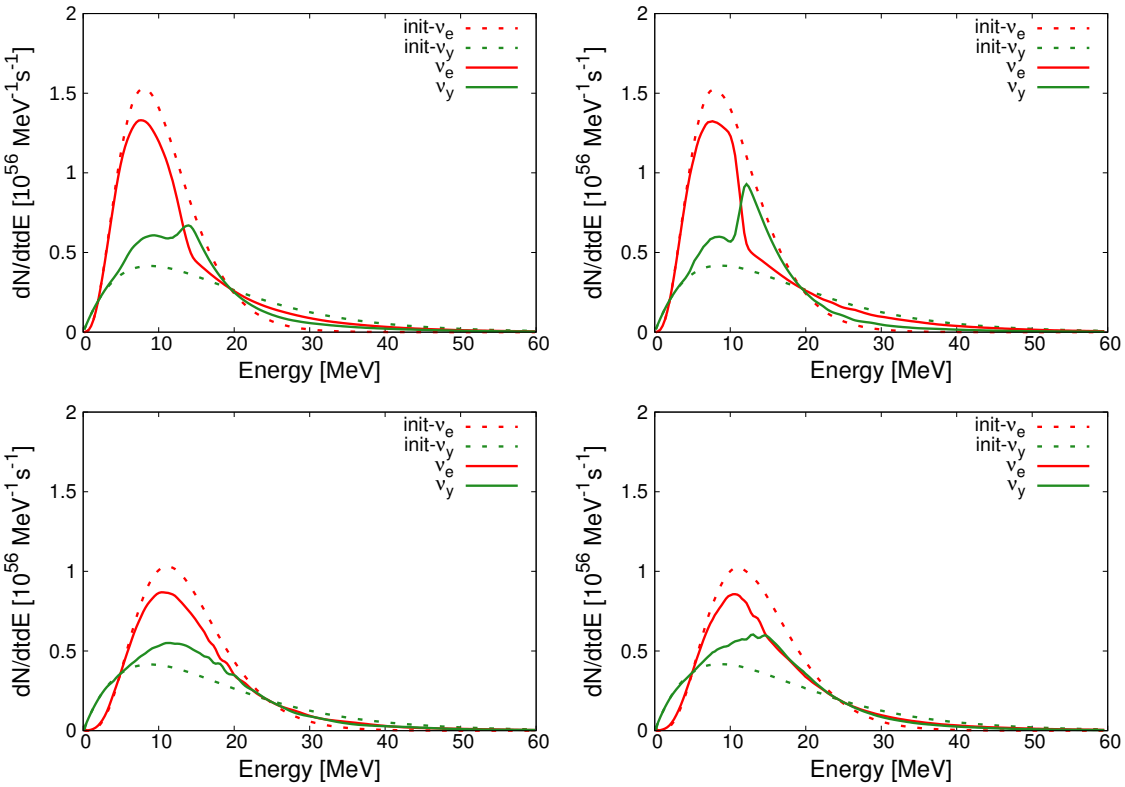

Figure 3.27. Neutrino spectra (upper panels) and antineutrino spectra (bottom panels) after the collective neutrino oscillation ceases at $r = 1200$ km at postbounce time 136 ms. Left panels are the no-halo case and right panels are the with-halo case. The e and y flavors are shown in red and green lines, respectively. The solid lines are for neutrino spectra after collective neutrino oscillation and the dashed ones for initial spectra.

no-halo, and with-halo cases. We used the SNOwGLoBES software package[*1] to model the detected signal corresponding to several time snapshots of out Z9.6 model. We have chosen to compare the neutrino event rates in Super-Kamiokande (SK) with inverse beta-decay (IBD) reaction (assuming the detector has completed doping with Gd, allowing for the tagging of IBD events), and in a 40 kt liquid argon (LAr) detector, projected to be DUNE, with $\nu_e - {}^{40}\mathrm{Ar}$ capture. We assume neutrino signals from a supernova event of our Z9.6 model emerging at a distance $d = 10$ kpc as a representative distance in our Galaxy.

Figure 3.28 shows the time variation of the event rate for IBD reaction in SK on the left panel and for $\nu_\mathrm{e} - {}^{40}\mathrm{Ar}$ capture in DUNE on the right. The presence of collective neutrino oscillation can be clarified through the divergent trends between the no collective neutrino oscillation and no-halo cases in the event rates at both neutrino detectors. The comparison between the IBD case at SK and the LAr case at DUNE exhibit the opposite divergent trend from the no collective neutrino oscillation case. In SK, the event rate of $\bar{\nu}_e$ significantly decrease due to the occurrence of collective neutrino oscillation, while that for ν_e increases in DUNE. Collective neutrino oscillation is completely suppressed due to the matter effects again at $t = 170$ ms and the event rates become identical to the absence of collective neutrino oscillation. The event rate during the survival of collective neutrino oscillation in SK is reduced an additional 10% when including the neutrino halo in collective neutrino oscillation, while that in the LAr case at DUNE does not show any significant difference between the no-halo and with-halo cases.

Next, we consider the energy dependence of ν_e and $\bar{\nu}_e$ in the signals observed in each

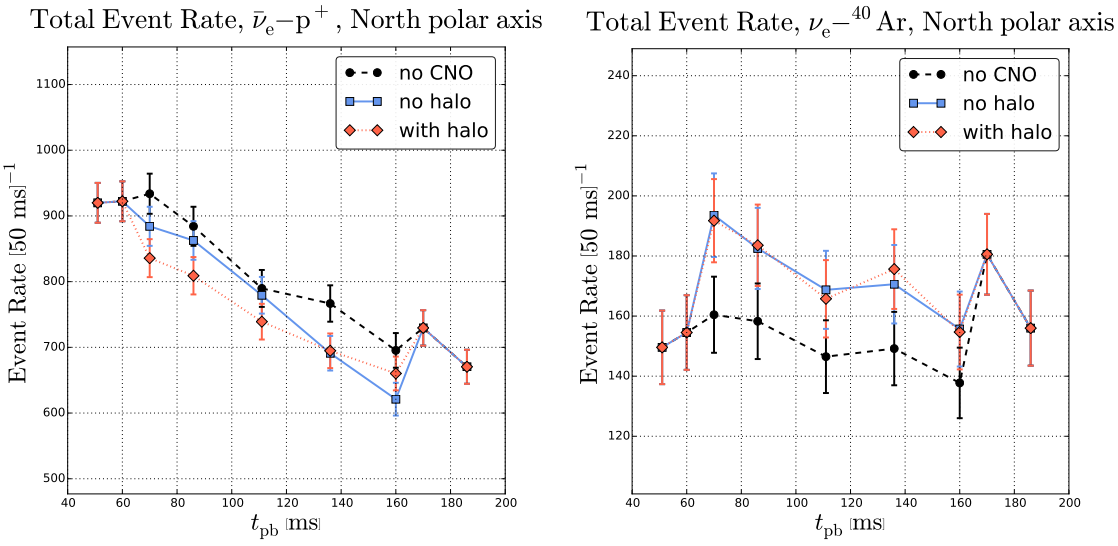

Figure 3.28. Left panel: the time evolution of the inverse beta decay event rate at SK. Right panel: the time evolution of the electron neutrino-^{40}Ar capture rate at DUNE. Black line is in the no collective neutrino oscillation (no CNO) case, blue is in the no-halo case, and red is in the with-halo case.

[*1] SNOwGLoBES: https://webhome.phy.duke.edu/ schol/snowglobes/

neutrino detector. To this end, we introduce the "Hardness Ratio" $R_{\mathrm{H/L}}$, which splits the event rates in each detection channel into two bins with detected neutrino energies above and below a cutoff energy, $E_{\mathrm{C}} = 15\,\mathrm{MeV}$. This means

$$R_{\mathrm{H/L}} = \frac{N|_{E>E_{\mathrm{C}}}}{N|_{E<E_{\mathrm{C}}}}\,, \tag{3.72}$$

Figure 3.29 shows the hardness ratio for IBD detection at SK on the left panel and the right panel shows that for $\nu_{\mathrm{e}} - {}^{40}\mathrm{Ar}$ capture detection at DUNE. Both the hardness ratio for ν_e and $\bar{\nu}_e$ are also expected to exhibit the trends from the no collective neutrino oscillation case similar to the time variation of the event rates in our Z9.6 model. Irrespective of the inclusion of collective neutrino oscillation, the hardness ratio $R_{\mathrm{H/L}}$ gradually increases for both detection channels due to stiffening neutrino spectra for all flavors as time passes. The occurrence of collective neutrino oscillation shows again the behaviors of simultaneously divergent trends in both detection channels. Likewise, there is very little distinction between the no-halo and with-halo cases for the $R_{\mathrm{H/L}}$ ratio.

To restore as much of the shape information as possible to our predicted signals from the Z9.6 simulation, we have performed a basic $\Delta\chi^2$ hypothesis test on the received event distributions (assuming a uniform $\Delta E = 4\,\mathrm{MeV}$ for energy bins between $0 - 60\,\mathrm{MeV}$ and 50 ms integrated observing time), taking the 'no collective neutrino oscillation' case as the null hypothesis for each channel. This will give us a measure of the raw statistical potential to extract information from the collective neutrino oscillation epoch of the Z9.6 signal.

Shown in the left panel of Fig. 3.30 are the results for the inverse beta decay channel in SK and results for $\nu_{\mathrm{e}} - {}^{40}\mathrm{Ar}$ capture detection at DUNE are shown in the right panel.

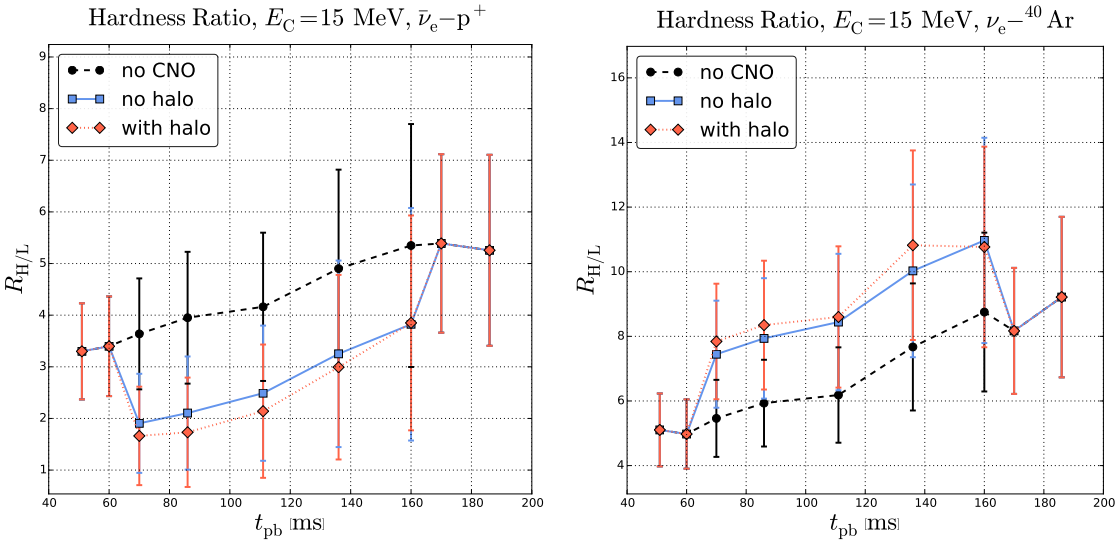

Figure 3.29. Left panel: the time evolution of the Hardness ratio, $R_{\mathrm{H/L}}$, for the inverse beta decay event channel at SK. Right panel: the time evolution of the Hardness ratio, $R_{\mathrm{H/L}}$, for the electron neutrino-^{40}Ar capture channel at DUNE.

These two figures illustrate the importance of including the halo neutrinos in collective neutrino oscillation calculations. Typically, although not uniformly, collective neutrino oscillation signals are more easily discriminated from non-collective neutrino oscillation signals when halo neutrinos are accounted for in both SK and DUNE. For the Z9.6 CCSN simulation, the effect is much more pronounced in SK, where there is a $\sim 60\%$ increase in $\Delta\chi^2$ integrated over the collective neutrino oscillation epoch. Although we do not attempt to make a detailed spectral reconstruction from the received signals in SK and DUNE, both panels of Figure 3.30 taken together indicate that the spectral shape of the collective neutrino oscillation signal is more easily discriminated from thermal neutrino emission when halo neutrinos are included in collective neutrino oscillation calculation. Put another way, because previous studies have omitted halo neutrinos in their collective neutrino oscillation calculations, their predictions for extracting meaningful signals from a supernova neutrino burst are likely to have been *overly pessimistic* with regard to strength of collective neutrino oscillation signals.

3.3.6 Section summary

We have performed the first-ever flavor evolution of collective neutrino oscillation including the contribution from a neutrino halo in an iron-core collapse supernova model. The halo neutrinos are generated by the coherent neutrino-nucleus elastic scattering outside the neutrino sphere and possess the broader angular distributions than the original bulb emission. The calculation results exhibit that there are qualitative and quantitative impacts on the signatures of neutrino oscillations compared to the flavor conversions

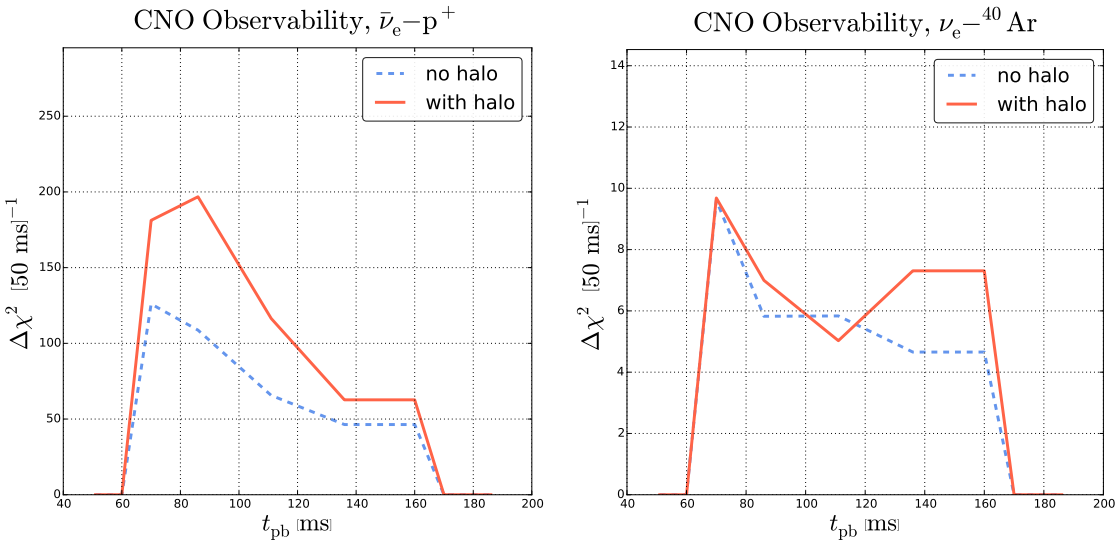

Figure 3.30. Left panel: the time evolution of $\Delta\chi^2$ for the inverse beta decay event channel at SK. Right panel: the time evolution of $\Delta\chi^2$, for the $\nu_e - {}^{40}$Ar capture channel at DUNE. For both cases we take the absence of collective neutrino oscillation to be the null hypothesis.

neglecting the halo neutrinos. We have shown that these changes have implications for the detectability of collective neutrino oscillation in the neutrino signals from a supernova event with a $9.6M_{\odot}$ progenitor at a distance $d = 10$ kpc.

The coherent scattering outside the emission source provides direction-changing effects for some fraction of escaping neutrinos and generates a neutrino halo. The halo neutrinos include the outward-propagating flux and the inwardly scattered one, and changes the description of the neutrino self-interaction potential. If the contribution from the inward-going neutrinos can not be neglected, the neutrino halo may destroy the traditional bulb framework and is much more difficult to compute the collective flavor conversions. We find that our Z9.6 model produces an suitable environment to calculating collective neutrino oscillation with the inclusion of halo neutrinos. There is multi-angle suppression of neutrino flavor transformations in the deep envelope both before $t_{\rm pb} = 70$ ms and after $t_{\rm pb} = 170$ ms. In between, at 100 ms, collective neutrino oscillations are not suppressed, but this intermediate window coincides with the epoch when the explosive shock wave front has not yet grown outward to the initial radius of the collective neutrino flavor conversion. In other words, the relatively small radius of the shock wave results in the formation of a neutrino halo that is overwhelmingly outward as far as collective neutrino oscillations are concerned. By the time of the collective neutrino oscillation, the inward neutrino flux is found to be a subleading order contribution to the Hamiltonian of the flavor transformation. This allows multi-angle calculations of collective neutrino oscillations for the outward flux of neutrinos during this time period.

The physical circumstances which proceed from the evolution of the explosion of the Z9.6 progenitor star produce an environment which is conducive to calculating collective neutrino oscillation with the inclusion of halo neutrinos. Collective neutrino oscillation is completely suppressed due to the dense envelope before the postbounce time $t_{\rm pb} = 70$ ms and after $t_{\rm pb} = 170$ ms. While collective neutrino oscillation survives outside the shock front for the interval 100 ms, the intermediate window coincides with the shock revival phase of core-collapse supernovae. The coherent scattering rates are relatively larger and the halo contribution can not be neglected inside the shock wave. However, the matter suppression is dominant in the regions and inhibits the impact of inwardly halo neutrinos on collective neutrino oscillation. This enables the multi-angle calculation of collective neutrino oscillation for the outgoing neutrino flux during this window of time.

We compare the results of collective neutrino oscillation to those which omit the neutrino halo population, as well as those which omit collective neutrino oscillation entirely. The presence of halo neutrinos with broader angular distributions strengthens the neutrino self-interaction potentials, while it provides additional phase dispersion and delays the onset of collective neutrino oscillation. Also, in the signal prediction from our Z9.6 model, we find that the occurrence epoch of the collective neutrino oscillation is clearly distinguishable from the exclusion case. And we find that broader neutrino halo population produces sharper features of spectral splits compared than the case omitting the coherent scattering. Importantly, we find that detected collective neutrino oscillation signals tend to be more clearly distinguished from thermal emission when including the halo neutrinos.

Chapter 4

Fast Flavor Conversion

Until the previous chapters, we have discussed the influences of slow modes in collective neutrino oscillation on core-collapse supernovae. In particular, we found that symmetry breaking and coherent scatterings, which are ignored in the traditional bulb model, have changed the flavor contents. However, we still have assumed isotropic neutrino emissions following the original bulb model or employed angular distribution which does not contain a zero crossing between neutrinos and antineutrinos. The conditions demonstrate only slow flavor conversions and suppress the excitation of fast modes. In this chapter, we consider the angular distribution with zero crossings and will discuss the impact of fast flavor conversions. Here, we focus on the local flavor evolution in the preshock region of core-collapse supernovae, based on my previous work [173].

4.1 Fast instability

We adopt the dispersion relation approach proposed by Ref. [96] to investigate the behaviors of fast modes in the linear regime. This approach can survey the growth rates in both the temporal and spatial flavor waves $K = (\Omega, \boldsymbol{K})$ simultaneously, different from the scheme introduced in chapter 3.

Linearized equation for the off-diagonal term $\rho^{\alpha\beta}$ in Eq. (2.2) is

$$\mathrm{i}\left(\partial_t + \boldsymbol{v}\cdot\nabla\right)\rho_\Gamma^{\alpha\beta} = \left[v^\mu\left(\Lambda_\mu^{\alpha\beta} + \Phi_\mu^{\alpha\beta}\right) - \omega_V\right]\rho_\Gamma^{\alpha\beta} - \sqrt{2}G_\mathrm{F}\int \mathrm{d}\Gamma'\ v^\mu v'_\mu g_{\Gamma'}^{\alpha\beta}\rho_\Gamma^{\alpha\beta}, \tag{4.1}$$

where the matter and self-interaction effects are

$$\Lambda_\mu^{\alpha\beta} = \Lambda_\mu^{\alpha\alpha} - \Lambda_\mu^{\beta\beta} \tag{4.2}$$

$$\Phi_\mu^{\alpha\beta} = \sqrt{2}G_\mathrm{F}\int \mathrm{d}\Gamma\ v_\mu g_\Gamma^{\alpha\beta}. \tag{4.3}$$

For the plane wave solutions

$$\rho_\Gamma^{\alpha\beta} = Q_\Gamma^{\alpha\beta}\mathrm{e}^{-\mathrm{i}(\Omega t - \boldsymbol{K}\cdot\boldsymbol{x})} = Q_\Gamma^{\alpha\beta}\mathrm{e}^{-\mathrm{i}K\cdot x}, \tag{4.4}$$

the EoM is

$$\left[v^\mu \left[K_\mu - \left(\Lambda_\mu^{\alpha\beta} + \Phi_\mu^{\alpha\beta}\right)\right] - \omega_V\right] Q_\Gamma^{\alpha\beta} = -\sqrt{2}G_{\rm F} \int {\rm d}\Gamma'\ v^\mu v'_\mu g_{\Gamma'}^{\alpha\beta} Q_{\Gamma'}^{\alpha\beta} \tag{4.5}$$

$$\equiv v^\mu a_\mu. \tag{4.6}$$

We can write a non-trivial eigenfunction for $(v^\nu k_\nu - \omega_V) \neq 0$ as

$$Q_\Gamma^{\alpha\beta} = \frac{v^\mu a_\mu}{v^\nu k_\nu - \omega_V} \tag{4.7}$$

where $k \equiv K - (\Lambda + \Phi)$ with $k = (\omega, \boldsymbol{k})$. The phase shift due to matter Λ and neutrinos Φ only changes the real parts of $(\Omega, \boldsymbol{K})$ into $(\omega, \boldsymbol{k})$, and both the frequency ω and the wave number $\boldsymbol{k}$ keep the same imaginary parts. Therefore, we can discuss the occurrence of flavor instability in a rotating frame, $\rho_\Gamma^{\alpha\beta} \to \rho_\Gamma^{\alpha\beta} {\rm e}^{{\rm i}(\Lambda+\Phi)\cdot x} = Q_\Gamma^{\alpha\beta} {\rm e}^{-{\rm i}k\cdot x}$. By substituting it into both the sides, we obtain

$$v^\nu a_\nu = v^\mu \left[-\sqrt{2}G_{\rm F} \int {\rm d}\Gamma'\ v'_\mu g_{\Gamma'}^{\alpha\beta} \frac{v'^\nu}{v'^\lambda k_\lambda - \omega_V}\right] a_\nu. \tag{4.8}$$

Therefore, we get using the metric $\eta^{\mu\nu} = {\rm diag}(+,-,-,-)$

$$v_\mu \Pi^{\mu\nu} a_\nu = 0, \tag{4.9}$$

where the "polarization tensor" is

$$(\Pi^{\alpha\beta})^{\mu\nu}(k) \equiv \eta^{\mu\nu} + \sqrt{2}G_{\rm F} \int {\rm d}\Gamma\ g_\Gamma^{\alpha\beta} \frac{v^\mu v^\nu}{v\cdot k - \omega_V}. \tag{4.10}$$

The polarization tensor explicitly does not contain any velocity mode v_μ, so it has non-trivial solutions providing the dispersion relation:

$$\det\left[\Pi^{\alpha\beta}(k)\right] = 0. \tag{4.11}$$

The dispersion relation $(\omega, \boldsymbol{k})$ is determined by the neutrino spectra $g_\Gamma^{\alpha\beta}$ and the vacuum frequency ω_V. If the dispersion relation shows a positive imaginary part of frequency k, the flavor correlation $\rho^{\alpha\beta}$ grows exponentially and leads to flavor conversions in the $\alpha - \beta$ sector. The presence of zero crossings in the neutrino spectra g_Γ results in the existence of collective flavor instability [81, 82]. Spectral crossings in the energy distribution provide slow flavor instability, while those in the angular distribution trigger fast flavor instability.

Since we now focus on the behaviors of fast modes, we neglect the vacuum term ω_V and suppress the excitation of slow modes. In the fast limit, $\omega_V \to 0$, the energy dependence in the r.h.s of Eq. (4.10) appears only in the neutrino spectra g_Γ, and we newly define the neutrino-flavor lepton number (NFLN) angular distribution for α flavor:

$$G_{\boldsymbol{v}}^\alpha = \sqrt{2}G_{\rm F} \int_{-\infty}^{+\infty} \frac{E^2 {\rm d}E}{2\pi^2} g_\Gamma^\alpha = \sqrt{2}G_{\rm F} \int_0^\infty \frac{E^2 {\rm d}E}{2\pi^2} \left[f_{\nu_\alpha}(\Gamma) - f_{\bar{\nu}_\alpha}(\Gamma)\right]. \tag{4.12}$$

Then, the polarization tensor is given by

$$\left(\Pi^{\alpha\beta}\right)^{\mu\nu}(k) = \eta^{\mu\nu} + \int \frac{{\rm d}\boldsymbol{v}}{4\pi} G_{\boldsymbol{v}}^{\alpha\beta} \frac{v^\mu v^\nu}{v\cdot k}, \tag{4.13}$$

where $G^{\alpha\beta}_{\boldsymbol{v}} \equiv G^{\alpha}_{\boldsymbol{v}} - G^{\beta}_{\boldsymbol{v}}$ is the NFLN difference:

$$G^{e\mu}_{\boldsymbol{v}} = G^{e}_{\boldsymbol{v}} - G^{\mu}_{\boldsymbol{v}} = \sqrt{2}G_{\rm F}\int \frac{E^2{\rm d}E}{2\pi^2}\left[(f_{\nu_e} - f_{\bar{\nu}_e}) - \left(f_{\nu_\mu} - f_{\bar{\nu}_\mu}\right)\right] \tag{4.14}$$

$$G^{e\tau}_{\boldsymbol{v}} = G^{e}_{\boldsymbol{v}} - G^{\tau}_{\boldsymbol{v}} = \sqrt{2}G_{\rm F}\int \frac{E^2{\rm d}E}{2\pi^2}\left[(f_{\nu_e} - f_{\bar{\nu}_e}) - (f_{\nu_\tau} - f_{\bar{\nu}_\tau})\right] \tag{4.15}$$

$$G^{\mu\tau}_{\boldsymbol{v}} = G^{\mu}_{\boldsymbol{v}} - G^{\tau}_{\boldsymbol{v}} = \sqrt{2}G_{\rm F}\int \frac{E^2{\rm d}E}{2\pi^2}\left[\left(f_{\nu_\mu} - f_{\bar{\nu}_\mu}\right) - (f_{\nu_\tau} - f_{\bar{\nu}_\tau})\right]. \tag{4.16}$$

Since the dispersion relation in the fast limit depends only on the NFLN angular distributions, the presence of the crossings become an important indicator diagnosing fast flavor conversions. In particular, the NFLN difference $G^{\alpha\beta}_{\boldsymbol{v}}$ is reduced to the electron leptron number (ELN) distribution $G^{e}_{\boldsymbol{v}}$ if we do not distinguish heavy-leptonic flavors, $f_{\nu_X} = f_{\bar{\nu}_X}$. On the other hand, if we consider core-collapse simulations with six-species treatments and the neutrino profiles contain the non-negligible muon leptron number (μLN) and tau lepton number (τLN) angular distributions, they may cancel out the ELN crossings [106]. Recent core-collapse simulation [39] has reported that muon creation inside a proto-neutron star provides the excess of $\bar{\nu}_\mu$ over ν_μ, while tauon creation still remains negligible because the rest mass of tauons ($m_\tau \approx 1777$ MeV) is much higher than the temperature and the electron chemical potential in the center. Shallow ELN crossings may disapper due to the negative μLN angular distribution. Also, the cross section of neutral-current scattering with nucleons for neutrinos is larger than for antineutrinos due to weak-magnetism corrections [174]. Thus, $\bar{\nu}_\tau$ is decoupled from matter at smaller radii than ν_τ and the asymmetry even for tauons emerges in the angular distributions.

4.2 Coherent scattering in the preshock region

The existence of ELN crossings in core-collapse supernovae has been surveyed by many works [100–103] and is classified into five possibilities [104]. Among them, the ELN crossing in the preshock region can be potentially generated regardless of the multidimensional effects of supernova dynamics [102]. The inwardly going components due to coherent neutrino-nucleus scattering form tiny ELN crossings and cause fast flavor conversions. The cross section depends on the square of neutrino energy, and antineutrinos generally have higher averaged energy than neutrinos. Thus, the scatterings of $\bar{\nu}_e$ are enhanced over ν_e due to the difference, giving rise to a backward negative crossing. However, this proposal is still limited to the linear stability analysis, and the flavor evolution in the nonlinear regime has not yet been explored. The discussion is also within the effective two-flavor case, where $\nu_X = \bar{\nu}_X$ is assumed, and the consideration of μLN and τLN angular distributions can lead to different results [106]. In particular, muon production in the supernova dynamics can make a significant difference in the heavy lepton number [39], obliterating shallow ELN crossings in the preshock region.

In this section, we focus on fast flavor conversions driven by tiny NFLN crossings in the preshock region. We calculate the nonlinear flavor evolution by decomposing it into radially parallel spatial Fourier modes. We also investigate the effect of heavy-leptonic

flavors on the excitation of fast modes in the three-flavor framework.

4.2.1 Evolution of Fourier modes

The flavor evolution is the same as Eq. 2.1 but for ignoring the collision terms. For neutrino density matrices ρ at space-time position $(t, \boldsymbol{x})$, it is given by

$$\mathrm{i}\left(\partial_t + \boldsymbol{v}\cdot\nabla\right)\rho(t,\boldsymbol{x},\Gamma) = [H(t,\boldsymbol{x},\Gamma), \rho(t,\boldsymbol{x},\Gamma)] \tag{4.17}$$

and

$$H(t,\boldsymbol{x},\Gamma) = U\frac{M^2}{2E}U^\dagger + v^\mu\Lambda_\mu + \sqrt{2}G_\mathrm{F}\int \mathrm{d}\Gamma' v^\mu v'_\mu \rho', \tag{4.18}$$

which expresses three types of neutrino oscillations: vacuum, matter, and collective neutrino oscillation. We can expand the density matrix to the polarization vectors and then the EoM can be recast to

$$\begin{aligned}(\partial_t + \boldsymbol{v}\cdot\nabla)\boldsymbol{P}_{\omega,\boldsymbol{v}} = {} & (\omega_\mathrm{V}\boldsymbol{B} + \lambda\boldsymbol{L}) \times \boldsymbol{P}_{\omega,\boldsymbol{v}} \\ & + \sqrt{2}G_\mathrm{F}\int \mathrm{d}\Gamma' v^\mu v'_\mu \boldsymbol{P}_{\omega',\boldsymbol{v}'} \times \boldsymbol{P}_{\omega,\boldsymbol{v}}.\end{aligned} \tag{4.19}$$

To confirm the dispersion relation from the linear stability analysis in the numerical nonlinear simulation, we transform the partial differential equation to a tower of ordinary differential equations decomposed by the Fourier expansion. The polarization vectors with spatial Fourier modes K are converted as

$$\boldsymbol{P}_{\omega,v}(t,x) = \sum_K \mathrm{e}^{\mathrm{i}Kx}\tilde{\boldsymbol{P}}^K_{\omega,v}(t). \tag{4.20}$$

Here, we assume an one-dimensional system only in the radial direction, and set the spatial modes $\boldsymbol{K}$ parallel to the radial direction as Ref. [102]. Also, we impose the axial symmetry around the radial direction and suppress the multi-azimuthal-angle instability in fast modes. Still in a nonlinear regime, the EoM is expressed by

$$\begin{aligned}\frac{\mathrm{d}}{\mathrm{d}t}\tilde{\boldsymbol{P}}^K_{\omega,v} = {} & -\mathrm{i}vK\tilde{\boldsymbol{P}}^K_{\omega,v} + (\omega_\mathrm{V}\boldsymbol{B} + \lambda\boldsymbol{L}) \times \tilde{\boldsymbol{P}}^K_{\omega,v} \\ & + \sum_{K'}\left[\sqrt{2}G_\mathrm{F}\int \mathrm{d}\Gamma' v^\mu v'_\mu \tilde{\boldsymbol{P}}^{K-K'}_{\omega',v'} \times \tilde{\boldsymbol{P}}^{K'}_{\omega,v}\right].\end{aligned} \tag{4.21}$$

The tower has a convolution term for the spatial modes K, and it can induce a cascade in the Fourier space. Here we discretize the spatial modes as $K = n_K K_0 = n_K \times 10\ \omega_\mathrm{V}$ to make it dimensionless and take them up to $n_K = 200$. Since we assume uniform angular distributions within the simulation system, we seed initial perturbation $\mathcal{O}(10^{-12})$ as white noise in the spacial Fourier modes. In this study, we take neutrino oscillation parameters as follows. We consider monochromatic energy spectra with the vacuum frequency $\omega_\mathrm{V} = 6.6\times10^{-4}\ \mathrm{m}^{-1}$ and the mass-squared difference ratio $\epsilon = \Delta m^2_{21}/\Delta m^2_{31} \sim 0.03$ within the three-flavor framework, and we assume the normal mass ordering. Also, we fix mixing angles $\theta_{12} = \theta_{13} = \theta_{23} = 10^{-3}$ to mimic the suppression due to matter oscillation, and $\lambda = 0$.

4.2.2 Angular distribution

The difference in the cross sections of coherent neutrino-nucleus scatterings between neutrinos and antineutrinos generates non-zero asymmetry in the preshock region. To investigate the nonlinear evolutions induced by zero crossings in the backward directions, we employ the following model for the radial angular distribution $g(v)$, which is the average of $G^{\alpha}_{\boldsymbol{v}}$ over the azimuthal angle and $v = \cos\theta$:

$$g(v) = g_b + g'_b(\mathrm{e}^{v+1} - 1) + g_f b^{v-1}, \tag{4.22}$$

where the parameters g_b, g'_b, g_f, and b for each flavor are chosen as shown in Table 4.1 (here $g(v)$ distinguishes neutrinos and antineutrinos) and the resultant NFLN angular distributions and their differences are shown in Fig. 4.1. This model is designed to reproduce the strongly forward-peaked angular distribution in the preshock region. We can understand the form of the distribution function by taking the asymptotic behaviors of $g(v)$ in $g_f \gg g_b, g'_b$ and $b^{-2} \ll g_b/g_f, g'_b/g_f$:

$$g(v) \sim \begin{cases} g_f b^{v-1} & \text{for } v \sim 1 \\ g_b + g'_b(v+1) & \text{for } v \sim -1 \end{cases} \tag{4.23}$$

and g_f is the intensity at $v = 1$, in the outgoing radial direction; b determines the sharpness of the forward peak and is considered to be larger for smaller radius of neutrinosphere R_ν (subscript ν is sometimes replaced by ν_e, for example, to denote R_ν for ν_e henceforth); g_b is the intensity at $v = -1$ and proportional to $L_\nu E_\nu R_\nu^{-2}$ in the bulb model in Ref. [102], where L_ν and E_ν are luminosity and mean energy, respectively; g'_b corresponds to the gradient at $v = -1$ and $\propto L_\nu E_\nu$ in the bulb model. We consider the following physical processes to choose the parameters in Table 4.1.

First, since $\bar{\nu}_e$ is decoupled from the matter at smaller radius than ν_e, $R_{\bar{\nu}_e} < R_{\nu_e}$ and $E_{\bar{\nu}_e} > E_{\nu_e}$ is satisfied. As a result, g_b, g'_b and b for $\bar{\nu}_e$ is larger than ν_e while g_f for $\bar{\nu}_e$ is usually smaller than ν_e. This process causes the ELN crossing as shown in the top panel of Fig. 4.1. The parameters we choose can indeed almost reproduce the angular distributions for ν_e and $\bar{\nu}_e$ in the realistic supernova model in Ref. [102]. Also, the luminosity of the heavy-leptonic neutrinos ν_X are smaller than ν_e and $\bar{\nu}_e$ while they have smaller (larger)

Flavor	g_b $(10^{26}\mathrm{cm}^{-3})$	g'_b $(10^{27}\mathrm{cm}^{-3})$	g_f $(10^{32}\mathrm{cm}^{-3})$	b (10^5)
ν_e	4	4.5	2.7	1.5
$\bar{\nu}_e$	4.5	6	2.5	2.5
$\nu_{\mu/\tau}$	3	6	1.5	4
$\bar{\nu}_\mu$	3.4	8.1	1.8	4.5
$\bar{\nu}_\tau$	3.2	7.2	1.6	4.5

Table 4.1. Parameters in the radial angular distribution function in Eq.(4.22).

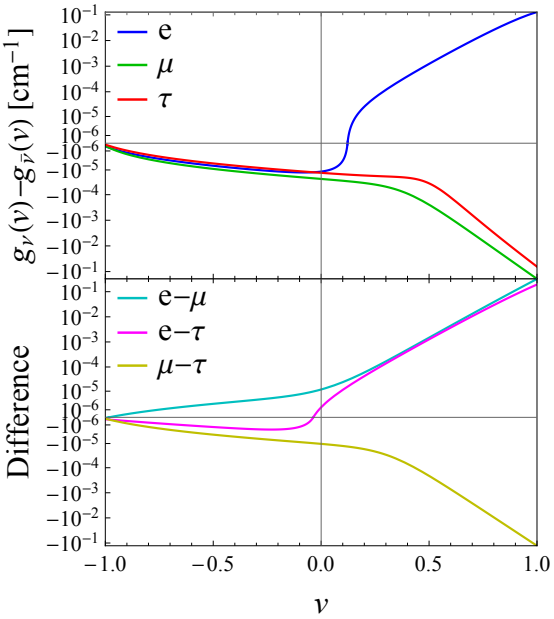

Figure 4.1. Top: the NFLN angular distribution G_v^α for each flavor α. The ELN angular distribution has a zero crossing, while the μLN and τLN angular distribution is always negative due to the effects of muon production and weak magnetism. Bottom: the difference $G_v^{\alpha\beta}$ between the NFLN angular distributions for two flavors α and β. Muon production in the supernova core enhances the emission of muon antineutrinos and erases the ELN crossing, while a crossing still survives only in the $e-\tau$ sector. In both panels, the vertical axes are scaled by the function $f(x) = \mathrm{sgn}(x)\log(1+10^6 x)$.

R_ν (E_ν) than $\bar\nu_e$. As a result, g_f (and possibly g_b) for ν_X is smaller than $\nu_e/\bar\nu_e$ while g_b' and b for ν_X may be larger.

Based on these ideas, we also take into account muon production [39, 175] and weak magnetism [174]. If muons were created deep in the core of the supernova, the μLN angular distribution would be lower due to the enhanced $\bar\nu_\mu$ emission. This effect cancels out the negative part of the ELN angular distribution and may eliminate the crossings in the NFLN difference in the $e-\mu$ sector. The weak-magnetism correction makes the cross section of neutral-current interactions for neutrinos larger than for antineutrinos. It makes R_ν for neutrinos larger than for antineutrinos, and thereby E_ν for neutrinos smaller than for antineutrinos. The model parameters for antinuetrinos reflect more forward-focusing and more scattered behaviors than for neutrinos. Smaller R_ν produces a more forward-focused angular distribution and larger E_ν enhances the coherent scattering. The effects of muon production and weak magnetism are not sufficiently clear to determine the angular distributions quantitatively, so we have used Ref. [39] as a reference to select the parameters that can generate the NFLN crossing. As seen in the bottom panel of Fig. 4.1, there exists a crossing only in the $e-\tau$ sector in our model. Note that if our model underestimates the correction to heavy-leptonic flavor neutrinos, the crossing may disappear. To obtain more accurate angular distributions of neutrinos, more realistic

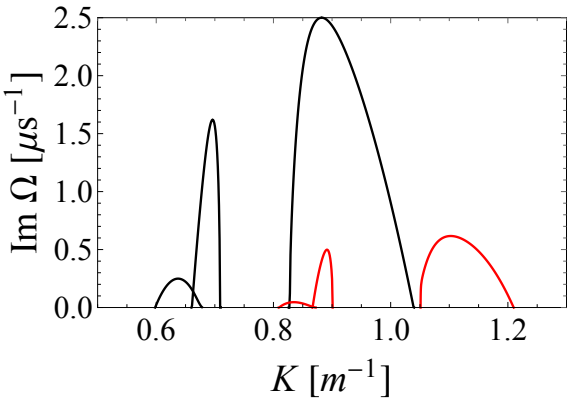

Figure 4.2. Growth rates ImΩ as a function of real K. Black lines are only for the ELN crossing $G^{e}_{\boldsymbol{v}}$ and red lines are for the NFLN difference $G^{e\tau}_{\boldsymbol{v}}$ within the three-flavor framework.

core-collapse simulations should be required.

Figure 4.2 shows the growth rate ImΩ as a function of real K. Black lines are unstable modes only for the ELN crossing within the effective two-flavor framework, and red lines are for the NFLN difference $G^{e\tau}_{\boldsymbol{v}}$ within the three-flavor framework. Since there are no crossings in $G^{e\mu}_{v}$ and $G^{\mu\tau}_{v}$, growing modes do not appear in the dispersion relation. Three branches are confirmed in the dispersion relation in both frameworks, and corresponding spatial modes are expected to be excited by the flavor instability in numerical simulation. The growth rate in the $e-\tau$ sector becomes about four times smaller than that for the ELN crossing within the two-flavor framework because the τLN angular distribution $G^{\tau}_{\boldsymbol{v}}$ partly weakens the ELN crossing. Note that we present the dispersion relation after transforming from (ω, k) in Eq.(4.11) into (Ω, K) because spatial modes given in numerical simulation are original K, not k.

For the angular distributions providing the two types of dispersion relation, we perform the flavor evolution as follows.

1. First, we consider only the ELN crossing within the effective two-flavor case, assuming $f_{\nu_X} = f_{\bar{\nu}_X}$. We perform the flavor evolution ignoring the vacuum term to confirm whether the flavor growth in the linear phase is consistent with the dispersion relation. The vacuum term not only triggers slow flavor conversions but has a role in generating flavor perturbation. We set white noise of $\mathcal{O}(10^{-12})$ in the initial spatial Fourier modes to mimic the role. To investigate the effect of the vacuum term, which is disregarded in the fast limit, we also perform the similar calculation including the vacuum term.
2. Second, we ignore the vacuum term to confirm the consistency, and perform the numerical simulation within the three-flavor framework considering the angular distribution of μLN and τLN. Similarly, we also perform the simulation including the vacuum term.

4.2.3 Effective two-flavor case only with ELN crossing

We first present the case omitting the vacuum term in the effective two-flavor case. The growth of flavor instability should follow the dispersion relation during the linear phase and can be read from the off-diagonal term of density matrix ρ_ν:

$$\begin{aligned} |\rho_{ex}^{n_K}| &= \left| \left\langle (\tilde{\boldsymbol{P}}^K_{\omega,v})^{(1)} - \mathrm{i}(\tilde{\boldsymbol{P}}^K_{\omega,v})^{(2)} \right\rangle \right| \\ &= \sqrt{\left| \left(\tilde{P}_r^{(1)} + \mathrm{i}\tilde{P}_i^{(1)} \right) - \mathrm{i} \left(\tilde{P}_r^{(2)} + \mathrm{i}\tilde{P}_i^{(2)} \right) \right|^2} \\ &= \sqrt{\left| \tilde{P}_r^{(1)} + \tilde{P}_i^{(2)} \right|^2 + \left| \tilde{P}_i^{(1)} - \tilde{P}_r^{(2)} \right|^2}, \end{aligned} \tag{4.24}$$

where $\tilde{P}_{r/i}^{(m)}$ are real and imaginary parts of the m-th components of the polarization vectors averaged over the angular distribution, respectively. Figure 4.3 shows the time evolution of the angle-averaged off-diagonal term. Flavor evolution in Fourier space shows two branches at early time $t < 6$ μs. The spatial Fourier space over which the excited modes spread coincides with the two unstable branches in Fig. 4.2. On the other hand, there are three branches in the dispersion relation, and the leftmost flavor instability with the lowest growth rate is missing. The growth rate of the leftmost flavor instability is about $\mathrm{Im}\Omega \sim (4\ \mu\mathrm{s})^{-1}$, which is an order of magnitude smaller than the peak of the rightmost branch with the largest growth rate. This means that the initial perturbation grows only about 4.5 times before the critical point $t \sim 6$ μs when a cascade starts to develop in Fourier space. As shown in Fig. 4.3, after $t \sim 6$ μs, the normally stable spatial modes grow rapidly through the nonlinear convolution term and cascade into all Fourier

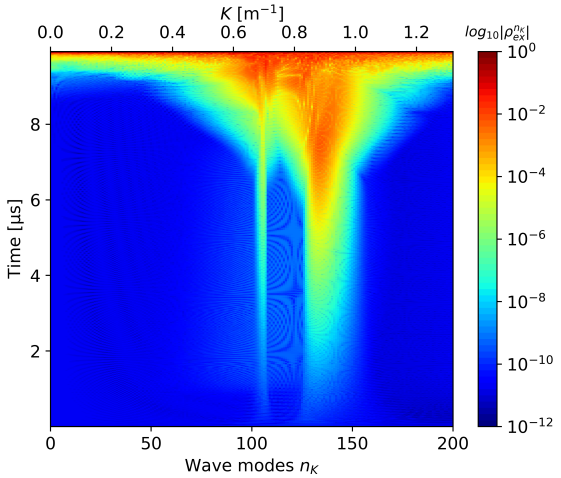

Figure 4.3. The case neglecting the vacuum term within the effective two-flavor framework. The time evolution of the angle-averaged off-diagonal term $|\rho_{ex}^{n_K}|$ for various spatial Fourier modes K. Spatial modes around $K = 0.7$ m^{-1} and 0.9 m^{-1} are first excited and then the flavor instabilities spread to different modes due to the nonlinear term after $t \sim 6\mu$s.

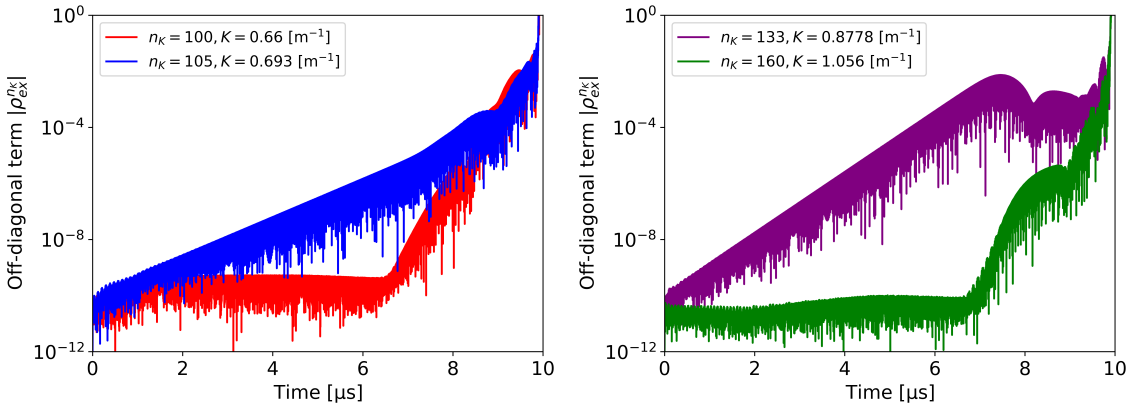

Figure 4.4. The time evolution of the off-diagonal term $|\rho_{ex}^{n_K}|$ with spatial Fourier mode K_n in the case omitting the vacuum term. Top panel is with $K = 0.66$ m^{-1} and 0.693 m^{-1}, inside and outside the middle branch, respectively. Bottom is with $K = 0.8778$ m^{-1} and 1.056 m^{-1}, inside and outside the rightmost branch, respectively.

modes. Therefore, the flavor growth due to the cascade covers up before this small flavor instability can grow sufficiently. Eventually, the flavor instability spreads over all spatial Fourier modes and small-scale structures appear in the flavor conversions.

Figure 4.4 shows the time evolution of the off-diagonal term $|\rho_{ex}^{n_K}|$ for some spatial modes. The top panel is for two spatial modes 0.66 m^{-1} and 0.693 m^{-1}, and the bottom for 0.8778 m^{-1} and 1.056 m^{-1}. For each panels, one corresponds to an unstable mode, as we can confirm in Fig. 4.2, and the other do a stable mode. The growth rates during the linear phase estimated from Fig. 4.4 are $\mathrm{Im}\,\Omega = 1.57$ μs^{-1} and 2.50 μs^{-1} for $K =$ 0.693 m^{-1} and 0.8778 m^{-1}, respectively. These growth rates coincide with the peaks of the two branches obtained by the dispersion relation in Fig. 4.2. On the other hand, the stable modes in Fig. 4.2 indeed do not grow in the linear phase before $t \sim 6$ μs while quickly grow after that due to the nonlinear effect.

For comparison, the flavor evolution including the vacuum term is performed and shown in Fig. 4.5. In this case, the spatial perturbation are naturally seeded by mixing angles within the vacuum term, and the self-interaction potential causes fast flavor conversion. The sharp excitation mode, corresponding to the middle branch in the Fig. 4.2, is noticeable, while the spatial modes, which seems to be the rightmost branch, are expanded and there is no gap between the two branches. In the preshock region, the self-interaction potential Φ is not large enough to completely neglect the vacuum frequency, and the slow instability associated with it may affect the evolution of fast modes. Ref. [176] suggests that unstable modes can emerge due to the mixing of fast and slow modes in the presence of the vacuum term, not only around the origin $k = 0$, but also at larger k. In our angular distribution model, the spatial mode k of the middle branch of Fig. 4.2 is located near the origin, and mixing of fast and slow modes may occur to fill the gap.

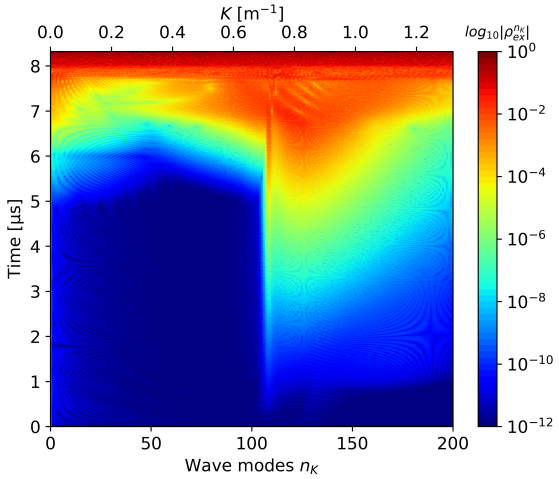

Figure 4.5. The same as Fig. 4.3 but for the inclusion of the vacuum term. The flavor evolution is largely different from the case omitting the vacuum term and may result from the presence of slow instability.

4.2.4 ELN+μLN+τLN angular distribution

Next, we show the nonlinear evolution within the three-flavor framework. In order to check the consistency with the results from the linear stability analysis, we first perform numerical simulations without the vacuum term similar to the effective two-flavor case. Figure 4.6 shows the three off-diagonal components of the density matrices $\rho^{e\mu}$, $\rho^{e\tau}$, and $\rho^{mu\tau}$. These evolution are derived from the NFLN differences $G^{e\mu}_{\boldsymbol{v}}$, $G^{e\tau}_{\boldsymbol{v}}$, and $G^{mu\tau}_{\boldsymbol{v}}$. Our model has a zero crossing only in $G^{e\tau}_{\boldsymbol{v}}$, leading to exponential growth in the $e-\tau$ sector. Excited spatial modes are absent in the $e-\mu$ and $\mu-\tau$ sectors because there are not crossings in both angular distributions. The fast instabilities evolve following the dispersion relation during the linear phase and reach the nonlinear phase around $t \sim 25$ μs, but the time scale is much slower than the two-flavor case. This is because the e-folding time predicted by the dispersion relation is about four times longer. Then, a cascade in Fourier space develops, and all spatial Fourier modes are excited at $t \sim 35\mu$s.

Similar to the two-flavor framework, we again consider the vacuum term. Figure 4.7 shows the flavor evolution of each off-diagonal part. The fast modes in the $e-\tau$ sector grow first same as the case of ignoring the vacuum term. Different from the absent case of the vacuum term is that the flavor instabilities in the $\mu-\tau$ and $e-\mu$ sectors are excited before a cascade in Fourier space begins. These behaviors are not seen in the linear stability analysis, and the propagation of the flavor instability across sectors is due to vacuum mixing and nonlinear terms. The fast modes in both inert sectors are not excited only by the difference in the corresponding NFLN angular distributions. The existence of growing modes is driven by the flavor instability leaking out of the $e-\tau$ sector due to vacuum mixing. The growing modes in the $e-\mu$ and $\mu-\tau$ sectors actually appear on exactly the same spatial modes K as in the $e-\tau$ sector. On the other hand, a slight

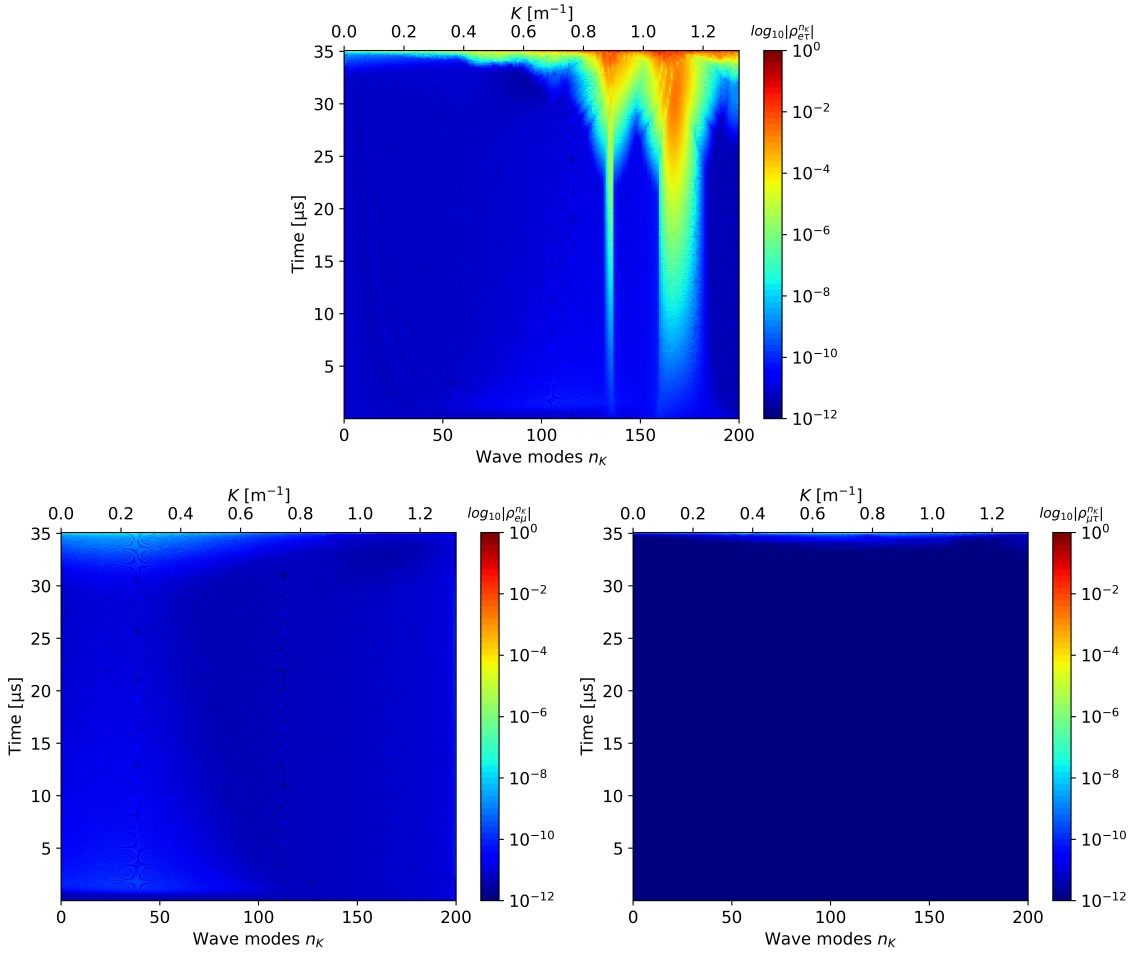

Figure 4.6. The same as Fig. 4.3 but for the three-flavor framework. From left to right panels: in the $e-\mu$, $e-\tau$, and $\mu-\tau$ sector. The flavor instability appears to grow only in the $e-\tau$ sector due to the crossing of the NFLN difference $G^{e\tau}_{\boldsymbol{v}}$.

difference between the vacuum mixing in the sectors results in the small difference, as seen in Fig. 4.7. Also, for the spatial modes $K > 1.2$ m^{-1}, unpredicted flavor instability emerges from the dispersion relation. Same as the effective two-flavor case in Sec.4.2.3, it may results from the existence of mixing between slow and fast modes [176].

Figure 4.8 shows the time evolution of the off-diagonal term $|\rho_{e\tau}|, |\rho_{e\mu}|, |\rho_{\mu\tau}|$ for $K = 1.089$ m^{-1} in each sector in the case including the vacuum term. The flavor instability in the $e-\tau$ sector first presents the linear growth, and then those in the $\mu-\tau$ and $e-\mu$ sectors start to evolve. The onset time of the linear growth in the inert sectors is later than the $e-\tau$ sector, while the growth rates are almost same. It is due to the difference among the mass term in three sectors. The three-flavor effects via the vacuum mixing have been reported in Ref. [108]. The propagation of flavor instability across sectors is derived by flavor mixing in the vacuum term.

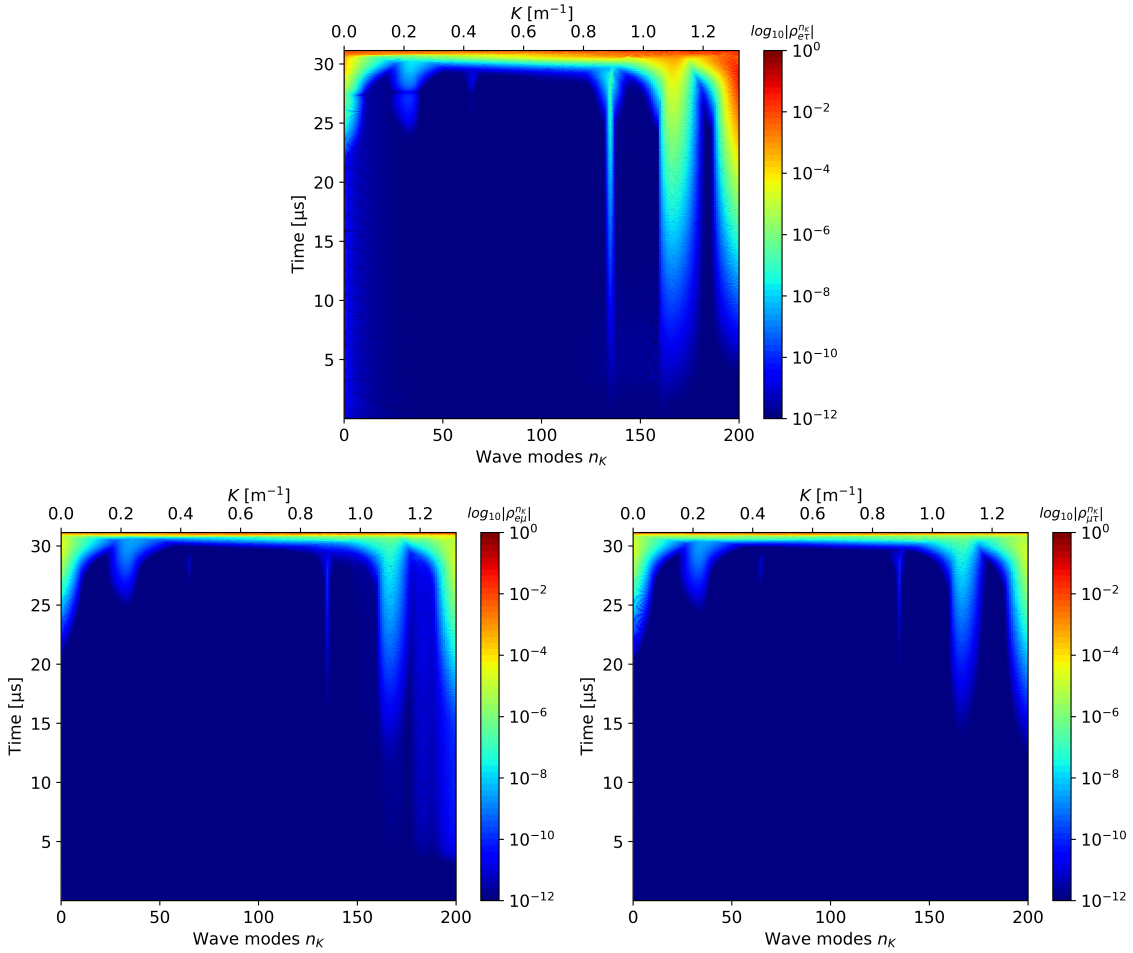

Figure 4.7. The same as Fig. 4.6 but for the inclusion of the vacuum term. The flavor evolution appears to grow not only in the $e-\tau$ sector but in both the $e-\mu$ and $\mu-\tau$ sectors, different from the case ignoring the vacuum term in Fig. 4.6.

4.2.5 Short summary

In this work, we have studied the nonlinear simulation on fast flavor conversion driven by a tiny NFLN crossing in the preshock region of core-collapse supernovae. We have exhibited that unstable fast modes obtained from the dispersion relation are indeed excited on the spatial Fourier space and reach the nonlinear phase. We have found that the mode convolution in the nonlinear self-coupling term drives induces the development of a cascade in Fourier space. Also, we have focused on the presence of non-zero μLN and τLN angular distributions, and have shown that the nonlinear flavor evolution presents the behaviors which are not predicted in the linear stability analysis.

Recent core-collapse simulation [39] has suggested out that the presence of heavy-leptonic flavors, particularly muon neutrinos, greatly influences fast flavor conversion through the NFLN difference. Muon production inside the proto-neutron star enhances the $\bar{\nu}_\mu$ emission. Also, within the six-species treatments $\nu_X \neq \bar{\nu}_X$, weak-magnetism cor-

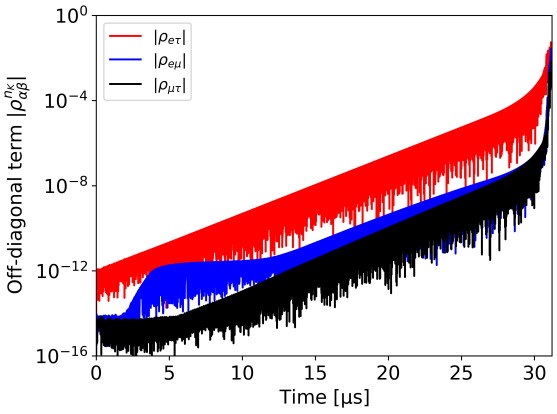

Figure 4.8. The same as Fig. 4.4 but for the three-flavor framework including the vacuum term. Red, blue, and black lines are for $e-\tau$, $e-\mu$, and $\mu-\tau$ sectors, respectively. The flavor instability in $e-\tau$ sector first grows, and then those in $e-\mu$ and $\mu-\tau$ sectors evolve.

rection makes the cross section of antineutrinos smaller. Therefore, the hierarchy $R_{\bar{\nu}} < R_{\nu}$ of the neutrino sphere radius is formed, and thereby the averaged energies and the angular distributions are modified. As a consequently, the negative μLN and τLN angular distributions are present and cancel out or weaken the ELN crossings. In our employed parametric model, the NFLN crossings in the $e-\tau$ sector only survive and induce the fast flavor instability. In our nonlinear simulation, flavor instabilities are excited only in the $e-\tau$ sector, but they propagate across the sectors via the vacuum mixings. In other words, the NFLN crossings even in only one sector can induce the collective fast flavor conversions among all flavors.

Also, In the linear regime, the vacuum term has usually been neglected and the unstable modes have been discussed in the fast limit. However, since the self-interaction potential in the preshock regime is not large enough to completely neglect the vacuum frequency, the slow instability associated with the vacuum term may affect the fast modes. The spatial Fourier modes have actually presented different flavor evolution compared to the case in the fast limit. Our findings suggest that more generic studies for several situations are required to clarify the flavor instability in the presence of the vacuum term.

4.3 Fast flavor conversion in 1D box

In Sec. 4.2, we demonstrated the behaviors of fast instability with spatial Fourier modes in the preshock region of core-collapse supernovae. A cascade develops in Fourier space as time passes, but it does not describe the time evolution of the spatial distribution in detail. Recently, Refs. [109–112] have investigated how fast flavor conversions develop in a one-dimensional box. The previous works have reported interesting features of fast flavor conversions such as coherent wave-like patterns and flavor equilibrium, though they employed non-realistic parametric angular distribution models only with a type-II crossing.

Here, we perform the time evolution of fast flavor conversion for three angular distributions with a type-I and II crossing in a local (1+1+1)-dimensional box by pseudo-spectral methods via Fast Fourier Transformation. In particularly, we focus how fast flavor conversions develop in the preshock region which we discussed in Sec. 4.2.

4.3.1 Formulation

Our calculation scheme is almost same as that in Sec. 4.2, but requires inverse Fourier transformation from Fourier space to configuration space in the last step. In the fast limit where we can ignore vacuum and matter term, the EoM for polarization vector $\boldsymbol{P}$ is given by

$$(\partial_t + v_z\partial_z)\boldsymbol{P}(t,z,v) = \boldsymbol{H}(t,z,v_z) \times \boldsymbol{P}(t,z,v_z). \tag{4.25}$$

Here, we assume the translation symmetries along the x and y directions and the axial-symmetry around z-direction. The Hamiltoninan for the neutrino self-interactions is

$$\boldsymbol{H}(t,z,v_z) = \mu \int_{-1}^{+1} \mathrm{d}v_z'(1 - v_z v_z') \left[g_\nu(v_z')\boldsymbol{P}(t,z,v_z') - \alpha g_{\bar{\nu}}(v_z')\overline{\boldsymbol{P}}(t,z,v_z') \right] \tag{4.26}$$

where $\mu = \sqrt{2}G_\mathrm{F} n_{\nu_e}$ and $\alpha = n_{\bar{\nu}_e}/n_{\nu_e}$ is a parameter which quantifies the asymmetry between neutrinos and antineutrinos. $g_{\nu(\bar{\nu})}$ are normalized angular distributions and the difference becomes the ELN angular distribution if we consider only electron type neutrinos:

$$G_e(v_z) \equiv g_{\nu_e}(v_z) - \alpha g_{\bar{\nu}_e}(v_z). \tag{4.27}$$

As long as we neglect the energy dependence derived from the vacuum frequency ω_V, we do not need to distinguish antineutrinos from neutrinos. Therefore, we can identify the polarization vector $\overline{\boldsymbol{P}}$ of antineutrinos with that $\boldsymbol{P}$ of neutrinos. We can rewrite Eq. (4.26) to

$$(\partial_t + v_z\partial_z)\,\boldsymbol{P}(t,z,v) = \left[\mu \int_{-1}^{+1} \mathrm{d}v_z'(1 - v_z v_z') G_e(v_z')\boldsymbol{P}(t,z,v_z') \right] \times \boldsymbol{P}(t,z,v_z). \tag{4.28}$$

The self-interaction potential μ is only a dimensional quantity in Eq. (4.28). Then, we redefine $\mu \equiv 1$ and set t and z as dimensionless ones with unit μ^{-1}.

In order to evaluate the spatial derivative ∂_z, we transform it into Fourier space. The spatial distribution of the polarization vector can be converted to the spatial Fourier modes K as

$$\mathcal{F}\left[\boldsymbol{P}(t,z,v_z)\right](K_m) = \frac{1}{N_\mathrm{FFT}} \sum_j \tilde{\boldsymbol{P}}^{K_m}(t,v_z)\ \mathrm{e}^{-\mathrm{i}K_m z_j} \tag{4.29}$$

$$\mathcal{F}^{-1}\left[\tilde{\boldsymbol{P}}^{K}(t,v_z)\right](z_j) = \sum_m \boldsymbol{P}(t,z_j,v_z)\ \mathrm{e}^{+\mathrm{i}K_m z_j}, \tag{4.30}$$

where $N_{\rm FFT}$ is a size of Fourier coefficients and also a normalization constant. Then, the EoM in the spacial Fourier space is

$$\partial_t \tilde{\boldsymbol{P}}^K(t,v_z) = -\mathrm{i}v_z K\tilde{\boldsymbol{P}}^K(t,v_z) + \sum_{K'} \tilde{\boldsymbol{H}}^{K-K'}(t,v_z)\times\tilde{\boldsymbol{P}}^{K'}(t,v_z) \tag{4.31}$$

$$= -\mathrm{i}v_z K\tilde{\boldsymbol{P}}^K(t,v_z) + \frac{1}{N_{\rm FFT}}\mathcal{F}\left[\mathcal{F}^{-1}\left[\tilde{\boldsymbol{H}}^K(t,v_z)\right]\times\mathcal{F}^{-1}\left[\tilde{\boldsymbol{P}}^K(t,v_z)\right]\right]. \tag{4.32}$$

The convolution term in Eq. (4.31) is converted according to the convolution theorem. The theorem allows the computational costs to reduce from $\mathcal{O}(N^2)$ in the convolution to $\mathcal{O}(N\log N)$ in the Fast Fourier transformation (FFT). The scheme which once returns from Fourier space to configuration space in calculating the nonlinear term is particularly called pseudo-spectral methods. Here, we perform the discrete Fourier transform using the `FFTW3` library[*1]. We can obtain the evolution of flavor contents in configuration space, solving the EoM for the polarization vector in Fourier space and returning it via the inverse FFT.

Note that we need to avoid aliasing errors due to the quadratically nonlinear interaction of Fourier modes. We explain the reasons below. We obtain by performing the Fourier transformation for the nonlinear term in the original EoM:

$$\mathcal{F}\left[\boldsymbol{H}\times\boldsymbol{P}\right] = \sum_{p=-K}^{K}\tilde{\boldsymbol{D}}_p\ \mathrm{e}^{\mathrm{i}px}. \tag{4.33}$$

On the other hand, since we perform the Fourier transformation for the individual polarization vectors not the whole EoM in the pseudo-spectral methods, the nonlinear term in Fourier space is

$$\boldsymbol{H}\times\boldsymbol{P} = \left(\sum_{p=-K}^{K}\tilde{\boldsymbol{H}}_p\ \mathrm{e}^{\mathrm{i}px}\right)\times\left(\sum_{q=-K}^{K}\tilde{\boldsymbol{P}}_q\ \mathrm{e}^{\mathrm{i}qx}\right) \tag{4.34}$$

$$= \sum_{r=-2K}^{2K}\tilde{\boldsymbol{D}}_r\ \mathrm{e}^{\mathrm{i}rx}, \tag{4.35}$$

where $\tilde{\boldsymbol{D}}_r$ are sum-products over $\tilde{\boldsymbol{H}}_p$ and $\tilde{\boldsymbol{P}}_q$. Comparing these two ways, we find that the nonlinear term in the pseudo-spectral methods includes an extra summation, particularly called *aliasing errors*:

$$\sum_{r=-2K}^{2K}\tilde{\boldsymbol{D}}_r\ \mathrm{e}^{\mathrm{i}rx} = \sum_{r=-K}^{K}\tilde{\boldsymbol{D}}_r\ \mathrm{e}^{\mathrm{i}rx} + \sum_{\substack{p+q=r\\ r=-2K}}^{2K}\left(\tilde{\boldsymbol{H}}_p\times\tilde{\boldsymbol{P}}_q\right)\ \mathrm{e}^{\mathrm{i}rx}. \tag{4.36}$$

The errors can not be resolved on the discrete Fourier space and are aliased into lower Fourier modes, leading to spurious rises. We need to eliminate the extra terms and de-alias the nonlinear term in the pseudo-spectral methods. The dealiasing procedure

[*1] Fastest Fourier Transform in the West, http://www.fftw.org

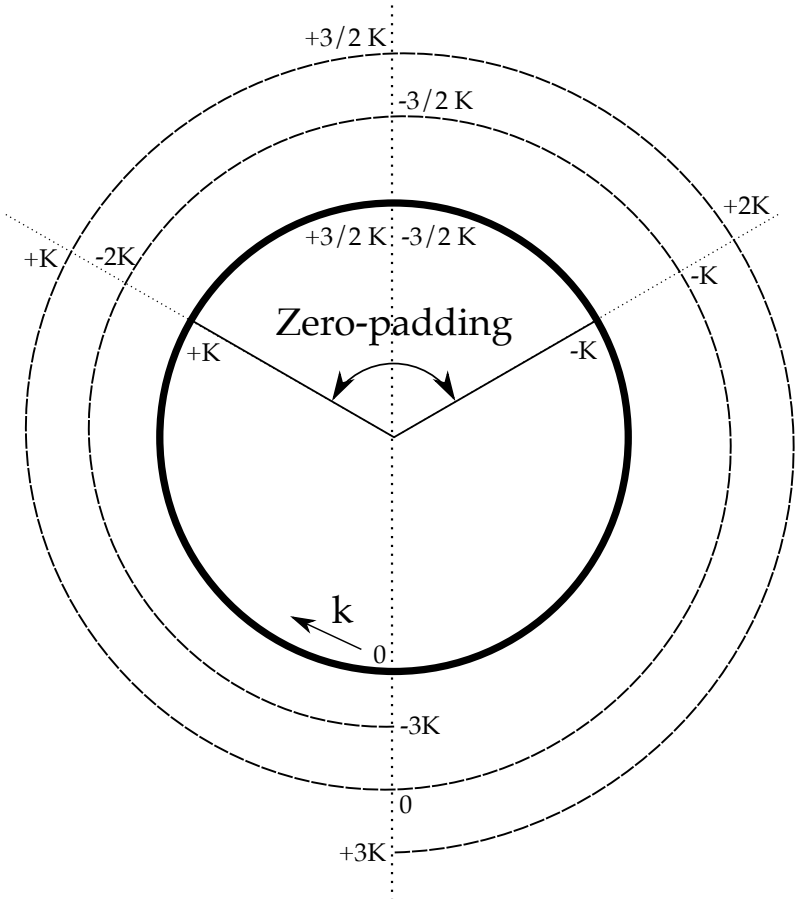

Figure 4.9. The "Aliasing Wheel", which describes the mechanism of the Two-Third Rule following Ref. [178]. Fourier mode k in the extended basis $k \in \left[-\frac{3}{2}K, +\frac{3}{2}K\right]$ is expressed as an angle of wheel in a polar coordinate system. Dashed line $k \in [-3K, 3K]$ corresponds to the Fourier modes generated by the quadratically nonlinear term. High zonal frequencies are aliased on the zero-padding range and we can obtain only the physical components.

has been studied extensively and the major one is the Two-Third (2/3) Rule by Orszag [177]. Figure 4.9 illustrates the mechanism of the Two-Third Rule, following Ref. [178]. We initially set the Fourier modes with $k \in [-K, K]$ on the polarization vectors. As the dealiasing procedure, we extend the Fourier basis into $k \in \left[-\frac{3}{2}K, \frac{3}{2}K\right]$, whose the extra Fourier modes $K < |k| \leq \frac{3}{2}K$ are zero-padded. The nonlinear term generates high zonal parts with the range $\frac{3}{2}K < |k| \leq 3K$ and they will be aliased onto the Fourier basis $k \in \left[-\frac{3}{2}K, \frac{3}{2}K\right]$ as shown with dashed line in Fig. 4.9. Since Fourier modes with $2K < |k| \leq 3K$ are combined between zero-padded frequencies through the nonlinear term, they also exhibit zero. On the other hand, there are non-zero products within $|k| \leq 2K$ and the extra terms with $\frac{3}{2}K < k \leq 2K$ are aliased into Fourier modes with $-\frac{3}{2}K < k \leq -K$. By discarding the zero-padded region $K < |k| \leq \frac{3}{2}K$ finally, we can obtain the nonlinear term only on the frequency range $|k| \leq K$. We require 3/2 times the size of the original Fourier basis and extract only 2/3 of the FFT data to remove aliasing

errors efficiently. This is the mechanism of the Two-Third Rule by Orszag.

4.3.2 Setup in Wu *et al.* 2021

Based on the above mentioned scheme, we simulate the developments of fast flavor conversions in an one-dimensional box. At first, we use the same initial conditions as adopted in Ref. [112] to confirm our numerical scheme. The employed angular distribution g_ν is the form presented in Ref. [98]:

$$g_{\nu(\bar{\nu})}(v_z) \propto \exp\left[-(v_z-1)^2/(2\sigma^2_{\nu(\bar{\nu})})\right] \tag{4.37}$$

satisfying normalization condition. Here we similarly take $\sigma_\nu = 0.6$ and $\sigma_{\bar{\nu}} = 0.5$, which describe more forward-peaked angular distribution of antineutrinos compared than neutrinos. Figure 4.10 shows the ELN angular distributions (left) with two types of asymmetry parameters $\alpha = 0.9$ and 1.3. This ELN angular distributions has a single zero crossing at $v_{z,c} \simeq 0.65$ for $\alpha = 0.9$ and $v_{z,c} \simeq 0.15$ for $\alpha = 1.3$, and are identified to type-II crossings according to the classification in Ref. [104]. The asymmetry parameter $\alpha = 0.9(1.3)$ expresses the excess of ν_e ($\bar{\nu}_e$) over $\bar{\nu}_e$ (ν_e), respectively. The numerical angular binning is spaced on the roots of the Legendre polynomial according to the Gauss-Legendre quadrature and the resolution is $N_v = 256$.

And we assume a one-dimensional box with the periodic boundary condition, which is always required using the spectral methods via Fourier space. We set the box size $L_z = 1200$ in $z \in [-600, 600]$ equally spanned with a fixed spatial resolution $N_z = 12000$. We also fix a timestep size $\Delta t = C_{\rm CFL}\Delta z$, where the Courant-Friedrichs-Lewy number $C_{\rm CFL} = 0.4$. Fast flavor conversion can evolve without the mass term, but actually requires the off-diagonal mixing angles in the vacuum term as a provider of perturbation seeds. In the fast limit, we need to provide some spatial perturbation artificially instead of the

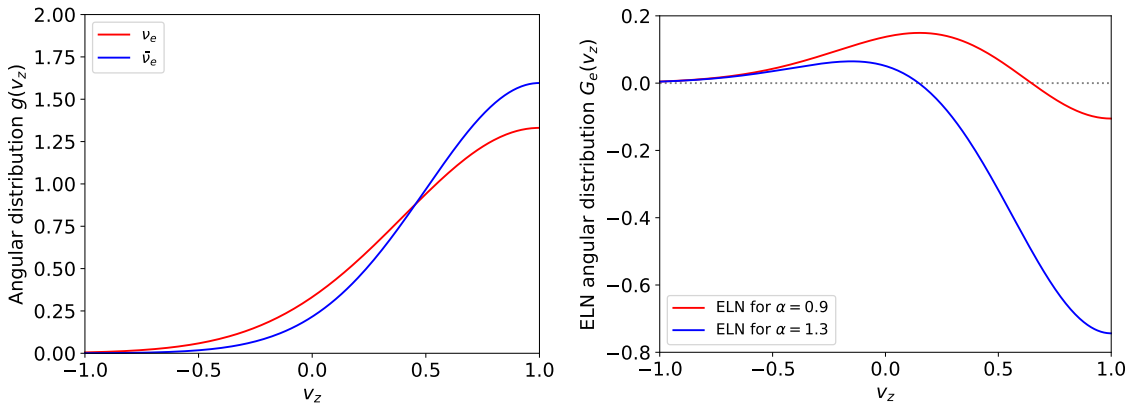

Figure 4.10. Left: angular distributions $g(v_z)$ of ν_e and $\bar{\nu}_e$. Right: ELN angular distribution $G_e(v_z)$. A zero crossing appears at $v_{z,c} \simeq 0.65$ for $\alpha = 0.9$ and at $v_{z,c} \simeq 0.15$ for $\alpha = 1.3$.

vacuum term. Then, we set each component of initial polarization vector,

$$P^{(1)}(t=0,z,v_z) = \epsilon(z) \tag{4.38}$$

$$P^{(2)}(t=0,z,v_z) = 0 \tag{4.39}$$

$$P^{(3)}(t=0,z,v_z) = \sqrt{1-\epsilon(z)^2}, \tag{4.40}$$

where $\epsilon(z)$ is the following spatial perturbation centered at $z=0$:

$$\epsilon(z) = \epsilon_0 \exp\left[-z^2/50\right]. \tag{4.41}$$

Here we take $\epsilon_0 = 10^{-6}$ similarly.

4.3.3 Results in Wu *et al.* 2021

Above the setup, we perform the flavor evolution in a one-dimensional box. Figure 4.11 shows the time evolution of $P_\perp(t,z,v_z) \equiv \sqrt{P_1^2+P_2^2}$ (left panels) and $P_3(t,z,v_z)$ (right panels) for $\alpha = 0.9$ at $t = 400, 600, 1000, 1800$, and 2800. $P_\perp$ corresponds to the absolute value of the off-diagonal term $|\rho_\nu^{eX}|$ of neutrino density matrix. The same time snapshots are chosen as left panels of Fig. 3 in Ref. [112] and we can confirm that our results are consistent with the Wu's studies with different simulation schemes in evaluating the spatial derivative. A spatial Gaussian perturbation centered at $z=0$ flows toward the positive z, spreading out as time passes. Simultaneously, flavor conversions $P_3 < 1$ occur at (t,z,v_z) where $P_\perp$ approaches $\mathcal{O}(1)$. The flavor conversions appearing around $z = 200$ at $t = 400$ propagate toward the positive-z direction, leaving a wave-like pattern

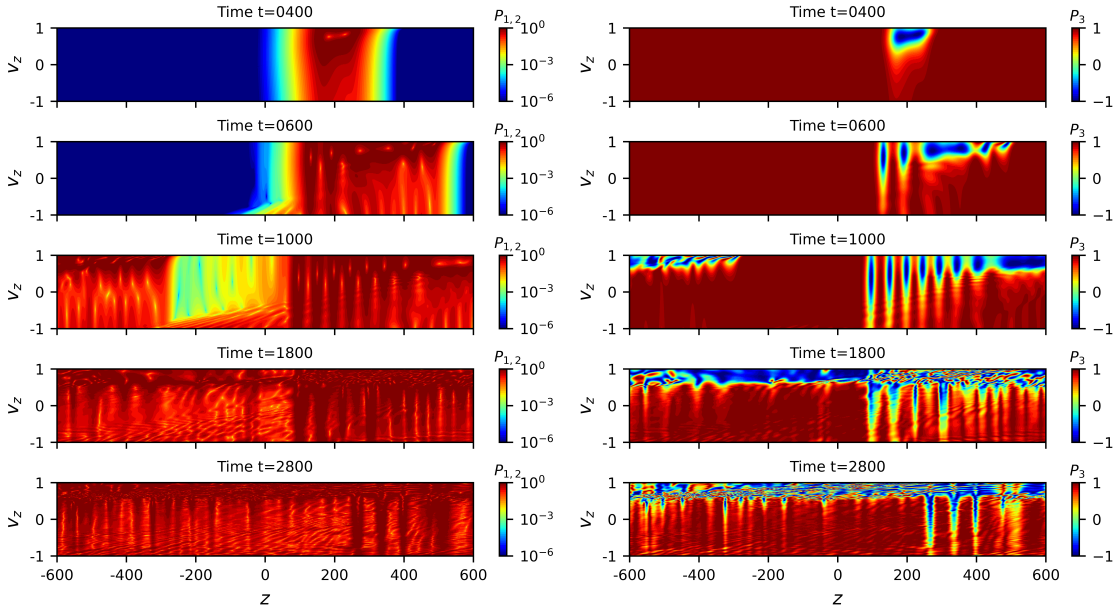

Figure 4.11. Snapshots of $P_\perp(t,z,v_z)$ (left panels) and $P_3(t,z,v_z)$ (right panels) at $t = 400, 600, 1000, 1800$, and 2800.

over all velocity directions behind. On the other hand, the forwardly-propagating waves are only on specific velocity modes, roughly above $v_{z,c} \simeq 0.65$. The stripe patterns slowly move backwards and the number also increases as time goes. If the box size we set is infinitely large, the wave-like patterns will fill the box and all velocity modes v_z will oscillate coherently. However, we assume the finite box size with periodic boundary conditions, and hence forwardly-going flavor instabilities crush the backwardly-moving components. The interaction happens at $t = 1200$ and we find that the coherent patterns are gradually broken. The collision with the flavor waves forms small-scale structures due to the nonlinear effects. Consequently, the flavor conversions develop for $v_z \gtrsim v_{z,c}$.

The check of the flavor growth in the spatial Fourier space helps us to understand such a flavor evolution. Figure 4.12 shows the time growth of the angle-averaged off-diagonal term $\langle \tilde{P}_\perp(t, K_z) \rangle$ of neutrino density matrix in Fourier space. Flavor instability with negative spatial modes $K \in [-0.3, 0]$ starts to evolve from initial Gaussian perturbation in the linear regime. After $t = 300$, flavor conversions appear in configuration space through the sufficiently growing flavor instabilities, which reach a nonlinear phase. A cascade develops in Fourier space due to the nonlinear effects and smaller-scale spatial modes are excited. The front part has small-scale structures at $t = 1000$ in Fig. 4.11, while

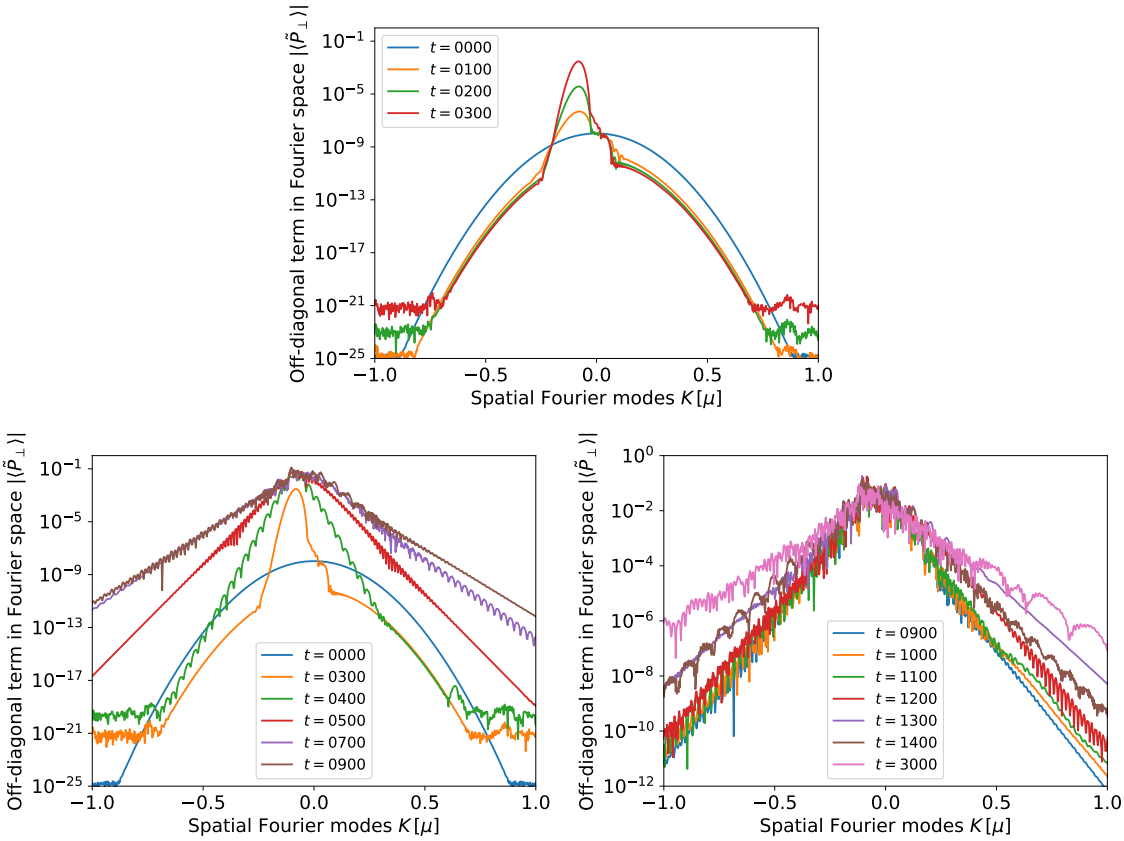

Figure 4.12. Top: the time evolution of $\langle \tilde{P}_\perp(t, K_z) \rangle$ before a cascade develops in Fourier space. Bottom left: after the cascade. Bottom right: after the flavor wave interacts with the slowly back-moving parts at $t = 1200$.

the development of the cascade reaches a limit. However, once the forward-propagating flavor wave interacts with the slowly backward-going component, the nonlinear interaction enhance the occurrence of small-scale structures. The behaviors appear in the spatial Fourier modes, and the saturated growth of flavor instabilities is accelerated again as seen in the bottom right panel of Fig. 4.12.

Figure 4.13 shows the averaged survival probabilities. The left panel expresses the time evolution of full-averaged survival probability:

$$\langle P_{ee}(t)\rangle = \int \mathrm{d}z\mathrm{d}v_z\ g_{\nu_e}(v_z)P_{ee}(t,z,v_z)\Big/\int \mathrm{d}z\mathrm{d}v_z\ g_{\nu_e}(v_z). \tag{4.42}$$

The survival probability starts to decrease at $t \sim 350$ and neutrino angular distributions abruptly approach the flavor equilibrium once flavor waves interact with slow-moving components at $t \sim 1200$. This behaviors mean that the coherent patterns over all velocity modes are broken and converted into the small-scale structures only on $v_z > v_{z,c}$. And the right panel of Fig. 4.13 is the space-averaged survival probabilities at each time snapshots:

$$\langle P_{ee}(t,v_z)\rangle = \int \mathrm{d}z\ P_{ee}(t,z,v_z)\Big/\int \mathrm{d}z. \tag{4.43}$$

The angular dependence of the averaged survival probability gradually appears as time passes. The formation of small-scale structures establishes the flavor equilibrium above the crossing point $v_{z,c}$, while eLN angular distribution $v_z \lesssim v_{z,c}$ roughly survives. Remaining large-scale flavor waves including coherent wave-like patterns is difficult to establish the full flavor equilibrium below the crossing direction.

The top panel of Fig. 4.14 shows the comparison between the space-averaged survival probability for $\alpha = 0.9$ and 1.3. In the both cases of asymmetry parameters, fast flavor conversions establish flavor equilibrium only in the some velocity directions. However, the side of the ELN angular distribution where flavor equilibrium occurs for $\alpha = 1.3$ is contrary to that for $\alpha = 0.9$. Although the initial ELN angular distribution for $\alpha = 0.9$ is negative above the crossing direction $v_{z,c}$, the total electron number density $n_{\nu_e} - n_{\bar{\nu}_e}$ is positive.

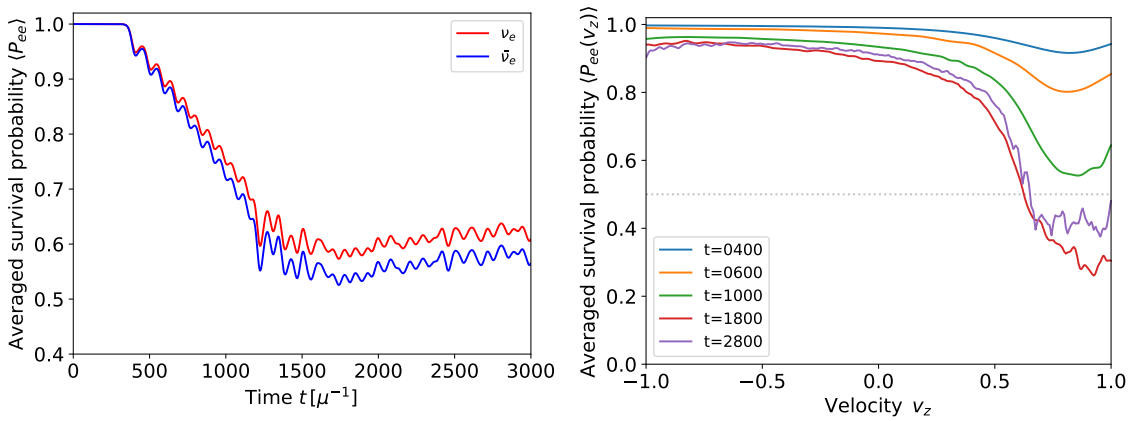

Figure 4.13. Left: averaged survival probability $\langle P_{ee}(t)\rangle$ over angular and spatial distributions. Right: space-averaged survival probability $\langle P_{ee}(t,v_z)\rangle$.

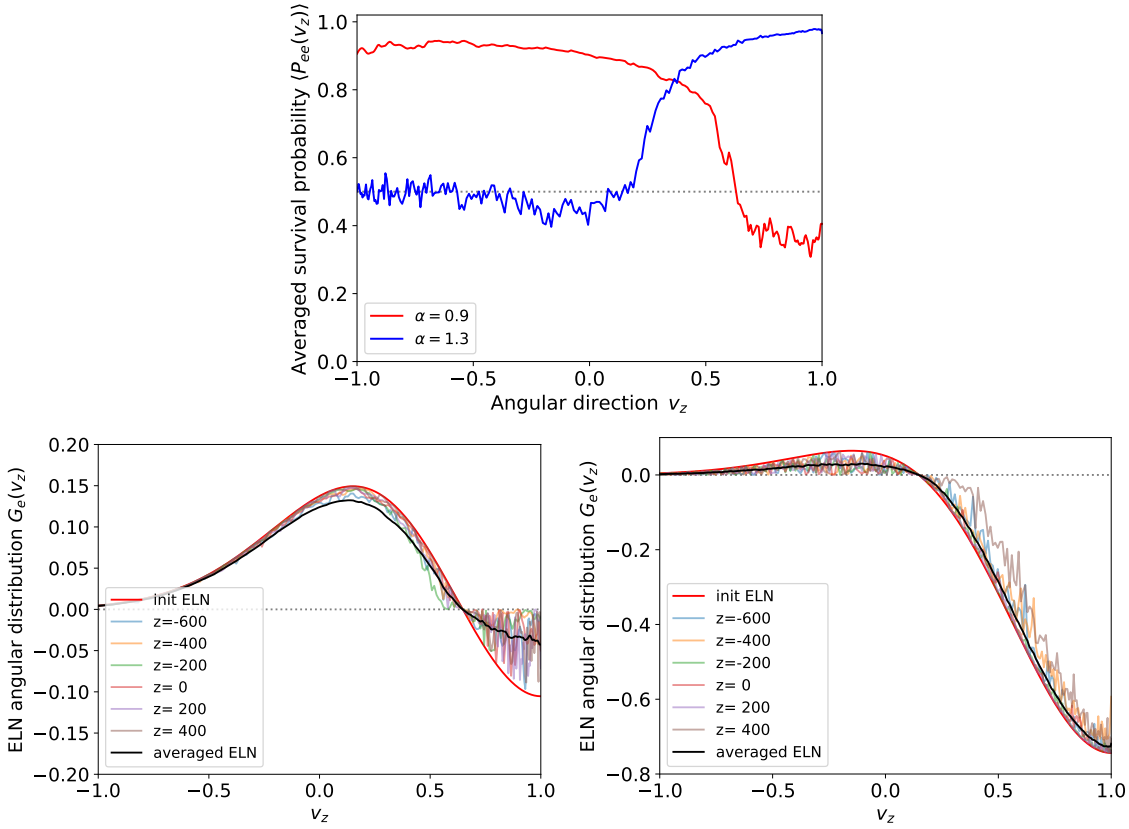

Figure 4.14. Top: Comparison in space-averaged survival probability $\langle P_{ee}(t, v_z)\rangle$ between $\alpha = 0.9$ and $\alpha = 1.3$ at $t = 3000$. Bottom: ELN angular distribution at each space z at $t = 3000$ for $\alpha = 0.9$ (left) and $\alpha = 1.3$ (right). Red and black thick lines are initial and final ELN angular distributions averaged over the spatial structure. Thin lines are final ELN distributions at each spatial point z.

The net electron-family number is globally conserved because fast instability induces the pairwise flavor conversion $\nu_e\bar{\nu}_e \leftrightarrows \nu_X\bar{\nu}_X$. Following the global conserved quantity when averaging over space, the flavor equilibrium weakens the type-II ELN crossing and tries to make the ELN angular distribution negative over all velocity modes. The bottom panels show the ELN angular distributions at $t = 3000$ for $\alpha = 0.9$ and 1.3, and thin solid lines are ones at each spatial point z. Comparing the initial ELN angular distribution to them, we find that the depths of the ELN crossing become shallower above the crossing direction. Globally, the angular distribution seems to be transferred from the positive side to the negative side of the ELN crossing. The behavior resembles the spectral splits appearing in the slow flavor conversions [120], triggered by the lepton number conservation. On the other hand, in the $\bar{\nu}_e$ excess case for $\alpha = 1.3$, the positive side of the ELN angular distribution, below the crossing direction, reaches flavor equilibrium and the ELN crossing becomes shallower. The angular distribution seems to be globally transferred from the negative side to the positive side of the ELN crossing because the net electron-family number density is negative.

4.3.4 With local perturbation in the preshock region

Next, we perform the flavor evolution for the angular distribution in the preshock region, similar to Sec.4.3.3. We assume the fast limit in order to focus only the development of fast flavor conversion and to neglect the impact of mixing between slow and fast modes as appeared in Fig. 4.5. The asymmetry parameter of the ELN angular distribution is $\alpha \sim 0.89$ and the strength of the self-interaction is $\mu_{\nu_e} \sim 1.5 \times 10^4$ km^{-1}. We set the box size as $L_z = 10000$ in $z \in [-5000, 5000]$ in unit of $\mu_{\nu_e}^{-1}$. We present the flavor evolution in the preshock region in Fig. 4.15. Flavor instability arising at $z = 0$ propagates toward the positive-z direction, but the growth of instability is slower than the case of the Wu's model in the previous subsection due to the growth rate. The front part mainly centered at the negative velocity modes spreads over all velocity directions, leaving coherent wave-like patterns behind. However, the backward-moving coherent flavor instabilities are too small to provide flavor conversions. When reaching the nonlinear regime at $t \sim 12000$, flavor conversions develop only in the backward directions. Moreover, the flavor waves interact with the slowly back-moving components before growing the coherent patterns and small-scale structures start to arise. Similarly, the growth of flavor instability in Fourier space helps us to understand the dynamics.

Figure 4.16 shows the angle-averaged off-diagonal term $\langle \tilde{P}_\perp(t, K_z) \rangle$ of neutrino density matrix with the spatial Fourier modes. In the left panel, the growth of flavor modes in Fourier space clearly exhibits the existence of two instability branches. The excited

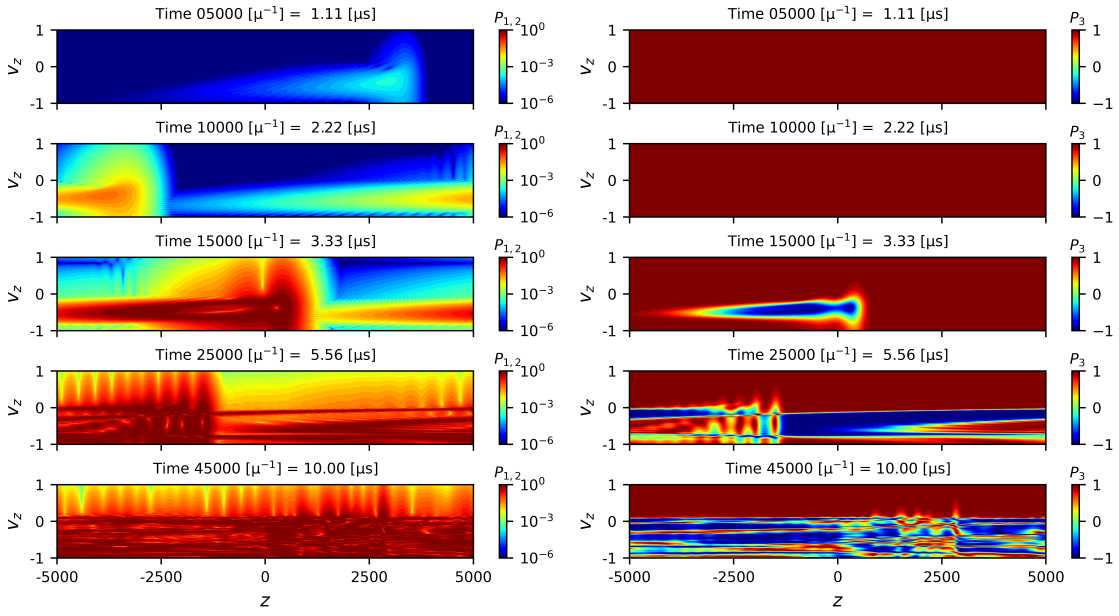

Figure 4.15. Dynamics of the polarization vector $\boldsymbol{P}(t, z, v_z)$ in the preshock region. Left panels are snapshots of $P_\perp(t, z, v_z)$ and right ones are $P_3(t, z, v_z)$ at $t = 5000, 10000, 15000, 25000$, and 45000.

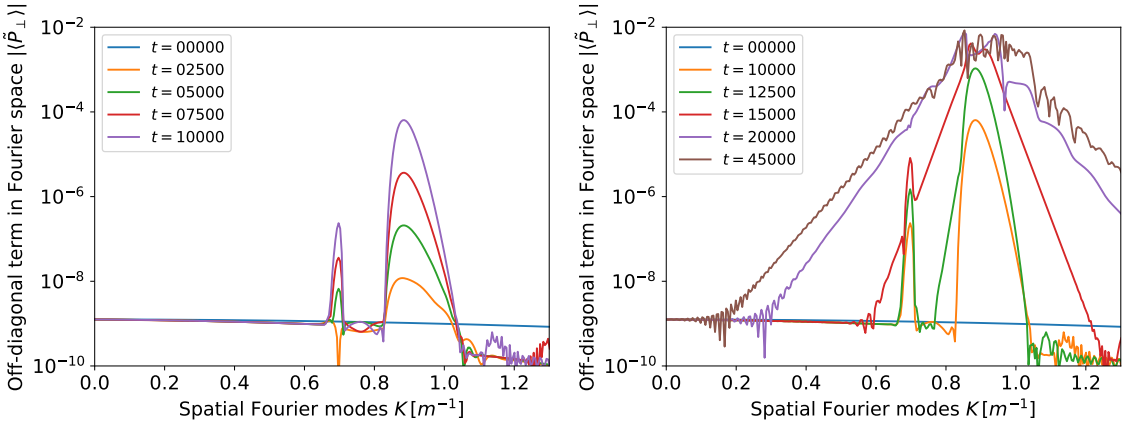

Figure 4.16. Left: the time evolution of $\langle \tilde{P}_\perp(t, K_z) \rangle$ before a cascade develops in Fourier space. Right: after the cascade.

Fourier modes K are consistent with the dispersion relation according to the linear stability analysis as seen in Fig. 4.2. As long as growing modes follow the dispersion relation, the flavor instability is within the linear evolution. Once flavor instability reaches the nonlinear regime at $t = 12500$, a cascade starts to develop in Fourier space. Simultaneously, flavor conversions appear on the P_3 plane as shown in Fig. 4.15 because the off-diagonal term can not be ignored compared to the diagonal term. Since the flavor wave interacts with the other components just after the occurrence of the flavor conversions, different from the cases in Fig. 4.12, the growth of the nonlinear cascade does not saturate.

Figure 4.17 shows the time evolution of full-averaged transition probabilities (left) and space-averaged survival probabilities at each time snapshot (right). The angular distribution in the preshock region is dominant in the forward directions $v_z > 0$ so that the averaged quantities over the angular distribution depend strongly on the forward components. That is why the full-averaged transition probability is much less than 1. The space-averaged survival probability in the right panel exhibits the angular dependence of flavor conversions. The survival probability decreases and reaches flavor equilibrium in the velocity modes below the crossing direction $v_{z,c} \sim 0.12$ as time passes. The flavor conversions occur mainly above the crossing direction $v_{z,c}$ in the type-II crossing case with the asymmetry parameter $\alpha = 0.9$ in Sec. 4.3.3, and the tendency is contrary to the type-I crossing case in the preshock region. As mentioned above, in the case of ν_e excess, the angular distribution seems to be transferred from the positive part of the ELN crossing to the negative. The ELN crossing in the preshock region is too shallow so that the positive part is hardly changed.

4.3.5 With random seed perturbation in the preshock region

We have assumed the periodic boundary condition to simulate how fast flavor conversion develops in an one-dimensional box. Spatial Gaussian perturbation centered at $z = 0$ propagates toward the positive direction and interacts with the slowly backward-moving

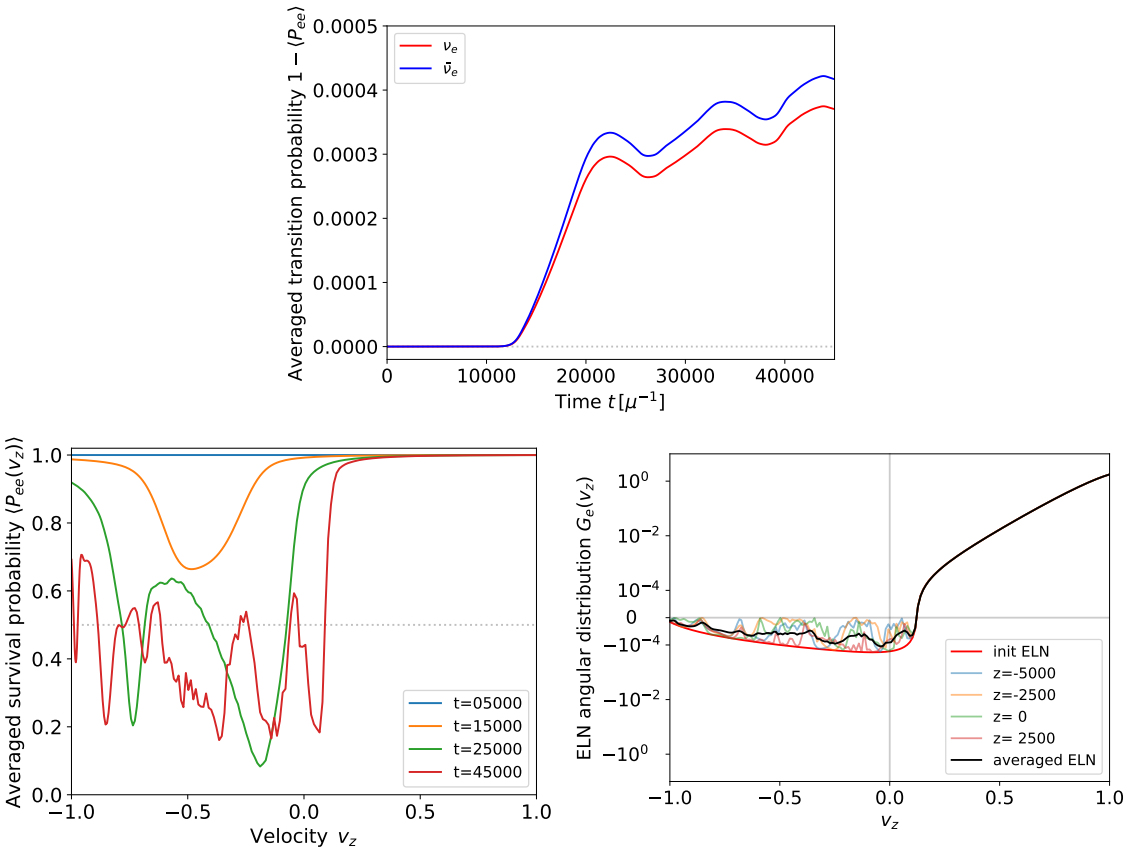

Figure 4.17. Top: averaged transition probability $1-\langle P_{ee}(t)\rangle$ over the spatial z and angular distribution v_z. Bottom left: averaged survival probability $\langle P_{ee}(t, v_z)\rangle$ only over the spatial distribution z. Bottom right: ELN angular distribution at each space z at $t = 3000$. Red and black thick lines are initial and final ELN angular distributions averaged over the spatial structure. Thin lines are final ELN distributions at each spatial point z.

components. That interaction only happens because we imposed the boundary conditions, which are not realistic descriptions. However, even in the realistic cases, the nonlinear interactions with nearby flavor waves can occur because fast flavor instabilities are triggered and excited everywhere by the spatial deviation of neutrino distribution. The more realistic evolution can be demonstrated to employ random seed perturbations as the initial conditions of the polarization vectors $P^{(1)}(t = 0, z, v_z) = \epsilon(z)$. We take $\epsilon(z)$ randomly scattered between 0 and ϵ_0 and present the time evolution in Fig. 4.18. In the top panel, flavor instabilities are excited everywhere by the randomly seeded spatial perturbations and interact with each other. That situation arises independently of the assumption of the periodic boundary conditions and demonstrates more realistic behaviors. Since the nonlinear interactions among the flavor instabilities immediately generate the small-scale structures, the flavor conversion does not possess the large-scale structures on the P_3 plane from the beginning. Therefore, the last stage of our simulation shows more depolarized fast flavor waves below the crossing direction. The difference between the local

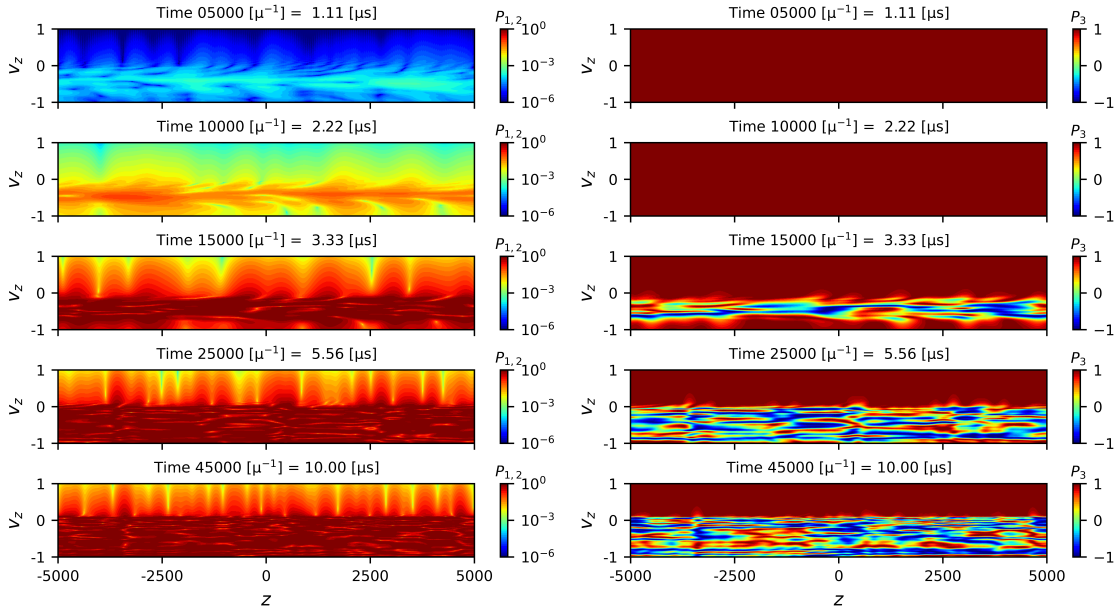

Figure 4.18. Same as Fig. 4.15, but for with the random seed perturbations.

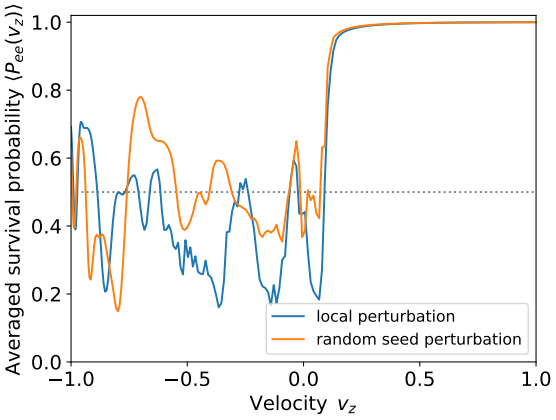

Figure 4.19. Same as Fig. 4.17, but for comparison between the local perturbation and the random seed perturbation.

Gaussian perturbation and the random seed perturbation shows in Fig. 4.19. In the case of the random seed perturbation, the space-averaged survival probability reaches flavor equilibrium $\langle P_{ee}\rangle \sim 0.5$ below the crossing direction, while the quantity in the case of the local perturbation is $\langle P_{ee}\rangle \sim 0.4$ and establishes the partial flavor equilibrium. The formation of large-scale structures such as coherent wave-like patterns is suppressed in the random perturbation case and the small-scale structures are dominant. Therefore, in more realistic spatial perturbation, the nonlinear interactions establish more complete flavor equilibrium.

4.3.6 Short summary

In this Sec. 4.3, we have investigated how fast flavor conversion occurs in a one-dimensional box. We have newly developed the solver with the pseudo-spectral methods via the Fast Fourier Transformation and performed the flavor evolution in the local (1+1+1)-D system (t, z, v_z) for three types of the ELN angular distributions: type-II crossing with asymmetry parameters $\alpha = 0.9$ and 1.3 employed by Wu *et al.* [112], and type-I crossing with $\alpha \sim 0.9$ corresponding to realistic models in the preshock region [102, 173].

With local spatial Gaussian perturbation, flavor instability arising at the box center evolves propagating toward the positive-z direction. In the linear phase at early time, the evolution follows the dispersion relation according to the linear stability analysis. Focusing the spatial Fourier modes of flavor instability, we clearly find when they go off the prediction by linear stability analysis and reach the nonlinear regime. In the nonlinear phase, fast flavor conversion shows the occurrence of wave-like patterns over all velocity modes and collisions between fast- and slowly-moving flavor waves. The nonlinear interactions break the coherent patterns and generate smaller-scale structures. Eventually, velocity modes above or below the crossing direction fill up with the small-scale structures and the ELN angular distribution reaches flavor equilibrium. In the case of type-II crossing for $\alpha = 0.9$, the flavor equilibrium occurs above the crossing point, while below the crossing direction for $\alpha = 1.3$. And the type-I crossing in the preshock region demonstrates the contrary behaviors to the type-II case.

Also, we have employed randomly-seeded spatial perturbation because descriptions that a flavor instability evolving from spatial perturbation centered at the origin interacts with itself are not realistic. In this case, flavor instabilities are excited everywhere and immediately interact with nearby components. Therefore, small-scale structures are formed before large-scale coherent patterns develop and closer states to flavor equilibrium are established when averaged over space.

Above the calculation results, the behaviors of flavor equilibrium in some velocity directions can be categorized by the crossing type and the asymmetry parameter α as Table 4.2. For $\alpha < 1$, the net electron-family number density is positive and the quantity is globally conserved. Fast flavor conversion triggered by the ELN crossing seems to transfer the distribution from the positive part to the negative. Thereby, the depth of the ELN crossing

	Type-I crossing	Type-II crossing
$\alpha < 1$ (ν_e excess)	FFC at $v_z < v_{z,c}$	FFC at $v_z > v_{z,c}$
$\alpha > 1$ ($\bar{\nu}_e$ excess)	Not investigated. But maybe FFC at $v_z > v_{z,c}$	FFC at $v_z < v_{z,c}$

Table 4.2. Categorization of fast flavor conversion (FFC) by the crossing type and the asymmetry parameter α. We describe the angular direction v_z where flavor equilibrium $\langle P_{ee} \rangle \sim 0.5$ occurs when averaging over space.

becomes shallower than the original angular distribution through the flavor equilibrium. The velocity modes where fast flavor conversion establishes flavor equilibrium are different in the crossing type. All the discussions are so far for the ELN angular distribution with a single crossing, but the existence of multiple crossings is possible in realistic core-collapse supernova models. We expect that fast flavor conversion would globally establish the flavor equilibrium and the ELN crossings are reduced to be shallower regardless of the number of crossings.

Chapter 5

Conclusion

In this dissertation, we have performed the nonlinear simulation on collective slow and fast flavor conversions in core-collapse supernovae. Collective neutrino oscillation is triggered by the asymmetry in the phase space distribution between neutrinos and antineutrinos. The spectral crossings, where the difference changes the sign at some momentum, are necessary and sufficient for the excitation of collective instabilities. The flavor instabilities are divided into two oscillation modes: slow and fast instabilities. Slow instability is triggered by the crossings in the energy distributions, while fast one is by the crossings in the angular distributions. Fast mode is driven only by the neutrino density n_ν and the growth is independent of the other vacuum and matter effects. On the other hand, slow mode is scaled by not only the self-interaction potential μ but the vacuum frequency ω_V. The two modes with different oscillation scales cause flavor conversions in core-collapse supernovae.

In chapter 3, we have mainly discussed the behaviors of slow flavor conversions. In the slow regime, we usually adopt the simulation model, called the bulb model, which requires a stationary and axisymmetric neutrino emission $(r; E_\nu, \theta_\nu)$ depending only on the radial direction. The bulb model demonstrates interesting spectral splits that the energy distribution is split above a critical energy. However, the flavor conversions can be suppressed by the high matter density such as near the proto-neutron star. The competition between the matter-induced phase dispersion due to the emission geometry and the phase synchronization due to the collective effects determines whether collective flavor conversion survives. In Sec. 3.1, we discussed the matter-induced suppression, following both the linear and nonlinear regime. Collective neutrino oscillation is completely suppressed due to the dense matter density profile at all time epochs, from the neutronization burst to the formation of a black hole, in our failed supernova model with a $40M_\odot$ progenitor. It means that emitted neutrinos undergo only the MSW resonances in the stellar envelope and are observed at the neutrino detectors. Therefore, the predicted neutrino event rate traces the time variation of neutrino luminosity and averaged energy, and provides the potential to solve the neutrino mass ordering problem. For less massive progenitors, collective neutrino oscillation can possibly overcome the matter suppression except during the accretion phase of core-collapse supernovae. In Sec. 3.2, we introduced symmetry breaking against the traditional bulb model: axisymmetry breaking and spatio-

temporal instability, which can potentially break the matter suppression. In particular, since non-zero pulsating modes $p \neq 0$ can decrease the effective matter effects $\bar{\lambda}$, slow flavor conversion could occur even during the accretion phase. Axial-symmetry breaking induces the multi-azimuthal-angle (MAA) instability in the geometry and can trigger flavor conversions independent of the neutrino mass orderings. Recent underground experimental results suggest that the normal mass ordering is favored over the inverted case and the traditional bulb model is generally unstable only in the inverted mass ordering. The inclusion of axial-symmetry breaking makes us possible to discuss more generally in the neutrino signal prediction. We have investigated the impact of axial-symmetry breaking adopting an electron-capture supernova model with an $8.8M_{\odot}$ progenitor. It is found that the growth of flavor instability is enhanced in the MAA case compared to the axial-symmetric bulb model and it breaks the complete matter suppression at some time snapshot. The behaviors are confirmed using our extended linear stability analysis scheme within the three-flavor framework including the mixing angles. Also, the revival and re-suppression of collective neutrino oscillation are present in the predicted neutrino event rate in the current and future neutrino detectors. In Sec. 3.3, we considered a neutrino halo, which generates broader intersection angles due to the coherent neutrino-nucleus scatterings. Neutrinos free-streamingly propagate through the stellar envelope after diffusing out of the proto-neutron star. However, a small fraction of them can be scattered off the background nuclei and nucleons and changes the propagating direction. The direction-changing scattering creates outward-going and inward-directed components and affects the self-interaction potentials. In our iron core-collapse supernova model with a $9.6M_{\odot}$, the contribution from the inward-scattered halo neutrinos can not be neglected compared to the outward-propagating neutrino flux inside the shock wave. However, at such a time epoch, high matter density completely suppresses collective neutrino oscillation and the halo effects together. On the other hand, the outward components induce a delay in the onset of collective flavor conversions outside the shock wave, where the contribution from the inward ones can be ignored. The inclusion of the halo neutrinos sharpens spectral swaps due to collective neutrino oscillation and makes the neutrino signal more clearly distinct from the thermal emission.

In chapter 4, we have mainly explored the nonlinear effects of fast flavor conversions. Fast instability is triggered by a zero crossing in the neutrino flavor lepton number (NFLN) angular distribution. The occurrence of fast flavor conversion is equivalent to the presence of the angular crossing, and various supernova dynamics provides the possibility of the appearance. Here, we focused on fast flavor conversion in the preshock region of core-collapse supernovae. As mentioned in Sec. 3.3, coherent neutrino-nucleus scattering can change the propagation direction, and generate inward- and outward-going neutrino flux. The cross section depends on the square of neutrino energy, and antineutrinos generally have higher averaged energy than neutrinos due to the hierarchy of the neutrino sphere radius. Therefore, antineutrinos become dominant in the backward direction, and a shallow angular crossing is produced. In Sec. 4.2, we considered the impact of the inclusion of the vacuum term and the angular distribution of the non-electron type neutrinos on the

fast instability. Muon production inside the proto-neutron star enhances the $\bar{\nu}_\mu$ emission. Also, weak-magnetism correction makes the neutrino sphere of antineutrinos smaller and the angular distribution more forward-focusing. As a consequence, the μLN and τLN angular distributions can not be neglected and affect the excitation of fast instability within six-species treatments $f_{\nu_X} \neq f_{\bar{\nu}_X}$. In our parametric angular distribution model, the ELN crossing is entirely vanished by the negative μLN angular distribution, and the NFLN crossing in the $e-\tau$ sector only survives. In the linear phase, flavor instability is excited only in the $e-\tau$ sector, following the dispersion relation. Still, the instability propagates across the other sectors and flavor conversion can appear among all flavors due to the flavor mixing in the vacuum term. In Sec. 4.3, we have performed the flavor evolution considering fast flavor instability in the local (1+1+1)-dimensional system (t, z, v_z). We employed two types of ELN angular distributions with type-I and type-II crossings. In both cases, the excited flavor wave propagates toward the positive-z direction and creates large-scale oscillation. After that, the forward-going component interacts with a backward-moving component and generates the smaller-scale structures. The nonlinear wave interaction establishes flavor depolarization when averaging over space only above or below the crossing directions. In the case of the ν_e excess, the positive parts of the ELN angular distribution seem to be transferred into the negative due to fast flavor conversions. In the case of the $\bar{\nu}_e$ excess, the contrary trends appear from the negative to the positive. The description is much simpler than expected, but if it is universal, it provides an important hint about the inclusion of fast flavor conversion to the core-collapse simulations.

We have discussed slow and fast flavor conversions in core-collapse supernovae following the nonlinear simulation models. However, several improvements in our employed simulation box still remain to be explored in the future. For slow flavor conversion, we have assumed the stationary emission. Spatio-temporal instability certainly can overcome the matter suppression, but it is a pulsating mode and not the time evolution. We need to consider time-growing modes in Laplace space not Fourier space like as the dispersion relation approach against fast instability. And, our simulation for fast flavor conversion is still local and does not include the global effects such as the geometry of neutrino trajectory, considered in the bulb model. We do not include the impacts of the vacuum term and heavy-leptonic flavors as considered in Sec. 4.2. Also, recent investigation suggests that the collision term enhances or damps fast flavor conversions [107, 110, 179, 180]. Although there remain many obstacles ahead to unravel collective neutrino oscillation, it will be achieved in the future if we take one step at a time.

Acknowledgments

First of all, I would like to express my greatest appreciation to my supervisor Hideyuki Umeda for his support, discussions, and encouragement on my research over the years. Thanks to him, I met many collaborators and accomplished excellent research. I would like to express my sincere gratitude to the collaborators Takashi Yoshida, Kohsuke Sumiyoshi, Kei Kotake, Tomoya Takiwaki, Shunsaku Horiuchi, and John F. Cherry. Discussions with them have constantly stimulated me and refined our works. I would like to thank my colleague, Taiki Morinaga, who has the same research field. It was a blessing that we collaborated and published our paper while still doctoral students. I am also profoundly grateful to all the members of the Department of Astronomy and, particularly, my laboratory members for their support and every discussion over many years. And I am grateful to the researchers who have discussed and commented with me in my participating conferences and workshops.

I appreciate indications and suggestions by the examiners, Toshikazu Shigeyama (chief), Tomonori Totani, Takeru Suzuki, Yudai Suwa, and Shoichi Yamada, which improve the quality of this dissertation.

Also, I would like to thank my many stuffed animals. Some of them have sometimes brought me a good night's sleep, some of them have sometimes watched over my research beside me, and some of them have sometimes helped me relax during breaks. And I want to thank my friends for playing games with me. Without the refreshments, I would not be able to achieve my works.

I would like to thank my parents and brother for their understanding and continuous support during my entire life. They have given me many opportunities to satisfy my interests in astrophysics.

Finally, I would like to thank my wife for understanding my career in academia and cheering me up. Thanks to her mental and financial support, I have continued my research without hesitation. This dissertation has never been accomplished without her help.

The author is supported by the Japan Society for Promotion of Science (JSPS) Grant-in-Aid for JSPS Fellows (Grants No. 20J13631) from the Ministry of Education, Culture, Sports, Science, and Technology (MEXT) in Japan. Numerical computations were in part carried out on Cray XC50 at the Center for Computational Astrophysics, National Astronomical Observatory of Japan.

References

[1] K. Hirata, T. Kajita, M. Koshiba, M. Nakahata, Y. Oyama, N. Sato, A. Suzuki, M. Takita, Y. Totsuka, T. Kifune, T. Suda, K. Takahashi, T. Tanimori, K. Miyano, M. Yamada, E. W. Beier, L. R. Feldscher, S. B. Kim, A. K. Mann, F. M. Newcomer, R. Van, W. Zhang, and B. G. Cortez, Physical Review Letters **58**, 1490 (1987).

[2] K. S. Hirata, T. Kajita, M. Koshiba, M. Nakahata, Y. Oyama, N. Sato, A. Suzuki, M. Takita, Y. Totsuka, T. Kifune, T. Suda, K. Takahashi, T. Tanimori, K. Miyano, M. Yamada, E. W. Beier, L. R. Feldscher, W. Frati, S. B. Kim, A. K. Mann, F. M. Newcomer, R. Van Berg, W. Zhang, and B. G. Cortez, Physical Review D **38**, 448 (1988).

[3] R. M. Bionta, G. Blewitt, C. B. Bratton, D. Casper, A. Ciocio, R. Claus, B. Cortez, M. Crouch, S. T. Dye, S. Errede, G. W. Foster, W. Gajewski, K. S. Ganezer, M. Goldhaber, T. J. Haines, T. W. Jones, D. Kielczewska, W. R. Kropp, J. G. Learned, J. M. LoSecco, J. Matthews, R. Miller, M. S. Mudan, H. S. Park, L. R. Price, F. Reines, J. Schultz, S. Seidel, E. Shumard, D. Sinclair, H. W. Sobel, J. L. Stone, L. R. Sulak, R. Svoboda, G. Thornton, J. C. van der Velde, and C. Wuest, Physical Review Letters **58**, 1494 (1987).

[4] W. D. Arnett, J. N. Bahcall, R. P. Kirshner, and S. E. Woosley, Ann. Rev. Astron. Astrophys. **27**, 629 (1989).

[5] J. Arafune and M. Fukugita, Physical Review Letters **59**, 367 (1987).

[6] J. N. Bahcall, T. Piran, W. H. Press, and D. N. Spergel, Nature **327**, 682 (1987).

[7] B. Jegerlehner, F. Neubig, and G. Raffelt, Physical Review D **54**, 1194 (1996).

[8] F. Vissani, Journal of Physics G: Nuclear and Particle Physics **42**, 013001 (2014).

[9] H.-T. Janka, Annual Review of Nuclear and Particle Science **62**, 407 (2012).

[10] S. Zha, S.-C. Leung, T. Suzuki, and K. Nomoto, The Astrophysical Journal **886**, 22 (2019).

[11] G. Martínez-Pinedo, Y. H. Lam, K. Langanke, R. G. T. Zegers, and C. Sullivan, Physical Review C **89**, 045806 (2014).

[12] S. Miyaji, K. Nomoto, K. Yokoi, and D. Sugimoto, Publications of the Astronomical Society of Japan **32**, 303 (1980).

[13] K. Nomoto, The Astrophysical Journal **277**, 791 (1984).

[14] F. S. Kitaura, H.-T. Janka, and W. Hillebrandt, Astronomy & Astrophysics **450**, 345 (2006).

[15] K. Takahashi, T. Yoshida, and H. Umeda, The Astrophysical Journal **771**, 28 (2013).

[16] S. Jones, F. K. Röpke, R. Pakmor, I. R. Seitenzahl, S. T. Ohlmann, and P. V. F. Edelmann, Astronomy & Astrophysics **593**, A72 (2016).

[17] S. Jones, F. K. Röpke, C. Fryer, A. J. Ruiter, I. R. Seitenzahl, L. R. Nittler, S. T. Ohlmann, R. Reifarth, M. Pignatari, and K. Belczynski, Astronomy & Astrophysics **622**, A74 (2019).

[18] D. Hiramatsu, D. A. Howell, S. D. Van Dyk, J. A. Goldberg, K. Maeda, T. J. Moriya, N. Tominaga, K. Nomoto, G. Hosseinzadeh, I. Arcavi, C. McCully, J. Burke, K. A. Bostroem, S. Valenti, Y. Dong, P. J. Brown, J. E. Andrews, C. Bilinski, G. G. Williams, P. S. Smith, N. Smith, D. J. Sand, G. S. Anand, C. Xu, A. V. Filippenko, M. C. Bersten, G. Folatelli, P. L. Kelly, T. Noguchi, and K. Itagaki, Nature Astronomy **5**, 903 (2021).

[19] Z. Barkat, G. Rakavy, and N. Sack, Physical Review Letters **18**, 379 (1967).

[20] G. Rakavy, G. Shaviv, and Z. Zinamon, The Astrophysical Journal **150**, 131 (1967).

[21] S. E. Woosley, A. Heger, and T. A. Weaver, Reviews of Modern Physics **74**, 1015 (2002).

[22] T. Yoshida, H. Umeda, K. Maeda, and T. Ishii, Monthly Notices of the Royal Astronomical Society **457**, 351 (2016).

[23] S. E. Woosley, The Astrophysical Journal **836**, 244 (2017).

[24] H. Umeda, T. Yoshida, C. Nagele, and K. Takahashi, The Astrophysical Journal **905**, L21 (2020).

[25] H. Umeda and K. Nomoto, The Astrophysical Journal **565**, 385 (2002).

[26] A. Heger and S. E. Woosley, The Astrophysical Journal **567**, 532 (2002).

[27] A. Kozyreva, S. Blinnikov, N. Langer, and S.-C. Yoon, Astronomy & Astrophysics **565**, A70 (2014).

[28] K. Takahashi, T. Yoshida, H. Umeda, K. Sumiyoshi, and S. Yamada, Monthly Notices of the Royal Astronomical Society **456**, 1320 (2016).

[29] K. Takahashi, The Astrophysical Journal **863**, 153 (2018).

[30] R. Farmer, M. Renzo, S. E. de Mink, P. Marchant, and S. Justham, The Astrophysical Journal **887**, 53 (2019).

[31] D. L. Tubbs and D. N. Schramm, The Astrophysical Journal **201**, 467 (1975).

[32] S. W. Bruenn, The Astrophysical Journal Supplement Series **58**, 771 (1985).

[33] C. J. Horowitz, Physical Review D **55**, 4577 (1997).

[34] A. Burrows, S. Reddy, and T. A. Thompson, Nuclear Physics A Special Isseu on Nuclear Astrophysics, **777**, 356 (2006).

[35] F. X. Timmes, S. E. Woosley, and T. A. Weaver, The Astrophysical Journal **457**, 834 (1996).

[36] Y. Suwa, T. Yoshida, M. Shibata, H. Umeda, and K. Takahashi, Monthly Notices of the Royal Astronomical Society **481**, 3305 (2018).

[37] K. Kotake, S. Yamada, and K. Sato, The Astrophysical Journal **595**, 304 (2003).

[38] J. R. Wilson, *Supernovae and Post-Collapse Behavior*, Numerical Astrophysics (1985) p. 422.

[39] R. Bollig, H.-T. Janka, A. Lohs, G. Martínez-Pinedo, C. J. Horowitz, and T. Melson,

Physical Review Letters **119**, 242702 (12 月 15, 2017).

[40] H.-T. Janka, Astronomy & Astrophysics **368**, 527 (2001).

[41] D. Radice, E. Abdikamalov, C. D. Ott, P. Mösta, S. M. Couch, and L. F. Roberts, Journal of Physics G: Nuclear and Particle Physics **45**, 053003 (2018).

[42] A. Burrows, J. Hayes, and B. A. Fryxell, The Astrophysical Journal **450**, 830 (1995).

[43] H.-T. Janka and E. Mueller, Astronomy and Astrophysics **306**, 167 (1996).

[44] J. M. Blondin, A. Mezzacappa, and C. DeMarino, The Astrophysical Journal **584**, 971 (2003).

[45] I. Tamborra and S. Shalgar, Annual Review of Nuclear and Particle Science (2021), 10.1146/annurev-nucl-102920-050505.

[46] N. Cabibbo, Physical Review Letters **10**, 531 (1963).

[47] M. Kobayashi and T. Maskawa, Progress of Theoretical Physics **49**, 652 (1973).

[48] B. Pontecorvo, Sov. Phys. JETP **6**, 429 (1957).

[49] B. Pontecorvo, Zh. Eksp. Teor. Fiz. **34**, 247 (1957).

[50] Particle Data Group, P. A. Zyla, R. M. Barnett, J. Beringer, O. Dahl, D. A. Dwyer, D. E. Groom, C. J. Lin, K. S. Lugovsky, E. Pianori, D. J. Robinson, C. G. Wohl, W. M. Yao, K. Agashe, G. Aielli, B. C. Allanach, C. Amsler, M. Antonelli, E. C. Aschenauer, D. M. Asner, H. Baer, S. Banerjee, L. Baudis, C. W. Bauer, J. J. Beatty, V. I. Belousov, S. Bethke, A. Bettini, O. Biebel, K. M. Black, E. Blucher, O. Buchmuller, V. Burkert, M. A. Bychkov, R. N. Cahn, M. Carena, A. Ceccucci, A. Cerri, D. Chakraborty, R. S. Chivukula, G. Cowan, G. D'Ambrosio, T. Damour, D. de Florian, A. de Gouvêa, T. DeGrand, P. de Jong, G. Dissertori, B. A. Dobrescu, M. D'Onofrio, M. Doser, M. Drees, H. K. Dreiner, P. Eerola, U. Egede, S. Eidelman, J. Ellis, J. Erler, V. V. Ezhela, W. Fetscher, B. D. Fields, B. Foster, A. Freitas, H. Gallagher, L. Garren, H. J. Gerber, G. Gerbier, T. Gershon, Y. Gershtein, T. Gherghetta, A. A. Godizov, M. C. Gonzalez-Garcia, M. Goodman, C. Grab, A. V. Gritsan, C. Grojean, M. Grünewald, A. Gurtu, T. Gutsche, H. E. Haber, C. Hanhart, S. Hashimoto, Y. Hayato, A. Hebecker, S. Heinemeyer, B. Heltsley, J. J. Hernández-Rey, K. Hikasa, J. Hisano, A. Höcker, J. Holder, A. Holtkamp, J. Huston, T. Hyodo, K. F. Johnson, M. Kado, M. Karliner, U. F. Katz, M. Kenzie, V. A. Khoze, S. R. Klein, E. Klempt, R. V. Kowalewski, F. Krauss, M. Kreps, B. Krusche, Y. Kwon, O. Lahav, J. Laiho, L. P. Lellouch, J. Lesgourgues, A. R. Liddle, Z. Ligeti, C. Lippmann, T. M. Liss, L. Littenberg, C. Lourengo, S. B. Lugovsky, A. Lusiani, Y. Makida, F. Maltoni, T. Mannel, A. V. Manohar, W. J. Marciano, A. Masoni, J. Matthews, U. G. Meißner, M. Mikhasenko, D. J. Miller, D. Milstead, R. E. Mitchell, K. Mönig, P. Molaro, F. Moortgat, M. Moskovic, K. Nakamura, M. Narain, P. Nason, S. Navas, M. Neubert, P. Nevski, Y. Nir, K. A. Olive, C. Patrignani, J. A. Peacock, S. T. Petcov, V. A. Petrov, A. Pich, A. Piepke, A. Pomarol, S. Profumo, A. Quadt, K. Rabbertz, J. Rademacker, G. Raffelt, H. Ramani, M. Ramsey-Musolf, B. N. Ratcliff, P. Richardson, A. Ringwald, S. Roesler, S. Rolli, A. Romaniouk, L. J. Rosenberg, J. L. Rosner, G. Rybka, M. Ryskin, R. A. Ryutin, Y. Sakai, G. P. Salam, S. Sarkar, F. Sauli, O. Schneider, K. Scholberg, A. J. Schwartz, J. Schwien-

ing, D. Scott, V. Sharma, S. R. Sharpe, T. Shutt, M. Silari, T. Sjöstrand, P. Skands, T. Skwarnicki, G. F. Smoot, A. Soffer, M. S. Sozzi, S. Spanier, C. Spiering, A. Stahl, S. L. Stone, Y. Sumino, T. Sumiyoshi, M. J. Syphers, F. Takahashi, M. Tanabashi, J. Tanaka, M. Taševský, K. Terashi, J. Terning, U. Thoma, R. S. Thorne, L. Tiator, M. Titov, N. P. Tkachenko, D. R. Tovey, K. Trabelsi, P. Urquijo, G. Valencia, R. Van de Water, N. Varelas, G. Venanzoni, L. Verde, M. G. Vincter, P. Vogel, W. Vogelsang, A. Vogt, V. Vorobyev, S. P. Wakely, W. Walkowiak, C. W. Walter, D. Wands, M. O. Wascko, D. H. Weinberg, E. J. Weinberg, M. White, L. R. Wiencke, S. Willocq, C. L. Woody, R. L. Workman, M. Yokoyama, R. Yoshida, G. Zanderighi, G. P. Zeller, O. V. Zenin, R. Y. Zhu, S. L. Zhu, F. Zimmermann, J. Anderson, T. Basaglia, V. S. Lugovsky, P. Schaffner, and W. Zheng, Progress of Theoretical and Experimental Physics **2020** (2020), 10.1093/ptep/ptaa104.

[51] Z. Maki, M. Nakagawa, and S. Sakata, Progress of Theoretical Physics **28**, 870 (1962).

[52] S. F. King and C. Luhn, Reports on Progress in Physics **76**, 056201 (2013).

[53] Super-Kamiokande Collaboration, Y. Fukuda, T. Hayakawa, E. Ichihara, K. Inoue, K. Ishihara, H. Ishino, Y. Itow, T. Kajita, J. Kameda, S. Kasuga, K. Kobayashi, Y. Kobayashi, Y. Koshio, M. Miura, M. Nakahata, S. Nakayama, A. Okada, K. Okumura, N. Sakurai, M. Shiozawa, Y. Suzuki, Y. Takeuchi, Y. Totsuka, S. Yamada, M. Earl, A. Habig, E. Kearns, M. D. Messier, K. Scholberg, J. L. Stone, L. R. Sulak, C. W. Walter, M. Goldhaber, T. Barszczxak, D. Casper, W. Gajewski, P. G. Halverson, J. Hsu, W. R. Kropp, L. R. Price, F. Reines, M. Smy, H. W. Sobel, M. R. Vagins, K. S. Ganezer, W. E. Keig, R. W. Ellsworth, S. Tasaka, J. W. Flanagan, A. Kibayashi, J. G. Learned, S. Matsuno, V. J. Stenger, D. Takemori, T. Ishii, J. Kanzaki, T. Kobayashi, S. Mine, K. Nakamura, K. Nishikawa, Y. Oyama, A. Sakai, M. Sakuda, O. Sasaki, S. Echigo, M. Kohama, A. T. Suzuki, T. J. Haines, E. Blaufuss, B. K. Kim, R. Sanford, R. Svoboda, M. L. Chen, Z. Conner, J. A. Goodman, G. W. Sullivan, J. Hill, C. K. Jung, K. Martens, C. Mauger, C. McGrew, E. Sharkey, B. Viren, C. Yanagisawa, W. Doki, K. Miyano, H. Okazawa, C. Saji, M. Takahata, Y. Nagashima, M. Takita, T. Yamaguchi, M. Yoshida, S. B. Kim, M. Etoh, K. Fujita, A. Hasegawa, T. Hasegawa, S. Hatakeyama, T. Iwamoto, M. Koga, T. Maruyama, H. Ogawa, J. Shirai, A. Suzuki, F. Tsushima, M. Koshiba, M. Nemoto, K. Nishijima, T. Futagami, Y. Hayato, Y. Kanaya, K. Kaneyuki, Y. Watanabe, D. Kielczewska, R. A. Doyle, J. S. George, A. L. Stachyra, L. L. Wai, R. J. Wilkes, and K. K. Young, Physical Review Letters **81**, 1562 (1998).

[54] C. Volpe, D. Väänänen, and C. Espinoza, Physical Review D **87**, 113010 (2013).

[55] L. Wolfenstein, Physical Review D **17**, 2369 (1978).

[56] S. P. Mikheyev and A. Y. Smirnov, Yadernaya Fizika **42**, 1441 (1985).

[57] W. C. Haxton, Physical Review Letters **57**, 1271 (1986).

[58] S. J. Parke, Physical Review Letters **57**, 1275 (1986).

[59] V. Barger, K. Whisnant, S. Pakvasa, and R. J. N. Phillips, Physical Review D **22**, 2718 (1980).

[60] H. W. Zaglauer and K. H. Schwarzer, Z.Phys.C **40**, 273 (1988).
[61] T. Ohlsson and H. Snellman, Journal of Mathematical Physics **41**, 2768 (2000).
[62] Z.-z. Xing, Physics Letters B **487**, 327 (8 月 17, 2000).
[63] K. Kimura, A. Takamura, and H. Yokomakura, Physical Review D **66**, 073005 (2002).
[64] T. K. Kuo and J. Pantaleone, Reviews of Modern Physics **61**, 937 (10 月 1, 1989).
[65] A. S. Dighe and A. Y. Smirnov, Physical Review D **62**, 033007 (2000).
[66] R. C. Schirato and G. M. Fuller, arXiv:astro-ph/0205390 (2002).
[67] C. Lunardini and A. Y. Smirnov, Journal of Cosmology and Astroparticle Physics **2003**, 009 (2003).
[68] G. L. Fogli, E. Lisi, A. Mirizzi, and D. Montanino, Physical Review D **68**, 033005 (2003).
[69] K. Takahashi, K. Sato, H. E. Dalhed, and J. R. Wilson, Astroparticle Physics **20**, 189 (2003).
[70] R. Tomàs, M. Kachelrieß, G. Raffelt, A. Dighe, H.-T. Janka, and L. Scheck, Journal of Cosmology and Astroparticle Physics **2004**, 015 (2004).
[71] M. Agostini, K. Altenmüller, S. Appel, V. Atroshchenko, Z. Bagdasarian, D. Basilico, G. Bellini, J. Benziger, D. Bick, G. Bonfini, D. Bravo, B. Caccianiga, F. Calaprice, A. Caminata, S. Caprioli, M. Carlini, P. Cavalcante, A. Chepurnov, K. Choi, L. Collica, D. D'Angelo, S. Davini, A. Derbin, X. F. Ding, A. Di Ludovico, L. Di Noto, I. Drachnev, K. Fomenko, A. Formozov, D. Franco, F. Gabriele, C. Galbiati, C. Ghiano, M. Giammarchi, A. Goretti, M. Gromov, D. Guffanti, C. Hagner, T. Houdy, E. Hungerford, A. Ianni, A. Ianni, A. Jany, D. Jeschke, V. Kobychev, D. Korablev, G. Korga, D. Kryn, M. Laubenstein, E. Litvinovich, F. Lombardi, P. Lombardi, L. Ludhova, G. Lukyanchenko, L. Lukyanchenko, I. Machulin, G. Manuzio, S. Marcocci, J. Martyn, E. Meroni, M. Meyer, L. Miramonti, M. Misiaszek, V. Muratova, B. Neumair, L. Oberauer, B. Opitz, V. Orekhov, F. Ortica, M. Pallavicini, L. Papp, Ö. Penek, N. Pilipenko, A. Pocar, A. Porcelli, G. Raikov, G. Ranucci, A. Razeto, A. Re, M. Redchuk, A. Romani, R. Roncin, N. Rossi, S. Schönert, D. Semenov, M. Skorokhvatov, O. Smirnov, A. Sotnikov, L. F. F. Stokes, Y. Suvorov, R. Tartaglia, G. Testera, J. Thurn, M. Toropova, E. Unzhakov, F. L. Villante, A. Vishneva, R. B. Vogelaar, F. von Feilitzsch, H. Wang, S. Weinz, M. Wojcik, M. Wurm, Z. Yokley, O. Zaimidoroga, S. Zavatarelli, K. Zuber, G. Zuzel, and The Borexino Collaboration, Nature **562**, 505 (2018).
[72] W. Haxton, R. Hamish Robertson, and A. M. Serenelli, Annual Review of Astronomy and Astrophysics **51**, 21 (2013).
[73] N. Vinyoles, A. M. Serenelli, F. L. Villante, S. Basu, J. Bergström, M. C. Gonzalez-Garcia, M. Maltoni, C. Peña-Garay, and N. Song, The Astrophysical Journal **835**, 202 (2017).
[74] J. N. Bahcall and C. Peña-Garay, New Journal of Physics **6**, 63 (2004).
[75] J. Pantaleone, Physical Review D **46**, 510 (1992).
[76] G. Sigl and G. Raffelt, Nuclear Physics B **406**, 423 (1993).

[77] Y.-Z. Qian and G. M. Fuller, Physical Review D **51**, 1479 (1995).
[78] A. B. Balantekin and Y. Pehlivan, Journal of Physics G: Nuclear and Particle Physics **34**, 47 (2006).
[79] B. Dasgupta, A. Dighe, G. G. Raffelt, and A. Y. Smirnov, Physical Review Letters **103**, 051105 (2009).
[80] A. Banerjee, A. Dighe, and G. Raffelt, Physical Review D **84**, 053013 (2011).
[81] T. Morinaga, arXiv:2103.15267 [astro-ph, physics:hep-ph] (2021).
[82] B. Dasgupta, arXiv:2110.00192 [astro-ph, physics:hep-ph, physics:hep-th] (2021).
[83] A. Esteban-Pretel, A. Mirizzi, S. Pastor, R. Tomàs, G. G. Raffelt, P. D. Serpico, and G. Sigl, Physical Review D **78**, 085012 (2008).
[84] S. Chakraborty, T. Fischer, A. Mirizzi, N. Saviano, and R. Tomàs, Physical Review Letters **107**, 151101 (2011).
[85] S. Chakraborty, T. Fischer, A. Mirizzi, N. Saviano, and R. Tomàs, Physical Review D **84**, 025002 (2011).
[86] G. Raffelt, S. Sarikas, and D. d. S. Seixas, Physical Review Letters **111**, 091101 (2013).
[87] A. Mirizzi, Physical Review D **88**, 073004 (2013).
[88] S. Chakraborty and A. Mirizzi, Physical Review D **90**, 033004 (2014).
[89] S. Chakraborty, R. S. Hansen, I. Izaguirre, and G. G. Raffelt, Journal of Cosmology and Astroparticle Physics **2016**, 028 (2016).
[90] S. Abbar and H. Duan, Physics Letters B **751**, 43 (2015).
[91] B. Dasgupta and A. Mirizzi, Physical Review D **92**, 125030 (2015).
[92] F. Capozzi, B. Dasgupta, and A. Mirizzi, Journal of Cosmology and Astroparticle Physics **2016**, 043 (2016).
[93] J. F. Cherry, J. Carlson, A. Friedland, G. M. Fuller, and A. Vlasenko, Physical Review Letters **108**, 261104 (2012).
[94] J. F. Cherry, J. Carlson, A. Friedland, G. M. Fuller, and A. Vlasenko, Physical Review D **87**, 085037 (2013).
[95] S. Chakraborty, R. S. Hansen, I. Izaguirre, and G. G. Raffelt, Journal of Cosmology and Astroparticle Physics **2016**, 042 (2016).
[96] I. Izaguirre, G. Raffelt, and I. Tamborra, Physical Review Letters **118**, 021101 (2017).
[97] F. Capozzi, B. Dasgupta, E. Lisi, A. Marrone, and A. Mirizzi, Physical Review D **96**, 043016 (2017).
[98] C. Yi, L. Ma, J. D. Martin, and H. Duan, Physical Review D **99**, 063005 (2019).
[99] F. Capozzi, G. Raffelt, and T. Stirner, Journal of Cosmology and Astroparticle Physics **2019**, 002 (2019).
[100] M. Delfan Azari, S. Yamada, T. Morinaga, H. Nagakura, S. Furusawa, A. Harada, H. Okawa, W. Iwakami, and K. Sumiyoshi, Physical Review D **101**, 023018 (2020).
[101] S. Abbar, H. Duan, K. Sumiyoshi, T. Takiwaki, and M. C. Volpe, Physical Review D **101**, 043016 (2020).
[102] T. Morinaga, H. Nagakura, C. Kato, and S. Yamada, Physical Review Research **2**,

012046 (2020).
[103] R. Glas, H.-T. Janka, F. Capozzi, M. Sen, B. Dasgupta, A. Mirizzi, and G. Sigl, Physical Review D **101**, 063001 (2020).
[104] H. Nagakura, A. Burrows, L. Johns, and G. M. Fuller, Physical Review D **104**, 083025 (2021).
[105] B. Dasgupta, A. Mirizzi, and M. Sen, Journal of Cosmology and Astroparticle Physics **2017**, 019 (2017).
[106] F. Capozzi, M. Chakraborty, S. Chakraborty, and M. Sen, Physical Review Letters **125**, 251801 (2020).
[107] S. Shalgar and I. Tamborra, Physical Review D **103**, 063002 (2021).
[108] S. Shalgar and I. Tamborra, Physical Review D **104**, 023011 (2021).
[109] J. D. Martin, C. Yi, and H. Duan, Physics Letters B **800**, 135088 (2020).
[110] J. D. Martin, J. Carlson, V. Cirigliano, and H. Duan, Physical Review D **103**, 063001 (2021).
[111] S. Bhattacharyya and B. Dasgupta, Physical Review Letters **126**, 061302 (2021).
[112] M.-R. Wu, M. George, C.-Y. Lin, and Z. Xiong, Physical Review D **104**, 103003 (2021).
[113] Y. Suwa, K. Kotake, T. Takiwaki, M. Liebendörfer, and K. Sato, The Astrophysical Journal **738**, 165 (2011).
[114] B. Dasgupta, E. P. O'Connor, and C. D. Ott, Physical Review D **85**, 065008 (2012).
[115] G. Kimura, Physics Letters A **314**, 339 (2003).
[116] S. Pastor, G. Raffelt, and D. V. Semikoz, Physical Review D **65**, 053011 (2002).
[117] S. Hannestad, G. G. Raffelt, G. Sigl, and Y. Y. Y. Wong, Physical Review D **74**, 105010 (2006).
[118] H. Duan, G. M. Fuller, J. Carlson, and Y.-Z. Qian, Physical Review D **75**, 125005 (2007).
[119] H. Duan, G. M. Fuller, J. Carlson, and Y.-Z. Qian, Physical Review D **74**, 105014 (2006).
[120] G. Fogli, E. Lisi, A. Marrone, and A. Mirizzi, Journal of Cosmology and Astroparticle Physics **2007**, 010 (2007).
[121] B. Dasgupta and A. Dighe, Physical Review D **77**, 113002 (2008).
[122] R. F. Sawyer, Physical Review D **72**, 045003 (2005).
[123] R. F. Sawyer, Physical Review Letters **116**, 081101 (2016).
[124] A. Mirizzi and R. Tomàs, Physical Review D **84**, 033013 (2011).
[125] I. Tamborra, B. Müller, L. Hüdepohl, H.-T. Janka, and G. Raffelt, Physical Review D **86**, 125031 (2012).
[126] I. Tamborra, G. Raffelt, F. Hanke, H.-T. Janka, and B. Müller, Physical Review D **90**, 045032 (2014).
[127] A. B. Balantekin and H. Yüksel, New Journal of Physics **7**, 51 (2005).
[128] H. Duan, A. Friedland, G. C. McLaughlin, and R. Surman, Journal of Physics G: Nuclear and Particle Physics **38**, 035201 (2011).
[129] G. Martínez-Pinedo, B. Ziebarth, T. Fischer, and K. Langanke, The European

Physical Journal A **47**, 1 (2011).

[130] M.-R. Wu, Y.-Z. Qian, G. Martínez-Pinedo, T. Fischer, and L. Huther, Physical Review D **91**, 065016 (2015).

[131] H. Sasaki, T. Kajino, T. Takiwaki, T. Hayakawa, A. B. Balantekin, and Y. Pehlivan, Physical Review D **96**, 043013 (2017).

[132] M. Zaizen, T. Yoshida, K. Sumiyoshi, and H. Umeda, Physical Review D **98**, 103020 (2018).

[133] M. Zaizen, J. F. Cherry, T. Takiwaki, S. Horiuchi, K. Kotake, H. Umeda, and T. Yoshida, Journal of Cosmology and Astroparticle Physics **2020**, 011 (2020).

[134] M. Zaizen, S. Horiuchi, T. Takiwaki, K. Kotake, T. Yoshida, H. Umeda, and J. F. Cherry, Physical Review D **103**, 063008 (2021).

[135] K. Sumiyoshi, S. Yamada, and H. Suzuki, The Astrophysical Journal **667**, 382 (2007).

[136] K. Sumiyoshi, S. Yamada, and H. Suzuki, The Astrophysical Journal **688**, 1176 (2008).

[137] T. Kuroda, K. Kotake, T. Takiwaki, and F.-K. Thielemann, Monthly Notices of the Royal Astronomical Society: Letters **477**, L80 (2018).

[138] S. E. Woosley and T. A. Weaver, The Astrophysical Journal Supplement Series **101**, 181 (1995).

[139] J. M. Lattimer and F. Douglas Swesty, Nuclear Physics A **535**, 331 (1991).

[140] S. Sarikas, D. de Sousa Seixas, and G. Raffelt, Physical Review D **86**, 125020 (2012).

[141] T. Morinaga and S. Yamada, Physical Review D **97**, 023024 (2018).

[142] H. Sekiya, Nuclear Physics B - Proceedings Supplements Proceedings of the Neutrino Oscillation Workshop, **237–238**, 111 (2013).

[143] H. Sekiya, Journal of Physics: Conference Series **718**, 062052 (2016).

[144] A. Strumia and F. Vissani, Physics Letters B **564**, 42 (2003).

[145] A. Ankowski, J. Beacom, O. Benhar, S. Chen, J. Cherry, Y. Cui, A. Friedland, I. Gil-Botella, A. Haghighat, S. Horiuchi, P. Huber, J. Kneller, R. Laha, S. Li, J. Link, A. Lovato, O. Macias, C. Mariani, A. Mezzacappa, E. O'Connor, E. O'Sullivan, A. Rubbia, K. Scholberg, and T. Takeuchi, arXiv:1608.07853 [astro-ph, physics:hep-ex, physics:hep-ph] (2016).

[146] T. Suzuki and M. Honma, Physical Review C **87**, 014607 (2013).

[147] T. Fischer, S. C. Whitehouse, A. Mezzacappa, F.-K. Thielemann, and M. Liebendörfer, Astronomy & Astrophysics **499**, 1 (2009).

[148] F. Capozzi, E. Di Valentino, E. Lisi, A. Marrone, A. Melchiorri, and A. Palazzo, Physical Review D **95**, 096014 (2017).

[149] F. Capozzi, E. Lisi, A. Marrone, and A. Palazzo, Progress in Particle and Nuclear Physics **102**, 48 (2018).

[150] P. F. de Salas, S. Gariazzo, O. Mena, C. A. Ternes, and M. Tórtola, Frontiers in Astronomy and Space Sciences **5** (2018), 10.3389/fspas.2018.00036.

[151] F. Capozzi, E. Di Valentino, E. Lisi, A. Marrone, A. Melchiorri, and A. Palazzo, Physical Review D **101**, 116013 (2020).

[152] I. Esteban, M. Gonzalez-Garcia, M. Maltoni, T. Schwetz, and A. Zhou, Journal of High Energy Physics **2020**, 178 (2020).

[153] P. F. de Salas, D. V. Forero, S. Gariazzo, P. Martínez-Miravé, O. Mena, C. A. Ternes, M. Tórtola, and J. W. F. Valle, Journal of High Energy Physics **2021**, 71 (2021).

[154] K. J. Kelly, P. A. N. Machado, S. J. Parke, Y. F. Perez-Gonzalez, and R. Z. Funchal, Physical Review D **103**, 013004 (2021).

[155] A. Kartavtsev, G. Raffelt, and H. Vogel, Physical Review D **91**, 125020 (2015).

[156] C. Döring, R. S. L. Hansen, and M. Lindner, Journal of Cosmology and Astroparticle Physics **2019**, 003 (2019).

[157] H. Sasaki, T. Takiwaki, S. Kawagoe, S. Horiuchi, and K. Ishidoshiro, Physical Review D **101**, 063027 (2020).

[158] M. Chakraborty and S. Chakraborty, Journal of Cosmology and Astroparticle Physics **2020**, 005 (2020).

[159] N. Tominaga, S. I. Blinnikov, and K. Nomoto, The Astrophysical Journal **771**, L12 (2013).

[160] K. Nakamura, T. Takiwaki, and K. Kotake, Publications of the Astronomical Society of Japan **71** (2019), 10.1093/pasj/psz080.

[161] E. O'Connor, R. Bollig, A. Burrows, S. Couch, T. Fischer, H.-T. Janka, K. Kotake, E. J. Lentz, M. Liebendörfer, O. E. B. Messer, A. Mezzacappa, T. Takiwaki, and D. Vartanyan, Journal of Physics G: Nuclear and Particle Physics **45**, 104001 (2018).

[162] K. Kotake, T. Takiwaki, T. Fischer, K. Nakamura, and G. Martínez-Pinedo, The Astrophysical Journal **853**, 170 (2018).

[163] T. Takiwaki, K. Kotake, and Y. Suwa, Monthly Notices of the Royal Astronomical Society: Letters **461**, L112 (2016).

[164] M. Liebendörfer, S. C. Whitehouse, and T. Fischer, The Astrophysical Journal **698**, 1174 (2009).

[165] A. Friedland, Physical Review Letters **104**, 191102 (2010).

[166] B. Dasgupta, A. Mirizzi, I. Tamborra, and R. Tomàs, Physical Review D **81**, 093008 (2010).

[167] A. Esteban-Pretel, S. Pastor, R. Tomàs, G. G. Raffelt, and G. Sigl, Physical Review D **76**, 125018 (2007).

[168] A. Heger and S. E. Woosley, The Astrophysical Journal **724**, 341 (2010).

[169] T. Takiwaki and K. Kotake, Monthly Notices of the Royal Astronomical Society: Letters **475**, L91 (2018).

[170] A. Mignone, Journal of Computational Physics **270**, 784 (2014).

[171] E. F. Toro, M. Spruce, and W. Speares, Shock Waves **4**, 25 (1994).

[172] T. Melson, H.-T. Janka, and A. Marek, The Astrophysical Journal **801**, L24 (2015).

[173] M. Zaizen and T. Morinaga, Physical Review D **104**, 083035 (2021).

[174] C. J. Horowitz, Physical Review D **65**, 043001 (2002).

[175] T. Fischer, G. Guo, G. Martínez-Pinedo, M. Liebendörfer, and A. Mezzacappa, Physical Review D **102**, 123001 (2020).

[176] S. Airen, F. Capozzi, S. Chakraborty, B. Dasgupta, G. Raffelt, and T. Stirner, Journal of Cosmology and Astroparticle Physics **2018**, 019 (2018).

[177] S. A. Orszag, Journal of the Atmospheric Sciences **28**, 1074 (1971).

[178] J. P. Boyd, *Chebyshev and Fourier Spectral Methods (Second Edition, Revised)* (Dover Publications, New York, 2001).

[179] C. Kato, H. Nagakura, and T. Morinaga, The Astrophysical Journal Supplement Series **257**, 55 (2021).

[180] H. Sasaki and T. Takiwaki, arXiv:2109.14011 [astro-ph, physics:hep-ph] (2021).